The University of Aston in Birmingham

Department of Physics

An Investigation into the Airflow over Heated Disruptive Surfaces by Holographic and Mathematical Techniques

A thesis submitted for the degree of Doctor of Philosophy by

Peter J. Bryanston-Cross

August 1977

To Rywka with many kind thoughts and much love

"Let him out when he's had enough"

Dr. Benjamin Spock

SUMMARY

An Investigation into the Airflow over Heated Disruptive Surfaces by Holographic and Mathematical Techniques

PETER JOHN BRYANSTON-CROSS

PhD 1977

This project, which is sponsored by a major motor manufacturer has set out to investigate the possibility of reducing the large amount of practical testing involved in the design of automotive heat exchangers.

This has been attempted by the use of non-contact measuring techniques, and Reynolds number scaled models. The two techniques developed are these of holographic interferometry and an electrically heated multiple strip element heat exchanger model.

A description has been made of the advantages and limitations of these techniques, and of the level to which mathematical analysis can be applied to the problem.

As part of the project a simple performance prediction model of an automotive heat exchanger has been constructed. Also a study has been made into the reconstruction techniques of three-dimensional refractive index fields.

A wind tunnel has been designed and constructed for operating in conjunction with the experimental techniques.

investigation surfaces holographic mathematical techniques

CONTENTS

Page

CHAPTER 1

CHAPTER 2

CHAPTER 3

CHAPTER 4

Page

CHAPTER 5

CHAPTER 6

Page

CHAPTER 7

CHAPTER 8

CHAPTER 9

APPENDIX 1

APPENDIX 2

APPENDIX 3

DIAGRAMS

CHAPTER 1 - Introduction

CHAPTER 2 - Holographic Techniques

CHAPTER 6 - Multiple Strip Heat Exchanger Model

CHAPTER 7 - Theoretical and Mathematical Considerations

CHAPTER 9 - Conclusions and Recommendations for Further Developments

APPENDICES

FIGURES

DRAWINGS

PLOTS

APPENDICES

TABLES

Page

CHAPTER 5 - Flat Plate Holographic Sample

CHAPTER 6 - Multiple Strip Heat Exchanger Model

CHAPTER 8 - Prediction Model

NOMENCLATURE

GENERAL SYMBOLS

u	velocity components
v	
x	components of length
y	
l	
L	
d	
D	
b	
U_∞, U_o	stream velocity
T_∞, T_o	stream temperature
∇T, θ	excess temperature
T	temperature

HEAT TRANSFER SYMBOLS

ρ	density
k, K	Thermal conductivity
α	diffusivity
δ	boundary depth
δ_{th}	thermal boundary depth
h	heat transfer coefficient
Q	heat transfer
μ	viscosity
ν	kinematic viscosity
Sa	surface area
Fa	flow rate
ξ	emmisivity
c_p	specific heat at constant pressure
σ	Stefans constant
hd	hydraulic diameter

OPTICAL SYMBOLS

α, β	angles
δ	small change
I	intensity
λ	wave length
n	fringe order number
n_t	refractive index (at temperature t)
R	path length

MATHEMATICAL SYMBOLS

$F(z)$	complex function
ϕ	complex function
ψ	complex stream function
i	$\sqrt{-1}$
p_o	stagnation pressure
p	pressure
q	velocity, vectorial, in general $q = ui + vj + wk$ but normally only considered in two dimensions
F	body force
c_i	general i_{th} coefficient of a series expansion
$\frac{\partial H}{\partial t}$	heat flow

DIMENSIONLESS FACTORS

(R)	Reynolds number
(Gr)	Grashof number
(Pr)	Prandtl number
(E)	Eckert number

INTRODUCTION

INTRODUCTION

The research undertaken in this project has been concerned with automotive heat exchangers with a view to providing techniques for the improvement of their design. The design of heat exchangers commonally termed radiators has changed progressively, since their introduction as a method of stabilizing the engine block temperature. The majority of these changes have been achieved on an empirical basis.

In a water cooled system, circulated water removes heat from the engine block and dissipates it to the ambient air via the radiator. Early radiators were large and ungainly, the Morris Bullnose took its name from the type of copper fin, brass tube assembly built for this purpose. Historically many of the advances have been introduced to enable radiators to be produced on a mass production basis. Small cost savings per radiator yield very large savings when the number of units manufactured is in the region of 10,000 per week.

Water enters the radiator at approximately 87°C. It is then passed through a series of tubes and leaves at between 5 to 15°C cooler. Air passes over the surfaces of the tubes and the attached fins or extended surfaces and leaves the system from 10 to 40°C hotter depending on its speed. A good radiator achieves this process as effectively as possible with minimum drain to the engine power and cost to the manufacture of the system.

One of the first objectives of the project was to define the extent to which variables, present in the problem affect the performance of radiators.

These variables are:-

1. The airside extended surface area S_A
2. The waterside surface area S_w
3. The materials used in the construction of the radiator m_t and m_f (materials used in tubes and fins).
4. The flow rate of air through the tubes F_a.
5. The water flow rate through the tubes F_w.

These factors can be combined to define the overall heat transfer coefficient U as:

$$1/U = 1/\left[h_a \ S_a\right] + 1/\left[h_w \ S_w\right] + 1/\left[h_t \ S_w\right] \qquad \{1.1\}$$

Where h_a and h_w are respectively dependent upon the flow rates F_a and F_w and the geometry of the materials used in the construction of the radiator.

$1/h_t$ the coefficient of heat transfer for the tube is the quotient ~~product~~ of the tube wall thickness and the thermal conductivity of the material used.

The overall heat transfer has further to be considered with respect to the pressure difference experienced by the air and water.

In simple terms it would be expected that if the surface area to cross-sectional area of the tubes could be made very large this would result in an increased heat transfer ability. In doing this, the tubes would have to be of very small diameter as the ratio increases as their radius decreases.

For a rectangular duct $2\frac{[A + B]}{A \quad B} = \frac{\text{surface area}}{\text{cross sectional area}}$

Where A is the width and B length. If B >> A then the expression reduces to 2/A. A consequence of this is that the pressure required to drive the water through the tubes is increased. As the work is produced via the water pump from the engine, the power available to drive the vehicle is reduced. At high speed this factor can account for as much as 10% of the total power. Plot 1.1 . In terms of the efficient use of the engine, this factor limits the permissible waterside pressure drop of the radiator, this is a limit to the advantages in heat transfer which can be achieved by tube size reduction.

As an alternative, extended surfaces or fins can be used to increase the surface area. An extended surface is normally made from copper aluminium or steel. It is common practice to produce a particular shape in the extended surface perpendicular to the air flow. Typically this is achieved by a cutting and twisting of the metal, to form the louvre shaping shown in drawing (1.1). The fins are joined normally using solder, to the water carrying tubes to form a direct heat path between the water and the air passing through the radiator. They also add rigidity to the radiator core.

In terms of equation {1.1} , particularly at low air speeds through the radiator: $h_w S_w >> h_a S_a$. Further, in general $h_t S_w >> h_w S_w$. Thus in the first instance equation {1.1} is reduced to the form:

$$U = \frac{\left[h_a S_a\right] \left[h_w S_w\right]}{\left[h_a S_a + h_w S_w\right]} \quad \text{where } 1/\left[h_t S_w\right] \simeq 0$$

and finally $U = h_a S_a$ {1.2}

U is thus dependent largely on the properties and shape of the extended surfaces used.

It is common practice to design a radiator to meet low air speed conditions, because if the performance is adequate at the low speed condition then there is normally little problem in meeting the dissipation required by the high speed end of the velocity range.

Therefore it is evident that for effective radiator design it is desirable to make a further study of heat transfer at low velocities.

Low velocity flow in the vicinity of a solid body such as a radiator fin has classically been assumed to be of a streamline viscous nature. This assumption is founded on the length based Reynolds number being small $\left|R \simeq 2\ 10^3\right|$. However, the possibility of turbulence due to the body or particular shaping of the secondary surface has also been considered. Such a flow system involves the concepts of hydrodynamic and thermal boundary layers.

With this as a background an investigation was made into the available experimental techniques likely to produce rewarding data. Each measuring technique has advantages and drawbacks.

It was considered that any technique involving "contact" methods (e.g. thermocouples) would create a degree of disturbance within the boundary layer such that the results would be valueless.

Contact measurement is defined as the introduction of a solid into the air stream. Typical devices in this category are hot wire anemometers and pitot tubes. The later were ruled out due to the small magnitude of the pressure differences involved at very low air flows. For low Reynolds' numbers the accuracy of this type of instrument is limited, even with the appreciable corrections suggested by A. MacMillan ref. {1.1} the standard of the results obtainable would still be expected to be poor. A typical hot wire anemometer as described by Comte-Bellot ref. {1.2} was evaluated in the wind tunnel and although the device proved useful in confirming the streamline nature of the air flow, particularly around the bell mouth entrance it was insensitive to the small velocity variations within the boundary layer regions of the samples. The anemometer was used to calibrate the flow through an orifice plate, situated downstream in the tunnel, which was used as a bulk velocity measuring device.

Different methods of temperature measurement have been explored. Conventional thermocouples have been introduced into the samples where the possibility of producing a disturbance to the experiment was minimal. Surface thermometry has been considered but rejected, due to the size of the thermometers ref {1.3}, which might have both disturbed the air flow and affected the heat flow from the sample to the air.

From the possible non-contact measuring techniques holography and doppler anemometry were studied in depth. Before the advent of the laser, interferograms of heat and fluid flow had been made by Schlieren and Mach-Zender systems Ref. {1.4}, the work being limited by the intensities of the available source and its coherence length. However, these problems have now been removed and the production of holograms using these systems is commonplace.

Laser doppler anemometry presents a highly accurate velocimeter. In air flow experiments there are potentially two disadvantages. Firstly a fine stream of particles must be introduced into the flow to provide seeding from which the doppler wavelength shift can be calculated and it is debatable whether these particles will behave in an analogous manner to air in the very small boundary layer under investigation. The second is the industrial consideration as to the cost of the system Ref. {1.5}. Holography represents an alternative which is truly a non-contact process. Again holographic techniques can be sub-divided into two groups, live and frozen fringe systems. In the live fringe system, a set of fringes is viewed, directly created by the path length difference between the reference and sample beams. Distortion in the field under investigation superimposes on the original set of fringes. The fringes are normally viewed via a telescope system DIA (1.1). Frozen fringe holography uses a photographic plate as an intermediate stage, two exposures being necessary in the formation of the hologram, the first exposure being the reference case, the second having a disturbance occurring in it. The resulting hologram contains only the fringes resulting from the disturbance frozen on the hologram at the instant when the second exposure was made. A great deal of work has been devoted to these fields, Ref. {1.6}, two major drawbacks lie in the live fringe system, firstly in producing photographic recordings of the system and secondly, in fringe interpretation, which in effect reduces the technique to a frozen fringe situation, Ref. {1.7}. The frozen fringes when used in conjunction with a pulse laser have the advantage of being vibrationally far more insensitive and are capable of recording instantaneous events, Ref. {1.8}. The merits of the various possible ways in which data could be obtained were considered. Frozen fringes holography satisfied all the criteria for a measuring device with only one major misgiving. The refractive index change required to produce a path length difference across the wind tunnel of one fringe occurs if either the air speed exceeds 60 ~~m~~ ft/sec. (fringes produced by air flow only) or by a ~~9.3~~ 9.2°C temperature difference between the two exposures - Appendix (1). Thus it follows that only the temperature profile of the boundary layer associated with the surface could be measured and not the hydrodynamic boundary.

This represents a major experimental limitation of the apparatus in terms of a strictly holographic technique.

Attempts have been made to introduce smoke particles into the air stream with the possibility of photographing the resulting traces.

A particular system was considered, ref. {1.9}; but was found to use a heavy volatile oil to generate smoke. In a test situation outside the wind tunnel the smoke left a heavy oil deposit. The system was not used inside the wind tunnel for the following reasons:

1. The oil vapour was much heavier than air, thus not representative of the actual air flow.
2. The oil was likely to condense inside the wind tunnel making further holographic work difficult.
3. Such a deposit would be difficult to remove from the test samples.

As an alternative method of obtaining information a new system has been developed which uses an electrically heated multiple strip element heat exchanger model. The model is constructed from a series of 5 10^{-6} m thick nickel strips mounted either side of a 10^{-3} m epoxy resin base. Each strip is isolated both electrically and thermally from the other strips making it possible to control its individual power input. The resistance of each strip has been used to measure its temperature. Thus by adjusting each separate power input all the strips can be maintained at approximately the same temperature independently of the air flow conditions present.

In the present simple form this technique is limited, but promises to be useful in complicated flow situations if improvements to the method of assembly and the electronic control system are made.

Another problem in the project was to define the type of samples which could be used to represent extended surfaces. Reynolds number scaling has been used for modelling the surfaces. A scale factor of five was introduced to provide the resolution of the fringe pattern. Larger test samples would have made the size and length of the wind tunnel impractical. The distance of the pulse laser from the sample was determined by the cross-sectional area of illumination required. To produce an even spread of the beam greater than 10 cm diameter would have necessitated the laser being more than 5 m from the sample.

Various different methods of producing experimental test shapes have been developed. The materials considered and used in construction being metal, resistance paper, carbon fibres, epoxy resin and conductive coated glass. The advantages and disadvantages of these different techniques have been explored experimentally.

Consideration has been made with respect to the design and development of the wind tunnel. The entry region has been designed to give an exponential bell mouth. This has been produced to keep any disturbance of the air flow entering the tunnel to a minimum. Attention has also been given to stabilizing the fan motor, such that the bulk air flow through the tunnel does not fluctuate for any particular setting. The material from which the tunnel was constructed, (specially laminated paper) was chosen such that the internal surfaces of the tunnel were as smooth as possible. This was to ensure that wall disturbances would have a minimal effect.

A description has been given with respect to the types of mathematical methods available to describe fluid flow over heated surfaces.

Any theoretical study of a flow is not capable of a precise analytic solution except in cases where the boundary conditions involve very simple geometry.

However, considerable flexibility is possible for potential flow in a two-dimensional system when it is possible to have a scalar velocity potential ϕ and stream function ψ. Thus a ψ and ϕ can be derived from any function $f(z)$.

It was hoped that a region of viscous flow could be fitted between the actual body and the boundary beyond which potential flow theory would be valid.

Other more complicated techniques which are developed from the Navier-Stokes equation Ref. {1.10} have been discussed and their limitations noted. Finally, an outline has been made to the use of holographic information in developing a more complete description of a boundary layer flow.

Considerable concern has been felt with respect to methods which assume constant properties. In the field of radiator design temperature differences produce density changes of up to 20% and viscosity changes of 10%. Equations have been derived to show that such density changes are significant with respect to the assumption $\nabla \cdot q = 0$.

During an early stage of the project a theoretical study was made of the possible interpretation if a large temperature variation existed across a heated sample. The fringe distribution which is an integration of the light ray path through the field would be expected to change if viewed from different angles due to local variations in refractive index. This study has been developed in Appendix (2) and concerns the three dimensional reconstruction of refractive index fields.

One further point which should be mentioned in the introduction related to the industrial side of the project. At present purely empirical methods are used in the development of radiator cores. During the project a prediction model, Chapter {8} based on works by Kays and London ref. {1.11} has been developed. The model is useful in inspecting alternative designs without the expense of practical testing.

SHORT REVIEW OF CURRENT LITERATURE

There is a large amount of literature available on the subject of heat transfer. An attempt has been made to outline some of the more recent publications on this subject. Saboya and Sparrow ref. {1.12} and Siegla and Mont ref. {1.13} present experimental results of developments made to perforated and herringbone heat exchanger surfaces respectively. Ota and Kong ref. {1.14} give both experimental and theoretical evidence of an increased local heat transfer at the leading edge of a flat plate. Several papers have proved useful with respect to the holographic part of the project and the interpretation of fringe fields. Sweeny and Vest ref.{1.15} and Kapur and Macleod ref. {1.16} describe techniques for fringe interpretation. Cooley ref. {1.6} relates fringes produced by natural convection to a mathematical solution derived by Sparrow and Gregg ref. {1.17}. Other areas of work researched, particularly with respect to the three dimensional refractive index reconstructions discussed in Appendix (2) were found in the X-ray field. Berry and Gibbs ref. {1.18}, Merserean ref. {1.19} and Smith and Gibson ref. {1.20} have all produced work related to body scan radiography.

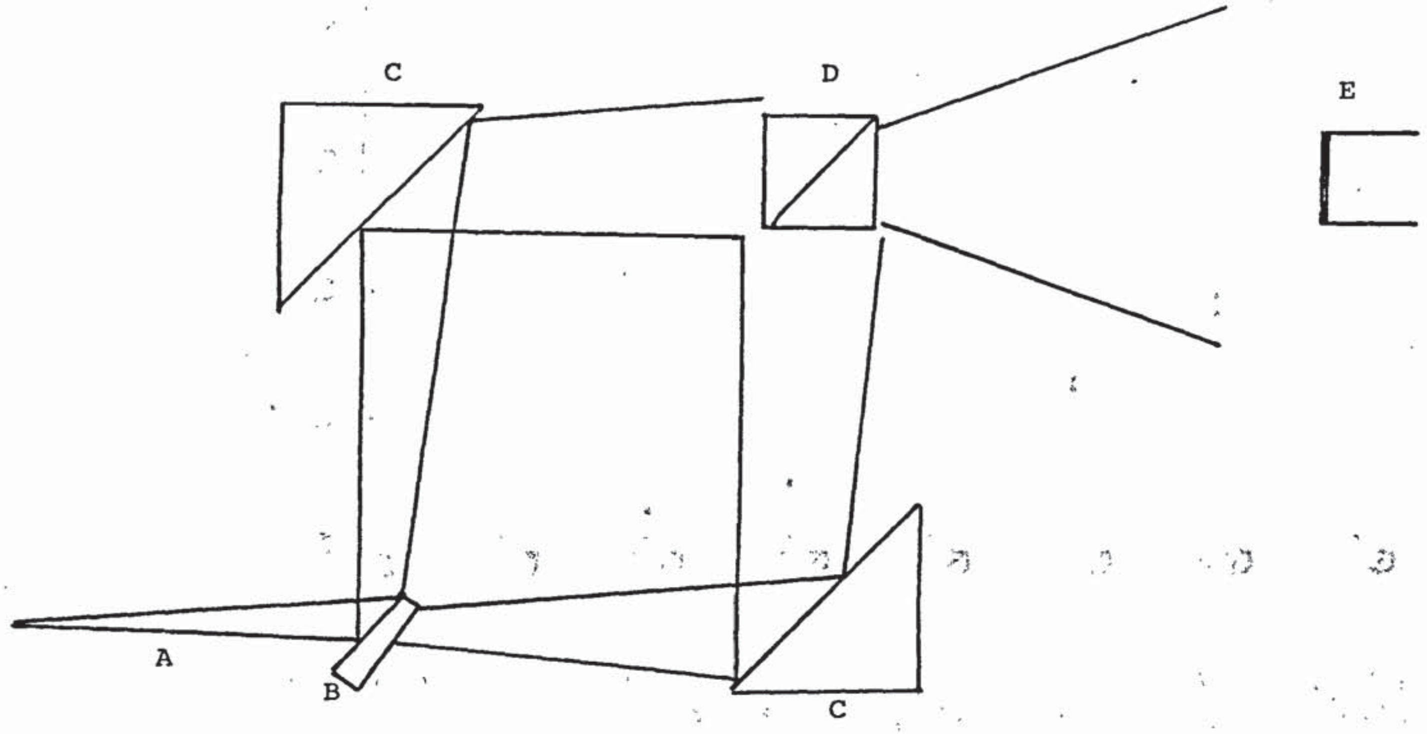

DIA (1.1) Telescopic system for viewing live fringes

A	Coherent expanding light beam
B	Half silvered mirror
C	Reflecting surfaces
D	Cube beam splitter
E	Telescope

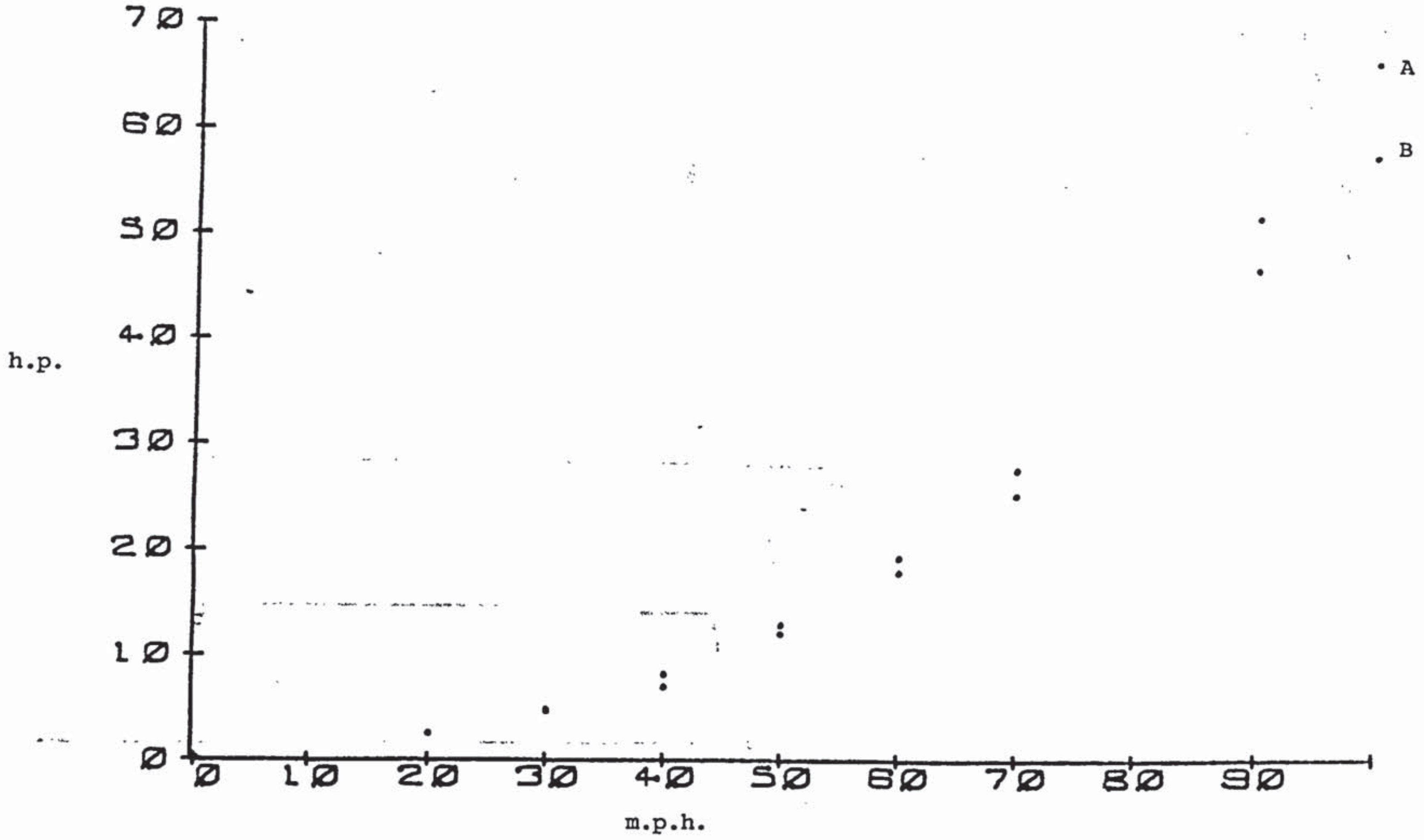

Plot (1.1) Plot showing engine power against road speed. The difference between curves A and B being the power taken by the cooling circuit (fan and water pump).

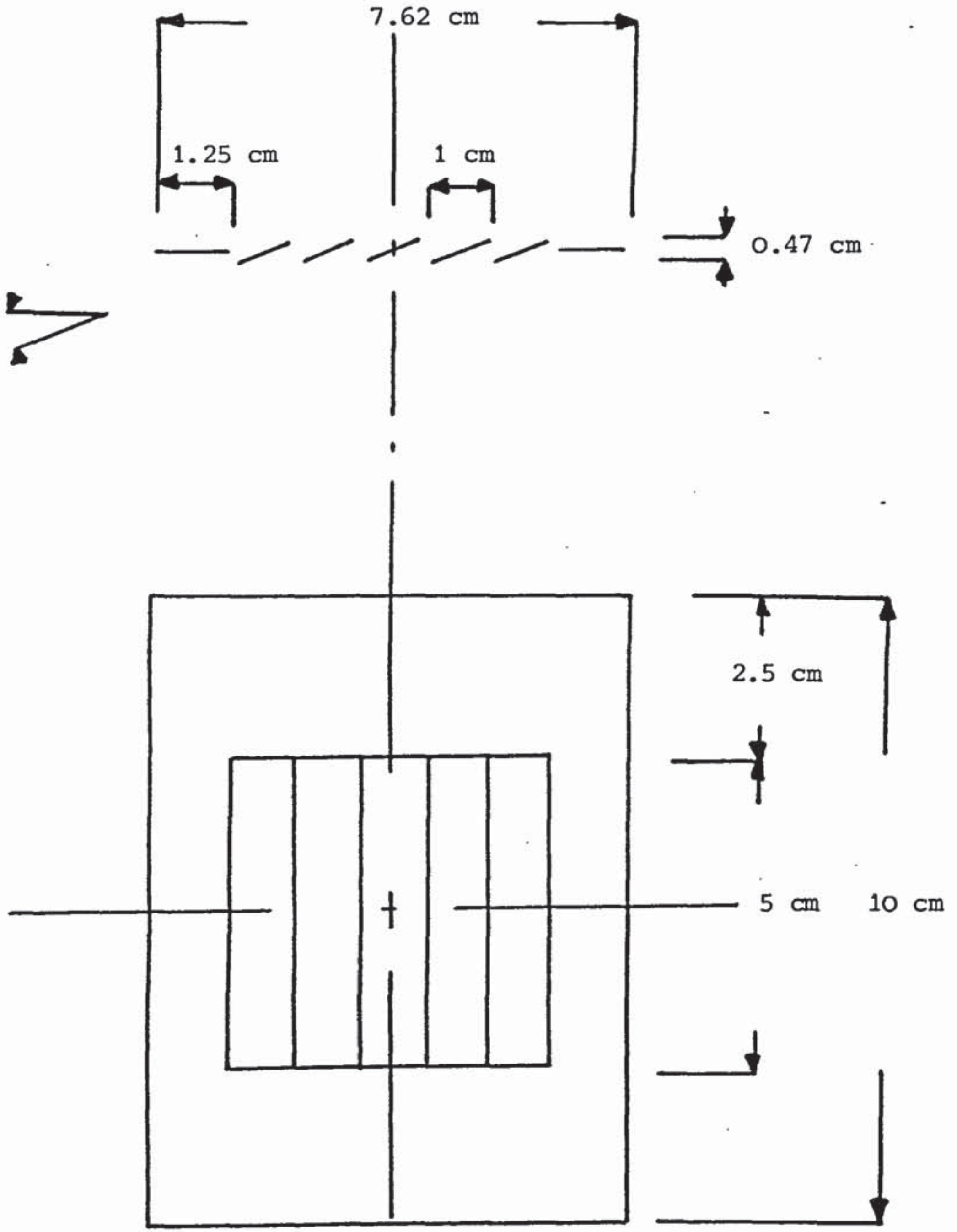

Drawing (1.1) Louvre Configuration

Drawing (1.1) is a schematic representation of both, an actual louvre shaping of a radiator fin and a scale model five times larger used in experimentation - fig.(18). The dimensions given are for those of the model.

CHAPTER 2

HOLOGRAPHIC TECHNIQUES

DOUBLE EXPOSURE HOLOGRAPHY

The first description of holographic techniques were made by Gabor ref. {2.1} who described the process by which coherent light could be used to form complicated interference patterns. These interference patterns when illuminated with coherent light reconstructed three dimensionally an image of the original object Dia {2.1}.. There were found to be two possible reconstructed images a real and virtual Ref {2.2}

A double exposure means literally one exposure made on top of another. The resulting reconstruction contains not only information relating to the original object but also information with respect to any small disturbances which have taken place between the exposures being made. The simplest method of describing mathematically the occurrance is by the superposition of coherent light waves.

Let $|I_o|^2$ represent the intensity variation when the reference wave $e^{i\beta x}$ and the sample wave $e^{i\alpha x}$ are added.

$$|I_o|^2 = |e^{i\alpha x} + e^{i\beta x}|^2$$

$$= 2 + e^{i(\alpha-\beta)x} + e^{-i(\alpha-\beta)x}.$$

Let $|I_2|^2$ represent the intensity of the second exposure recorded after a change δ to the sample wave.

$$|I_2|^2 = 2 + e^{i(\alpha+\delta-\beta)x} + e^{-i(\alpha+\delta-\beta)x}$$

The resulting intensity distribution produced on the photographic plate is then:

$$I_o^2 + I_1^2$$

$$= 4 + e^{i(\alpha-\beta)x} + e^{i(\alpha+\delta-\beta)x} + e^{-i(\alpha-\beta)x} + e^{-i(\alpha+\delta-\beta)x}$$

equation (2.1)

If the plate is illuminated with the reference beam the resulting reconstruction can be expressed as:

$$R = 4\ e^{i\beta x} + e^{i(\alpha)x} + e^{i(\alpha+\delta)x} + e^{-i(\alpha-2\beta)x} + e^{-i(\alpha+\delta-2\beta)x}$$

In diagram (2.1) the reconstructed virtual image will be formed in the same position as the original object. The resulting image reconstruction intensity will take the form:

$$[R]^2 = \left[e^{i\alpha x} + e^{i(\alpha+\delta)x}\right] \quad \left[e^{-i\alpha x} + e^{-i(\alpha+\delta)x}\right]$$

$$= 2 + 2\cos\delta x.$$

Cos (δx) is a maximum whenever $\delta x = \pi n$, n being a integer, for even values of n $2\cos(\delta x) = 2$, thus constructive interference occurs and bright fringes are seen. Dark fringes are produced for odd values of n.

The second possible image described in equation (2.1) is formed by the terms $e^{-i(\alpha-2\beta)x} + e^{-i(\alpha+\delta-2\beta)x}$. This represents the real image and would be formed if the plate was illuminated by the reference beam at the position $(\alpha-2\beta)$. In the experiments made $\alpha = \beta = 45^{\circ}$, thus the position of the real image is in line with the reference beam. However, a real image reconstruction was made by illuminating the holographic plate with a reference beam in the opposite direction $e^{-i\beta x}$, which produced a real image at the original position of the previous virtual image.

In the case of an experiment using a diffuser, the phase of the sample beam is spacially randomised. Changes of δ are localized in the reconstructed image to the area around or in the sample where variations between the two exposures have occurred.

METHOD OF PRODUCING HOLOGRAMS

In the previous section the theory by which a beam of coherent light can be used to form an interference pattern was outlined. Experimentally there are several ways in which this effect may be achieved.

Reflection Holography

This is the simplest method used in holographic image formation. The incident beam illuminates both a mirror and the surface of interest. The reflections from both combine on a photographic plate to produce a holographic image, ref. {2.3}. The method is used when on the surface distortions of a body are to be investigated and there are no disturbances in the surrounding air to distort the observed fringe patterns.

Transmission Holography

The method forms the basis for all work when either the influence of a shape with respect to its immediate environment is to be investigated or when the object is semi-transparent. In this case the beam is split into two parts, the reference beam and the sample beam. The reference beam is shifted away from the field of interest by a beam splitter and recombined after with the sample beam to form a holographic image. It is common practice for a diffuser to be placed in the sample beam path directly before the sample itself. The diffuser is usually made from ground glass, its action being to randomise the phase of the incident light and illuminate the sample. The beam may be allowed to either diverge or be held parallel by the use of a lens system.

EXPERIMENTAL WORK

The first experiments made were to test out the viability of the double exposure technique. These used a He/Ne 5 mW. continous laser and a transmission holographic method - Dia {2.2}. The sample used was a small lightbulb, the first exposure being made with the bulb cold, the second after a suitable period of time with the bulb hot. Scientina 10 E 75 plates were used for recording the two, four minute exposure periods and developed in Kodak B8 developer. Heating was achieved by switching the bulb on between the two exposure periods. Good holograms resulted, the localised heating of the air could be seen as thick halo like fringes around the bulb - Fig. (1). Photographic reconstructions of the holograms were made using a 35mm Exacta camera and FP4 film.

The next step was to use a pulse laser to take holograms of the same object. The reason for using a pulse laser was to reduce the exposure time of the plate. This meant that instead of viewing a time averaged isothermal picture, a near instantaneous one could be achieved. This had great importance with respect to the aims of the project, which was to obtain holograms of air flowing over heated surfaces and to freeze any particular instantaneous event which may be present in the heat flow. The speed of operation of the pulse laser would reduce vibrational problems likely to arise during the experiments.

Production of Holograms Using a Pulse Laser

It was apparent that the divergent-pinhole method of producing a clean diverging beam - Dia {2.3} which had been used to diverge the continuous laser beam, could not be used in conjunction with the pulse system. The intensity of the beam simply melted the aperture. Without the pinhole aperture the intense pulse beam was not clean enough to produce a hologram. A system was devised using a X10 microscope objective focused on a thin piece of material - ref. {2.4}. The converged beam had enough intensity to melt a small hole in the material, thus producing a clean aligned pinhole for the next firing of the laser. Different materials were experimented with the most effective being platinum foil of $3.8.10^{-3}$ cm thick.

To produce holograms using the pulse laser, the object had to be moved approximately ten feet from the laser due to the intensity of the pulse. Further the divergence of the beam was not as great as that produced by the continuous laser system. Various experiments were made to overcome this problem. Firstly a X20 microscope objective was used to focus the pulse beam. The focal point of the lens proved too close to the surface and the intensity of the beam melted it. Several types of neutral density filters were used to reduce the pulse intensity, it was found that if the filter was placed before the microscope objective, it was damaged. Alternatively placing the filter after the pinhole added noise to the beam making it difficult to produce holograms. The pulse laser also burnt out the centre of the X10 objective, but over a long period of time. For this reason care was taken to keep the objective lens clean, in order to reduce absorbed energy.

Having proved the transmission system a hologram of a heated surface was made. The surface was made of steel and heated using a low voltage, high current transformer. The power applied was typically 4 watts and good holograms resulted from this arrangement. The reconstructions of the holographic images shows an uneven temperature profile produced over the surface (Figs. 2a, b, c). These experiments were made to test the possibilities of the system and that the reference beam was kept far enough from the sample area to assume that the temperature variation has not also affected it.

The Design and Development of a Mach-Zehnder Interferometer

In view of the success of the transmission holography proving tests it was decided to construct a Mach-Zehnder interferometer and at the same time design a low flow scale wind tunnel, to work in conjunction with it. Dia {2.4}. The advantage of this type of interferometer was that it separated the reference and sample beams, without producing a large path length difference between either. It could also be designed to accommodate a reasonably large test sample. The interferometer was set up in the conventional manner - ref. {2.5} and failed for several reasons.

1. Lack of rigidity in the system.
2. The low quality of optical mirrors used.
3. External vibrations now seriously affected results.
4. Intensity of the pulse laser, the size and efficiency of the beam splitter.

Optical Surfaces

Consequently the system was redesigned and high quality optical flats ordered. (Up to this point the student had been making partially and fully silvered mirrors by evaporation techniques using a laboratory vacuum system). Two front silvered mirrors, checked on a Twyman-Green interferometer, with a surface flatness of λ/2 were supplied by ICOS Limited - ref. {2.6}. They also ground a 13° angle prism which acted as the beam splitter.

Mechanical Frame

Drawings were made for a redesigned frame of increased rigidity which was machined at RALPART, British Leyland. The frame consisted of three flat plates of steel plate 1/2" thick connected and supported by eight 1/2" square steel bars. On the plates were fitted angled pieces of steel to carry the mirrors and prism - Dia {2.4}. Each was mounted using spring-loaded screws to produce the necessary fine adjustment. The mechanical frame was made of steel for rigidity and to facilitate the use of close tolerances. It was also sprayed and baked matt black to diminish internal reflections.

Mounting of Interferometer

To ensure that the interferometer was isolated from external vibrations it was mounted on a 1/2 ton cast iron base which itself rested on an expanded polystyrene raft.

Proving Experiments and Modifications made to the Interferometer

The first proving experiments were made using a continuous laser. It was founded possible to produce weak single and double exposure holograms. Vibrational checks were made with an Etalon ref. {2.7}, and also by setting the interferometer to view live fringes - Dia (1.1). Both these tests indicated stability in the system, so the lack of visibility in the holograms was due to a miss-match between the intensities of the reference and sample beams. The system was simplified by removing the beam splitting prism - Dia (2.5).

Holographic Processing

The holograms in the early development stages had been made using Agfa Scientenai 8E75 plates developed in Kodak D8 high contrast developer. The 8E75 plates were used with the pulse laser as they required a long or bright exposure and produced detailed holograms. Other types of holographic plates were tried, but did not prove advantageous. In making the transition from the continuous to the ruby laser two effects became apparent. Firstly the exposed plates exhibited a large grained or excessively mottled effect. Secondly the lack of control which could be exercised over the pulse laser intensity. The lack of control is related to the physical distance and divergence of the beam from the object. It is also due to the fact that a particular striking voltage was required below which the laser would not lase. This lack of control in the beam intensity could not be accommodated by the attentuation of the signal; inserting either filters or lense into the system degraded the quality of the beam and moving the laser further from the object was a physical impossibility, due to the laboratory space available. As a result the photographic plates were heavily overexposed. Reduction in developer concentration merely produced a loss of image, so a bleaching process was introduced after the development stage of the plates.

Initially a dichromate bleach was used reducing the silver halide in the plate and producing a wholly phase object in the reconstruction. The results obtained were good as long as the plates remained wet. On drying the viewing of the image was as "looking through a pebbled bathroom window". The problem was overcome by using a complicated Kodak reversal bleach process ref. {2.8} which produced very clear images, the only drawback being a fading effect produced over a long period of time by moisture absorption into the gelatine of the plate.

Cleanliness of Optical Surfaces

This point was first considered during the early development stages of the project, which were carried out in a more hostile industrial atmosphere. It was found that despite protection a thin layer of grease accumulated on the mirror surface, there was also a slight problem of condensation. The effect was dramatic, reducing the visibility of the holograms. Hence a procedure for cleaning the surfaces was necessary.

1. Careful light wash with isopropyl alcohol to degrease surfaces.
2. Wash with distilled water.
3. Final light wash with isopropyl alcohol to aid air drying.

The problem was somewhat reduced when the apparatus was set up under laboratory conditions, but careful periodic cleaning with isopropyl alcohol was still required. To ensure good lasing careful cleaning of the mirror reflectors either side of the ruby rod in the pulse laser had also periodically been carried out.

Alignment of System

The alignment of the laser and the interferometer has been reduced to a simple and easy procedure. Firstly the pulse laser was set to produce a good lase, this was achieved by aligning the resonant reflecting mirrors with an autocorrelating telescope. Then a continuous laser was aligned along the direction of the pulse. By adjusting the two mirror beam splitter (Fig. 4) the continuous beam is first set via the top mirror to produce a spot in the centre of the plate holder after passing through the sample section. This procedure was then repeated using the lower mirror in the beam splitter, this time producing a spot in the centre of the plate holder via the lower mirror surface mounted in the interferometer. Finally small lateral adjustments were made, repeated pulses from the pulse laser were centralized by a horizontal rotation of the whole beam splitter assembly.

Type of Diffuser

The function of the diffuser is to randomise the phase of the incident light on the sample. Different types of material have been experimented with in an attempt to maximise the efficiency of the diffuser used in the interferometer. Coarse grained ground glass was found to produce sharp pinpricks of light which obscured the fringe patterns, effectively adding to the speckle already present. Too fine a surface tended not to diffuse the pulse beam, producing a high intensity spot at the centre of the reconstructed image, and not throwing out enough secondary illumination to make all the sample visible. A holographic diffuser was also attempted, as this seemed to give the required effect without the stopping power of ground glass - ref. {2.9}. Unfortunately deflecting the intense direct beam and subsequent over-exposure of the plate provided an obstacle to this method. Such methods are useful when the reference and sample beams do not require separation. Various other materials were tried, such as neutral density filters and thin plastics, but again these acted as finely ground glass. The diffuser which yielded the best results during experimentation was the glass which was produced at Culham Laboratories by gradually grinding down the surface of float glass by successive grain sizes of diamond paste.

A graticule was drawn on the ground glass surface of the diffuser. This has been used to locate, scale and reference, the observed fringe distributions. Fig. (5).

Fringes produced on the photographic plates surface by internal reflections.

During the early proving experiments of the Mach-Zehnder interferometer fringes were observed on the photographic plate surfaces. These fringes were due to back reflection from the plate carrier. An Agfa 8E75 plate with antihilation coating had been prevoously available but was found to be out of production. The problem was solved by mounting black felt onto the plate carrier surface thus absorbing any light transmitted through the photographic plate.

RECONSTRUCTION METHODS

Once the production of clear holograms had been achieved it was essential that good photographs of the image could be produced from which reliable results could be taken, both as a permanent record and for comparison with mathematical models. There are two possible images available for reconstruction in a hologram, the real and the virtual.

Virtual Image Reconstruction

The virtual image reconstruction was made by using a He/Ne 5 mW continuous laser. The image lies behind the holographic plate (Dia 2.1) and cannot be projected. The problems in producing a photographic picture of such an image can be expressed as laser speckle, depth of image, resolution of information, variation of pulse intensity of the laser and degradation due to the type of developing process.

Apart from the straightforward technique of using a single lens reflex camera several other possibilities were attempted. These included placing a large lens between the plate and the camera and telecentric viewing system. Despite the experimentation the camera alone gave the best results. The majority of the photographs of reconstructed images being made with the camera aperture set to F5.6, with an exposure 13 to 20 seconds onto FP4 film. Reduction in aperture produced larger speckle (Fig. 6a) and too large an aperture failed to keep the whole image in focus (Fig. 6b), i.e. lack of focal depth.

Real Image Reconstruction

The alternative to reconstructing a virtual image was real image reconstruction. Preliminary experiments were made at Aston University and the final part of the work was completed at Strathclyde University with the help and assistance of Dr. S. Fraser. The advantage of this type of reconstruction was that it did not require a camera but produced a projected image which could be located on a photographic plate - Dia {2.6}. The reasons for visiting Strathclyde University was to use a more powerful He/Ne spectra physics 1/2W continuous laser and to meet Dr. Fraser's project student who had been working in a similar field - ref. {2.10}. The experiments made illustrated two very useful points. Firstly by illuminating the whole photographic plate, only one plane of the image was sharply focussed on the diffusing screen, the remaining field being out of focus, and as the screen was traversed different planes could be explored. An amount of knowledge of this phenomena existed at Strathclyde - ref. {2.9} where experiments had been made to locate specific hot-spots in a test sample. It illustrated the fact that the fringes in my holograms were located over the test area and were not being produced in the glass wall or outside the area of interest. No particular hot-spots were located and the fringes lay evenly across the test surface. Depth of field in the object was achieved by reducing the area of holographic plate illuminated. In the limit an undiverged beam was directed at the plate producing a sharply defined real projected image (Fig. 7). The images were produced by using a two minute development in Acutol, a high contrast X-ray developer. Conventional developers (i.e. Universal) produced a very low contrast image.

The disadvantages of this system is that only a very small area of the plate is being used to form the hologram, hence the high speckle noise which can be seen. The high level of speckle noise and use of a high contrast developer obscures broad fringes which fall below the general grain noise. This was illustrated with a series of micro-densiometer measurements made on a real image (HP3 plate) (Fig. 7). Even with heavy damping, which slows the response of the instrument and tends to average the grain noise, it was impossible to determine the area in which large fringes can lie. These fringes could easily be detected in the virtual reconstructions. The area of plate illuminated also reduced the amount of high frequency information available in the reconstruction; however, in terms of the type of object viewed this was not a disadvantage.

Viewing of Holograms

The viewing of holograms for interpretation is a further area into which experimentation has been made. The most successful process required that a large plano convex lens be placed close to the holographic plate on the viewing side of the hologram. The resulting image was highly magnified and made it possible to determine the fringe patterns close to the heated sample. A good large lense was required for this method. Smaller leses produced large distortions in the field making observation difficult. Attempts to place a camera in the focal plane of the lense (telecentric viewing) to produce a photographic image, has not, as yet, proved possible.

DIA (2.1) Reconstruction of Holographic Images

S	Reconstruction of sample
D	Reconstruction of diffuser
P	Holographic plate
i_1	Incident beam representing $e^{i\beta}$
i_2	Incident beam representing $e^{-i\beta}$
r_1	Virtual reconstruction $e^{i\alpha}$
r_2	Real reconstruction $e^{i\alpha}$

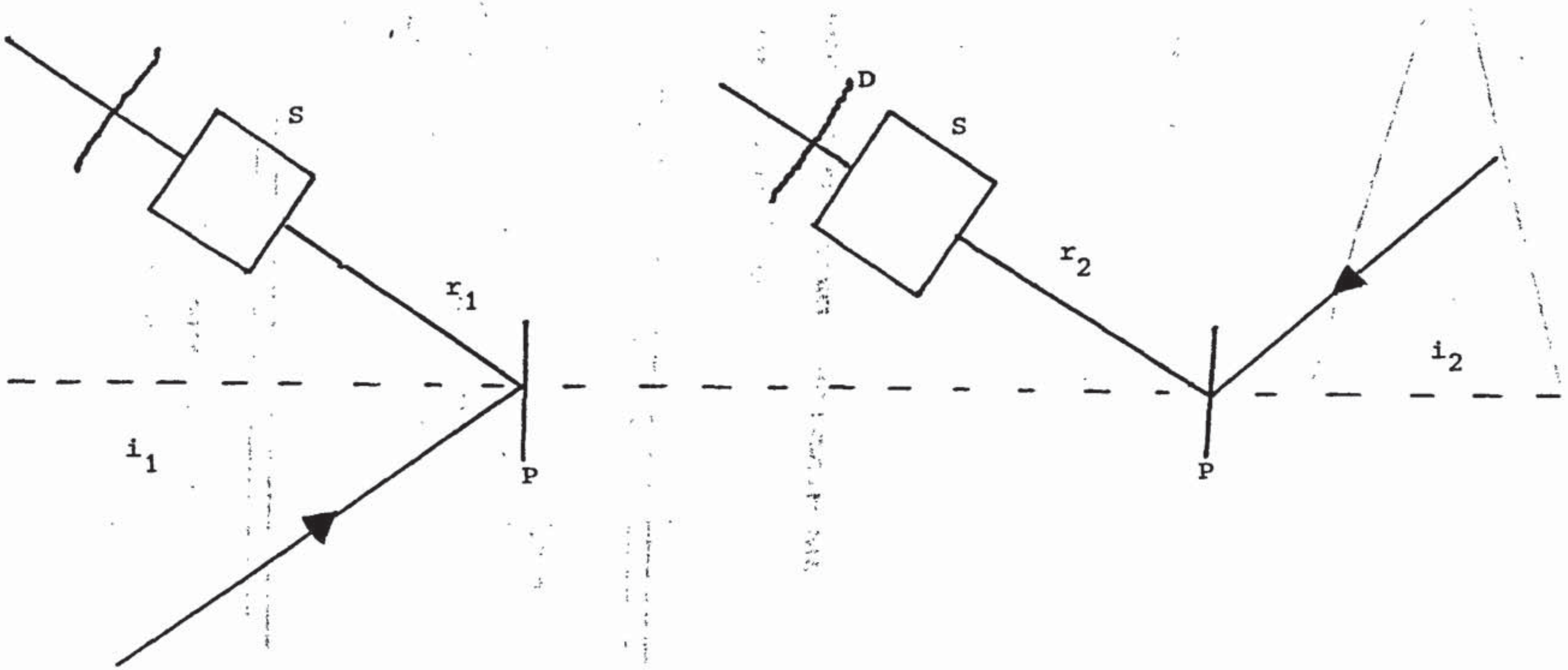

DIA. (2.3)

DIVERGENT PINHOLE SYSTEM USED IN CONJUNCTION WITH A CONTINUOUS LASER

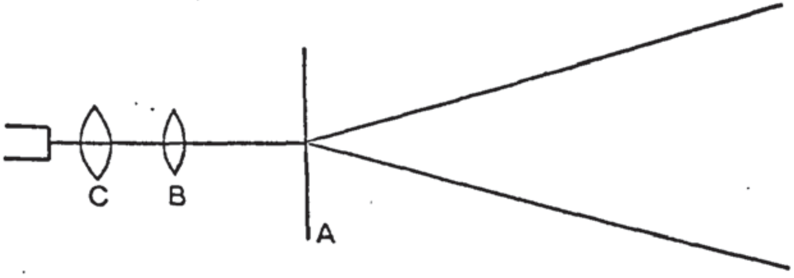

A Pinhole

B Microscope objective lens (x10)

C Divergent lens

DIA. (2.2)

EXPERIMENTAL TECHNIQUE FOR PRODUCING HOLOGRAMS BY TRANSMISSION

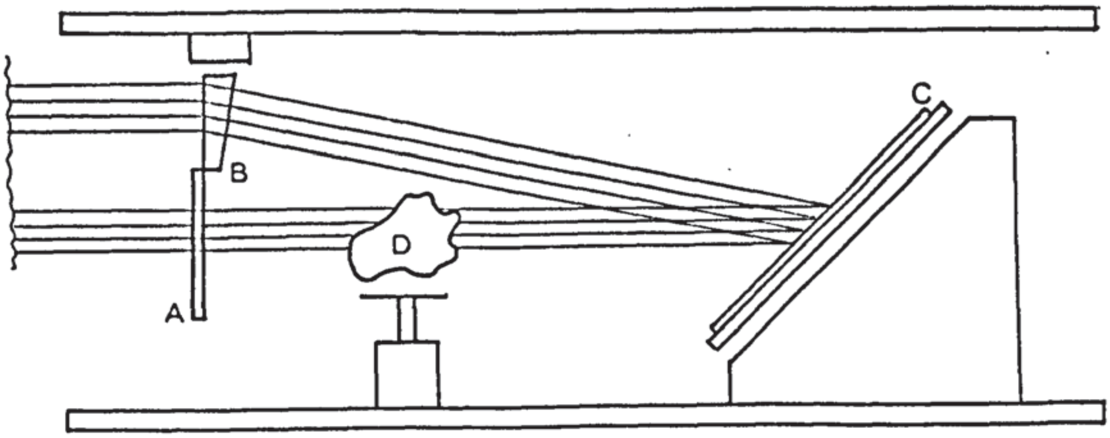

A Ground glass diffuser

B Prism

C Photographic plate

D Sample

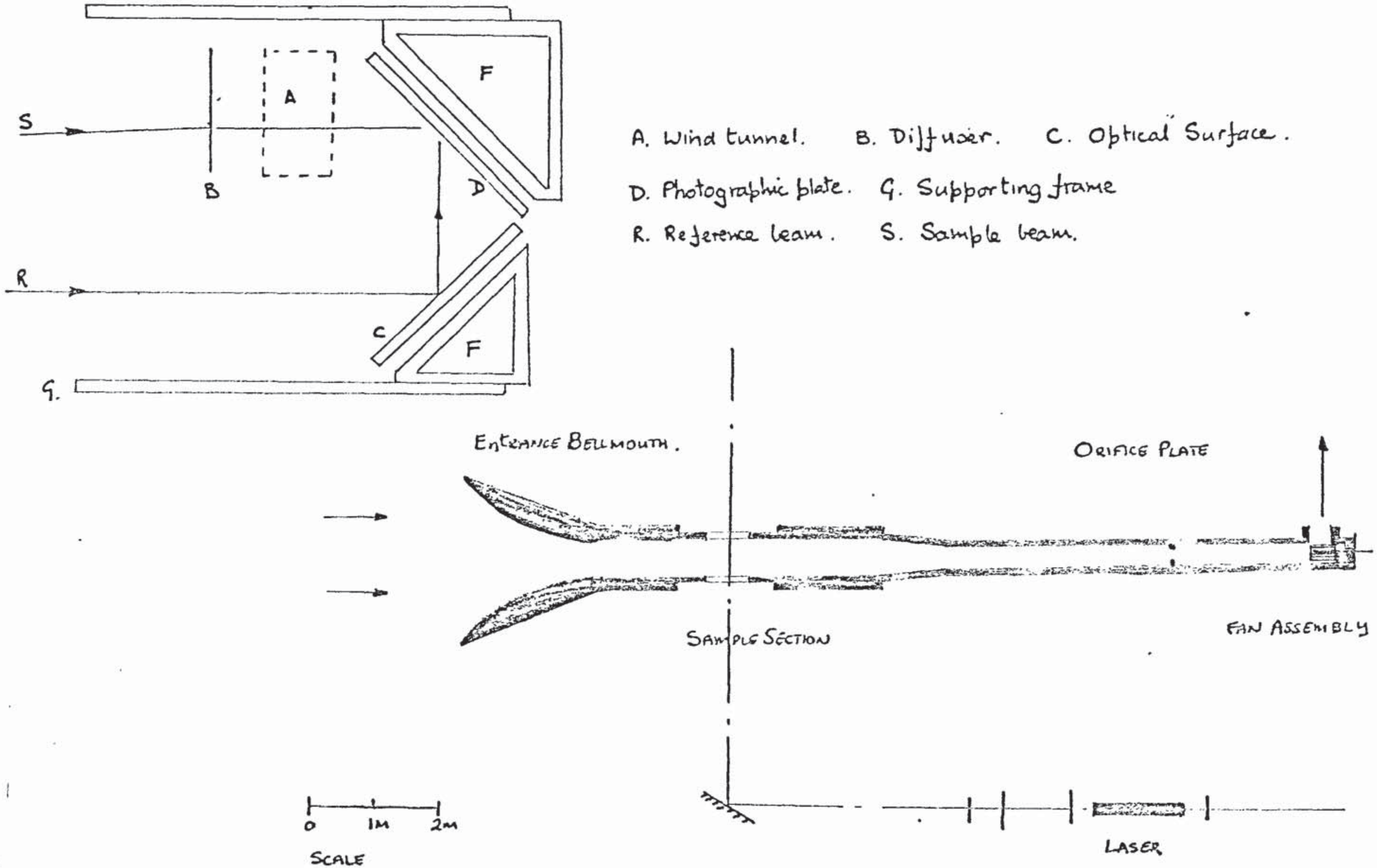

Drawing (2.4) Mach Zehnder Interferometer and Associated Wind Tunnel Assembly

A Beamsplitting mirror
C Photographic plate
B Mirror surface
D Ground glass diffuser

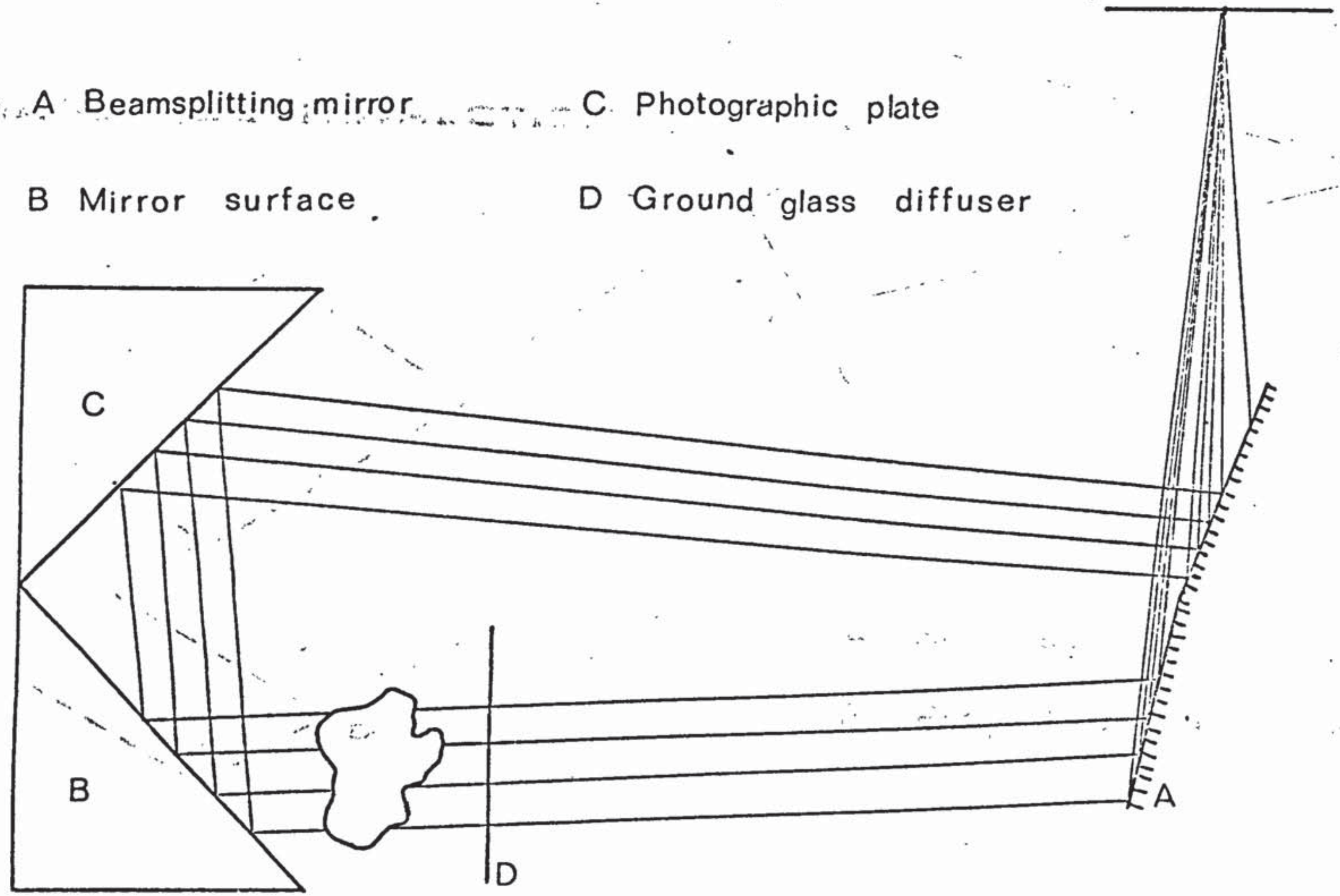

DIA. _2.5) EXPERIMENTAL INTERFEROMETER

DIA. (2.6)

REAL IMAGE RECONSTRUCTION

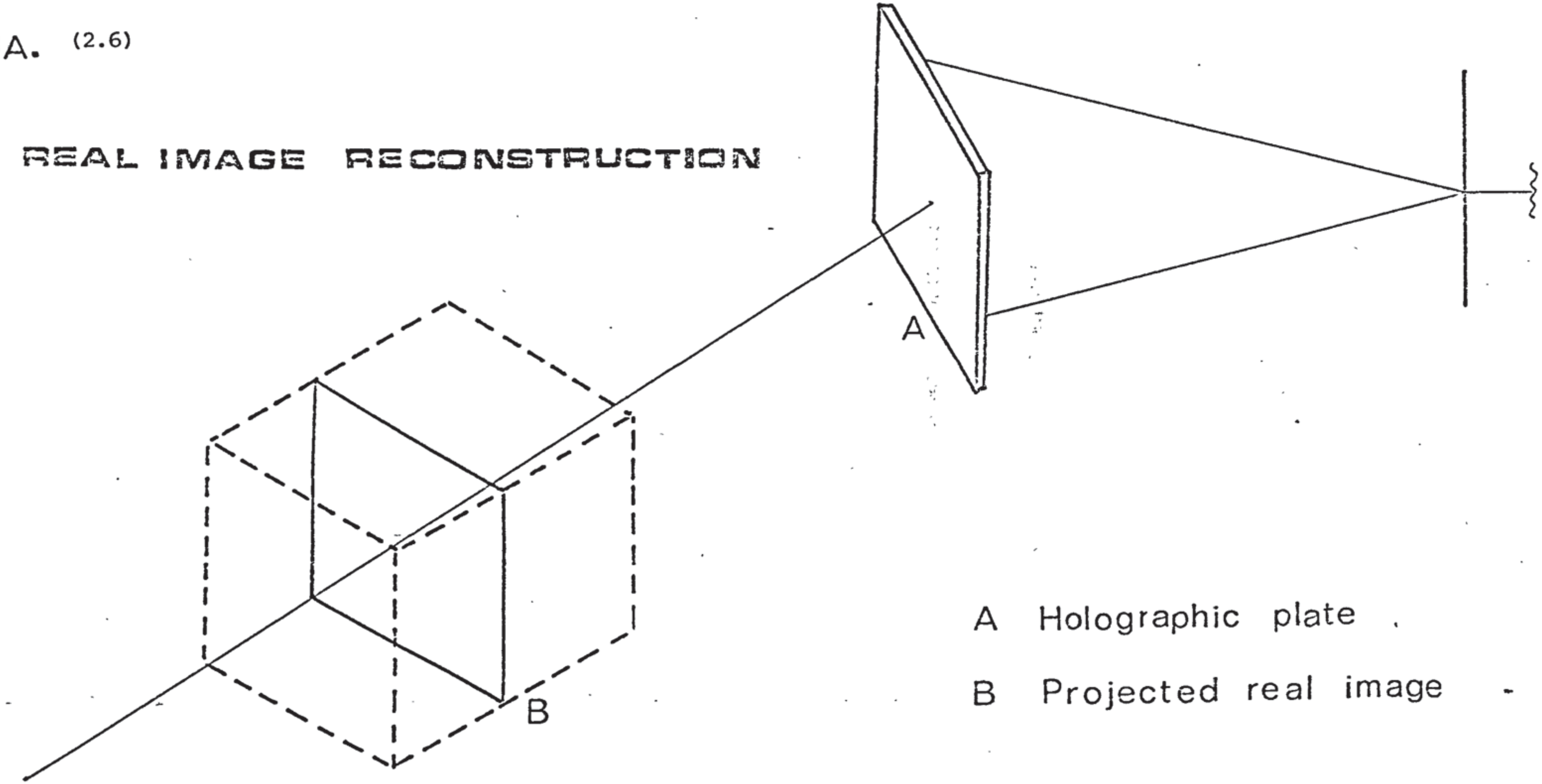

A Holographic plate .

B Projected real image -

CHAPTER 3

EXPERIMENTAL PROCEDURE

EXPERIMENTAL PROCEDURE

The procedure by which reliable test results could be obtained was evolved on a purely experimental basis. Firstly the sample to be tested was placed in the rigid free-standing central test unit of the tunnel (Fig. 8). Current was then applied at a gradually increasing rate from a variac transformer. The voltage and current was monitored by two Avo meters, one set to read the voltage applied across the sample, the other the current flow. This test, made in free air was used as an indication of the range of power that could be applied to the sample under experimental conditions. The power input was varied between 10 to 25 watts depending on the material and shape of the sample under test.

Before commencing an experimental series, several tests were made to ensure the efficiency of the system. Firstly the X10 microscope objective was checked for laser damage. Secondly the pin-hole was aligned using a telescope system (Fig. 9), such that the foil lay in the focal plane of the objective lens. Thirdly the laser was fired and the resultant beam directed onto a white card. A good lase was indicated by a red disc of illumination, whilst a poor one had a white incoherent edging. Finally a series of test holograms were made. These holograms were developed immediately after exposure using D8 developer and dichromate bleaching solution. Poor optical alignment of the system could be seen in terms of an uneven illumination of diffuser and degradation of image. External influences resulted in fringes obscuring the whole field of view (Fig. 3). An example of such an external influence was created by a compressor operating in the same building, when in operation it caused bad fringing on the doubly exposed plates, the fringes being locatable on the diffuser. Here the vibration was causing movement of the apparatus between the two exposures.

Once these test experiments were completed the sample mounted in the free standing unit was located into the main section of the wind tunnel (Fig. 8). The fan motor was then connected and set to give a reading of 0.5 inches water gauge pressure across the orifice plate. A sensitive calibrated liquid manometer was used to measure the pressure differences across the orifice plate (Fig. 10). The air flow required a short period of stabilisation. Then the 4" x 5" Agfa Scientina plate was loaded into the plate carrier at the rear of the interferometer. Care was taken not to rock the apparatus by body contact during this act. The first exposure was made, a previous lase having already been used to form the pinhole aperture. The heat input was then applied to the apparatus with a twenty minute period allowed for the sample to reach a stabilized temperature. A second firing of the laser was then made and the plate removed for development. Before the heating circuit was switched off recordings were made of the voltage, current and thermocouples placed in the sample. A cooling down period was allowed and further holograms were made at lower air flows. Several air speeds were used for each run, giving a fair range to the thermal boundary layer development. Other experiments which have been made in the wind tunnel have been to monitor the heat transfer at different air speeds and variable heat inputs using thermocouple measurements and to produce double exposure holograms to investigate natural convection (Fig. 11). Care has been taken throughout all the experimental work that the internal surfaces of the wind tunnel were smooth. This was to eliminate the possibility of any other disturbances except those due to the test samples - ref. {3.1}.

The wind tunnel/interferometer assembly has worked well in producing holograms. Soon after the proving experiments were completed a DISA hot-wire anemometer - ref. {1.2} was placed at different points in the tunnel to check the flow entry conditions, and monitor levels of turbulence. (Fig. 17)

There was no measurable turbuluence around the mouth of the tunnel and only a low percentage even when probes were placed behind an extremely abrupt and large louvre sample (Fig. 12). Smoke traces were also attempted - ref. {3.2} but did not give any indications of the nature of the flow. Experiments using small hydrogen bubbles were considered but on the advice of the Aerodynamic Design Division of the Motor Industries Research Association were not attempted. An alternative method of looking at the fluid velocity would have been by laser doppler - ref. {1.5} but was ruled out in terms of cost and difficulty in operation.

CHAPTER 4

SAMPLE FABRICATION

(PROVING STAGES)

SAMPLE FABRICATION

One of the problems associated with this project has been the fabrication of experimental samples. Several methods of producing such samples have been investigated.

Preliminary work

During the proving stages of the experimental work two types of samples were used. The need at this stage was to produce a heated surface and little attention was given to its controllability. The first surface was made of steel and required a low voltage and high current to be passed through it to produce the required heating effect. Connections were made to the sample via silver soldered thick braided copper wire. Attempts were also made to shape the steel plate to produce an even distribution of the current flow. Steel plate was chosen because the sample in a wind tunnel environment should closely resemble a distributive surface of a heat exchanger which is made from copper of approximately 5.10^{-3} cm in thickness. Thus the sample thickness, in order to keep to a scaling factor of 5 was between 25.10^{-3} cm and 38.10^{-3} cm. The steel plate had a thickness of 30.10^{-3} cm. The second type of test sample was closer to that normally associated with heat transfer work - ref. {4.1}. This sample was constructed from resistance wire held flat by two sheets of mica, the total thickness of the sample being in the order of 0.1 cm.

The samples although proving useful for the evaluation of the double exposure holographic technique were unsuitable in terms of producing useful results. The steel plate tended to have an uneven temperature distribution and fringes due to heating were detected around the copper connections. In such a variable situation no experimental investigations could be made as to the nature of the flow passing over it. The resistance wire sample deformed on heating also making measurements impossible. From these early trials certain criteria were laid out as to what constituted an ideal specimen. Firstly the material should be thin, (approximately 3.10^{-2} cm) undeformable with respect to temperature changes ($\Delta T = 70^{\circ}C$) and preferably transparent to allow a maximum transmitted light. The sample material had also to have a reasonable electrical resistance (250 Ωs/□) and the possibility of being formed into particular shapes. Three methods of achieving these standards were pursued.

Development of Experimental Samples

Having now experienced the disadvantages of making direct replicas of the surfaces, composite materials were investigated. On the advice of the Plastic Division, British Leyland, an epoxy resin cabable of withstanding high temperature without distortion was used. The basis of the model was to mount on either side of the sheet of resin a layer of electrically resistive materials. Materials tried in this operation were carbon resistance paper, resistive paint supplied by Hunderlec - ref. {4.2} graphic particles sprayed onto the surface and carbon fibres added to the epoxy resin mix. The graphite particle and paint methods both produced highly uneven resistive coatings. The carbon resistance paper (Fig. 13) produced tough, evenly coated surfaces, which were limited in the amount of heat which could be applied before the paper began to singe. The carbon fibre technique varied in its resistivity depending on the direction in which the fibres were laid and the electrical contact from one fibre to the next. A useful side effect was found which was used in later experimental work in that the carbon fibre added strength to the basic shape and thus made it possible to keep the sample within the desired scale factor thickness.

As uniformity of resistance was of importance, experimental work was made using a resistance paper model. By painting strips of conducting paint down the sides of the specimens it was possible to ensure that an even voltage was produced across it. Hence only those areas of material lying inside the tunnel were heated eliminating the possibility of the free convection fringe patterns being superimposed from heating outside the tunnel.

Finally thin wires were now used to carry the A/C power to produce the heating effect. This had the result that less of the holographic information was obscured by large connections.

Glass Sample Fabrication

Parallel to the development of the resistance paper specimens, methods of using glass to form the sample base with a conductive coating in or on it were also being investigated. The major difficulty was not in obtaining flat glass with a good resistance coating, such materials are available in the production of heated rear screens for the motor industry, Triplex Ltd. ref {4.3}, but in forming the material into the scaled shapes suitable for experimental work. Drawing { 1.1 }. Via British Leyland, Culham Laboratories were involved in this problem. They suggested a technique which was in its early development stages and arrangements were made to fabricate the samples from Pyrex. The Pyrex was heated to a temperature of over 650°C in a furnace with an inert atmosphere. It was mounted between two carbon moulds - Drawing (4.1) the weight of the top mould pressing the shape required into the glass. A high quality carbon was used to ensure no imperfections from the mould surface were impressed onto the glass and that no impurities in the carbon were assimilated into the glass. Such impurities cause excessive stresses in the glass during the cooling stages, which can result in breakage. The sample after cooling was then removed from the furnace and transferred to a second furnace and heated to 300°C. Temporary electrical connections were made down the sides of the samples and stannous chloride formed a pseudomorphic layer - ref. {4.4} a few molecules thick on the surface, producing an even conductive coating irrespective of the complexity of the material shaping.

Finally two conductive strips of gold were evaporated by conventional vacuum techniques down the sides of the sample for the purpose of electrical connection and to define the heated area within the working area of the tunnel. As an initial test piece a conductive layer was evaporated onto a flat piece of material. The resistance was found to be 500 Ωs over a 7.62 cm width, 10.16 cm long, by creating a 100 volt D.C. across the sample a potential plot was made showing the variation to be approx. 5%, which was well within the limits required to assume an even coating. Four different shapes were projected as examples of disruptive surfaces. The flat plate, dimple, half and full louvre.

The flat plate as described was also used to evaluate the stannous chloride evaporation techniques. The material used to form the shape in all these cases was Pyrex glass of thickness 8 x 10^{-2} cm. The thickness was a necessary compromise because of the high stresses involved in the moulding process and the material thinning as it was drawn between the moulds. The first shape to be produced was that of the dimple, which proved to be a very useful sample. Problems, however, became apparent when a half louvre shape was attempted. It had been hoped that the extreme material thinning in the region between the trailing edge of a louvre and the start of the next (Drawing 4.1) could be cut away to form the gap required. Only three successful shapes were obtained before the sample shattered inside the mould during the cooling period. The mould was damaged irrevocably. From these three samples two shattered during the hand washing finishing stage and the third during the first experiment made on it. To overcome this problem an alternative approach was used, allowing the laboratory workers to use their skill of cutting and shaping glass by hand rather than a remote forming process. A precoated sheet 7.10^{-2} cm thick flat Pyrex glass was supplied by Triplex Limited, cut to shape (Drawing i.1) at Culham and assembled using a flexible epoxy resin. The sample was formed by cutting a square out from the centre of a sheet of conductive glass. A series of conductive glass strips were then mounted to form the louvres, and held in a machined jig until the epoxy resin had set. The jig determined the angle of attack the louvres were to make to the air flow. The angle was calculated with respect to the thickness of the louvre, the length of the louvre and the channel width (i.e. distance between one set of louvres and the set directly above or below). These dimensions were based upon actual production shapes and scaled by a factor of five. Appendix (4) describes the method by which the angle of attack was determined. Two full louvre samples were fabricated, one to be used in the single fin experiments, the other as the live fin in the block experiment. The size of the removed square was 6.35 cm long by 7.62 cm wide. Each of the five louvre strips were 1.27 cm wide, 7.3 cm long with a small flange of 0.158 cm to locate them into the gap.

Block Sample

The block sample was designed to simulate an actual radiator core. Nine fins were mounted in parallel, the central one of which being one of the conductive full louvre shapes. The other eight dummy fins were made to identical specifications as the live sample. They were made from high temperature epoxy resin strengthened with carbon fibres. The samples were made at Cowley Body Plant (British Leyland). Different types of material were tried in order to add strength to the shapes i.e. glass fibre cloths of varying weave and thickness. However, it was found that the carbon fibre samples were the most even in thickness and distorted the least with heating. They were also the most robust.

The mounting of the nine fins to form the test specimen was a delicate operation. Four thin brass strips with grooves at 1.27 cm intervals along their sides were produced. Two strips were first held in position with a soluble adhesive against the large glass windows of the wind tunnel test section. The central live fin was clamped between these two windows and located in the pair of central grooves. The remaining dummy fins were fixed into position locating into pairs of grooves. Finally the front strips were located to hold the whole system rigid. A series of experiments were then made on the sample.

General Discussion of Sample Fabrication

A description has been made of the various techniques available for the production of the samples.

The glass samples were found to be advantageous with respect to the standard of holographic images obtained. These samples acted as secondary sources of illumination producing much brighter holograms. They were also found not to warp or distort with successive heating and cooling, thus yielding the most reliable results. The input power which could be applied to them was far higher than that which could be applied to the epoxy resin samples (maximum power input to the glass samples in the region of 40 watts).

Although holograms of several complex shapes have been obtained interpretation of the holographic fringe information is complicated by several factors:

1. It was not possible to determine the exact temperature of the surfaces; and it is unlikely that the samples were isothermal.
2. The limitations of photographic resolution made the interpretation of the fringe information difficult.
3. Particular areas in the holographic images fall below the laser speckle noise level and are obscured.

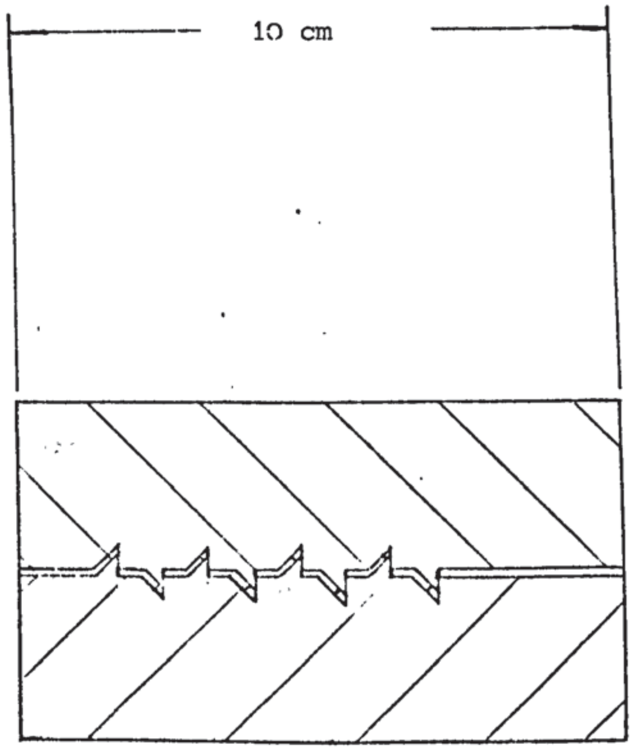

Drawing (4.1)

Mould used for making the louvre sample.

SECTION ON ℄

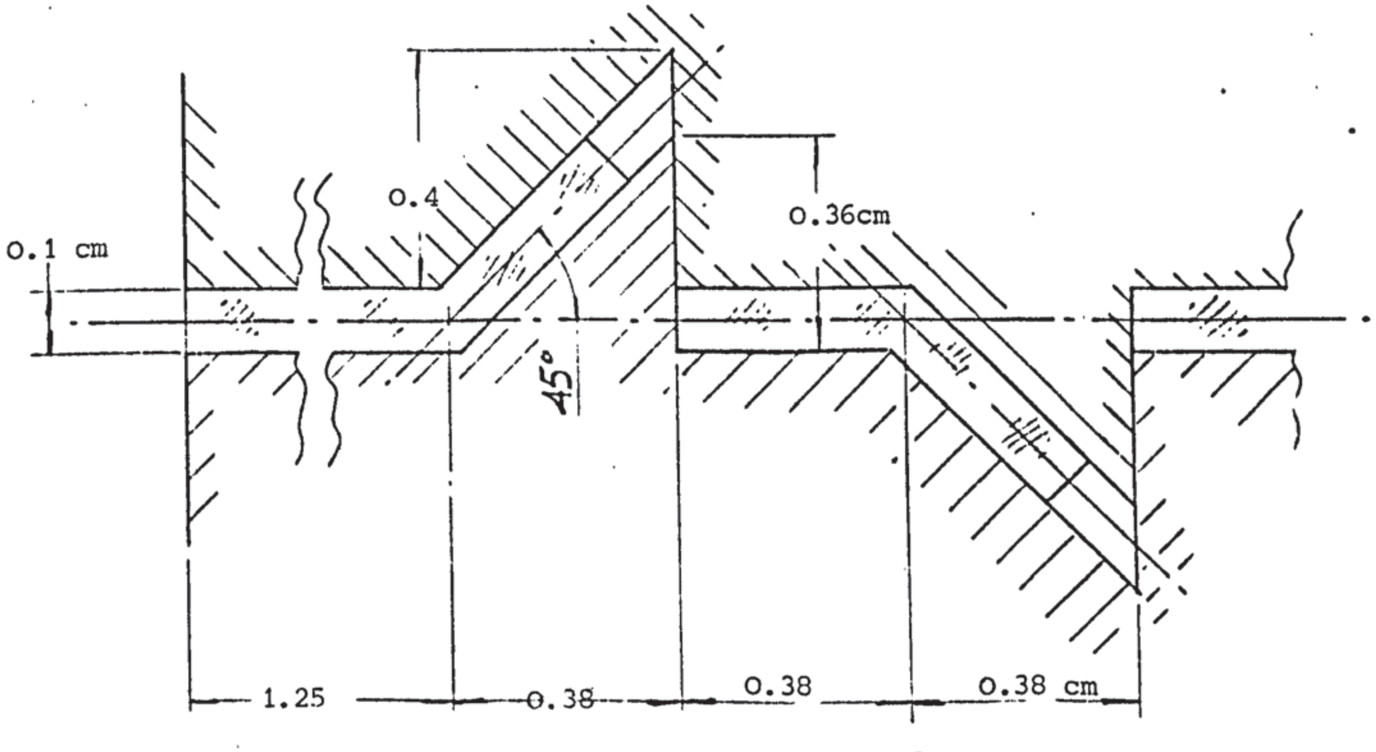

DETAIL OF FORM. SCALE 10:1

CHAPTER 5

FLAT PLATE HOLOGRAPHIC SAMPLE

FLAT PLATE HOLOGRAPHIC SAMPLE

An investigation has been made into the isothermal distribution on air surrounding a heated flat plate. A comparison has been made between the distribution anticipated and that actually observed. The surface temperature of the plate has been monitored at three points using thermocouples, the results obtained have also been presented. Particular attention has been given to the design of the sample so that:-

The surface of the sample could be considered as isothermal when heated.

A surface temperature of over 100°C above ambient conditions could be achieved.

The sample was chosen such that the thermal boundary layer was large enough to be visualized holographically.

The shape was chosen as one likely to correspond with known theory.

Several of the points discussed in this chapter are also similar to those considered with respect to the multiple strip model (Chapter 6). Many of the design features required that an average heat transfer coefficient be calculated, laminar boundary layer theory as described by Schlichting ref {5.1} has been used. However, it is noted that the solutions used are of an approximate nature, to give magnitude to the design criterion, and assume incompressible flow.

Thermal Conductivity of Sample

The surface of a flat plate could be considered isothermal if the surface heat transfer coefficient is much lower than that of the heat transfer through the cross-sectional area of the plate material.

The flat plate used for experimentation was constructed from two sheets of copper $1.58.10^{-3}$ m thick. A heating element was sandwiched between the two sheets. The sheets were joined at the front and rear using silver solder, care being taken to produce a smooth aerodynamic shape along the leading edge.

An estimate of the temperature difference likely to be experienced between the front and rear of the sample was made using laminar boundary layer theory to calculate the local heat transfer coefficient, and the known thermal conductivity of copper. Two extreme coefficients have been calculated, the first at a point 1 cm from the leading edge and the second at the trailing edge of the plate.

$\bar{h}_1$ (1 cm from stagnation point)

$$= \overset{0{\cdot}332}{\cancel{0.664}} \times (Pr)^{1/3} \; (R\;)^{1/2} \; k/l$$

$$= \overset{0{\cdot}332}{\cancel{0.664}} \times 0.89 \times 0.028 \times \left\{\frac{1.6 \quad 10^{6}}{10^{-2} \quad 19.6}\right\}^{1/2}$$

$$\bar{h}_1 = \overset{23}{\cancel{47}} \text{ Watts/m}^2 \, {}^{o}C$$

$\bar{h}_2$ (at the trailing edge of the plate)

$$\bar{h}_2 = 0.332 \times 0.89 \times 0.028 \left\{\frac{1.6 \; . \; 10^{6}}{7.62 \; . \; 10^{-2} \; . \; 19.6}\right\}^{1/2}$$

$$= 8.5$$

The temperature extremes at the front and rear of the plate can now be approximated by a further assumption. It is assumed that h_1 the heat transfer coefficient applies to the first half of the plate, and h_2 to the rear half. Thus the heat lost from the front half of the plate can be expressed as

$$h_1 \, Sa_1 \, \theta_1 - Qp \, (\theta_1 - \theta_2) \;=\; P_1 \qquad (5.1)$$

where Sa_1 is half the surface area of one side of the plate

Qp is the power transmitted down the plate by the existence of a temperature difference,

θ_1 temperature above ambient at the front of the plate,

θ_2 the temperature at the rear of the plate.

$$Qp = \frac{KA}{(1/2)}$$

where K is the thermal conductivity of copper 380 W/m °C

A is the cross-sectional area of the plate

1/2 is half the length of the plate

A similar expression to that of (5.1) can be obtained for the rear of the plate where

$$h_2 \, Sa_1 \, \theta_2 + Qp \, (\theta_1 - \theta_2) = P_1 \qquad (5.2)$$

and by combining these two expressions

$$h_1 \, Sa_1 \, \theta_1 - 2 \, Qp \, (\theta_1 - \theta_2) = h_2 \, Sa_1 \, \theta_2 \qquad (5.3)$$

$$Qp = \frac{(380 \times 1.58.10^{-3} \times 2.5 \times 0.0254)}{1.5 \times 0.0254} = 1.25 \text{ Watts/}^{\circ}\text{C}$$

$$h_1 \, Sa_1 = 47 \times 2.5 \times 1.5 \times (0.0254)^2 = 0.11$$

$$h_2 \, Sa_1 = 8.4 \times 2.5 \times 1.5 \times (0.0254)^2 = 0.02$$

If these values are substituted back into equation (5.3) then an approximate relationship between θ_1 and θ_2 can be found

$$0.11 \, \theta_1 - 2.5 \, (\theta_1 - \theta_2) = 0.02 \, \theta_2$$

$$0.96 \, \theta_1 = \theta_2$$

If as an example the average plate temperature was 100°C $((\theta_1 + \theta_2)/2)$, then $\theta_1 = 49$ and $\theta_2 = 51$, indicating a difference of $(\theta_2 - \theta_1) = 2^{\circ}$C.

As a correlation to this calculation, three thermocouples were placed between the two copper sheets. One was mounted 1 cm from the leading edge, another 1 cm from the trailing edge and the third centrally. No temperature difference larger than 3°C was found to occur during the experimental work. This largest difference occurred when the mean temperature was 120°C above ambient temperature.

Biot and Fourier Moduli

The Biot and Fourier moduli have been calculated in order to satisfy two design requirements. The first is with respect to the method by which the sample is heated. 50 Hz alternating current was applied to the heater sandwiched between the copper plates. A calculation has been made as to the possibility of the wave form of the current producing any significant variation to the surface temperature. The second consideration was the time required for a sample to reach its maximum surface temperature for a given constant applied power input.

The Biot modulus is given as $\frac{hD}{k}$

and the Fourier modulus $\frac{\alpha\tau}{D^2}$

D is the characteristic length and is found from the ratio of volume to surface area.

For each plate the volume is $l \cdot w \cdot d$,

where l is the length $7.62.10^{-2}$ m

w is the width $6.99.10^{-2}$ m

d the thickness $1.58.10^{-3}$ m,

and the surface area available for heat conduction to the airstream

$$2\ (l \times w + l \times d + w \times d)$$

as $d \ll l$ or w.

The characteristic~~s~~ taken, d the thickness of material

$$T = T_o \quad \exp - \frac{\tau\alpha}{D^2} \quad \frac{hD}{k}$$

If To is the starting temperature, then T is the temperature after τ seconds for a cooling body.

Where α is the diffusivity of copper. 115.10^{-6} m/sec

d is the thickness

k the thermal conductivity of copper 380 W/m $^\circ$C

h is the average heat transfer coefficient - 19 $W/m^2 \, ^\circ C$ (at 5.4 ft./sec 1.65 m/s).

$$\therefore \quad \frac{\alpha h}{d\,k} = 3.64.10^{-3} \; \frac{1}{\text{secs}} \simeq 0.218 \;\; 1/\text{mins}$$

Thus it can be seen that the effect of the 50 Hz A/C is negligible, even if for calculation purposes; the wave form was taken as a square pulse, which allowed cooling for a full half cycle.

If $\tau = 1/\underset{100}{\cancel{50}}$, the fall in temperature is

$$T = T_o \quad e^{-(7.10^{-5})}$$

An estimate of the time required for the sample to reach 0.9 of its full temperature can be found from the expression

$$T = T_{max}\left(1 - e^{-(\tau L)}\right) \tag{5.4}$$

where $L = \frac{\alpha h}{dk}$

T_{max}, is the maximum temperature the body can reach for a constant input power; and T is the temperature after a time τ.

Thus for T = 0.9 To, $\tau \simeq$ 10 mins

T = 0.99 To, $\tau \simeq$ 20 mins.

The factor L is a function of the heat transfer coefficient of the surface to air, which in turn is dependent on the free stream velocity. Radiation losses have not been taken into account and contribute a further factor to equation (5.4).

The calculated time for the sample to reach 99% of its maximum temperature can be compared with a series of experiments. The plots, plot (5.1) to plot (5.8) represent excess temperature °C against time in minutes (i.e. the time taken for the sample heat-up for a set power input). It can be seen in the majority of cases the predicted time is close to that observed.

Natural Convection

In considering the flat plate experiment it was necessary to calculate when natural as opposed to forced convection was likely to contribute to the heat transfer from the surface. This effect has also been considered with respect to the multiple strip heat exchanger model in the next chapter, where the Grashof and Reynolds numbers have been defined (page no. 66)

Natural convection is anticipated to make a contribution to the heat transfer if:

$$\frac{Gr}{R^2} \gtrsim 1$$

For air at 100°C $\frac{Gr}{l^3\theta} \hat{=} 0.5.10^8/m^3\,{}^\circ C$ (values taken from Ede - Ref.{5.2})

$$\text{Thus} \quad \frac{Gr}{R^2} \hat{=} \frac{0.5.10^8\ (80)\ (7.62.10^{-2})^3}{\left\{\frac{V\ .\ 7.62.10^{-2}}{2.10^{-5}}\right\}^2} \simeq \frac{0.5.10^8\ \theta l^3}{\left(\frac{Vl}{\nu}\right)^2} \geq 1$$

Where V is the velocity of the air m/sec

l is the characteristic length of the sample

ν is the kinematic viscosity

θ is the excess temperature

Rewriting the previous expression in terms of V

$$V = \left(0.5.10^{8}\ \theta(\nu)^{2}\ l\right)^{1/2}$$

$$= 0.4 \text{ m/s}$$

The velocity of 0.4 m/sec is within the range of velocities used in the wind tunnel. The difference as seen holographically between natural and forced convection - fig. (11) and fig. (15) is quite definite. The fringe distribution obtained for natural convection forms a classical plume above the plate whereas forced convection can be seen as a thermal boundary.

If there were a contribution to the heat transfer by natural convection as opposed to forced, its effect would be to distort the otherwise symmetrical thermal boundary profile. The upper boundary would be expected to be thicker than the lower.

From the thermocouple readings no significant effect can be related directly to natural convection except in a no air flow condition.

In conclusion, the factor $\frac{Gr}{R^2}$ predicts that natural convection is likely to be present at low speed. Due to the error factor associated with making low speed measurements and the lack of definition in the holographic information, it was not possible to observe a contribution from natural convection. However, the more characteristic effect illustrated by - fig. (11) was not found present, thus if there was a natural convection contribution it was not significally disturbing the temperature distribution in the thermal boundary layer.

Finally, an estimate has been made of the power that would be theoretically dissipated by a plate operating in natural convection. For natural convection in the laminar region Fishenden and Saunders - Ref {5.4} suggest the following expressions, for an upward facing horizontal plate,

$$Nu = 0.54 \quad (Gr\ Pr)^{1/4}$$

and for a downward facing plate

$$Nu = 0.25 \quad (Gr\ Pr)^{1/4}$$

The power dissipated can be expressed as

$$Q = 0.79 \left\{ \beta g \frac{\ell^3 \theta}{\mu^3} \right\}^{1/4} . \frac{k}{\ell} . \ell . b . \theta$$

and terms of the particular sample tested $Q = 2.10^{-3} \quad \theta^{1.25}$ Watts.

This theoretical estimated value of Q has been compared with the measured value at various values of θ in plot (5.9).

Estimation of Thermal Boundary Layer Thickness

The thickness of the thermal boundary layer formed by air flowing over a flat plate at zero angle of attack can be approximated from the following expression

$$\delta_{th} = \frac{1}{(Pr)^{1/3}} \quad \frac{5\ \ell}{\left[\frac{\ell\ V}{\nu}\right]}^{1/2} \qquad (5.5)$$

This expression was obtained from the Handbook of Heat Transfer - Ref. {5.4}.

The value δth represents the distance from the surface where the temperature within the boundary layer is 1% greater than that of the temperature of the stream flow. From experience it has been found advisable for the size of the boundary to be of the order of 5.10^{-3} m thick. This is to allow suitable detail in the subsequent holographic reconstruction. It has been found for thermal boundary depths of less than 3.10^{-3} m the fringes produced can no longer be photographically resolved.

Table (5.1) uses expression (5.5) to determine variations in thermal boundary depth with different free air stream velocities at a distance $7.62,10^{-2}$ m from stagnation point for a flat plate sample.

TABLE (5.1) Thermal Boundary Layer Depth as a Function of Stream Velocity at a Distance 7.62 cm from Stagnation.

Velocity m/s	Boundary Depth m
1.6	$5.4\ 10^{-3}$
1.5	$5.6\ 10^{-3}$
1.25	$6.2\ 10^{-3}$
1.0	$6.9\ 10^{-3}$
0.75	$8.0\ 10^{-3}$
0.5	$9.8\ 10^{-3}$

Values calculated from expression $\delta th \triangleq \frac{5}{(Pr)}\ 1/3 \left(\frac{\ell\ .\nu}{V}\right)^{1/2}$

where ℓ characteristic length ($7.62.10^{-2}$ m)

ν kinematic viscosity (2.10^{-5} m^2/s)

V free stream velocity

Radiation Losses

The heat lost from the surface of the plate by radiation has also been considered. Using Stefans equation for heat lost by radiation this factor has been calculated as:

$$R = Sa\ \sigma\ \xi \left((T + \theta)^4 - T^4\right)$$

where Sa is the surface area of the plate (5.10^{-3} m^2)

σ is Stefans constant ($5.67\ 10^{-8}$)

T the ambient temperature (300 ^{o}K)

θ the excess temperature ξ is the emmisivity factor associated with the material for copper this factor can vary from 0.1 for a highly polished surface to 0.9, representing a dull finish. In these calculations the figure of 0.25 has been used as the surface was slightly dulled due to continual heating and cooling - ref. {6.2}

$$R = 0.68.10^{-10} \left((\theta + T)^4 - T^4 \right)$$

The following table is an estimate of the heat loss in Watts from the sample at various temperatures above ambient.

TABLE (5.2) Temperature of Flat Plate Holographic Sample against Calculated Radiation Heat Losses

(excess temperature $^{\circ}$C)	Radiation loss Watts
40	0.36
50	0.47
60	0.59
70	0.72
80	0.87
90	1.0
100	1.2

Forced Convection, Thermocouple Measurements

As a cross-check to the holographic data a series of experiments were made to determine the amount of electrical power being applied to the sample and its resulting surface temperature. It has previously been mentioned that three thermocouples were situated in the sample. All three were sandwiched between the two copper plates, one near the leading edge, a second near the trailing edge and the third centrally.

During the experimental work the largest temperature difference between the front and rear thermocouples at 100°C temperature difference was 3°C. The rear thermocouple showing the greater temperature.

A series of experiments were made increasing the power applied to the sample at twenty minute periods and noting the temperature. The experiments were carried out in the range of 0 to 100°C temperature difference. The heating period was to allow the sample to reach its full temperature as described previously. The results obtained have been compared with theoretical power dissipations as presented by Schlichting - Ref. {5.1} and Ede - Ref. {5.2} for the power dissipation from a flat plate to air. In the laminar situation

$$Q_L = 1.328 \times k \times \overset{w}{\cancel{b}} (Pr)^{1/3} (R_e)^{1/2} \Delta \theta \qquad (5.6)$$

and $$Nu = (R_e)^{1/2} (Pr)^{1/3} 0.664 \qquad (5.7)$$

In the turbulent situation:

$$Q_T = 0.0\overset{7}{\cancel{6}}4 (Pr)^{1/3} (R_e)^{0.8} \times \overset{w}{\cancel{b}} \times k \times \Delta\theta \qquad (5.8)$$

$$Nu = 0.037 (Pr)^{1/3} (R_e) 0.8 \qquad (5.9)$$

This is the form stated for the equation neglecting both natural convection and frictional heating for a fluid of $0.6 < Pr < 10$.

As a further consideration calculations have been made with respect to the effect of different temperatures on the constant property terms in the equation and the heat transfer coefficient which can be calculated from them. The results have been tabulated in table (5.3) and show that for both the laminar and turbulent cases the variations are small. In the case of the laminar equation the variation in the heat transfer coefficient is 1% over a 100°C change in temperature.

In an example calculation Eckert and Drake - Ref. {6.3} define when using equation (5.6) an average temperature θ_A, where $\theta_A = (\theta_W + \theta_S)/_2$.

Where θ_A - average temperature
θ_W - wall temperature
θ_S - stream temperature

Table (5.3) shows that for a laminar heat transfer coefficient calculated for air at between 0°C to 100°C the choice of θ_a is arbitrary.

It has been shown in table (5.3) that the Nusselt Number can vary with temperature thus an average temperature of 50°C has been used to determine Nu, both practically and theoretically. As illustrated in table (5.3) the variation in Nusselt number is ± 15% over the temperature range 0°C to 100°C.

TABLE (5.3) Variation of Properties with Temperature for air

Laminar		Turbulent		ν	k	Pr	T
H_T/H_o	N_{ut}/N_{uo}	H_r/H_o	N_{ut}/N_{uo}	10^{-5}	10^{-2}		
1	1	1	1	1.33	2.41	0.72	0
0.996	0.944	0.958	0.903	1.51	2.57	0.71	20
0.996	0.889	0.927	0.825	1.69	2.72	0.71	40
0.995	0.836	0.898	0.751	1.88	2.88	0.70	60
0.993	0.795	0.868	0.693	2.08	3.02	0.70	80
0.989	0.752	0.839	0.636	2.30	3.18	0.69	100

H_T	heat transfer coefficient at temperature T
H_o	heat transfer coefficient at temperature 0°C
ν	kineamtic viscosity
Pr	Prandtl number
T	Temperature
N_{ut}	Nusselt number at temperature T
N_{uo}	Nusselt number at temperature 0°C

Thermocouple Results

The experimentally determined power against surface temperature has been plotted for various air velocities - plot (5.10). A second set of results - plot (5.11) - shows the same data after a correction has been made for radiation losses from the surface (previous section, page 46). For all the velocities considered the graphs show a definite linear relationship, $Q = h\Delta\theta \cancel{\pm c}$,

where Q is the heating removed by the air

h is heat transfer coefficient

Δθ temperature of surface above ambient.

From the graph - plot (5.11) - it is possible to tabulate the Nusselt against the Reynolds numbers where $N_u = \frac{Q}{\cancel{W} . k . \Delta\theta}$ and $R_L = \frac{V . L}{\nu}$

TABLE (5.4) Nusselt and Reynolds Numbers

Air velocity m/s	Reynolds no.	Nusselt (M)	Nusselt (C_1)	Nusselt (C_2)
1.56	6680	70	52	38
1.3	5650	66	48	33
1.06	4540	60	43	28
0.6	2560	45	32	27
0.4	1920	32	28	14

Where Nusselt (M) is the Nusselt number calculated from actual data plot (5.11)

Nusselt (C_1) and Nusselt (C_2) are calculated from equations (5.7) and (5.9) for laminar and turbulent flow respectively.

Holographic Fringe Formation over a Heated Surface

It has been mentioned in the introduction and described in detail in appendix (1) that holographic fringes could only be achieved by heating the sample. Fringes could not be produced by an unheated air flow.

In calculating the provable fringe distribution several factors have been taken into account.

(a) The path length of the light ray passing through the sample section.

(b) The relationship between temperature, density and refractive index of air.

(c) The effect of introducing a heating effect into the Navier-Stokes equation and the possible manner it will effect the thermal distribution within the boundary layer.

These points have been dealt with in other parts of the thesis in greater detail, parts (a) and (b) in appendix (1) and (2) and part (c) in Chapter (7). In this particular set of experiments the surface temperature of the sample was known and the amount of electrical power applied to it.

The number of fringes produced by heating the plate can be estimated from the following equation:

$$\frac{n\lambda}{2} = R\ (n_1 - n_2) \qquad (5.10)$$

Where n is the order number of the fringe

n_1 is the refractive index at ambient temperature T_1

n_2 is the refractive index at T_2 the heated condition.

λ wave length of coherent light source $(n_1 - n_2)$ change in refractive index between exposures.

R optical pathlength over which change in refractive index has occurred.

The refractive index change of air can be rewritten as a temperature change first by a substitution for density.

$$\frac{n_1 - 1}{\rho_1} = \frac{n_o - 1}{\rho_o} = \text{constant}$$

Which can also be replaced by the approximate expression relating to the absolute temperature of the air to the density such that:

$$\rho^1 = \frac{T_o \rho_o}{T_1}$$

This equation (5.10) now becomes

$$\frac{n\lambda}{2} = R\ (n_o - 1)\left(1 - \frac{T_o}{T}\right)$$

Where T_o is the temperature of the air at the ambient condition and

T is the surface temperature of the sample after heating has been applied.

For an actual example the first black fringe would be produced at $\frac{1}{2}\lambda$, the second at $\frac{3\lambda}{2}$ and so on for odd ~~integral~~ integer values of n. Even powers of n produce bright fringes.

In the case of a flat plate heated to 90°C from an ambient condition of 20°C with a pathlength of $6.35.10^{-2}$ m. The number of expected black fringes would be:

$R = 6.35.10^{-2}$ m $\quad \lambda = 0.69.10^{-6}$ m wavelength of laser (ruby red)

$T_o = 293\ ^oK$

$T = 363\ ^oK$ $\quad n_1$ refractive index of air at 20°C - 1.00028.

$$n = \frac{2 \; . \; 6.35.10^{-2}}{0.69 \; . \; 10^{-6}} \quad 28.10^{-5} \quad \left(1 - \frac{293}{363} \right)$$

$$= 9.9$$

Thus five black fringes would be expected and five bright fringes.

Description of Holographic Results

Fig. (23) and fig. (24) represent two holograms made of the holographic sample at different air velocities. Superimposed over the photographs are theoretical solutions for the thermal distribution as described by the Pohlhausen profile - Ref. {5.5} . The data for the curve being taken from Goldstein - Ref. {5.6} . The thermal distribution is calculated from

$$\theta(\eta) = \alpha_1(\sigma) \int_0^{\eta} \left[\frac{\overset{f}{\partial}''(\eta)}{f''(o)} \right]^{\sigma} d\eta$$

where $\theta(\eta)$ is the thermal distribution,

$\alpha_1(\sigma)$ is a factor of the Prandtl number as found by Pohlhausen.

η is the similarity variable. The function

$f''(\eta)$ is found from the Blasius series described in chapter (7).

The resulting comparisons do not show a particularly good match between the theoretical and actual distributions. There is similarity between the curve describing the growth of the boundary in the x direction. The shape of this boundary is found by substituting the relevant η value into the incompressible flow solution developed in appendix (5).

$$\delta_{th} = \eta \left(\frac{\ell \nu}{v} \right)^{1/2}$$

Where δ_{th} is the distance in the y direction with respect to ℓ at which the the particular isothermal corresponding to η lies

ℓ is the distance from stagnation

v the velocity of the air flow.

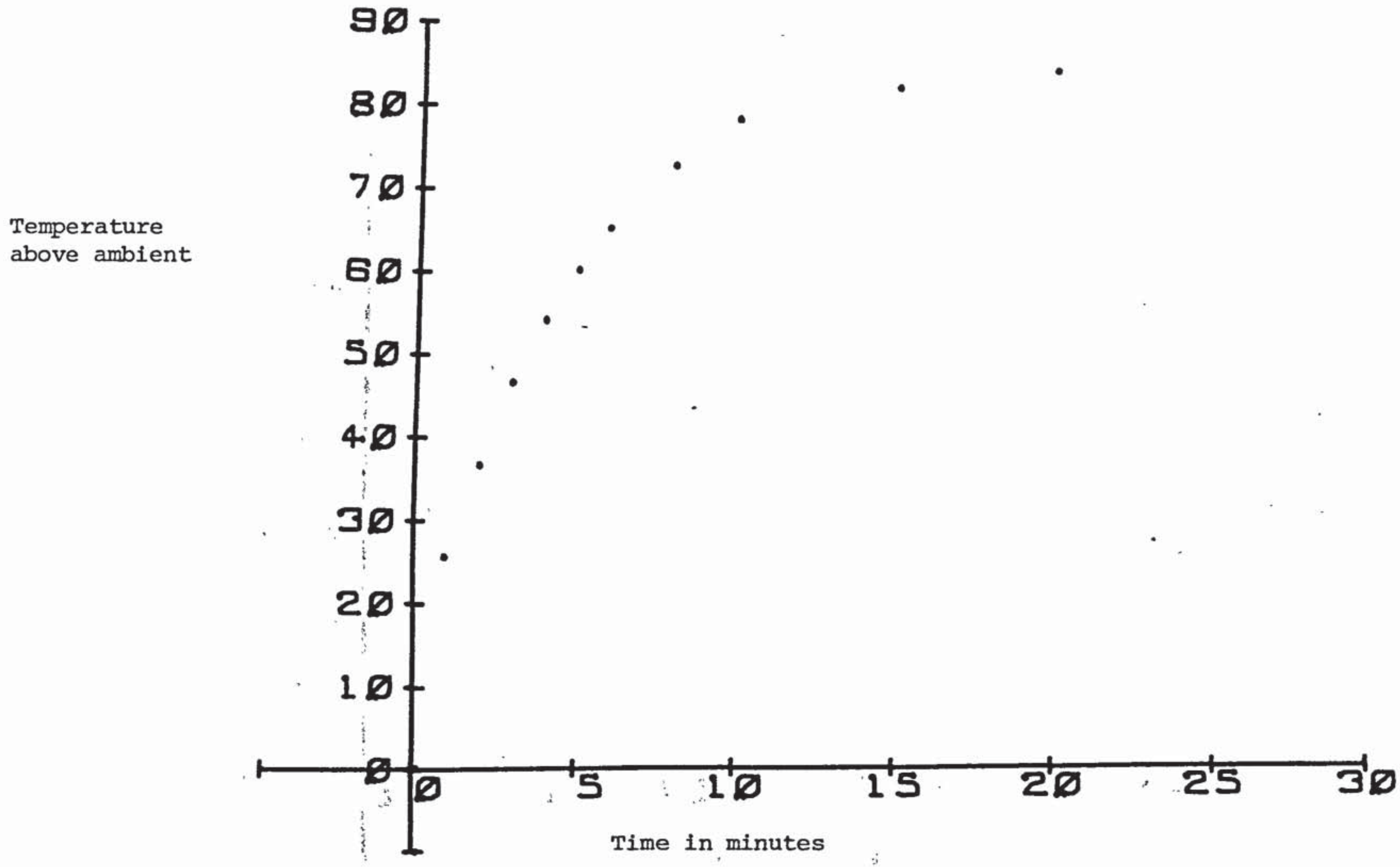

PLOT (5.1) Time taken for sample to reach a stable temperature.Velocity of air 1.6 m/sec.

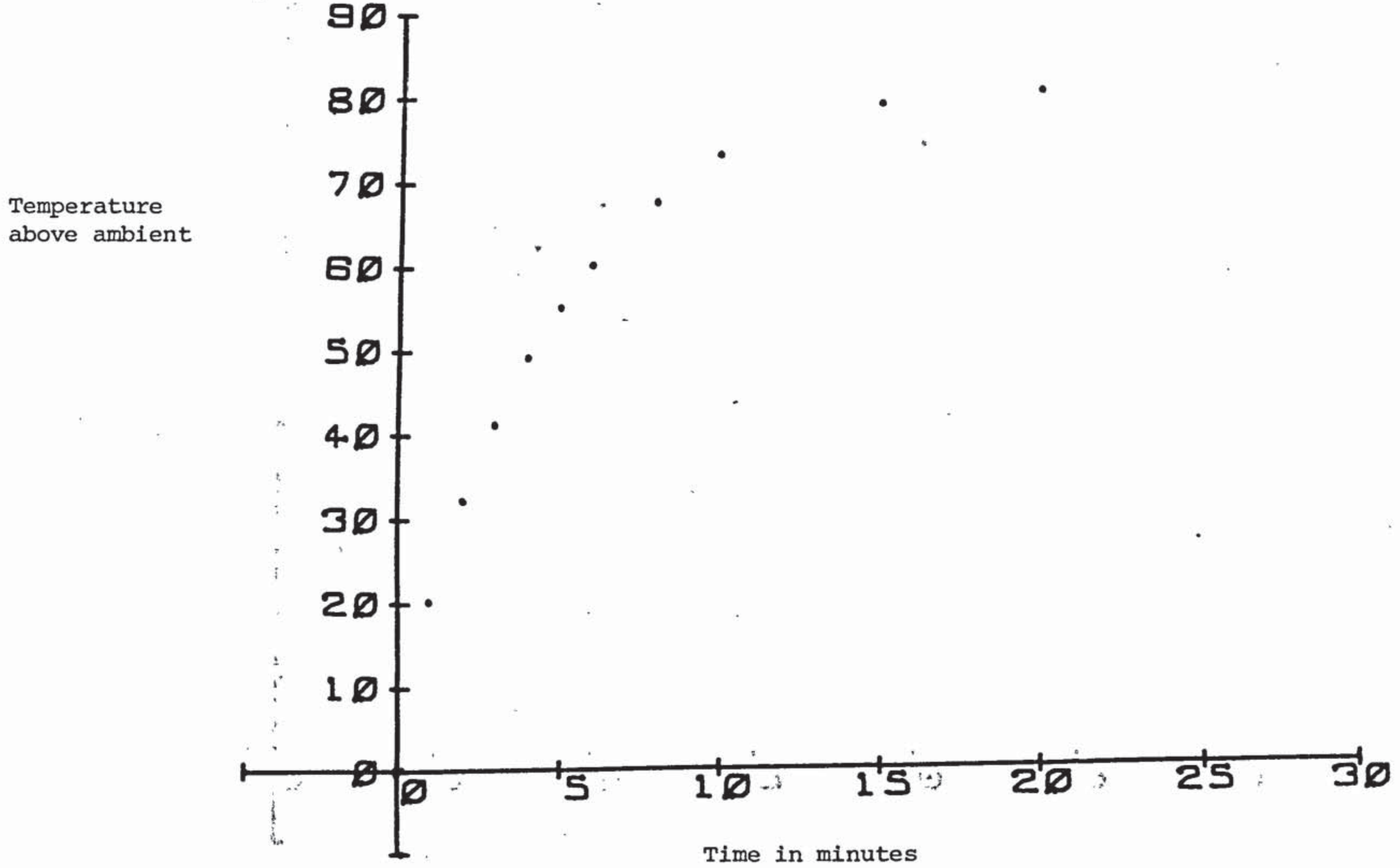

PLOT (5.2) Time taken for sample reaching a stable temperature
Velocity of air 1.5 m/sec.

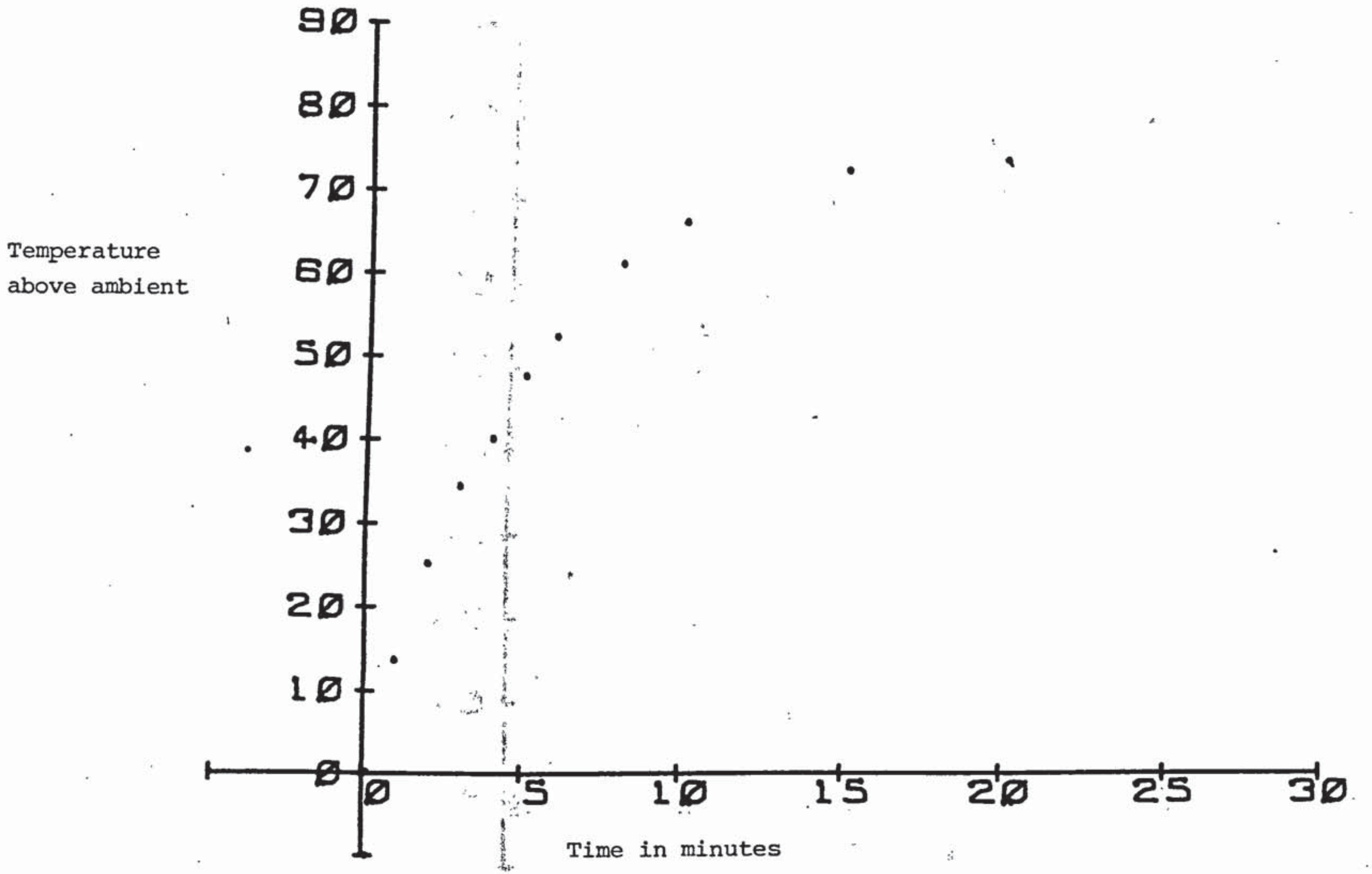

PLOT (5.3) Time taken for sample to reach a stable temperature
Velocity of air 1.4 m/sec.

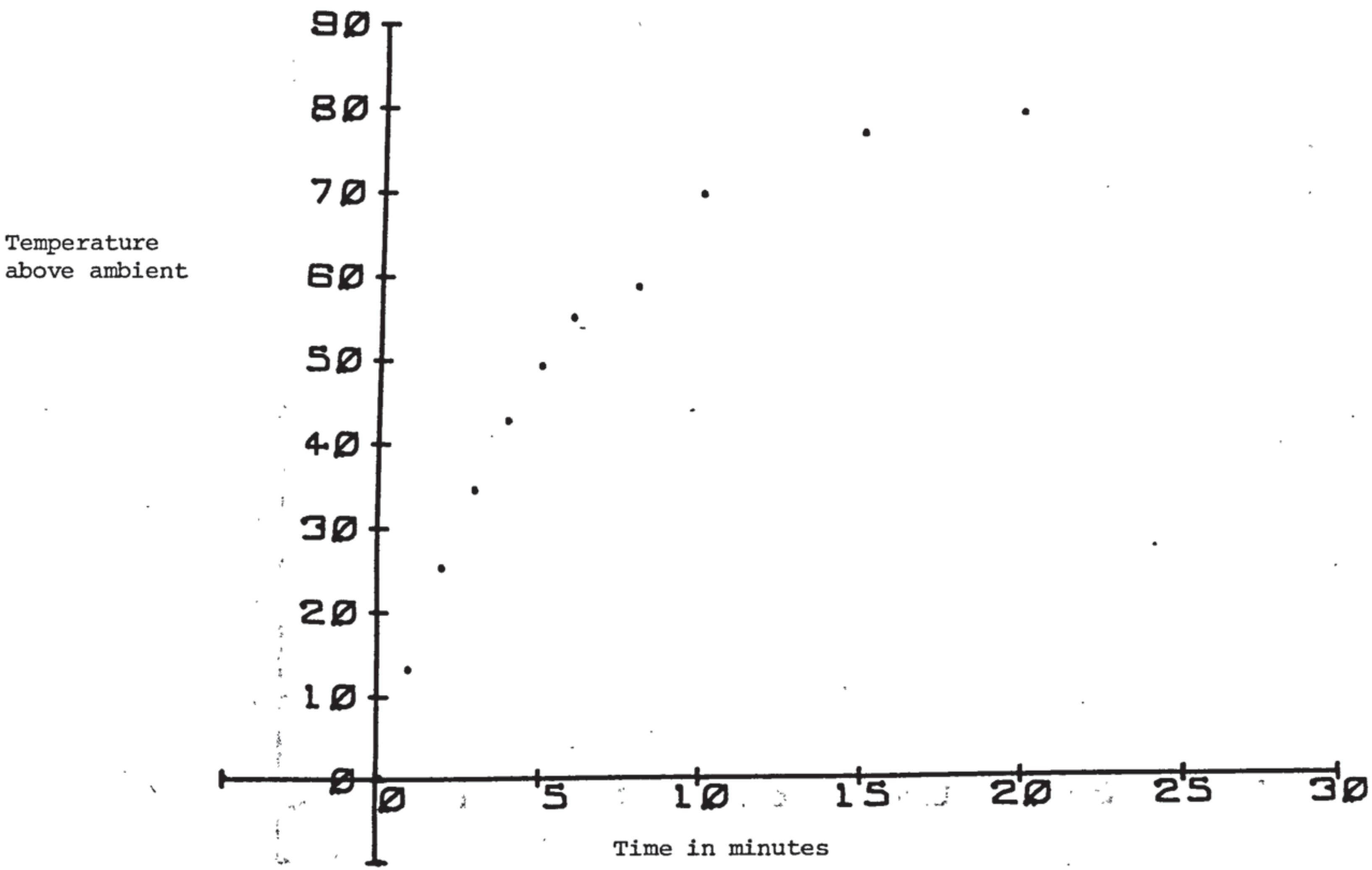

PLOT (5.4) Time taken for sample to reach a stable temperature, Velocity of air 1.3 m/sec.

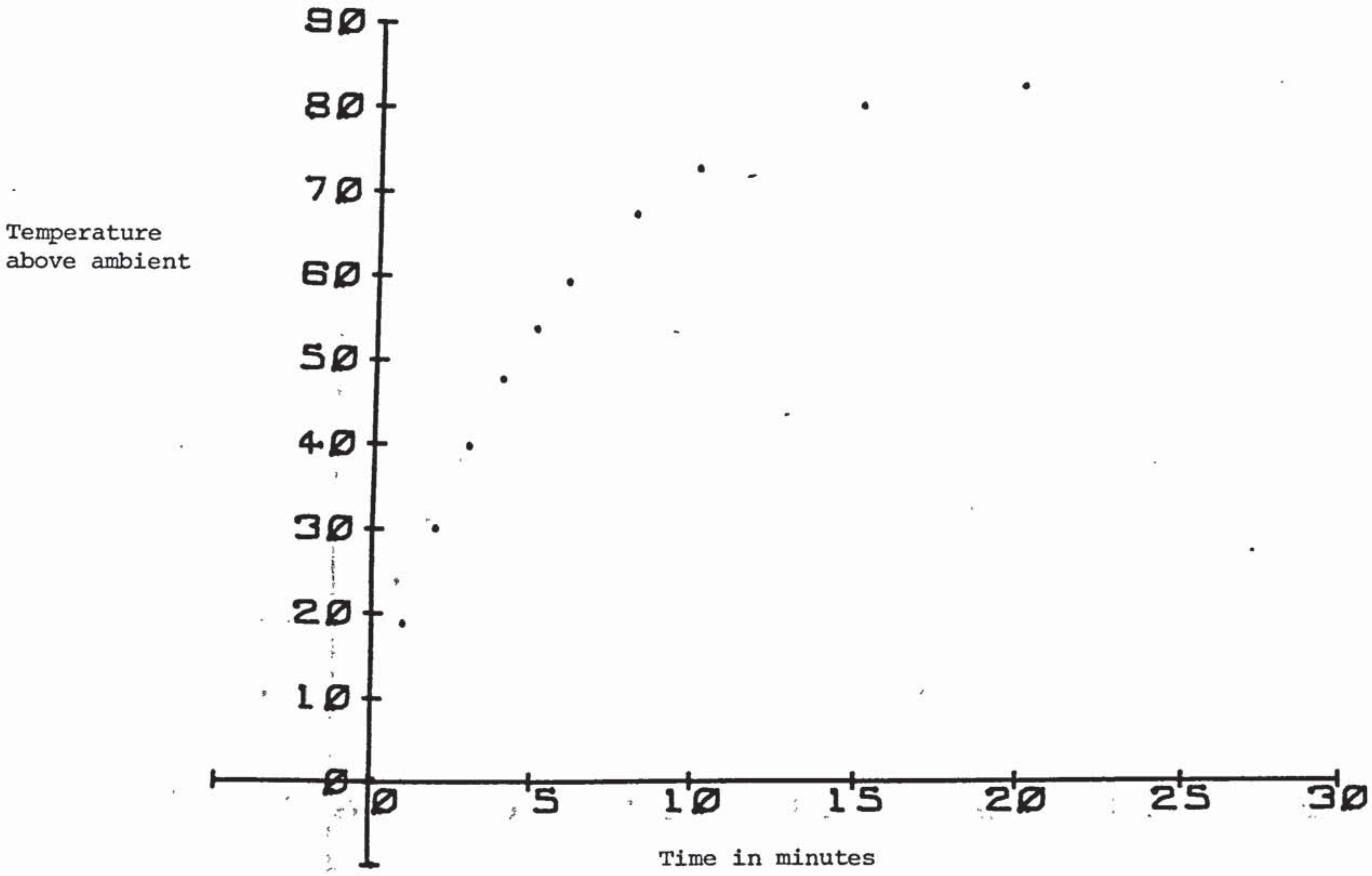

PLOT (5.5) Time taken for sample to reach a stable temperature.
Velocity of air 1.1 m/sec.

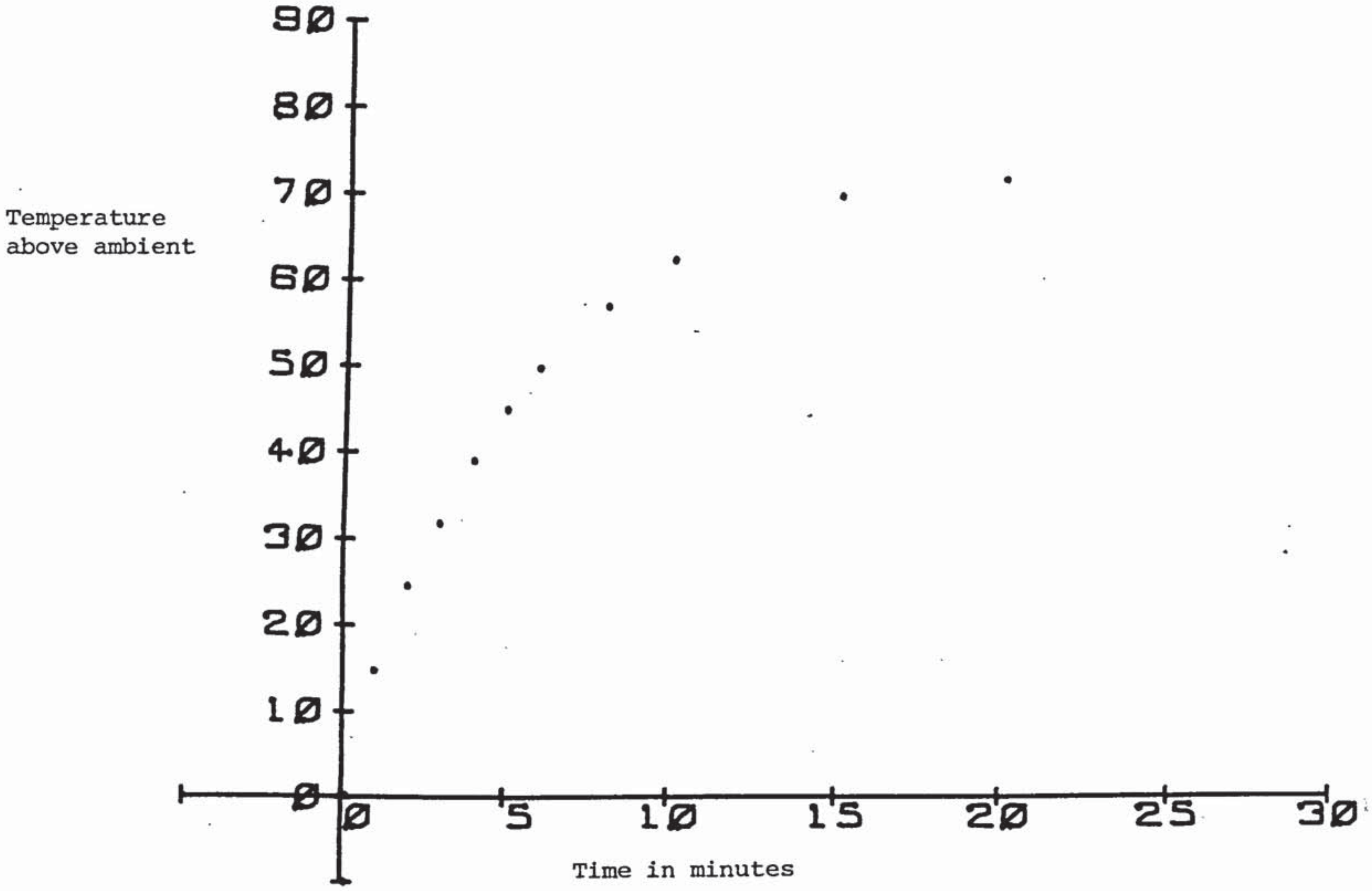

PLOT (5.6) Time taken for sample to reach a stable temperature
Velocity of air 1.0 m/sec.

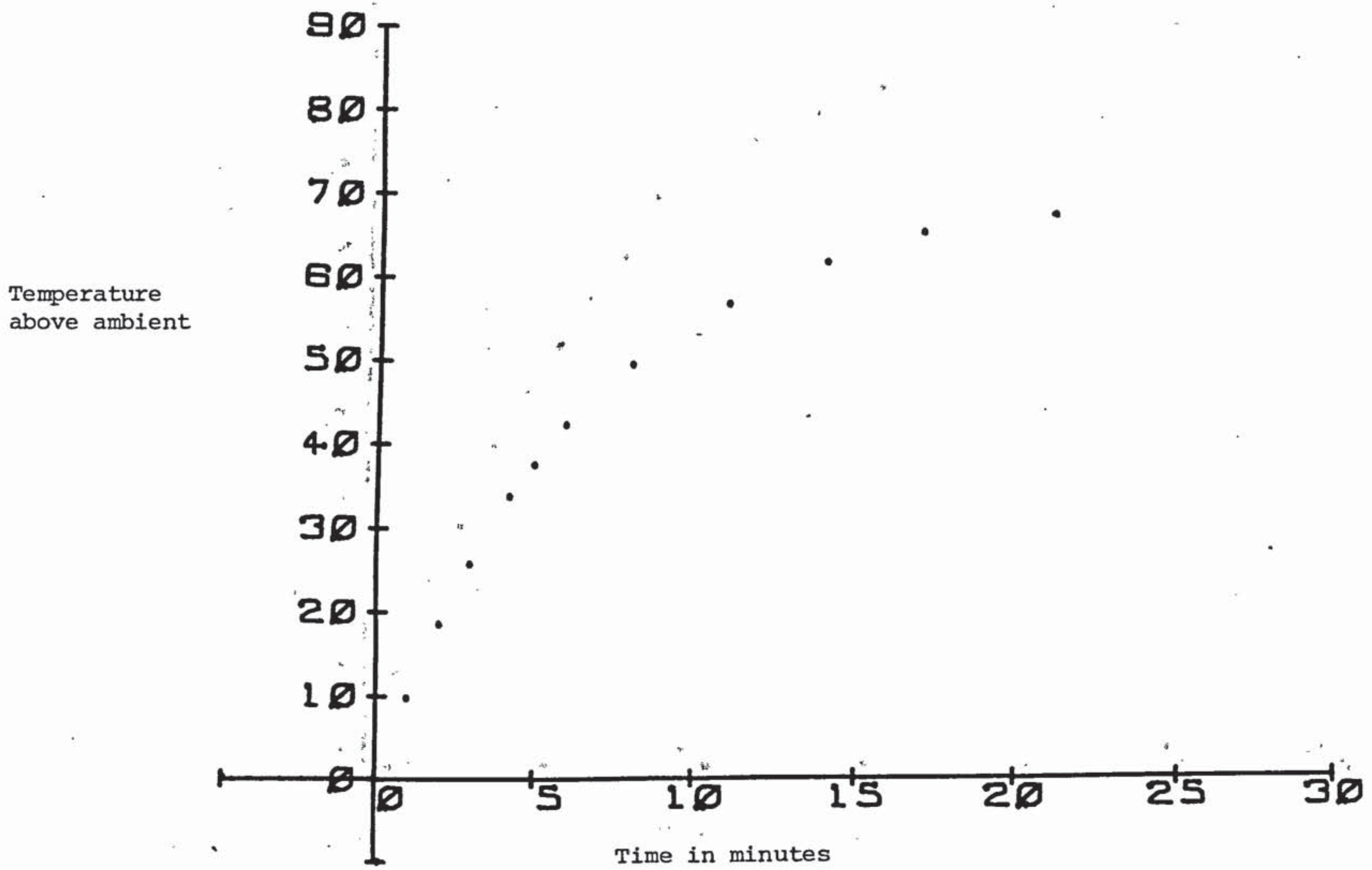

PLOT (5.7) Time taken for sample to reach a stable temperature
Velocity of air 0.8 m/sec.

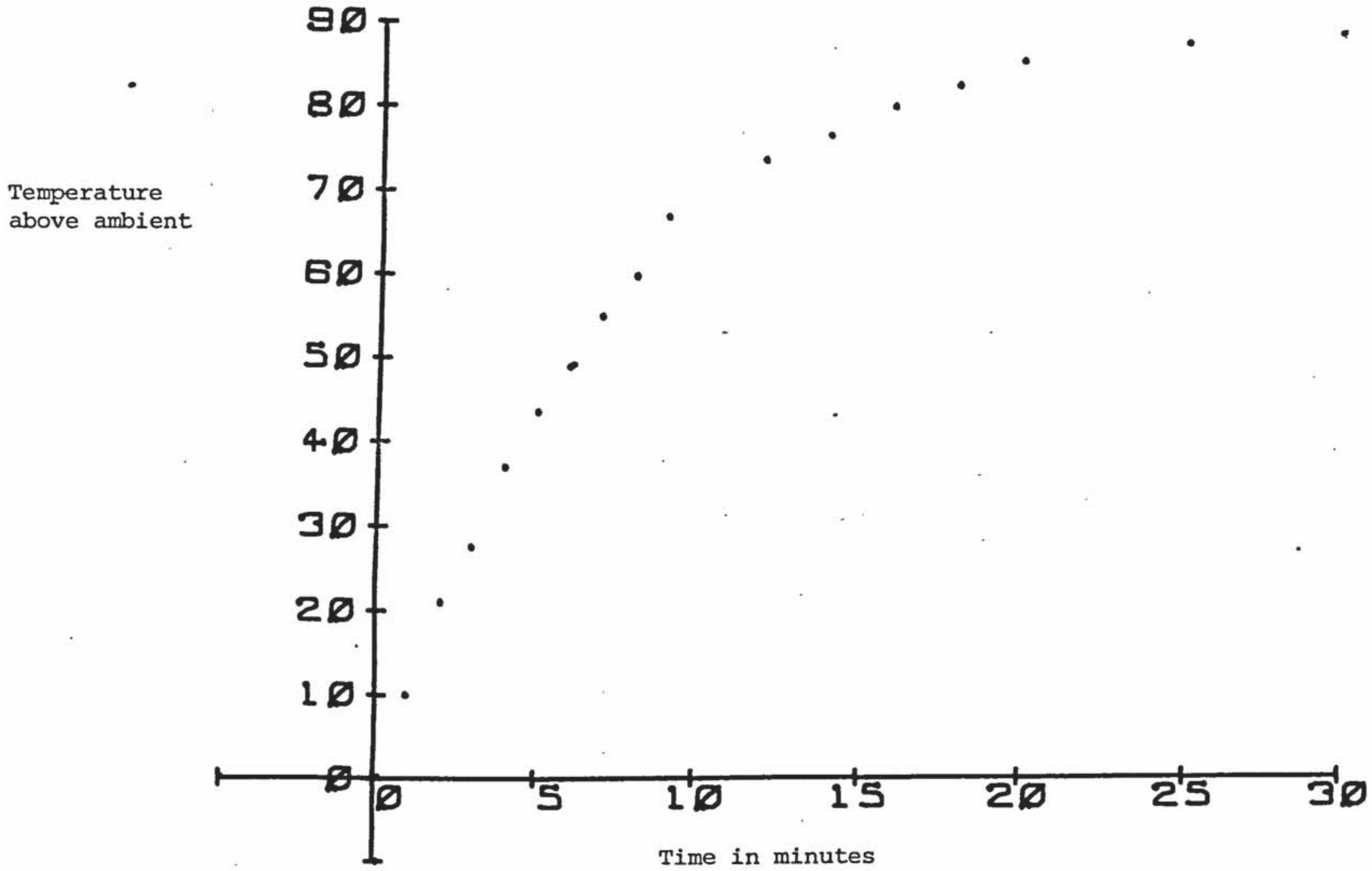

PLOT (5.8) Time taken for sample to reach a stable temperature.
Velocity of air 0.5 m/sec.

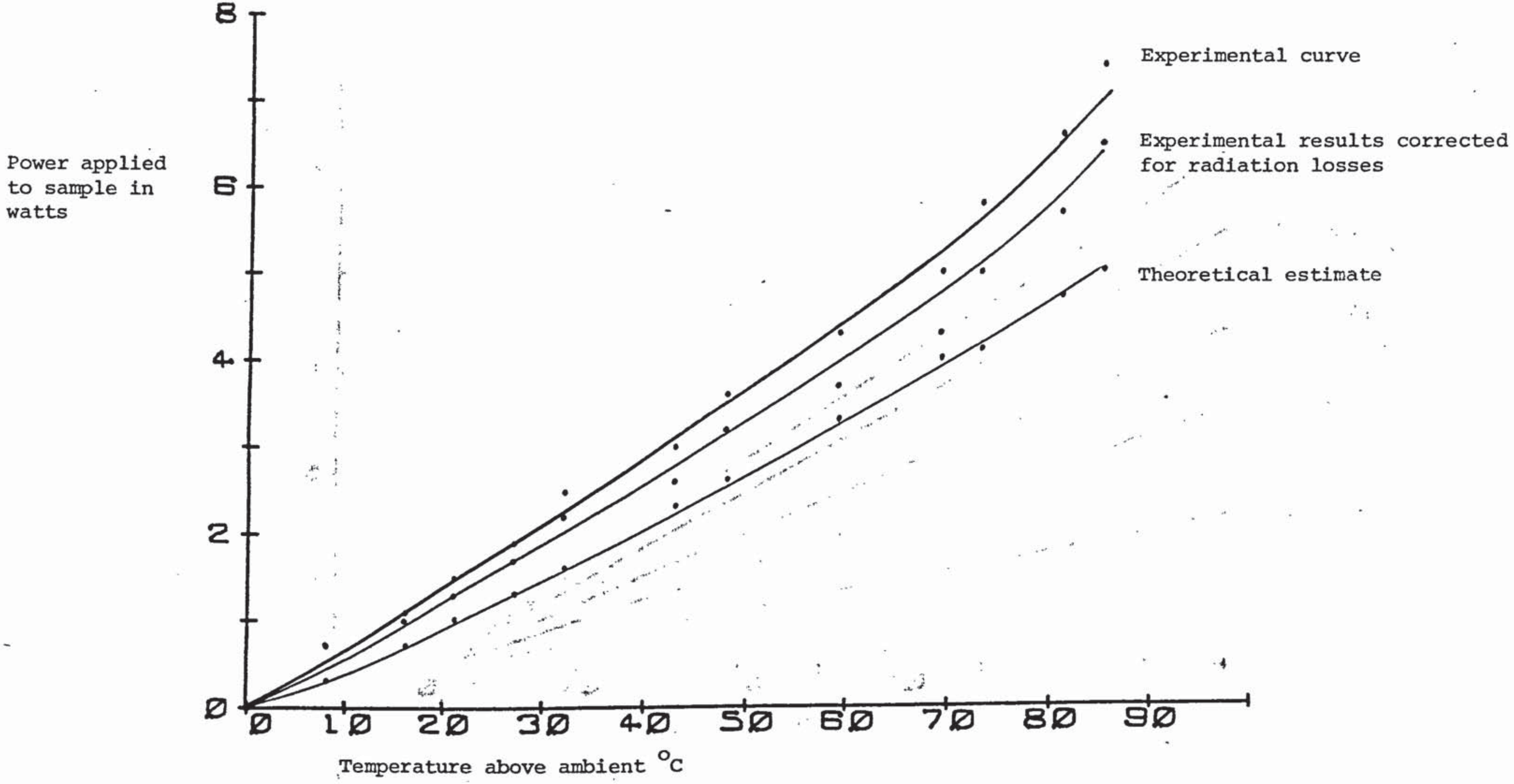

PLOT (5.9) Natural convection. Applied power against excess temperature.

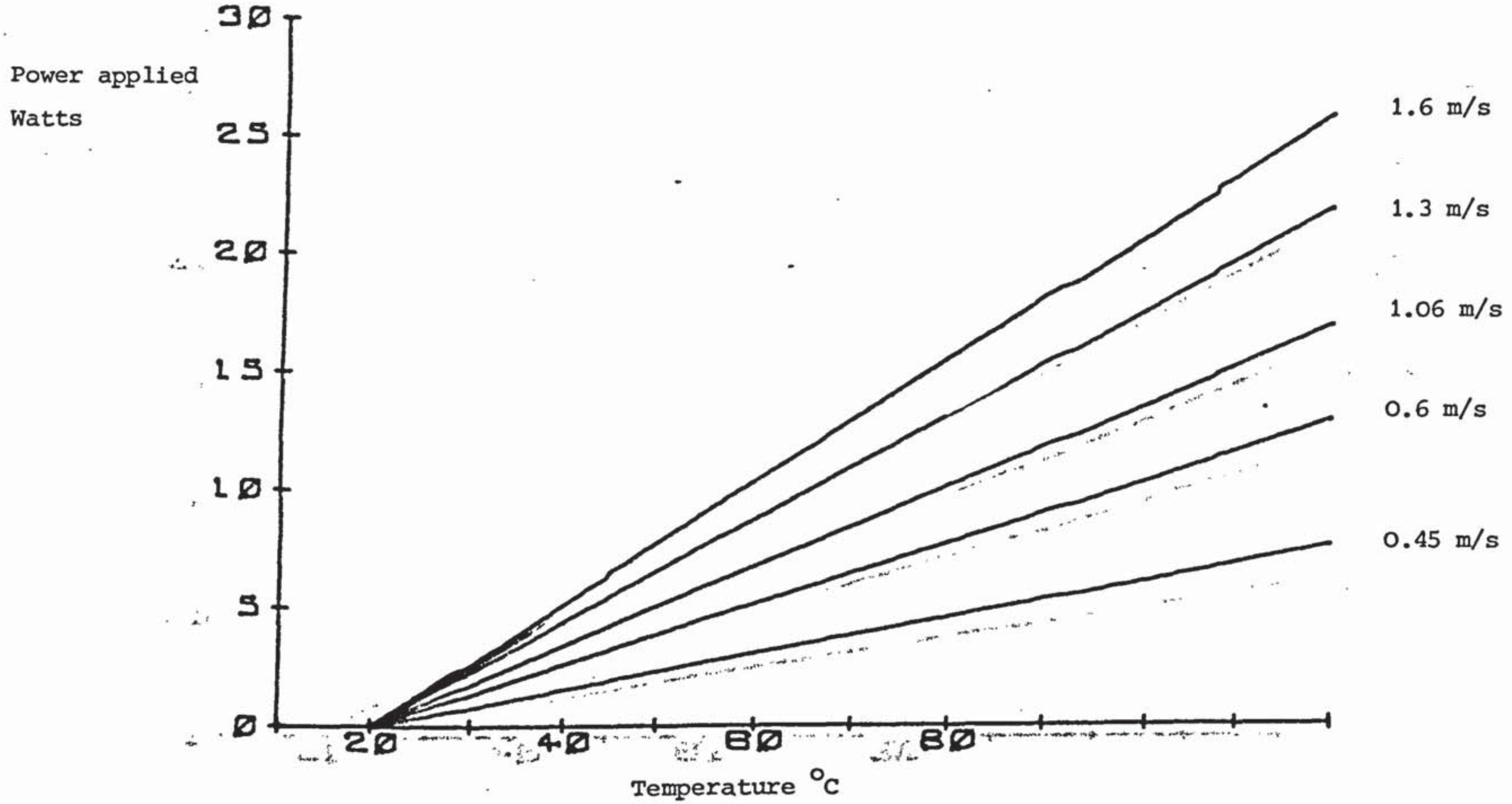

PLOT (5.10) Forced Convection
Power applied to sample against sample temperature
for various air speeds.

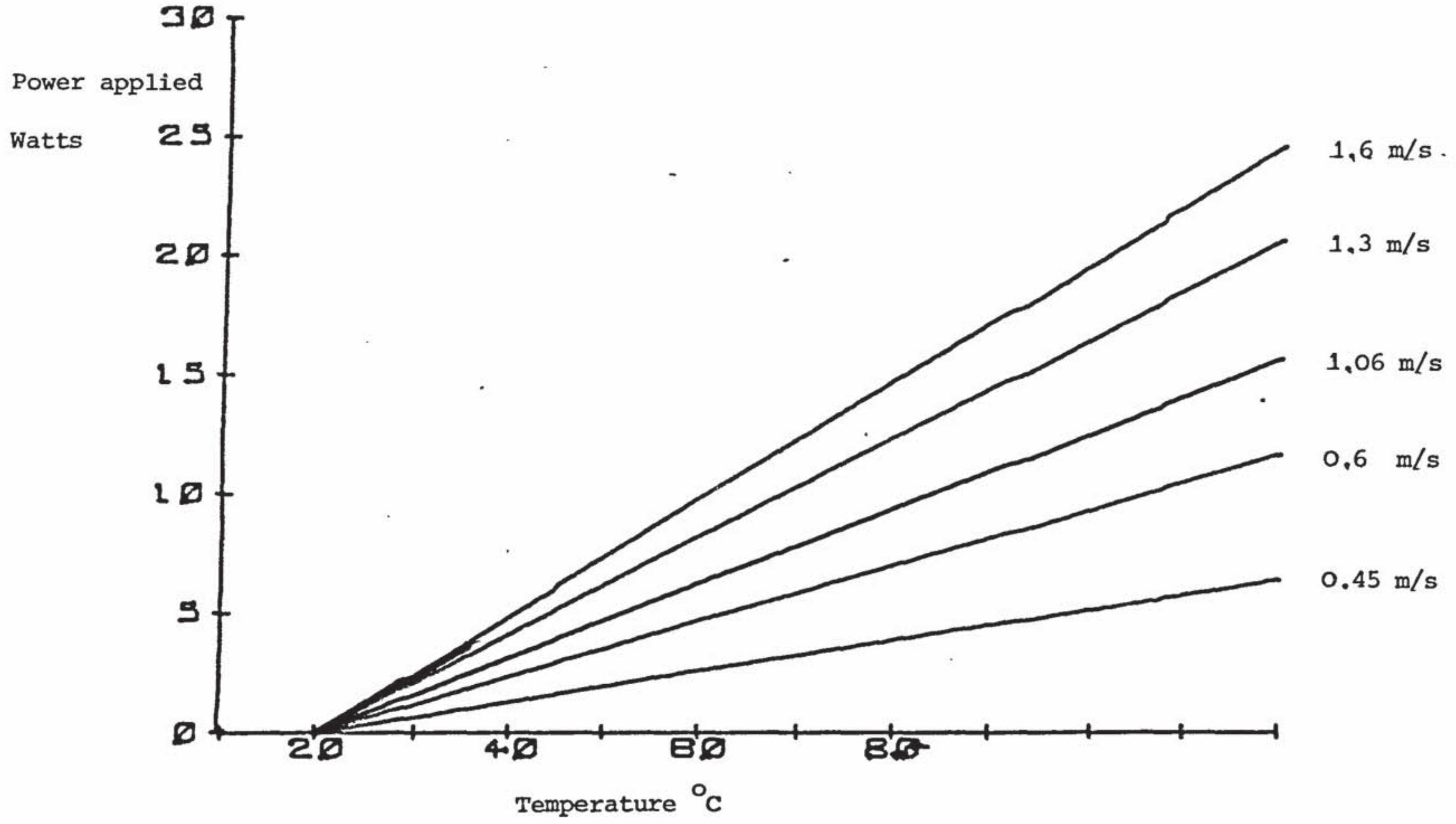

PLOT (5.11) Forced Convection
Power applied to sample against temperature (results, the same as Plot (5.10) but now corrected for radiation.

CHAPTER 6

MULTIPLE STRIP HEAT EXCHANGER MODEL

MULTIPLE STRIP HEAT EXCHANGER MODEL

This model was conceived to investigate the heat transfer over a surface, and was constructed from a number of separate fine strip elements with independent electrical heating. By the means of such a construction it is possible to control the power input, and at the same time, determine the temperature of each strip.

The object of this experimental technique was to maintain all the strips at the same temperature. By achieving this the heat transfer coefficient of each strip could be determined and also a bulk description of the thermal performance of the sample could be found. It is assumed that no thermal gradient exists down the length of the sample and it has been shown theoretically that the temperature profile across the width of the sample is also uniform.

Design of System

The design problems considered were:-

A suitable technique for applying electrical power to the shapes.
The thickness of the strip material.
The nature of the material.
A technique for mounting the strips onto a substrate.
A suitable method of measuring the resistance and power in each strip.
Theoretical calculations as to the response of the technique.
Techniques considered for applying electrical power to the heating elements.

The following methods have been considered as techniques by which electrical power could be supplied to a series of strip elements individually:-

D.C. Heating

This method required that each strip be connected in series with a variable resistance or that its current be controlled by a transistor acting with a servo device. Both systems involve the measurement of both voltage and current in each element and the determination of power and resistance.

A.C. Heating

The possibility of using 50 Hz sinusoidal voltage instead of the previously considered D.C. system was rejected due to the thermal response of the strip. It was estimated that in 2.10^{-2} sec the temperature of the strip could fall by 25% making the possibility of monitoring the power input to the strip accurately extremly difficult (see section - Analysis of pulse repertition rate - page no. 63).

Square Wave Pulse System

The technique used in the experimentation was developed to produce a constant current with a variable pulse duration. A square wave input from a signal generator at 1 kHz was fed into eight retriggerable monostable multi-vibrators, each multi-vibrator being identified with a particular strip element. The duration of the output pulse from the multi-vibrator was determined by the external resistance and capacitance connected across its external triggering input pins. The values chosen for these components were calculated from information found in the Handbook of Electronics - Ref. {6.1}. The pulse duration could be ranged from totally on to 99% off.

The output from each multi-vibrator was then used to switch a BC109 transistor which in turn switched a 2N3055 power transistor. Dia (6.1). The circuit was designed such that the power transistor was either totally on or off, hence the emitter collector voltage was either very small, or the full D.C. voltage. This was to ensure that the current flowing through the resistive load R_L and the strip is determinable.

The BC109 transistors, multi-vibrators and associated triggering components were mounted upon the same circuit board and used a common 5.1 V power supply. The power transistors and load resistances were mounted upon separate bases, the load resistors being submerged in a bath of running water to ensure their constant temperature. The power part of the circuit was connected to a second D.C. supply whose negative side is common to the 5.1 volts supply.

Each test element was connected in series with a load resistance, care being taken to make all the connections between strips and loads the same length. 0.3 cm thick copper wire was used for this purpose to prevent unnecessary resistive or heating losses in the circuit.

The D.C. voltage applied to the power circuit was monitored using a digital voltmeter (D.V.M.) and the current calculated from the joint resistance of the load and the element.

A further measurement has been made with respect to the voltage across the collector/emitter of the power transistor. Although this quantity was found to be very small (approx. 1%) it has been taken into account when the value Va (Applied Voltage) has been used. This can be seen in tables (6.3) and (6.20) where the applied voltages are quoted slightly less than a whole number. The difference being that voltage lost across the power transistor.

The major advantage achieved by the pulse circuit over the alternative methods described,is that both the voltage across the sample and the current passing through it can be determined accurately. This is a consequence of using a pulse of known shape and duration.

A method by which this type of signal could be digitized and processed has been described in Chapter 9, whereas the equivalent analogue techniques for obtaining the sample resistance value V/I are unlikely to have the accuracy required by the system.

The Thickness of the Strip Material

The size and thickness of each strip was determined by the experimental requirements. The width of each strip was 3", ($76.2\ 10^{-3}$ m) (width of wind tunnel); and each strip was $2.54\ 10^{-3}$ m long. In order that the power dissipated in each strip could if necessary be in the order of 1 W a resistance of approximately 0.5 Ω was required. The value of 1 watt was calculated using the estimate power dissipation for a flat plate as reported by Schlichting - Ref. { 5.1 }

From the equation for resistance

$R = \rho^{\ell}/wt$

Where R is the resistance of the strip 0.5 Ω

ρ is the coefficient of resistivity

($6.4\ 10^{-8}$ to $10.4\ 10^{-8}$ Ω m for Ni)

ℓ is the width of strip ($76.2.10^{-3}$ m)

w is the length of the strip ($2.34.10^{-3}$ m)

t is the thickness of the strip

For a resistance of 0.5 Ω the thickness of the material required is given by

$$t = \rho^{\ell}/WR$$

$$= \frac{10.4.10^{-8}}{2.34.10^{-3}} \quad \frac{76.2.10^{-3}}{0.5}$$

$$t = 6.24.10^{-6} \text{ m}$$

The actual nickel foil used was 99% pure and 5.10^{-6} m thick.

The Nature of the Material

The material chosen for the construction of the strip elements was that of nickel, for the following reasons:-

1. Nickel has a high temperature coefficient of electrical resistance over the temperature range 20°C to 100°C.
2. The temperature coefficient can be assumed linear over this range.
3. Nickel has a low value of thermal conductivity which enables a uniform temperature profile across the width of the strip (see Theoretical Considerations) to develop.
4. It is available as a thin foil and has a reasonable resistance to oxidation.

Other materials were also considered such as semi-conductors, which also have high resistivity and low thermal conductivity, but were considered too brittle for this application.

A Technique for Mounting the Nickel Strips onto a Substrate

In the previous section a description of the type of nickel strip required for the experiment was given. The nickel was only found available in sheet form, thus a method of cutting and mounting each strip onto a supporting surface has been developed.

The cutting stage necessitated a very sharp scalpel, a facing block and a ground strip 22.10^{-2} cm thick and 10 cm long. The ground strip was 33.10^{-3} cm less than 0.254 cm in width to allow for the cut width of the scalpel and the separation between mounted nickel strips. The technique used was to hold the facing block with the ground strip against its surface down upon the nickel foil with clamps. A first cut was taken by running the blade along the edge of the ground strip, then the ground strip was removed and a second cut made. Thus two cut lines had been produced in the nickel sheet 22.10^{-2} cm apart and parallel to each other, which formed one nickel strip. The process was then repeated several times until a large number of similar nickel strips had been produced.

The nickel strips were then mounted onto an epoxy resin strip 3" (7.62 cm) x 0.4" (1.02 cm) x 0.1 cm thick. Four nickel strips per side were used in the formation of each sample. They were positioned and glued to the surface using epoxy resin. Once the position had been set and the excess resin squeezed out a sheet of PTFE was placed onto the strips and then held with strong spring clips to hold the model rigidly. Finally, a current of 3 Amps was passed through each nickel strip for a short period to achieve polymerisation. The sample was then left to cure for 24 hours.

Following construction and curing of the test sample it was mounted into a supporting frame and connected electrically - Dia (6.2). The epoxy resin strip had been designed such that it formed the fourth side of a square, the remaining sides being made from an electrically non-conductive material. The strip was held in position by the use of a contact adhesive. On the sides of the square adjacent to the strips, strips of copper foil had been mounted to act as terminals to the nickel foil. On one side of the sample all the nickel strips were joined to one common piece of copper foil. On the other side each nickel strip was joined to a separate copper terminal using braided copper wire.

Finally, heavier current carrying wires were attached to the copper terminals to connect them to the power transistors. The model was held in the wind tunnel, two sides being clamped between window pairs to provide support.

This particular method of construction was advantageous against others attempted. The epoxy resin filled the small gaps between the nickel foil producing an overall smooth surface. An earlier problem experienced had been that of the nickel pealing away when the sample reached temperatures in the region of 80°C. This was overcome by careful rolling out of the excess resin and thorough polymerisation of the mixture.

Method Developed for Measuring the Resistance and Power in each Element

The validity of the strip element technique is dependent upon the accurate measurement of the voltage produced across each element. The first attempt to do this was made by measuring the voltages directly from an oscilloscope display. The accuracy was found poor but was used in the initial trial stages of the experimental work (Appendix 6). In the wind tunnel situation this technique proved too insensitive in detecting the voltage changes. An attempt was made to magnify the display optically, but this did not improve the accuracy of the results.

The problem was finally overcome by the use of a differential input operational amplifier inserted between the probe point of the element and the oscilloscope (Dia 6.3). The input voltage was fed into the non-inverting side of the operational amplifier (op-amp) with a voltage gain of 10. The inverting side of the op-amp was fed from an accumulator with a fixed and a variable resistance in series across it. A voltage taken across the fixed resistance (100 Ω) produced the input and was varied by changing the variable resistance (max. 10 kΩ). A balance could thus be achieved between the inverting side of the op-amp and the incoming signal from the strip element.

Using this technique a 1°C rise in element temperature produced a 1/4 screen or 1.5 cm deflection on the display. During each experiment a digital voltmeter was used to monitor both the accumulator voltage, and the power pack voltage.A d.v.m. or any similar device could not have been used to monitor the element directly due to its pulse wave form. Further it was felt important to keep a careful check on the display to ensure that the signal observed was that of the resistance change and not a circuit malfunction.

The sample voltage was determined from the value of the variable resistance used in the balance circuit.

$$\frac{100\ V_s}{100 + R} = V\ out \qquad (6.1)$$

Where V_s is the voltage produced by the accumulator cell

R is the variable resistance

The fixed resistance in the balance circuit = 100Ω.

V out the balance voltage applied to the negative stage of the op-amp.

A minimum value of V_{out} is produced when R is at its maximum value, R = 10 k Ωs. Thus the actual voltage measured across the surface (Va) can be expressed in terms of the resistance value measured.

$$Va = Vs \; . \; 100 \left\{ \frac{1}{100 + R} - \frac{1}{10{,}100} \right\} \text{ volts} \qquad (6.2)$$

In a similar manner the voltage Va is used to calculate the resistance of the strip.

$$Ra = 9 \; Va/\left(Vp - Va \right) \qquad (6.3)$$

Where Ra is the resistance of the strip

Vp is the voltage applied by the power pack

Standard resistance of value 9 Ω

The temperature of the strip can be determined from the resistance change from its value at 20°C. Let Ro be the resistance of the strip at 20°C and Ra at temperature T. The temperature T is calculated from the expression

$$(T + 20) \; {}^{o}C = \left\{ \frac{R_a}{R_o} - 1 \right\} 180 \qquad \text{resistivity of nickel taken from ref } \{6.2\} \qquad (6.4)$$

Finally the power given to each strip was calculated from the expression

$$\left\{ \frac{V_p}{9 + R_a} \right\}^2 R_a \qquad (6.5)$$

and multiplied by the pulse length duration.

THEORETICAL EVALUATION OF MULTIPLE STRIP HEAT EXCHANGER MODEL

Analysis of the Pulse repetition rate

A further consideration was made as a consequence of the electronic circuiting used to apply power to the strips; this was an approximation to the amount the strip could cool in 10^{-3} sec after the power being switched off. This factor was calculated using the Biot and Fourier moduli, as outlined by Eckert and Drake - Ref. {6.3}.

The Biot modulus is expressed as $\frac{h \,.\, D}{k}$

Where h is the rate of heat transfer from the surface to the surrounding air

(Maximum value of h calculated at 1.6 m/sec for one side of a flat plate $\doteq$ 100 $J/m^2/sec/^oC$, the value of h being calculated from equation used to approximate for forced convection

$h = 0.663\ k/l\ \ Pr^{1/3}\ \ R^{1/2}$ Ref. { 5.1 }

k thermal conductivity of nickel 90 $J/m/sec/^oC$

D is the ratio of volume to surface area of the strip and defines the characteristic length.

The factor D can be considered as the thickness of the strip 5.10^{-6} m.

The Fourier modulus is expressed as $\frac{\alpha\ \tau}{D^2}$

Where α is the thermal diffusivity of nickel $\doteq 75.10^{-6}\ m^2/sec$

τ is the decay time and is expressed in units compatible with α, normally either seconds or minutes.

A body cools exponentially from its initial condition and is described by the equation

$$T = T_o \exp\left(- \frac{\tau}{c}\right)$$

Where T is the temperature of the body after a time has elapsed.

T_o is the starting condition, and is the temperature of the body above its surroundings

c is the decay constant and is defined by the Biot and Fourier moduli

$$T = T_o \exp - \left(\frac{\tau\alpha}{D^2} \quad \frac{hD}{k}\right)$$

inserting values

$$T = T_o \exp\left(- \frac{75.10^{-6}}{5.10^{-6}} \tau \frac{10^2}{90}\right)$$

$$T = T_o \exp\left(- 16.7 \tau\right)$$

In terms of a nickel strip, a decay time of approximately 10^{-3} sec would produce a temperature drop of ≃ 2% which was considered an acceptable temperature fall. It would take ≃ 0.04 sec for the temperature to fall by 50%.

Theoretical Solution to the Temperature Profile across the Width of each Strip

The theoretical considerations which have been used to correlate results and predict the temperature profile along each strip has been developed from a differential equation of the form.

$$\frac{d^2\theta}{dx^2} - k\theta + c_1 = 0 \qquad (6.6)$$

Where C_1 represents the constant power input to the strip

k represents the heat transfer from the sample

x is a variable distance from the centre of the strip to the edge from x = L to x = - L.

The factors involved in the differential equation are:-

1. The heat applied electrically to the sample
2. Heat lost in forced convection from the surface of the sample
3. Heat lost at very low airflows due to natural convection.
4. Radiation losses from the sample.

Electrical Heating

Item 1 refers to the power input I^2R, but R the resistance of sample is temperature dependent and has two components. I^2R_o the power input at ambient temperature and $I^2(R_1\theta)$ where R_1 is the resistance change at θ.

Forced Convection

The forced convection has been calculated from the approximate expression $Q = 0.664 \, . \, k \, . \, b \, . \, (Pr)^{1/3} \, (R\ )^{1/2} \, \theta$, where k is the thermal conductivity of air, b is the length of the strip, Pr is the dimensionless factor Prandtl number and R the Reynolds number based upon length. The expression is derived by Schlichting Ref {5.1}, Q is the amount of power lost by the sample to the air.

Natural convection

Natural convection has been considered in terms of the air velocity over the sample below which it would play a significant part. Using an order of magnitude technique the ratio between the Grashof~~f~~ and

Reynolds numbers have been used to find this velocity

where Gr(Grashof~~f~~ number) = $\frac{g\,\beta(\theta)\,\ell^3}{\nu^2}$ (6.7)

R (Reynolds number) = $\left(\frac{\ell v}{\nu}\right)$ (6.8)

l is the characteristic length of the sample

θ is the temperature difference

ν kinematic viscosity

v velocity of air over sample

β coefficient of thermal expansion

g acceleration due to gravity

Body forces are anticipated to have an effect on the air flow when $Gr \geq R^2$.

For air at $\theta = 40^\circ C$ $\frac{Gr}{\ell^3\theta} = 0.82.10^8/m^3/^\circ C$ (values taken from Ede ref {5.2})

In the particular case of the nickel strip technique, the total width of the sample was 0.01 m; thus by inserting this value into equations (6.7) and (6.8) the significant velocity can be determined.

$v^2 = 10^8\ \ell\theta\ (1.69\ 10^{-5})^2$

$v \doteq 0.1$ m/sec. (6.9)

Thus the air speed below which natural convection would be expected to act would be in the region of 0.1 m/sec for the electronic strip technique.

The effect of natural convection has not been included in the solution to the differential equation, but would be anticipated to have a heat transfer coefficient proportional to $(\theta)^{1.25}$, as reported by McAdams - Ref. {6.4} and not be dependent upon Reynolds number.

Radiation

Radiation losses take the form $k\sigma\,((\theta + T)^4 - T^4)\,S_a$,

where k is the emmisivity of the material,

σ is Stefan's constant and

Sa is the surface area of the sample.

If k, σ and Sa are written as a constant C_2 then the radiation losses can be expressed as

$$G = C_2\,((\theta + T)^4 - T^4) \tag{6 10}$$

where θ is the temperature excess above ambient °K

T is the ambient temperature °K

Equation (6 10) can be expanded using a bi-nomial expansion as

$$G = C_2\left(T^4 + 4\,\theta T^3 + 6\theta^2T^2 + 4\theta^3T + \theta^4 - T^4\right)$$

$$G = C_2\left(4\theta T^3 + 6\,\theta^2T^2 + 4\theta^2T + \theta^4\right)$$

In terms of the maximum temperature experienced by the sample ($\theta \simeq 80^\circ K$), ($T = 300^\circ K$), the error in neglecting the θ^4 and $4\theta^3T$ terms is not more than 10% reducing the expression to:

$$G = C_2\left(4\theta T^3 + 6\theta^2T^2\right)$$

Approximations made to the Differential Equation

The differential equation required to describe the thermal profile is of a non-linear second order form

$$\frac{d^2\theta}{dx^2} - k_1\theta^2 - k_2\theta - k_3\theta + k_4\theta + C_1 = 0 \tag{6.11}$$

where k_1 and k_2 are the coefficients relating to the radiation losses

k_3 the coefficient due to forced convection

k_4 the excess heat input due to the resistance change of the strip from an ambient condition per °C

C_1 the I^2R_o heat input, where R_o is the resistance of the strip at ambient.

A solution to equation (6.11) may be developed using a power series expansion of the form

$$\theta = \sum_{m=0}^{\infty} \frac{Cmx^m}{m!} + A$$

The solution (Appendix 3) is found to be complicated by the θ^2 term, so a simplification has been introduced such that $k_1\theta^2$ becomes $k_1 \cdot 40 \cdot \theta = k_5\theta$. The error in making such an assumption has been found to be 6% with respect to the forced convection coefficient k_3 over the temperature range 60°C ± 20°C. The error is largest at low velocities, where k_3 has its minimum values.

For the nickel strip experiments the heat transfer coefficients have been calculated as:-

$k_1 \hat{=} 1.7.10^{-6}$ w/(°C)^2 $k_5 \hat{=} 1.0.10^{-4}$ w/°C

$k_2 \hat{=} 5.10^{-4}$ w/°C

k_3 ranges between 0·002 to 0·02 w/°C depending on the particular air velocity and strip considered,

k_4 varies with respect to the particular strip considered $\hat{=} 2.5.10^{-3}$ W/°C

C_1- The input power I^2R_o, has been varied from 0·3 to 1 watt.

The solution obtained for $\overline{\theta}$ the average strip temperature, equation (6·17) can be applied with one modification. The value λL must be dimensionless, as L is length, λ has the dimensions of 1/length and $\lambda^2 = k_1 + k_2 + k_3 - k_4$; thus the coefficients have the units of 1/(length)^2. This has been achieved by dividing the coefficients by a factor which is the product~~ion~~ of the volume of the nickel strip and its thermal conductivity.

Thermal Conductivity of Nickel Strip

Consideration has been made as to the value assumed for the thermal conductivity of nickel. As previously described the nickel strips were mounted upon a base. This base was constructed of epoxy resin with carbon fibre strands laid in it to add rigidity. The thermal conductivity for the base has been taken as 0.2 W/m°C from Kaye - Ref. {6.5}. The epoxy resin would be expected to contribute to the heat conduction down the strip.

Thickness of nickel foil	5×10^{-6} M
Thickness of epoxy base	10^{-3} M

As the nickel strips are mounted either side of the substrate, only half of the thickness was considered in determining the ratio of the product of thermal conductivity and thickness of the strip, against base.

$$\frac{(5 \times 10^{-6} \times 90)}{(500 \times 10^{-6} \times 0.2)} = 4.5 : 1$$

In order that this factor be accounted for a correction has been made to the values used to determine the differential equation, equation (6.12). Instead of dividing the heat transfer coefficients by the volume and conductivity of Ni alone the expression takes into account the contribution of the epoxy substrate.

$$(k_2 + k_3 - k_4)/[(L \times B) \times (t_1 K_1 + t_2 K_2)]$$

where L is the length of the strip

B is the width

t_1 thickness of Ni

K_1 thermal conductivity of Ni

t_2 thickness of epoxy

K_2 thermal conductivity of epoxy

Application of Boundary Conditions

The boundary conditions for such a situation are defined by $\theta = \theta_o$ at the edges of the plate. θ_o is the ambient temperature. By assuming a solution of the form to eq. (6.6)

$$\theta = Ae^{\lambda x} + Be^{-\lambda x} + \frac{c}{K}1 \qquad (6.12)$$

and applying the boundary conditions $\theta = 0$ at $x = \pm L$ where θ is the excess temperature of the sample above ambient temperature θ_o, then:

$$Ae^{\lambda L} + Be^{-\lambda L} = Ae^{-\lambda L} + Be^{\lambda L}$$

thus either A = B = 0 which is a trivial solution or A = B. Equation (6.12) can now be written as

$$\theta = A \cosh \quad (\lambda x) + \frac{C_1}{K} \qquad (6.13)$$

Also at $x = \pm L$, $\theta = 0$, hence

$$A = -\frac{c_1}{k}\left(\cosh\ (\lambda L)\right)^{-1} \qquad (6.14)$$

By substituting equation (6.14) into equation (6.15) a solution for θ can now be obtained of the form

$$\theta = \frac{c_1}{k_1}\left[1 - \frac{\cosh\ (\lambda x)}{\cosh\ (\lambda L)}\right] \qquad (6.15)$$

The maximum value of θ can be shown by differentiating the previous expression to occur at the centre of the strup where $x = 0$.

$$\frac{d\theta}{dx} = -\frac{c\lambda}{k_1}\frac{\sinh\ (\lambda x)}{\cosh\ (\lambda L)}$$

$$\theta\text{max} = \frac{c_1}{k_1}\left\{1 - 1/\cosh\ (\lambda L)\right\}$$

The average value of θ $(\overline{\theta})$ can also be found by integrating equation (6.15) with respect to the total length of the strip.

$$\bar{\theta} = \frac{\int_{-L}^{L} \frac{C_1}{K} \left\{ 1 - \frac{\cosh(\lambda x)}{\cosh(\lambda L)} \right\} dx}{\int_{-L}^{L} dx}$$

$$\bar{\theta} = \frac{C_1}{K} \left\{ 1 - \frac{1}{\lambda L} \tanh(\lambda L) \right\} \quad (6.16)$$

As a further simplification it has been found that $\lambda L > 5$ for the nickel strip experiments; thus equation (6.16) reduces to the form

$$\bar{\theta} = \frac{C_1}{K} \left(1 - 1/\lambda L \right) \quad (6.17)$$

APPLICATION OF DIFFERENTIAL EQUATION AND EXPERIMENTAL RESULTS

The solution developed for the equation describing the temperature distribution across each strip has been evolved as follows:-

The radiation coefficient has been considered as a variable of θ alone and not both θ and θ^2, the error incurred in doing this is small provided θ the temperature excess of the strip is not above 80°C. The coefficient $R_3 4$ has been calculated as $\left(\frac{Vapp}{9 + R1}\right)^2 \frac{Ro}{180}$ w/°C where R1 is the measured resistance of the strip at temperature θ. A possible error in R1 of 10% would produce a resulting error in $\left(\frac{Vapp}{9 + R1}\right)^2$, the current passing through the resistance of 1%.

Equation (6.6) can thus be expressed as:

$$\frac{d^2\theta}{dx^2} - \frac{A\theta}{Vol.K} + \frac{B\theta}{Vol\ K} + \frac{I^2 Ro}{Vol\ K} = 0$$

where Vol is the volume of each strip and K is the thermal conductivity (the effect of the epoxy resin base being taking into account by the factor K).

The coefficients A, now represent the total heat loss from the strip per °C. B represents the excess heating effect $\left(\frac{Vapp}{9 + RI}\right)^2 \frac{Ro}{180}$ W/°C

λ represents $\left(\frac{A - B}{\text{Vol } K}\right)^{1/2}$. The average strip temperature has been calculated by inserting these values into equation (6.17). The effects of velocity and strip position on the factor λL have been shown in PLOT (6.1) and (6.2).

Method of Determinating the Pulse Duration Applied to Each Nickel Strip

In his book Boundary Layer Theory Schlichting - Ref (5.1) develop~~e~~s relationships between the dissipation from a flat plate and Reynolds number for a zero angle of attack to the air stream. In the case of laminar flow $Q_L = C_L\ (Pr)^{1/3}\ (R_L)^{1/2}$ where C_L is a constant of the system; and $\overset{\text{in}}{\text{Th}}$ the case of turbulent flow,

$$Q_T = C_T\ (Pr)^{1/3}\ (R_L)^{0.8}$$

Where R_L is the length based Reynolds number defined from a point of stagnation $x = o$, $R_L = \frac{Uo\ L}{\nu}$.

For a particular constant velocity the two expressions can be further simplified to be dependent on the length L thus:

$$Q_L = C_{L1}\,(X)^{1/2}, \qquad Q_T = C_{T1}\,(X)^{0.8}$$

This relationship has been used to determine the relative power dissipation for a series of strips lying one directly after the other. If the power dissipated from a strip of unit length is unity then C_{L1} and C_{T1} can also be considered unity. For a second strip directly behind the first also of unit length the dissipation would be expected to be. In the laminar case $(2)^{1/2} - (1)^{1/2} = 0.414$ and for the turbulent $(2)^{0.8} - (1)^{0.8} = 0.741$.

The values for four such strips lying directly behind each other have been calculated for laminar and turbulent flows respectively.

TABLE (6.1) Heat Transfer Coefficient Distribution of a Flat Plate at Zero Angle of Attack

Strip no.	1	2	3	4
Laminar distribution	1	0.414	0.318	0.268
Turbulent distribution	1	0.741	0.667	0.623

Thus if the strips all had the same resistance value at the ambient condition then table (6.1) would determine the pulse duration applied to each. Due to experimental limitation it was not possible to produce exactly the same resistance values for each element and ~~that~~, the longest possible pulse duration was 90% of the full cycle. Thus the pulse duration for each strip was calculated individually.

The resistance values for the strips were measured at 20°C using a digital Wheatstone bridge.

TABLE (6.2) Pulse Duration Determination

Resistance 20°C		Corr	0.9	Power		Actual	
				L	T	L	T
Bottom strip							
R(5)	0.376	0.896	0.9	1	1	0.81	0.81
R(6)	0.365	0.923	0.9	0.414	0.741	0.34	0.61
R(7)	0.380	0.887	0.9	0.318	0.667	0.25	0.52
R(8)	0.313	1.077	0.9	0.268	0.623	0.26	0.6
Top strip							
R(1)	0.337	1	0.9	1	1	0.9	0.9
R(2)	0.308	1.094	0.9	0.414	0.741	0.41	0.73
R(3)	0.333	1.012	0.9	0.318	0.667	0.29	0.61
R(4)	0.351	0.96	0.9	0.268	0.623	0.23	0.53

Resistance at 20°C, resistance measured using digital Wheatstone Bridge.

Corr	All the resistance corrected to R(1). Corr = R(1)/R(N)
0.9	Longest possible pulse duration 0.9 of whole cycle.
Power	Power factors as calculated from Table (6.1).
Actual	Actual pulse duration applied.

Evaluation of the Strip Data

The nickel strips laid four on each side of an epoxy resin base have been mounted at zero angle of attack to the air flow in the wind tunnel - Dia (6.1). The pulse duration for each strip has been calculated for both laminar and turbulent velocity profiles. The resistance variation with respect to the total power input for a range of air velocities has been found. From the data obtained it is possible to estimate the temperature of each individual strip and compare the variation of this with respect to the temperatures calculated from the solution to the differential equation (6.15). Three plots have been made, the first two show the variation between the power applied to the individual strips and the air velocity passing over them. Plot (6.3 and 6.4). The third shows the variation of Nusselt with Reynolds numbers for the four top and bottom strips - plot (6.5).

Presentation of Strip Data

The theoretical comparison in the laminar region was made by calculating the anticipated heat transfer coefficient for each strip as shown in table (6.1). The individual pulse durations were taken into account as shown in table (6.2).

Using a computer the average temperature of each strip was calculated as:-

$$\bar{\theta} = \frac{I^2R_o\ P(J)}{\left(h\ D(J)+RAD-\frac{I^2R_oP(J)}{180}\right)}\left\{1 - \frac{1}{\left(\frac{h\ D(J)+RAD-I^2R_o^{P(J)}/180}{Vol.\ K}\right)^{1/2}}\right\} \quad (6.18)$$

P(J) is the pulse duration applied to the strip

D(J) is the particular heat transfer fraction anticipated depending upon the strip position.

It was found that the leading strips R(1) and R(5) required D(J) to be increased to bring the average calculated temperature down to that measured. This factor D(J) = 1.15 not as expected D(J) = 1 is referred to as H_c(c) in the following tables.

Key to tables (6.3) to (6.20)

RJ	resistance value of the strip during heating
T(M)	measured average temperature of strip
T(C)	calculated average temperature of strip
$T_C(C)$	corrected value of T(C) for strips R1 and R5 only
H(C)	calculated heat transfer coefficient
$H_C(C)$	corrected heat transfer coefficient
Power	measured power passing in strip

Average values of T(M), T(C) and $T_C(C)$ are given for top set of four strips R1, R2, R3 and R4.

The total power applied to the set is also given.

The average value for R5, R6, R7 and R8 the bottom set are also quoted.

Units

T(M), T(C) and $T_C(C)$ are expressed as °C above the ambient condition.

H(C), $H_C(C)$ and Power are all expressed in watts.

All temperatures are given to the nearest °C.

Results of multiple strip element experiments for various air velocities and power inputs at zero angle of attack

TABLE (6.3) V = 5.4 ft/sec (1.62 m/s) Applied Volts (11.89)

		T(M)	T(C)	T_C(C)	H(C)	H_C(C)	Power
R1	.379	22	27	22	0.018	0.0207	0.55
R2	.347	22	23	-	0.0074	-	0.22
R3	.373	22	20	-	0.0057	-	0.16
R4	.394	22	23	-	0.0046		0.16
Average		22	23	22	Total Power		(1.09)
R5	.422	22	26	22	0.018	0.0207	0.54
R6	.410	22	22	-	0.0074	-	0.22
R7	.427	22	21	-	0.0057	-	0.17
R8	.351	22	23	-	0.0046	-	0.16
Average		22	23	22	Total Power		(1.10)

TABLE (6.4) V = 4.8 ft/sec (1.45 m/s) Applied Volts (11.89)

		T(M)	T(C)	T_C(C)	H(C)	H_C(C)	Power
R1	.380	23	28	23	0.0170	0.0196	0.55
R2	.349	24	24	-	0.0070	-	0.23
R3	.377	23	21	-	0.0054	-	0.16
R4	.397	23	24	-	0.0044	-	0.16
Average		23	24	23	Total Power		(1.10)
R5	.424	23	28	24	0.0170	0.0196	0.55
R6	.412	23	24	-	0.0070	-	0.22
R7	.430	23	22	-	0.0054	-	0.17
R8	.353	23	24	-	0.0044	-	0.16
Average		23	25	24	Total Power		(1.10)

TABLE (6.5) V = 4.18 ft/sec (1.25 m/s) Applied Voltage (11.89)

		T(M)	T(C)	T_C(C)	H(C)	H_C(C)	Power
R1	.383	24	30	25	0.0159	0.0182	0.55
R2	.353	26	25	-	0.0065	-	0.22
R3	.380	25	22	-	0.0050	-	0.16
R4	.400	25	25	-	0.0041	-	0.16
Average		25	26	25	Total Power		(1.11)
R5	.428	25	30	25	0.0159	0.0182	0.55
R6	.415	25	25	-	0.0065	-	0.23
R7	.432	24	23	-	0.0050	-	0.17
R8	.356	24	25	-	0.0041	-	0.18
Average		25	26	25	Total power		(1.11)

TABLE (6.6) V = 3.41 ft/sec (1.02 m/s) Applied Volts (11.89)

		T(M)	T(C)	T_C(C)	H(C)	H_C(C)	Power
R1	.389	28	34	28	0.0143	0.0165	0.56
R2	.358	29	28	-	0.0059	-	0.23
R3	.384	27	24	-	0.0045	-	0.17
R4	.404	27	28	-	0.0037	-	0.16
Average		28	28	27	Total Power		(1.12)
R5	.435	28	34	28	0.0143	0.0165	0.56
R6	.422	28	28	-	0.0059	-	0.23
R7	.432	27	24	-	0.0045	-	0.17
R8	.360	27	27	-	0.0037	-	0.16
Average		28	29	28	Total Power		(1.13)

TABLE (6.7) V = 2.4 ft/sec (0.72 m/s) Applied Volts (11.89)

		T(M)	T(C)	T_C(C)	H(C)	H_C(C)	Power
R1	.397	32	41	34	0.0120	0.0138	0.57
R2	.365	33	33	-	0.0050	-	0.24
R3	.393	33	28	-	0.0038	-	0.17
R4	.412	31	32	-	0.0031	-	0.17
Average		32	33	31	Total Power		(1.14)
R5	.443	32	41	33	0.0120	0.0138	0.57
R6	.430	32	32	-	0.0050	-	0.23
R7	.448	32	29	-	0.0038	-	0.18
R8	.367	31	32	-	0.0031	-	0.17
Average		32	33	31	Total Power		(1.15)

TABLE (6.8) V = 1.7 ft/sec (0.5 m/s) Applied Volts (11.89)

		T(M)	T(C)	T_C(C)	H(C)	H_C(C)	Power
R1	.403	35	49	40	0.0101	0.0116	0.58
R2	.373	38	38	-	0.0042	-	0.24
R3	.398	35	32	-	0.0032	-	0.17
R4	.418	34	36	-	0.0026	-	0.17
Average		36	39	37	Total Power		(1.16)
R5	.453	37	49	40	0.0101	0.0116	0.58
R6	.438	36	38	-	0.0042	-	0.24
R7	.455	35	34	-	0.0032	-	0.18
R8	.372	34	36	-	0.0026	-	0.17
Average		35	39	37	Total Power		(1.17)

TABLE (6.9) V = 5.4 ft/sec (1.62 m/s) Applied Volts (12.87)

		T(M)	T(C)	T_C(C)	H(C)	H_C(C)	Power
R1	.387	26	32	27	0.018	0.0207	0.66
R2	.349	24	27		0.0074		0.26
R3	.382	26	24		0.0057		0.20
R4	.402	26	27		0.0046		0.19
Average		26	28	27	Total Power		(1.30)
R5	.434	28	32	27	0.018		0.66
R6	.419	26	27		0.0074		0.27
R7	.436	26	25		0.0057		0.20
R8	.357	25	28		0.0046		0.19
Average		26	28	27	Total Power		(1.31)

TABLE (6.10) V = 4.82 ft/sec (1,45 m/s) Applied Volts (12.87)

		T(M)	T(C)	T_C(C)	H(C)	H_C(C)	Power
R1	.388	27	34	28	0.0170	0.0196	0.66
R2	.352	25	29		0.0070		0.27
R3	.385	28	25		0.0054		0.20
R4	.404	27	29		0.0044		0.19
Average		27	29	28	Total Power		(1.31)
R5	.437	29	34	29	0.0170	0.0196	0.66
R6	.421	28	28		0.0070		0.27
R7	.439	28	26		0.0054		0.20
R8	.361	27	29		0.0044		0.19
Average		28	29	28	Total Power		(1.32)

TABLE (6.11) V = 4.18 ft/sec (1.25 m/s) Applied Volts (12.87)

		T(M)	T(C)	T_C(C)	H(C)	H_C(C)	Power
R1	.398	30	37	31	0.0159	0.0182	0.66
R2	.355	28	31		0.0065		0.27
R3	.388	30	27		0.0050		0.20
R4	.407	28	31		0.0041		0.19
Average		29	31	30	Total Power		(1.32)
R5	.442	31	37	31	0.0159	0.0182	0.67
R6	.426	30	30		0.0065		0.27
R7	.442	29	28		0.0050		0.21
R8	.363	28	31		0.0041		0.19
Average		30	31	30			(1.33)

TABLE (6.12) V = 3.41 ft/sec (1.02 m/s) Applied Volts (12.87)

		T(M)	T(C)	T_C(C)	H(C)	H_C(C)	Power
R1	.399	33	41	34	0.0143	0.0165	0.67
R2	.361	31	34		0.0059		0.27
R3	.393	32	29		0.0045		0.20
R4	.412	31	33		0.0037		0.19
Average		32	34	32	Total Power		(1.35)
R5	.448	34	41	34	0.0143	0.0165	0.68
R6	.428	31	34		0.0059		0.28
R7	.448	32	29		0.0045		0.20
R8	.367	31	33		0.0037		0.20
Average		32	35	33	Total Power		(1.35)

TABLE (6.13) V = 2.41 ft/sec (0.72 m/s) Applied Volts (12.87)

		T(M)	T(C)	T_C(C)	H(C)	H_C(C)	Power
R1	.405	36	50	40	0.0120	0.0138	0.68
R2	.368	35	40		0.0050		0.28
R3	.399	35	34		0.0038		0.20
R4	.419	34	38		0.0031		0.20
Average		35	40	38	Total Power		(1.35)
R5	.456	38	49	40	0.0120	0.0138	0.68
R6	.437	35	39		0.0050		0.28
R7	.456	36	35		0.0038		0.21
R8	.372	34	39		0.0031		0.20
Average		36	41	39	Total Power		(1.37)

TABLE (6.14) V = 1.7 ft/sec (0.512 m/s) Applied Volts (12.87)

		T(M)	T(C)	T_C(C)	H(C)	H_C(C)	Power
R1	.420	44	60	49	0.0101	0.0116	0.71
R2	.380	42	46		0.0042		0.29
R3	.411	42	39		0.0032		0.21
R4	.430	40	44		0.0026		0.20
Average		42	47	44	Total Power		(1.40)
R5	.473	46	60	49	0.0101	0.0116	0.71
R6	.453	43	46		0.0042		0.29
R7	.467	41	41		0.0032		0.22
R8	.382	40	44		0.0026		0.20
Average		40	44	41	Total Power		(1.41)

TABLE (6.15) V = 5.4 ft/sec (1.62 m/s) Applied Volts (13.84)

		T(M)	T(C)	T_C(C)	H(C)	H_C(C)	Power
R1	.394	30	38	32	0.0180	0.0207	0.77
R2	.342	20	33		0.0074		0.30
R3	.388	29	28		0.0037		0.23
R4	.406	28	33	—	0.0046		0.22
Average		27	33	32	Total Power		(1.52)
R5	.446	33	38	32	0.0180	0.0207	0.78
R6	.422	28	32		0.0074		0.31
R7	.441	29	30		0.0057		0.24
R8	.356	25	33	—	0.0046		0.22
Average		29	33	32	Total Power		(1.52)

TABLE (6.16) V = 4.8 ft/sec (1.45 m/s) Applied Volts (13.84)

		T(M)	T(C)	T_C(C)	H(C)	H_C(C)	Power
R1	.398	32	41	34	0.0170	0.0196	0.78
R2	.346	22	34		0.0070		0.30
R3	.390	31	30		0.0054		0.23
R4	.409	30	34	—	0.0044		0.22
Average		29	35	34	Total Power		(1.53)
R5	.447	34	44	34	0.0170	0.0196	0.78
R6	.425	29	37		0.0070		0.31
R7	.444	32	32		0.0054		0.24
R8	.359	31	36	—	0.0044		0.22
Average		30	35	32	Total Power		(1.55)

TABLE (6.17) V = 4.18 ft/sec (1.25 m/s) Applied Volts (13.84)

		T(M)	T(C)	T_C(C)	H(C)	H_C(C)	Power
R1	.404	35	44	36	0.01533	0.0182	0.79
R2	.350	24	37		0.0065		0.31
R3	.393	32	32		0.0050		0.23
R4	.412	31	36	—	0.0041		0.22
Average		31	37	35	Total Power		(1.55)
R5	.453	36	44	36	0.01533	0.0182	0.79
R6	.430	32	36		0.0065		0.32
R7	.447	32	33		0.0050		0.24
R8	.362	28	37	—	0.0041		0.22
Average		32	38	36	Total Power		(1.56)

TABLE (6.18) V = 3.41 ft/sec (1.02 m/s) Applied Volts (13.84)

		T(M)	T(C)	T_c(C)	H(C)	H_c(C)	Power
R1	.411	39	49	41	0.0143	0.0165	0.80
R2	.354	27	40		0.0059		0.31
R3	.398	35	35		0.0045		0.23
R4	.418	34	40		0.0037		0.22
Average		34	41	39	Total Power		(1.57)
R5	.458	39	49	40	0.0143	0.0165	0.80
R6	.436	35	40		0.0059		0.32
R7	.453	34	36		0.0045		0.24
R8	.366	30	40		0.0037		0.22
Average		35	41	39	Total Power		(1.58)

TABLE (6.19) V = 2.4 ft/sec (0.74 m/s) Applied Volts (13.84)

		T(M)	T(C)	T_c(C)	H(C)	H_c(C)	Power
R1	.421	44	60	48	0.0120	0.0138	0.82
R2	.363	32	48		0.0050		0.32
R3	.406	39	40		0.0038		0.24
R4	.425	38	46		0.0031		0.23
Average		38	48	45	Total Power		(1.60)
R5	.470	45	60	48	0.0120	0.0138	0.81
R6	.446	40	47		0.0050		0.33
R7	.463	39	42		0.0038		0.25
R8	.373	34	46		0.0031		0.23
Average		39	49	46	Total Power		(1.62)

TABLE (6.20) V = 1.7 ft/sec (0.51 m/s) Applied Volts (13.84)

		T(M)	T(C)	T_c(C)	H(C)	H_c(C)	Power
R1	.434	52	74	58	0.0101	0.0116	0.84
R2	.376	39	56		0.0042		0.33
R3	.419	46	46		0.0032		0.24
R4	.438	44	53		0.0026		0.24
Average		45	57	53	Total Power		(1.65)
R5	.487	53	73	58	0.0101	0.0116	0.84
R6	.459	46	44		0.0042		0.33
R7	.478	46	49		0.0032		0.26
R8	.371	33	54		0.0026		0.22
Average		45	58	54	Total Power		(1.66)

DIA (6.1) Pulse generator and power circuit for one element in the multiple strip heat exchanger.

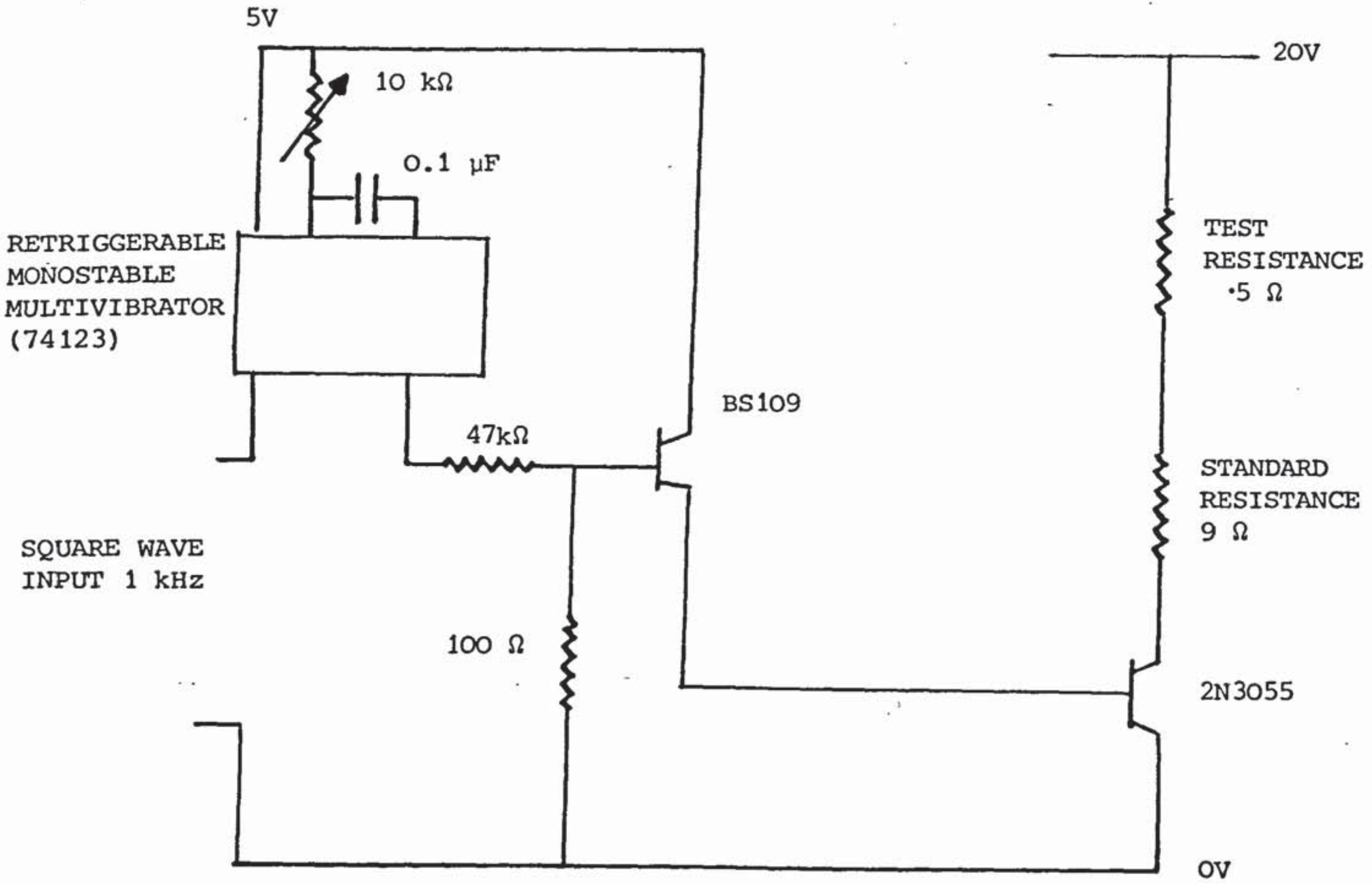

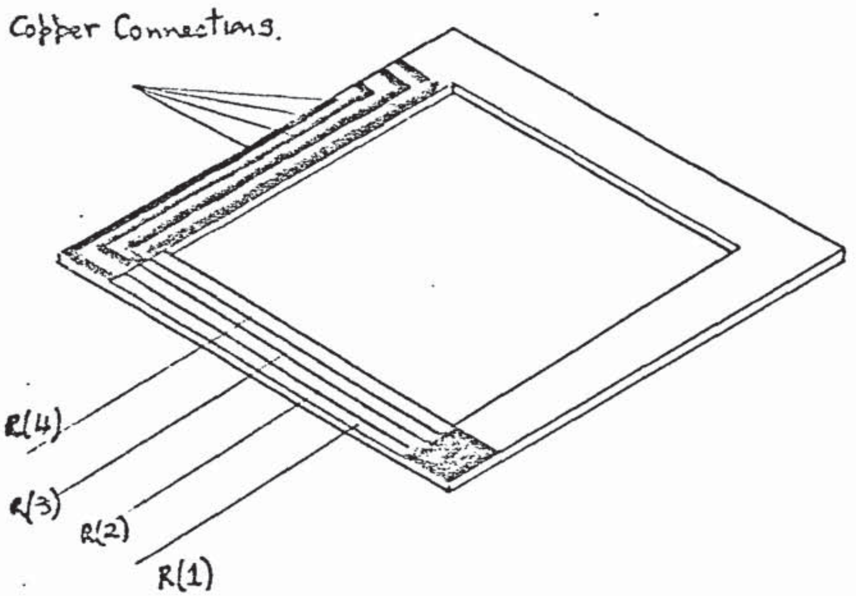

Diagram (6.2)

Construction of nickel element test sample

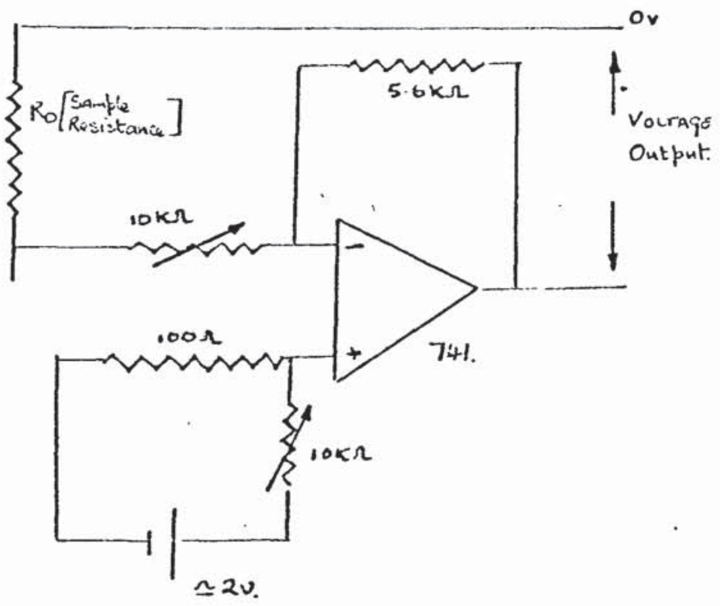

Diagram (6.3)

Operation aplifier circuit used to amplify and measure the element voltage

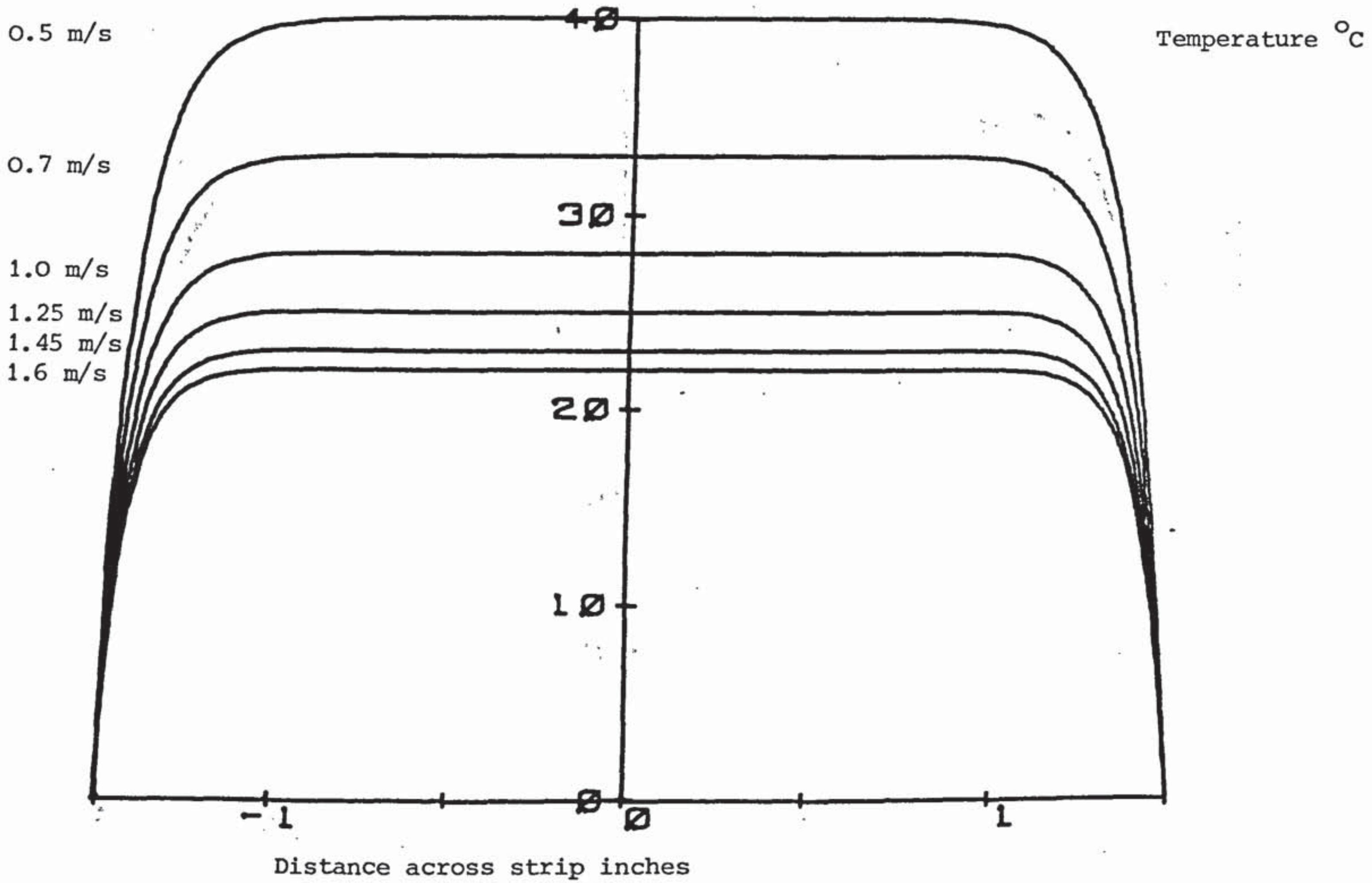

PLOT (6.1) Theoretical variation of the strip temperature and thermal profile with respect to different air velocities passing over the leading strip.

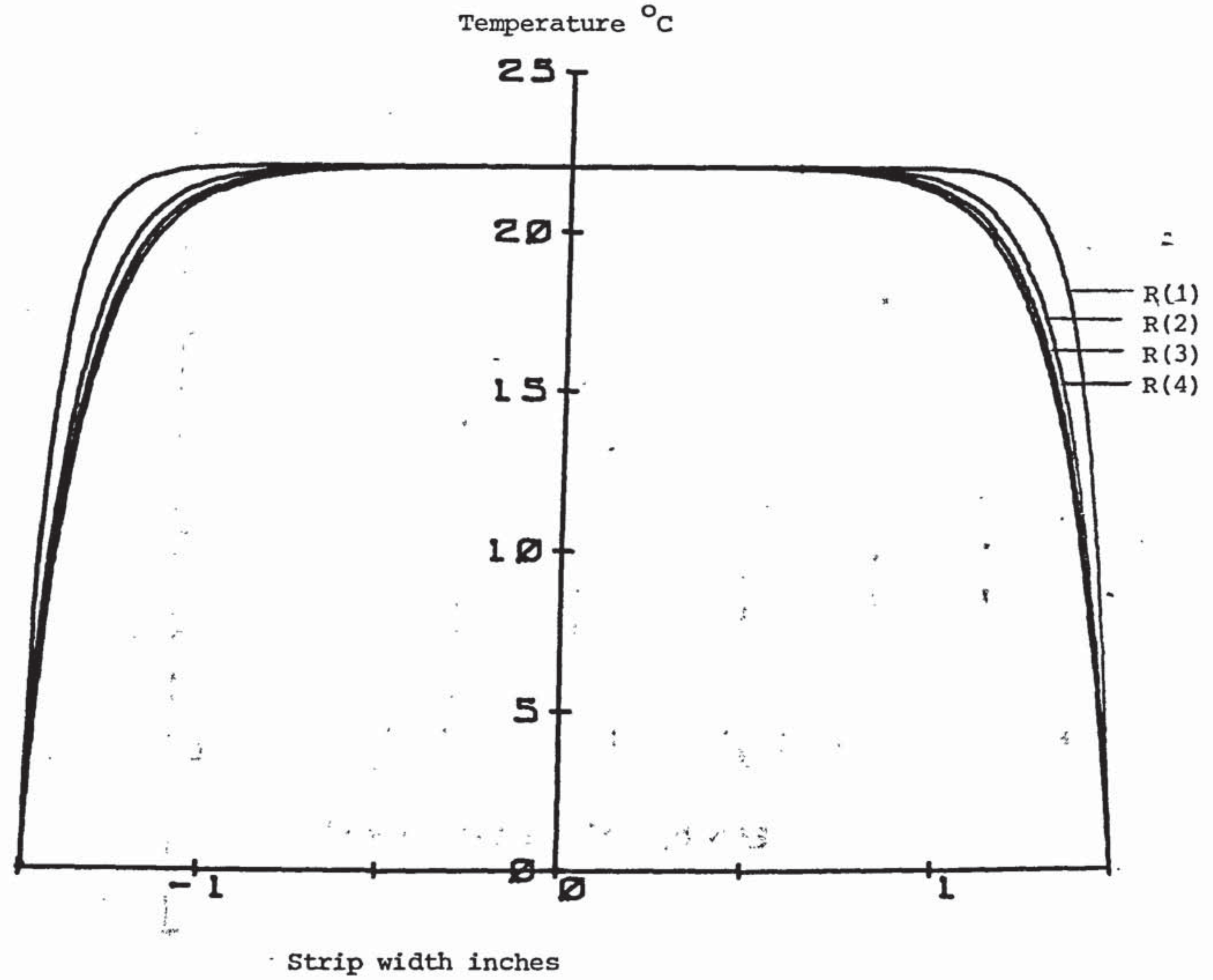

PLOT (6.2) Normalized plot showing the theoretical variation of the temperature profile across the top four strips. Air velocity 1.6 m/sec and applied voltage 11.89 volts.

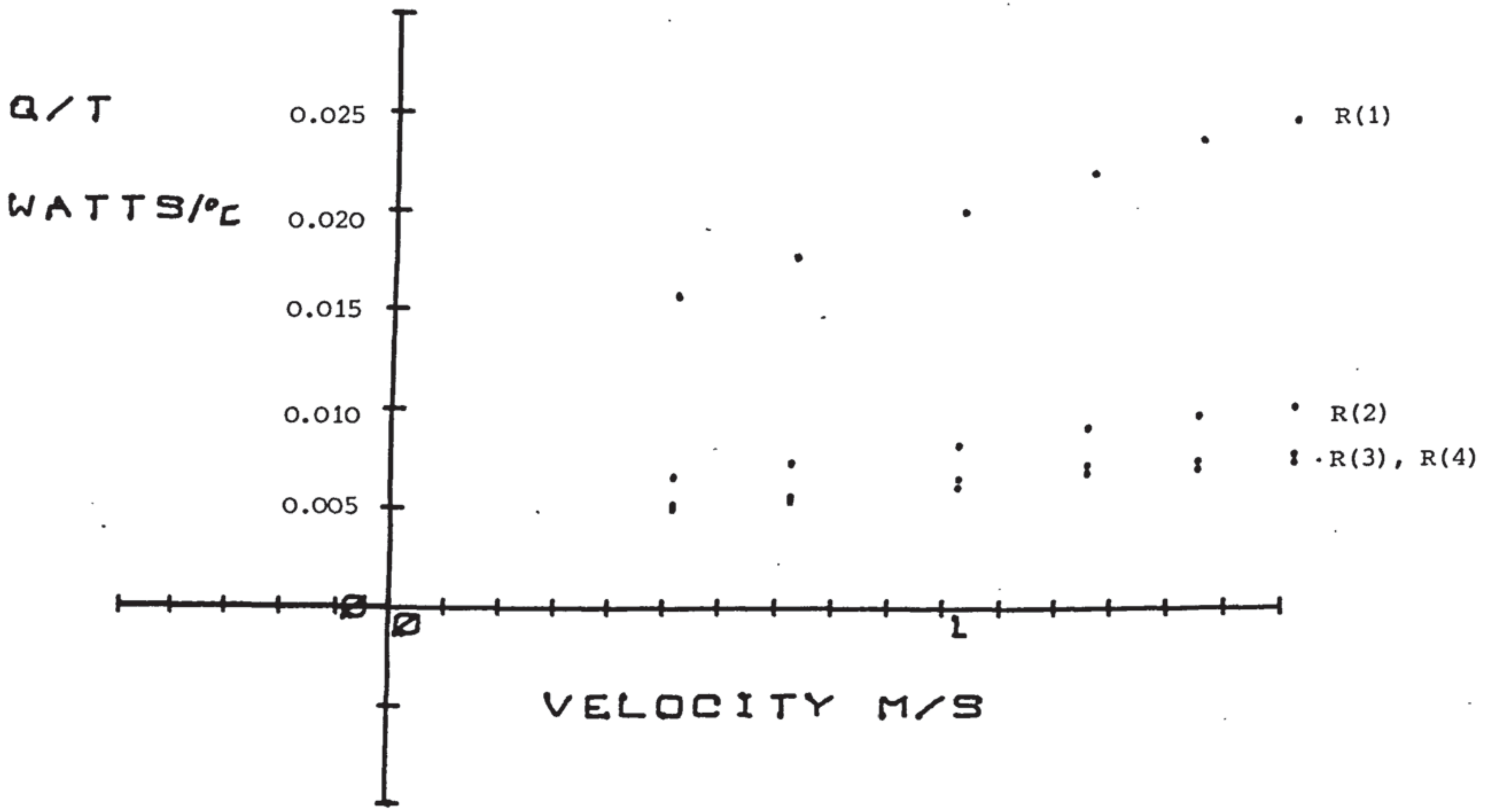

PLOT (6.3) Air velocity against input power for individual top elements R(1) to R(4).

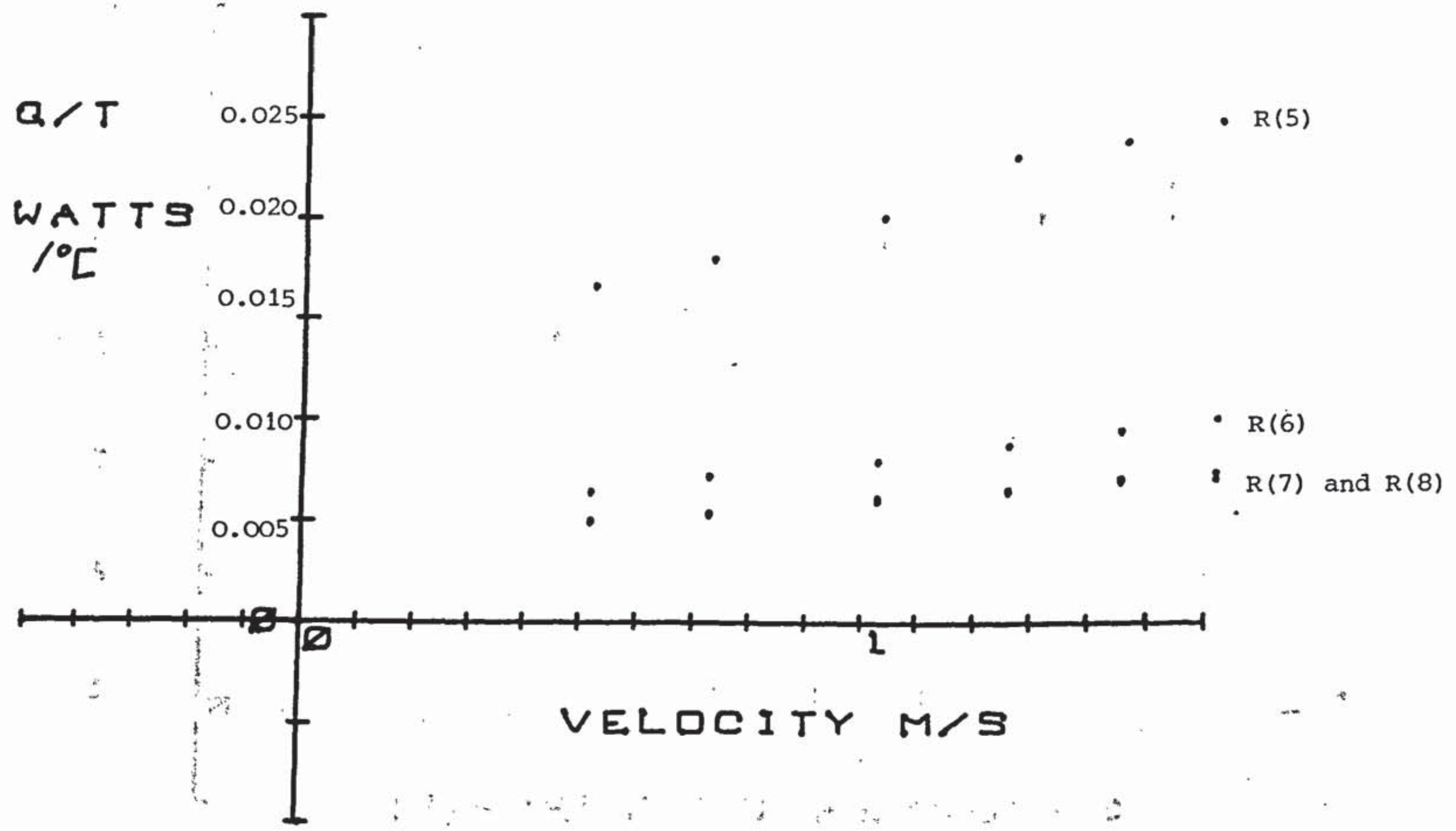

PLOT (6.4) Air velocity against input power for individual bottom elements R(5) to R(8).

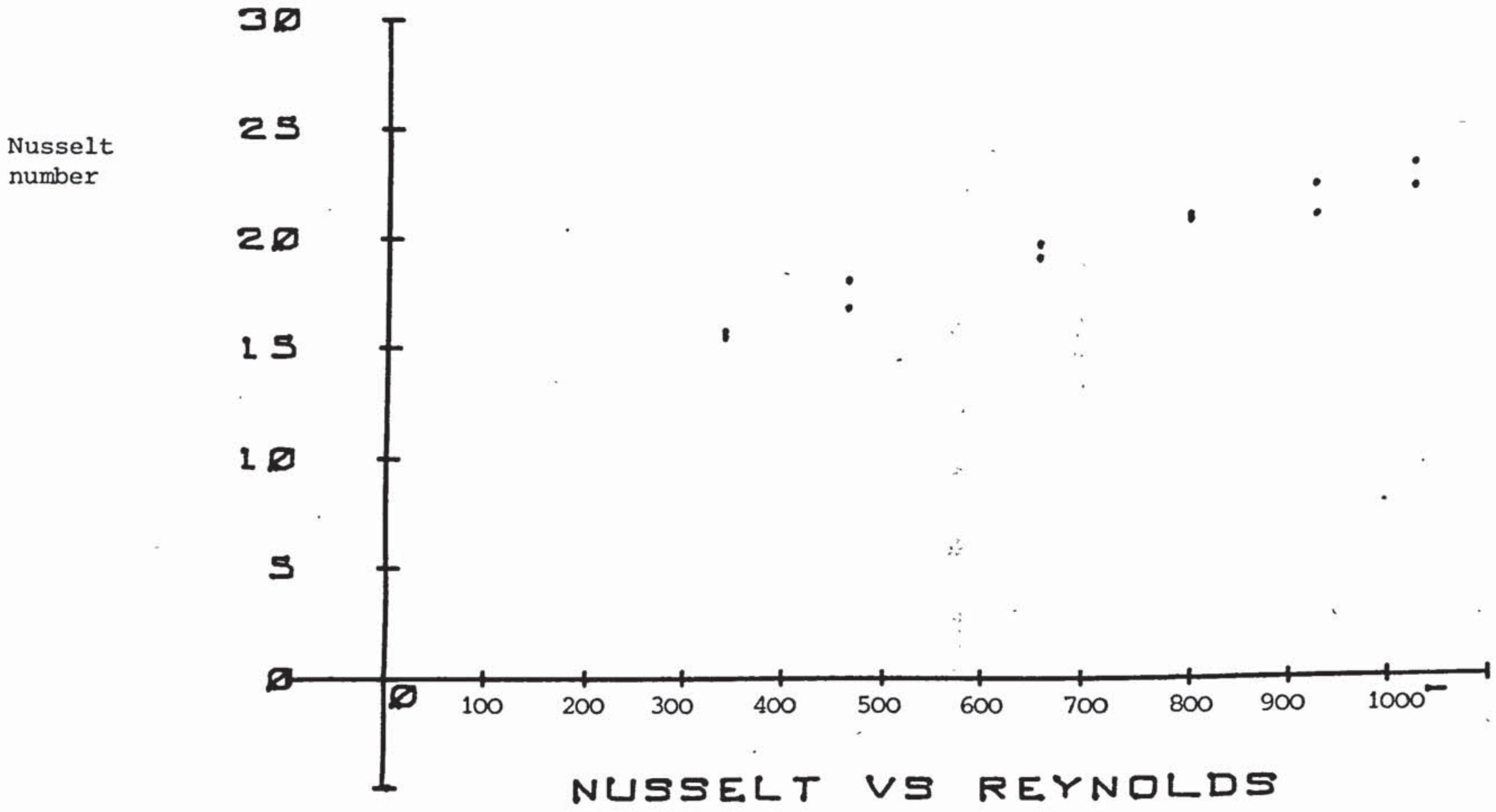

PLOT (6.5) Plot of Nusselt against Reynolds for the top and bottom sets of elements separately.

CHAPTER 7

THEORETICAL AND MATHEMATICAL CONSIDERATIONS

THEORETICAL AND MATHEMATICAL CONSIDERATIONS

During the preliminary stages of this project particularly with respect to the design of the experimental samples several dimensionless factors have been introduced, the most important of these being the Reynolds number. Reynolds number can be defined either by a characteristic length or a hydraulic diameter depending upon the situation under investigation - Ref. {7.1}.

By hydraulic diameter $R = \frac{hd \ . \ U\infty}{\nu}$

By characteristic length $R_L = \frac{\ell \ . \ U\infty}{\nu}$

Where the hydraulic diameter (hd) is defined as (4 cross sectional area)/(wetted perimeter) and ν is the kinematic viscosity. $U\infty$ is the stream velocity m/s and ℓ is the characteristic length.

It is used to indicate the onset of turbulence; the transition from laminar occurs between the Reynolds numbers 2.10^3 to 5.10^5 according to the flow situation. Due to its dimensionless form it can also be used to introduce a scale factor. The samples used in this project have been scaled up by a factor of five in comparison with fins used in practice. The stream velocity has been reduced by a factor of five, thus keeping the Reynolds number constant.

Other factors were:

(Pr) Prandlt number = $\frac{\mu Cp}{\cancel{K}k} = \frac{\alpha}{\nu}$

(Nu) Nusselt number = $\frac{h\ell}{k}$

(Gr) Grashof = $\frac{g\beta\ell^{3}(\Delta T)}{\nu^{2}}$ and Eckert = $\frac{U^{2}_{\infty}}{cp\ (\Delta T)}$ = (E)

where	μ	viscosity (kg/ms)
	cp	specific heat at constant pressure (J/kg °C)
	β	coefficient of expansion (/%)
	α	thermal diffusivity (m^2/s)
	g	acceleration due to gravity (m/s^2)
	k	thermal conductivity (W/m^2 °C)
	l	characteristic length (m)

The Reynolds, Grashof and Eckert numbers can be calculated, to give an indication of the type of heat transfer mechanisms likely to be present for a particular flow situation. Reynolds number is associated with forced convection, Grashof with natural convection and Eckert with changes in a gas due to high velocities or temperature change. The first two terms have been used as an aid both in the design of test samples and for giving an estimate of their performance.

At the outset of the project it had been hoped that a more complete mathematical picture of the velocity and temperature profiles over complicated shapes could be obtained. It became apparent that only for relatively simple situations was it possible to achieve a representation of the flow.

MATHEMATICAL DESCRIPTIONS OF A FLUID FLOWING PAST A BODY

The section describes different methods by which mathematical descriptions can be made of a fluid flowing past an object.

Streamline Potential Flow

This is the simplest method of approach which can be applied to the problem and defines a two dimensional flow field. The field is assumed to be incompressible non-viscous and irrotational; as such the field can be described by a complex function F(Z) for which there exists a potential and stream function.

$$F(Z) = \phi + i\psi$$

Where ϕ is the complex potential and

ψ is the complex stream function

$Z = x + iy$

The field also satisfies the Cauchy-Riemann conditions:

$$\frac{\partial \phi}{\partial x} = \frac{\partial \psi}{\partial y} \qquad \frac{\partial \phi}{\partial y} = -\frac{\partial \psi}{\partial x}$$

The function F(z) can also be resolved into its complex velocity components such that $\frac{\partial F(z)}{\partial z} = \frac{\partial \phi}{\partial x} + \frac{\partial \Psi}{dx} = u - iv$

where u and v are the complex velocity components.

The effect of a body in the flow is found by introducing a further complex function into F(Z). An example of this would be the flow around a cylinder, where $F(Z) = -Uo\ (Z + \frac{a^2}{Z})$

The complex function can be separated into its potential and stream functions as:

$$\phi = -Uo\left(x + a^2x/(x^2 + y^2)\right)$$

$$\psi = -Uo\left(y - ya^2/(x^2 + y^2)\right) \qquad \text{DIA (7.1)}$$

The complex velocity can also be found as a function of x and y:

$$\frac{\partial\phi}{\partial x} = u = -Uo\left(1 - a^2\ (x^2 - y^2)/(x^2 + y^2)^2\right)$$

$$\frac{\partial\psi}{\partial x} = -v = -Uo\left(\ 2\ xya^2/(x^2 + y^2)^2\right)$$

combining $(u^2 + v^2)^{1/2}$ yields

$$\overline{V}^2 = \left(1 + \frac{a^4}{(x^2 + y^2)} + \frac{2a^2\ (y^2 - x^2)}{(x^2 + y^2)^2}\right)^{1/2} Uo \qquad (7.1)$$

If a streamline potential field is developed, then superposition of one flow upon another is also possible.

For $F(z_1) = Re^{i\alpha}$ and $F(z_2) = Re^{i\beta}$

then $\quad F(z_1) + F(z_2) = R\left(e^{i\alpha} + e^{i\beta}\right)$

In using this technique it is possible to describe the potential flow around bodies at angles of approach other than zero. DIA (7.2).

Streamline potential flow is limited in its direct applications to perfect fluids such as described by Euler's equation of motion $\rho\,\frac{Dq}{Dt} = F - \nabla(p)$ which in a steady flow reduces to Bernoullis equation

$p_o - p = \frac{1}{2}\ \rho q^2$ (Ref 7.2)

Where ρ is the density of the fluid

q is vectorial representation of velocity,

$q = iu + jv + kw$

F represents the body forces.

$\frac{Dq}{Dt}$ is the total differential of q

po is the stagnation pressure and p a change in pressure as a result of a change in q.

As a mathematical method it can be applied if the body considered is very large with respect to the viscous boundary layer. Examples of this type of flow can be seen in the passage of ships through water - Ref {7.3}. Also, according to Stafford - Ref. {7.4} potential modelling can be used to describe the airflow distribution over a convential motorcar with a view to aerodynamic drag reduction. However, in developing this technique it is pointed out that the turbulent wake created by a bluff body travelling through air - Ref. {7.5} is approximated from experimental results and cannot be obtained mathematically.

Boundary Layer Flow

Boundary layer flow takes into account the previously neglected viscous drag experienced by a fluid flowing past a body. For an incompressible flow an extra term is now added to Euler's equation representing the viscosity of the fluid, forming a simplified Navier-Stokes equation

$$\rho\frac{Dq}{Dt} = F - \nabla(P) + \mu\nabla^2 q \qquad (7.2)$$

Where μ is the viscosity of the fluid.

This expression describes the boundary layer flow provided the properties of the fluid, i.e. density and viscosity remain constant. In the case of a steady flow eqaution (7.2) reduces to

$$\frac{u\partial u}{\partial x} + \frac{v\partial u}{\partial y} = \frac{1}{\rho} Fx \overset{-}{\cancel{+}} \frac{1}{\rho}\ \frac{dp}{\partial x} + \frac{\mu}{\rho}\left[\frac{\partial^2 u}{\partial x^2} + \frac{\partial^2 u}{\partial y^2}\right]$$

in the x direction,

where Fx is the x component of F, the body force and $\frac{dp}{dx}$ is the pressure loss in x direction, and in y direction

$$\frac{u\partial v}{\partial x} + \frac{v\partial v}{\partial y} = \frac{1}{\rho}Fy - \frac{1}{\rho}\frac{dp}{dy} + \frac{\mu}{\rho}\left[\frac{\partial^2 v}{\partial x^2} + \frac{\partial^2 v}{\partial y^2}\right]$$

Schlichting - Ref. {5.1} shows by introducing the concept of boundary depth (δ), that the previous two equations reduce to the form

$$\frac{u\partial u}{\partial x} + \frac{v\partial u}{\partial y} = \frac{1}{\rho}Fx - \frac{1}{\rho}\frac{dp}{dx} + \frac{\mu}{\rho}\frac{\partial^2 u}{\partial y^2} \qquad (7.3)$$

Boundary Layer Flow over a Flat Surface

The solution to this particular boundary layer formation problem was first solved by Blasius - Ref {7.6} . A full explanation of his technique has been given in appendix (5) and only the major points in the method have been expanded in this chapter.

For a steady incompressible fluid flowing over a flat plate at a low velocity equation (7.3) reduces to:

$$\frac{u\partial u}{\partial x} + \frac{v\partial u}{\partial y} = \nu\frac{\partial^2 u}{\partial y^2} \qquad (7.4)$$

where $\frac{dp}{dx} = 0$, $\frac{1}{\rho}Fx = 0$

The continuity equation can be expressed in two dimensions for an incompressible fluid as:

$$\frac{\partial u}{\partial x} + \frac{\partial v}{\partial y} = 0 \qquad (7.5)$$

Blasius assumes a velocity profile within the boundary layer (the area close to the surface were viscous force acts on the fluid) such that at $y = o$, $u = o$ and $V = o$, at $y = \delta$ (δ being the thickness of the boundary layer), $u = U\infty$. It is further assumed that equation (7.5) can be reduced from two variables, u and v to a new variable defined by the stream function $u = \frac{\partial\psi}{\partial y}$ and $v = -\frac{\partial\psi}{\partial x}$. This is possible as $\nabla \cdot q = 0$, but no equivalent ϕ potential function can be developed as previously for a potential stream function.

The technique yields an expression for the boundary layer depth:

$$\delta = 5 \left(\frac{\nu L}{U\infty}\right)^{1/2} \qquad (7.6)$$

it can also be used to develop the velocity profile of u and v.

$$\frac{U}{U\infty} = \frac{C_2\eta}{} - \frac{C_2^{\,2}\eta^{\,4}}{4!} + \frac{11\ C_2^{\,3}\eta^{\,7}}{7!} - \frac{375\ C_2^{\,4}\eta^{10}}{10!}$$

where $C_2 = 1.328$ - PLOT (A.1)

Boundary Layer Profiles over other than Flat Bodies

In the previous section it was shown that for the laminar boundary layer profile over a plate equation (7.3) could be reduced to the form of equation (7.4). If due to the shape of the body $\frac{dp}{dx} \neq 0$ then an approximation can be made from Bernoullis' equation, in that if

$$-\frac{dp}{dx} = \frac{d}{dx}\left(\rho\frac{1}{2}\ v^2 - po\right)$$

thus $-\frac{1}{\rho}\ \frac{dp}{dx} = U\infty\frac{dU\infty}{dx}$

Where $U\infty$ the stream velocity is also the potential velocity outside the boundary layer U(x). Thus equation (7.3) can be rewritten in the form

$$\frac{u\partial u}{\partial x} + \frac{v\partial u}{\partial y} = U(x)\frac{dU(x)}{dx} + \nu\frac{\partial^2 u}{\partial y^2} \qquad (7.7)$$

Beyond the boundary δ, the effect of the viscous forces are considered negligible and thus the flow can be described by two dimensional potential flow theories. In his treatment of laminar boundary layer flow over surfaces Blasius uses a potential function derived from streamline theory (equation (7.1) is an example of this for a cylinder) to replace the stream velocity function U(x) in equation (7.7).

Thermal Boundary for a Flat Plate

This case has been dealt with in more detail in appendix (6). If the same constant property conditions apply as in the previous examples and $\nabla \cdot q = o$. Then the equation describing the thermal situation for an isothermally heated plate being cooled by forced convection is given by Eckert and Drake - Ref {6.3} as:

$$u \frac{\partial T}{\partial x} + v \frac{\partial T}{\partial y} = \frac{\alpha}{\cancel{\nu}} \frac{\partial^2 T}{\partial y^2} \qquad (7.8)$$

where the ratio $\frac{\nu}{\alpha}$ is the Prandtl~~e~~ number (Pr). By introducing a stream function ψ and η in a similar manner to that used previously and by defining $\theta = \frac{T_w - T}{T_w - T_s}$, where T_w is the temperature of the wall, and T_s the free stream velocity.

Equation (7.7) reduces to

$$y'' + Pr\ f\ y' = 0 \qquad (7.9)$$

Where f is the series solution obtained from solving equation (7.4), equation (7.9) can then be solved by means of a power series method as described by Kreyszig - Ref. {7.7}.

If the value of the Prandtl number was unity then equation (7.~~9~~8) reduces to that of equation (7.4) and the thermal boundary depth would be the same as that of the velocity boundary depth. As a close approximation - Ref {5.4} (Handbook of Heat Transfer), the thermal boundary depth can be related to the velocity boundary for gases of Prandtl close to unity.

$$\delta_{th} = \frac{1}{Pr^{1/3}} \quad 5 \left(\frac{\ell\ \nu}{U\infty}\right)^{1/2}$$

This implies that for fluids with a Prandtl number less than unity the thermal boundary layer is thicker than that of the hydrodynamic boundary layer

$$\frac{\delta th}{\delta} = \frac{1}{(Pr)}^{1/3} .$$

where δ_{th} is the thermal boundary depth

δ is the hydrodynamic depth

for a $Pr = 0.71$ (air)

then $\frac{\delta th}{\delta} = 1.12$

Limitation of Boundary Layer Theory

To quote Curlé - Ref {7.8} with respect to his solutions of temperature fields at low flows, "the density should be kept sensibly constant". The implication of this statement is that $\nabla . q = 0$, however as shown in the flat plate holographic chapter (5) the density change through the boundary for a plate at 100°C is approximately 25%. This implies $\nabla . (q\rho) = 0$, but $\nabla . q \neq 0$ and $\rho\nabla . q = - q . \nabla\rho$. As ρ the variable density can be related to its absolute temperature ~~than~~ $\rho = \frac{\rho o\ To}{T}$, thus substituting this value into the previous equation.

$$\frac{\rho o\ To}{T}\ \nabla . q = - q . \nabla\ \frac{\rho o\ To}{T}$$

$$\frac{\partial u}{\partial x} + \frac{\partial v}{\partial y} = \frac{1}{T}\left(\frac{u\partial T}{\partial x} + \frac{v\partial T}{\partial y}\right) \qquad (7.10)$$

which can now be compared with earlier equation (7.5) where $\nabla . q = 0$.

A similar argument can also be applied to the equation of heat flow

$$\frac{\partial H}{\partial t} = \frac{\partial(\rho cpT)}{\partial t} = 0 = + k\nabla^2 T - \nabla . (\rho\ cp\ T\ q)$$

It has been pointed out that it is possible to define a stream function such that

$$\rho u = \frac{\partial \psi}{\partial y}, \quad \rho v = -\frac{\partial \psi}{\partial x}$$

when $\nabla \cdot (\rho q) = 0$.

Again if $\rho = \frac{\rho o\ To}{T}$, by substituting and differentiating it is possible to obtain

$$-\frac{k}{\rho_0 cp\ To} \quad \nabla^2 T = \nabla \cdot q \qquad (7.11)$$

By combining equation (7.11) and (7.10).

$$\frac{1}{T}\left(\frac{u\partial T}{\partial x} + \frac{v\,\partial T}{\partial y}\right) = +\frac{k(T)}{\rho o\ cp\ To}\left(\frac{\partial^2 T}{\partial_x 2} + \frac{\partial^2 T}{\partial_y 2}\right) \qquad (7.12)$$

$$\frac{k\,KT}{\rho o\ cp\ T_0} = \cancel{\alpha}\ \alpha$$

Thus equation (7.12) reduces to that describing the thermal boundary layer previously used, equation (7.8) with a sign change.

$$\frac{u\partial T}{\partial x} + \frac{v\partial T}{\partial y} = + \overset{\alpha}{\cancel{\alpha}}\left(\frac{\partial^2 T}{\partial x^2} + \frac{\partial^2 T}{\partial y^2}\right) \qquad (7.13)$$

Although this equation has the same form as equation (7.8), $\nabla \cdot q \neq 0$. Thus it is not possible to assume a stream function $u = \frac{\partial\psi}{\partial y}$, $v = -\frac{\partial\psi}{\partial x}$, which would have reduced the number of variables present in the equation.

After consideration it is felt that this may be the limit to the mathematical reduction which can be applied. However, a further amount of experimental information is theoretically available in terms of the holographic fringe reconstructions. A plot has been made of the boundary layer fringe distribution for several values of x (distance from stagnation). The profile is thus an expression of T (x, y). If A suitable two dimensioned curve fitting solution is applied, of the form:

$$T = \sum_{m}^{\infty} \frac{a_n y^m}{m!} \quad \sum_{m}^{\infty} \frac{B_m x^m}{m!}$$

than the function could be obtained and the differentials $\frac{\partial T}{\partial y}\ \frac{\partial T}{\partial x} \cdot \frac{\partial^2 T}{\partial_y 2}\ \frac{\partial^2 T}{\partial x^2}$ be determined.

However, even if T(x,y) can be found, u and v the components of the fluid velocity still have to be determined. A possible solution to these remaining variables may be possible by integrating numerically.

Further Limitations to the Applications of Boundary Layer Theory

In the previous methods outlined in this chapter there is a major assumption in that the flow is of a laminar nature. It is stated by Van Dyke - Ref. {7.9} in the development of pertubation theory, which combines potential flow with boundary layer formation that, his methods are not valid in any other than an incompressible laminar flow situation. Both Terrill - Ref. {7.10} and Cheng - Ref. {7.11} develop boundary layer flows over cylindrical shapes and use the velocity profiles to predict flow separation. This is taken as the limitation of the theoretical flow description, a different type of description being required for separated flow.

An alternative technique for using the available holographic information, to determine the heat flow from the surface, has been considered in appendix (8). This develops the rate of heat transfer across a defined surface S

$$\frac{dQ}{dt} = \int_S - \rho C_p T \, q \, . \, d\,S$$

into a volume integral

$$\frac{dQ}{dt} = -\rho o \;\; To \; C_p \int_V \nabla \, . \, q \; dV \qquad (7.14)$$

By substituting from equation (7.11) equation (7.14) can be rewritten as

$$\frac{dQ}{dt} = \rho o \;\; To \; C_p \int_V k \, \nabla^2 \, T \, dV.$$

The implications of this equation have been further discussed in appendix (8).

DIA. (7.1)

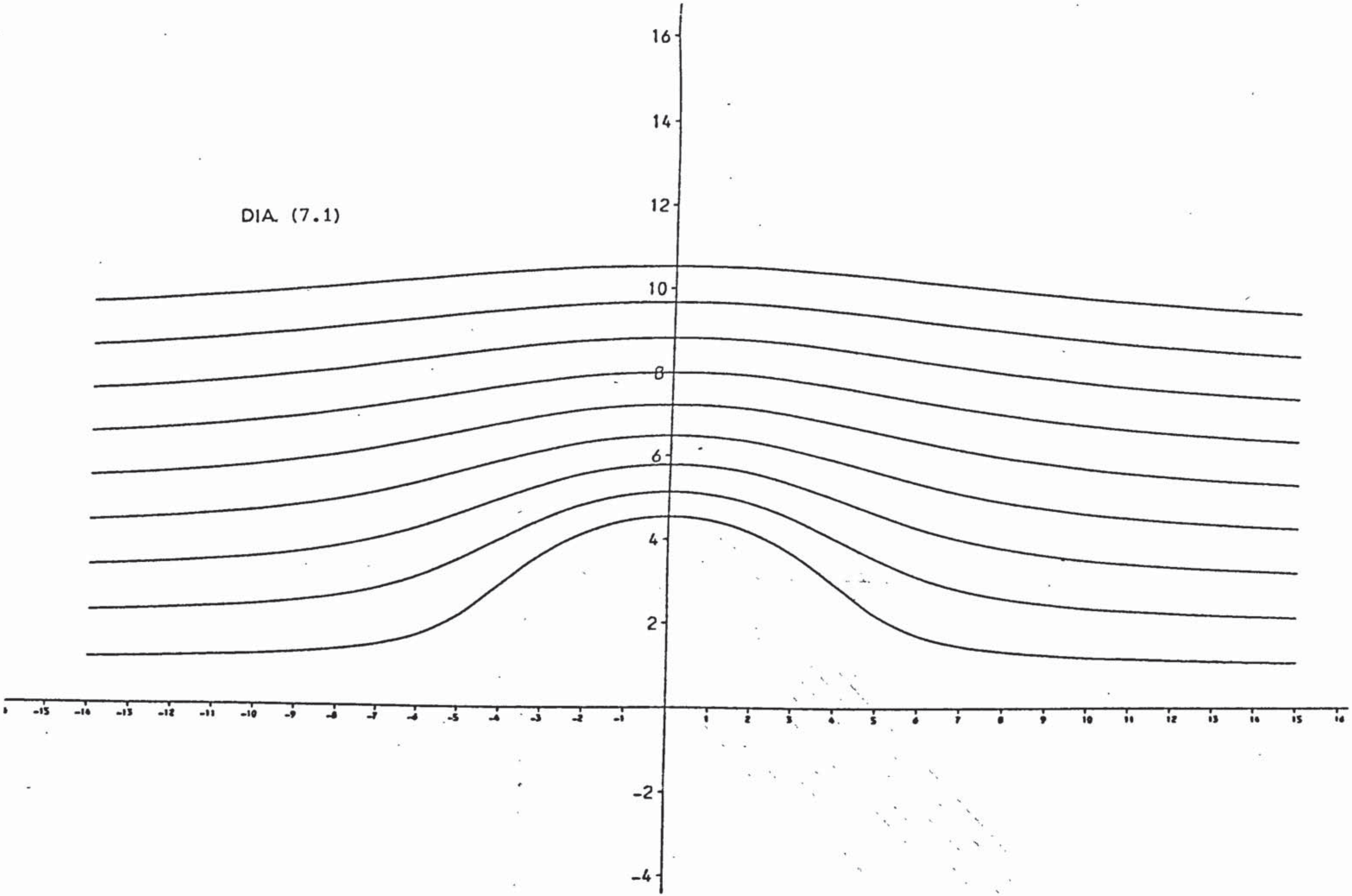

Example of the-function $\psi = uo\left(y - ya^2/(x^2 + y^2)\right)$

(Potential stream function for the flow around a cylinder)

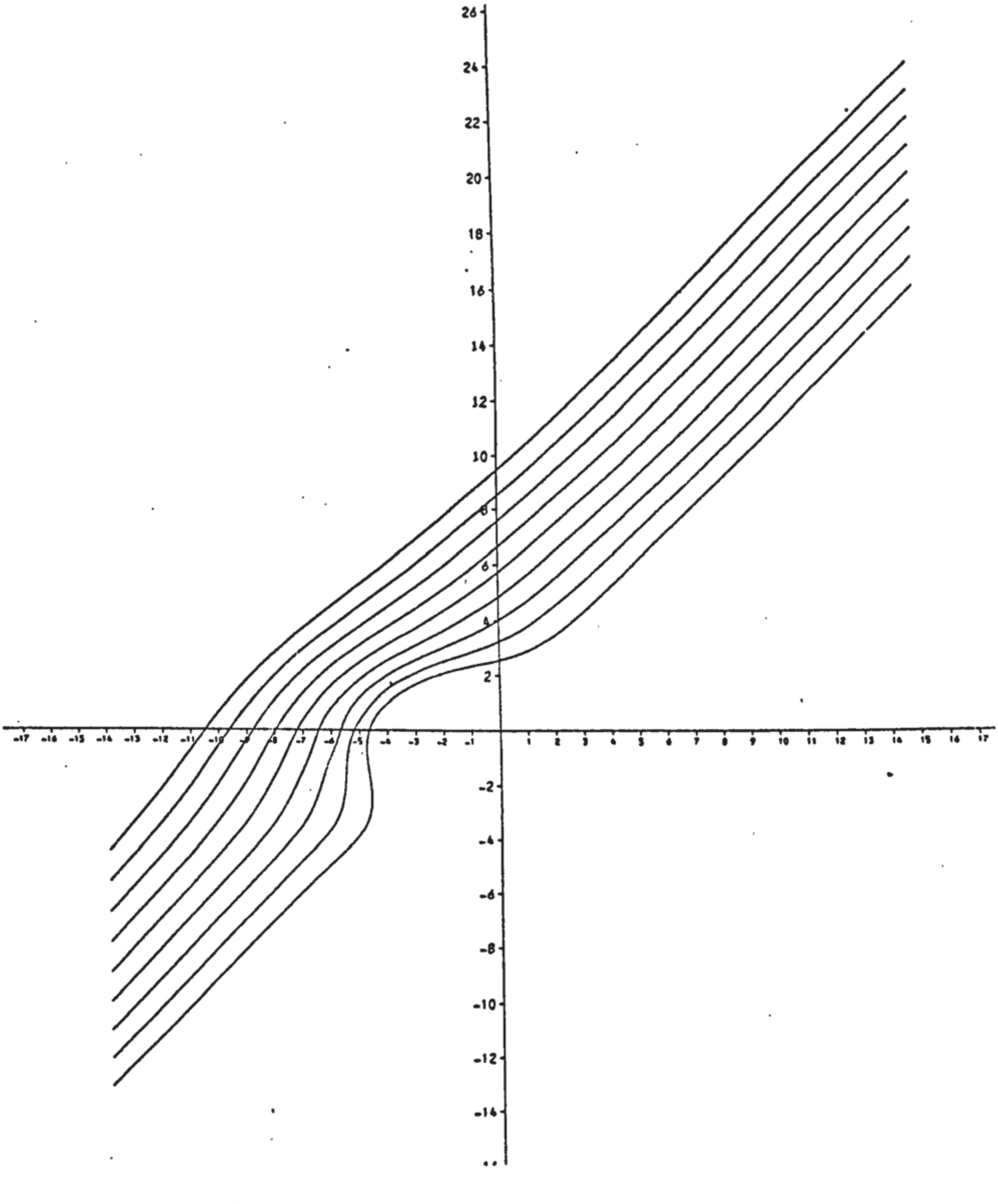

DIA (7.2) Example of two stream functions superimposed to produce a representation of the streamline potential flow around an ellipse.

CHAPTER 8

PREDICTION MODEL

PREDICTION MODEL

This part of the project has been completed in collaboration with Mr. L. Tubb of S.U. Butec (British Leyland). British Leyland suggested that such a programme would be of use to them in terms of forward planning. The purpose of the model was to predict with accuracy the performance of an automotive heat exchanger from given geometric data and test results from specific samples. The aim is to use the model as an aid which presents a development engineer with several alternative multi-louvre configurations, all the configurations being capable of satisfying a specified minimum performance. Using such information it is thus possible to find the most economic and efficient design with the minimum of experimental requirement.

Construction of Model

The model has been built to run on a mini computer (Wang 2200) and uses BASIC as its programming language - Prog. (8.1). It was constructed and operates in five sections culminating in a print-out of the simulated performance characteristics, upon which a development decision can be made.

The first stage is data entry which follows closely the data required in specifying a conventional radiator design.

Data Entry

L_1	Downstream length of secondary surface
L_2	Step length, producing a decrease in the length L_1
n_1	Number of steps
	Thus for each time the programme is run, n_1 steps are made from a length of L_1 to $L_1-n_1L_2$, in steps of L_2. This specifies a number of different fin lengths
D_1	Distance between centres of water carrying tubes
D_2	Step length reduction of D_1
n_2	Number of steps
	i.e. D_1 to $(D_1 - D_2n_2)$ in steps of n_2
T_1	Thickness of water carrying tubes
T_2	Step length reduction of T_1
n_3	Number of reductions
	i.e. T_1 to $(T_1 - T_2n_3)$ in steps of n_3
E_1	Number of rows of water carrying tubes
G_1	Fin density, distance between each secondary surface
G_2	Step length reduction of G_1
n_4	Number of reductions
	i.e. G_1 to $(G_1 - G_2n_4)$ in steps of n_4
TH_1	Thickness in material
TH_2	Step length reduction
n_5	Number of reductions

Finally the type of material for the secondary surface can be determined as either copper, aluminium or steel. Typically the number of permutations theoretically available are 5,000 ($3\ n_1 n_2 n_3 n_4 n_5$). In practice only one material was chosen for each run and several configurations were rejected, reducing those considered to ≈ 1000.

The second stage of the programme was the calculation of the secondary surface hydraulic diameter and surface area. The manufacture of the fin produces a triangular cross-sectioned duct. An allowance has been made for material thickness as this can reduce the hydraulic diameter considerably - Ref. {8.1}. Further if the fin has an unrealistic form, i.e. the fin spacing is too close to allow louvres to be positioned the configuration is rejected.

The third stage of the programme calculates the waterside heat transfer coefficient. From the input data the waterside tube hydraulic diameter was calculated. The hydraulically based waterside Reynolds number could thus also be found for a range of flow rates from 18.1 litres/min to 90.9 litres/min in steps of 18.1 litres/min.

The third stage of the model calculated the pressure loss, fin efficiency and heat transfer for the secondary surface. Initially a fin efficiency of the form $\frac{\tanh\ (ml)}{ml}$ - Ref. {6.3}. Where l was taken as half the width of the channel and $m = \left(\frac{hc}{ka}\right)^{1/2}$; k is the thermal conductivity of the rod, h is the heat transfer coefficient of the rod to the air passing over it, c/a is the ratio of surface area to volume. This assumed the louvre to act as a thin rod.

As the object of the programme was to predict performance an amount of trial data was used which had a experimentally determined solution. A reasonable fit between experiment and the programme was obtained if the following parameters were applied.

1. The fin efficiency was considered as

$$\left(\frac{\tanh \quad (ml)}{ml}\right)^{n1} \qquad n1 = 1.5$$

2. The airside heat transfer coefficient was calculated from

$$ha = K_1 \; C_1/\left(R.\right)^{n_2}$$

$$K_1 = 0.076, \; n_2 = 0.377$$

where R is the Reynolds number based upon hydraulic radius of the channel

G is the mass flow through the channel

3. The airside friction factor was taken as

$$f = k_2/R \qquad k_2 = 0.4756$$

The first time the programme passed through the third stage the airside heat transfer and pressure loss coefficients were calculated. By multiplying the airside heat transfer coefficient with the fin efficiency and combining with the waterside heat transfer coefficient, the overall heat transfer for the whole radiator core was found.

$$\frac{1}{u} = \frac{1}{h_a s_a} + \frac{1}{h_w s_w}$$

where U is the overall heat transfer coefficient

h_a is the airside heat transfer coefficient

h_w is the waterside heat transfer coefficient

s_a is the airside surface area

s_w is the waterside surface area

This calculation was made for the largest experimental velocity normally used. (15.2 m/sec). A test was then made against a maximum permissible pressure loss for the core and a minimum value heat transfer coefficient. If the calculated values either exceeded the first or fell below the second the configuration was rejected. If the test was successful then the third part was re-entered. The overall heat transfer coefficient was recalculated for a range of velocities from (3.05 m/sec) to (15.2 m/sec) in steps of 3.05 m/sec.

The final stage produces a print out displaying

1. The specifications of the successful configuration
2. The volume and type of materials used in the simulated experiment
3. For a range of velocities 3.05 m/sec to 15.2 m/sec in steps of 3.05 m/sec and a range of waterflow from 18.2 to 90.9 litres/min in steps of 18.18 litres/min.

The overall heat transfer ability of the surface
The pressure loss experienced by the simulated core
The fin efficiency factors
The separate heat transfer coefficients of the water and air side

Application of Model

There are several interesting points illustrated by the use of this programme. There is a marked independence of the overall heat transfer coefficient from the waterside heat transfer coefficient - Table (8.1). At low air speeds there is a difference of approximately 8 per cent in u_a between a water flow of 18.1 to 90.9 litres/min which increases to 20 per cent at 15.2 m/sec. At low air speed the heat transfer coefficient is much lower thus as $h_a s_a << h_w s_w$ the expression $u_a = \frac{h_a s_a h_w s_w}{h_a s_a + h_w s_w}$ tends to $h_a s_a$.

The variation in fin efficiency - Plot (8.1) can be seen to be falling with increased fin density. This is a particular point which interests motor manufacturers with regard to future designs. The match between simulated and experimental data was found to be within an 8 per cent error.

The experimental data was taken over a fin density range of 3.15 fins/cm to 9.45 fins/cm, the original curve fitting solution to solve k_1, k_2, n_1 and n_2 was made at 6.9 fins/cm. Finally, the heat coefficient and pressure loss parameter were defined for an actual situation. The configuration generated by the programme bore a close resemblance to those known experimentally to achieve this specification.

TABLE (8.1)

Radiator characteristics

Depth of core 1.25 ins. Number of tube rows 1.

Fin density 16 per ins. Thickness of material 0.002 ins.

Dimensions of water tubes 1.25 ins by 0.08 ins. Type of material copper.

Volume of material used in cubic inches:-

Airway 4.75 Water tubes 4.39

Heat transfer and pressure loss data for water side

G.P.M.	4	8	12	16	20
BTU/MIN 100F	2640	4597	6359	8005	9562
ins. water	0.2	0.71	1.47	2.47	3.69

Performance data

Vel	P.D.	Heat	Finf	4	8	12	16	20
50	3.47	1751	.78	1513	1773	1894	1967	2015
40	2.42	1562	.80	1379	1591	1689	1746	1784
30	1.51	1343	.83	1211	1372	1444	1485	1513
20	0.78	1078	.86	989	1094	1139	1164	1181
10	0.25	731	.91	665	711	730	740	747

(Continuation of TABLE (8.1)

Airflow (Vel) ft./sec. Pressure across core (P.D.) ins. water

Fin efficiency (Finf). Airside heat transfer coefficient (Heat)

Calculations made for five water flow rates gals./min.

Pressure above which configuration is rejected P.D. = 4.2

Heat transfer performance below configuration is rejected

1800 BTU/min 100F MTD. (20 G.P.M., 50 ft/sec.)

Programme (8.1)

Prediction Model

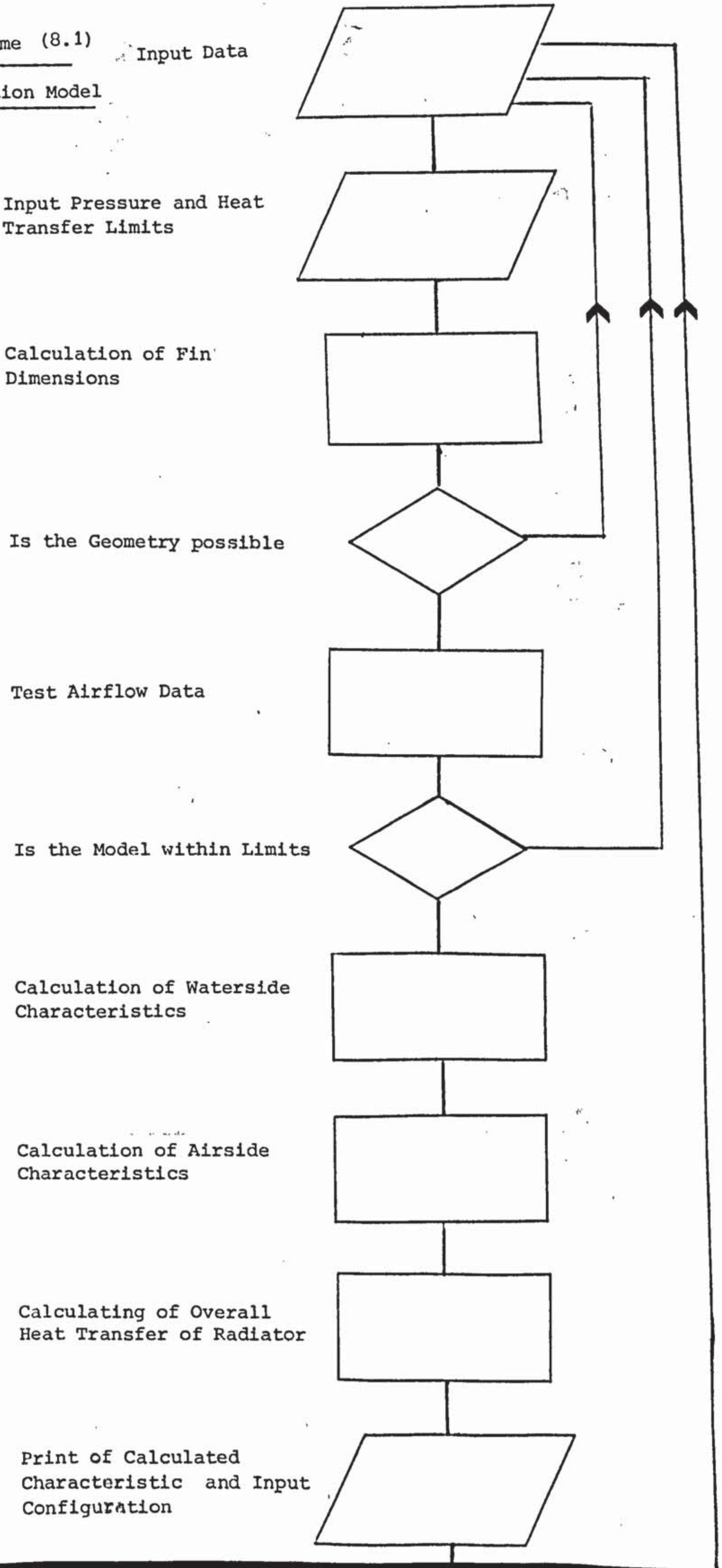

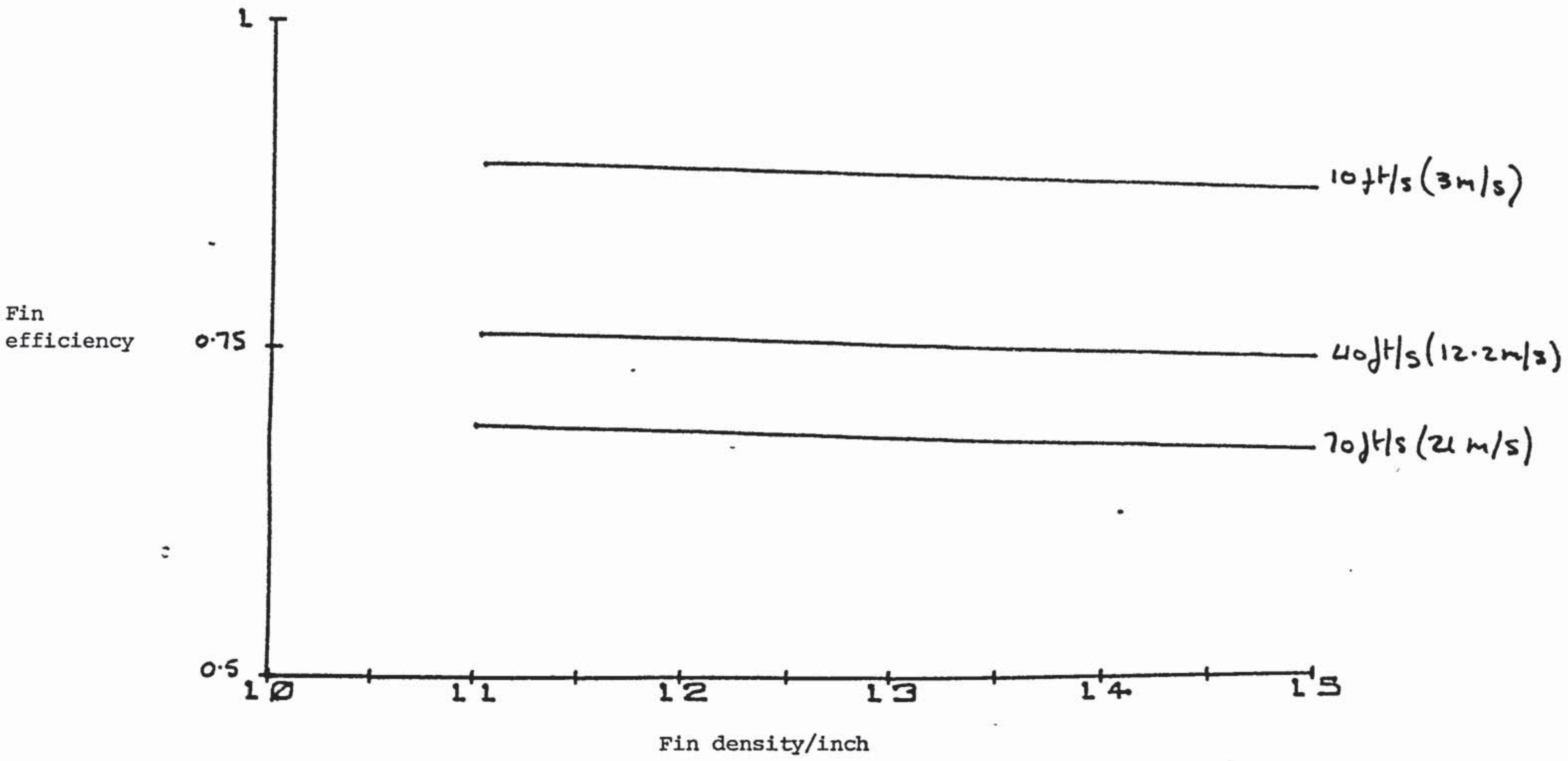

Plot (8.1) Plot of fin efficiency against density

CHAPTER 9

CONCLUSIONS AND RECOMMENDATIONS FOR FURTHER DEVELOPMENTS

CONCLUSIONS AND RECOMMENDATIONS FOR FURTHER DEVELOPMENTS

The object of this project was originally defined as an investigation of the air flow over heated disruptive surfaces. In particular it had been hoped to establish an experimental method which would provide an analysis of the air flow distribution occurring in the core of an automotive radiator.

A second objective has been to investigate the possibility of reducing the large amount of empirical testing which at present accompanies the development of a new or modified configuration.

The conclusions deal with each area of research, first separately and then combined as a general summing up of the completed work and future applications.

Holographic Studies

The work covered in this section represents essentially an attempt to gain information of air flowing over heated surfaces. Initially several holograms - fig. (7), (11), (12), (16), (18), (19) to (22) - were made of complicated surfaces. Although the fringing which can be seen in the reconstruction has a resemblance to streamline flow a direct comparison is not possible for the following reasons.

These early samples were not isothermal and it is likely that the rear of the samples were hotter, thus temperature fringes may have "grown" from the surface and not originated either at, or close to the stagnation points.

The flow over the shapes is in general complicated by the possibility of pressure gradients which would make a mathematical analysis of the problem difficult.

Finally, two assumptions implicit in the Blasius type boundary layer solutions are not applicable. Firstly, the thermal boundary is not small with respect to the size of the sample and secondly, $\nabla \cdot q \neq 0$. The first assumption is true irrespective of Reynolds number scaling, further ~~as~~ the ratio between the thickness of the boundary layer and the length of the sample remains constant, because of scaling. The second is due to the heating causing the density ρ to change.

There are, however, several observations which may be made from the holograms. Firstly, with reference to the difference between fig. (18) and fig. (22). In fig. (18) the sample which constitutes a series of louvre fins mounted one behind the other appears to have a general boundary layer which has developed over the structure as a whole. In the second experiment - fig. (22) - the same sample has now been mounted with several unheated similar louvre shapes above and below it. The interpretation which is suggested is that each single louvre is now acting as an individual element with air passing over its surface. There appears to be an individual boundary layer to each element in fig. (22) which mixes after leaving the surface with the general heating of all the strips.

The present difficulty is substantiating such a statement without knowledge of the velocity distribution around the surface.

A second observation which has been possible is to determine the difference between natural and forced convection. Double exposure holography makes it possible to discriminate between the two processes when one or the other is predominate. Fig. (11) and fig. (14) are reconstructions of natural and forced convection of a flat plate respectively.

Finally, an isothermal flat sample has been constructed, and holograms have been made from this fig. (23) and fig. (24).

Attempts have been made to apply a classical boundary layer approximation for the temperature profile.

It is noted that the curve of any particular isothermal approximates to that expected by theory, but the fringe distribution does not.

It was proposed in chapter (7) that in order to make a comparison with the equation

$$u \frac{\partial T}{\partial x} + v \frac{\partial T}{\partial y} = \alpha \frac{\partial^2 T}{\partial y^2} \qquad (9.1)$$

a knowledge of the function T (x, y) is required. At present, the inability to resolve the fringe distribution within the boundary layer, particularly when the density changes are largest, presents a limitation.

However, if sufficient detail could be obtained, as theoretically discussed in appendix (8), it would be possible to describe the temperature profile with a power series of the form

$$T\ (x, y) = \sum_{M=0}^{\infty} \frac{A_M x^M}{M!} \sum_{N=0}^{\infty} \frac{B_N y^N}{N!}$$

From such a function it is hoped that the first and second differential forms could be obtained, making possible a comparison with equation (9.1) or providing a direct method of evaluating the power dissipation of the system from the integral

$$\frac{dQ}{dt} = k \int_V \nabla^2 T \, dV$$

also described in appendix (8).

It is a reasonable comment that although double exposure interferograms have been made to illustrate natural convection over simple surfaces, the production of double exposure holograms to illustrate a thermal distribution in forced convection over a complicated surface has not been presented in literature. Thus although the technique can be seen to have limitations it represents a new development in holographic flow visualization.

Multiple Strip Heat Exchanger Model

The object of this technique was to produce a surface which by the use of an electronic control circuit could be maintained isothermally independent of the surrounding air flow conditions.

The test elements were constructed as described in chapter (6) from nickel foil strips mounted upon an epoxy resin base. The results obtained show that such a system is viable and that it can be used to determine the nature of the heat transfer from its elements.

The experimental work has shown that before the elements can be used in a more complicated flow situation further development is necessary.

Secondly, if a system of any complexity were to be considered, a method of directly displaying the element voltage or element temperature would be advantageous. It is proposed that this may be achieved by gating the incoming signal with a further monostable multivibrator of fixed frequency through a cmos device - DIA (9.1). The resulting d.c. voltage would then represent the peak voltage height of the pulse signal. Such a signal should then be in a suitable form either to be displayed using a digital voltmeter or be digitalized and manipulated using a microprocessor.

It was observed that in order to compare the experimental results with those theoretically calculated table (6.3) to table (6.20), the heat transfer coefficients associated with the leading elements only were increased. One possibility for this difference may have been due to local separation and reattachment at the leading edge of the elements, which is a conclusion drawn by Ota and Kong - Ref. {1.14} for a similar situation.

It may be concluded that the multiple strip heat exchanger model has been found viable and sensitive to both changes in air flow and input power and with further development presents a useful research tool.

To develop the holography to visualize the heat flow over such shapes, to a standard such that the data can be evaluated numerically may prove more difficult.

Prediction Modelling

It is at present the ambition of many workers in the field to construct a theoretical model which predicts the performance of a radiator. Burn - Ref. {9.1}, Beard and Smith - Ref. {9.2} and Tenhel - Ref. {9.3} are examples of this.

At the outset of the project it was hoped that in developing an understanding of the air flow over disruptive surfaces that, the knowledge gained, could be used to construct such a predition model.

In practice, however, it has not been possible to achieve this type of detailed description.

A prediction model has been constructed as described in chapter (8), which uses a combination of geometric data combined with actual performance data. The resulting performance predictions have been found accurate provided they represent a configuration similar to that used for the original data.

As a future development it is intended to introduce a cost factor. Thus enabling the radiator designer to explore the performance of several configurations and evaluate the various cost factors without initially resorting to practical testing. The cost factor could include both the material cost and the manufacturing cost at different stages of assembly.

GENERAL CONCLUSIONS

As a general conclusion the objective of combining the different sections of the work to produce a complete description of the flow distribution within an automotive radiator core has not as yet been found possible.

In attempting to achieve this ambition several new techniques have been developed. They have been proved both viable and useful.

Finally, Reynolds number scaling of particular shapes is possible, but care must be taken not to incur difficulties such as: Velocity reduction increases the possibility of a contribution to the heat transfer process by natural convection. Particular measurements, such as pressure determination becomes increasingly more difficult as the velocity is reduced.

DIA (9.1) A possible method by which, the peak voltage of a variable duration pulse waveform can be converted into a proportional d.c. voltage.

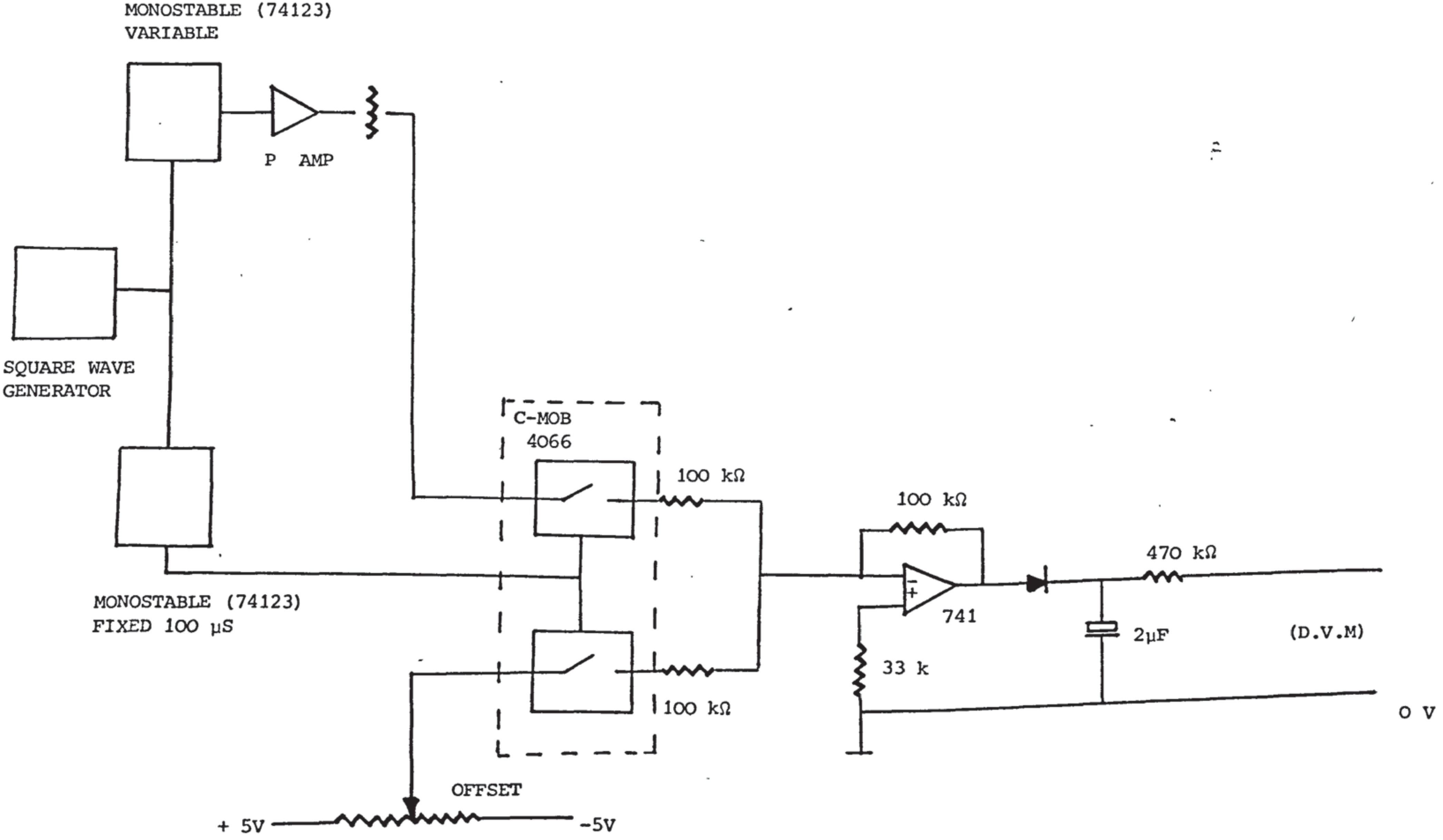

APPENDIX 1

REFRACTIVE INDEX CHANGE DUE TO PRESSURE VARIATION ONLY

APPENDIX 1

Refractive index change due to pressure variation only

Experiments were made using a Rayleigh Gas Refractometer - Dia {A.1} (Ref 1.4) to determine the change in density of air required to produce one fringe shift over a defined path length at constant temperature. The experiment was basically a modified Youngs slit system with two tubes t_1 and t_2 of known length (100 cm). Initially both tubes were at atmospheric pressure. The pressure in t_1 was increased and a compensator adjusted until the original fringe situation was restored. In order to produce one complete fringe shift a pressure of 4.06 $\mathrm{lbf/ft^2}$ (1.46 mm Hg) was required in t_1.

This pressure change was then compared with that likely to occur directly in front of a flat plate - Ref. {A.1}.

$$\Delta P = \frac{1}{2}\ \frac{\rho V^2}{g}$$

where ΔP is the pressure difference
ρ is the density of the air
g is acceleration due to gravity and
V^2 the velocity of the air.

For a velocity of 1.83 m/sec (6 ft/sec) and a density of air of 0.00234 $\mathrm{lbf/sec^2/ft^4}$ 20°C the pressure change is given as

$$\Delta P = \frac{(0.00234)\ (6)^2}{2}$$

$$= 0.042\ \mathrm{lb/ft^2} \quad (0.0015\ \mathrm{cm\ Hg})$$

This is approximately 1/100th that required to produce a single fringe shift over a path length of 100 cm. The velocity required to produce this being 18.3 m/sec (60 ft/sec).

In terms of experimental measurement the fringe shift distortion created by localised pressure changes in an isothermal set of fringes can be considered negligible over a path length of 7.62 cm (the width of the wind tunnel).

Formation of Fringes in a Temperature Varying Field

As the temperature of air increases there is a change in its density. Density is related to refractive index by the Gladstone Dale equation - ref. {A.2}.

$$\frac{n-1}{\rho} = \frac{n_o-1}{\rho_o} = \text{constant} \qquad (A.1)$$

where n_o is the refractive index of air at S.T.P., ρ_o is the density of air at S.T.P., n and ρ refer to the refractive index and density of air at a different temperature.

The velocity of light is defined as $V_{air} = \frac{V_{vacc}}{n_{air}}$

If the path of a light ray across the tunnel is considered, the time taken for it to travel will vary with the velocity of light in the medium. The first exposure of a hologram refers to a ray travelling through a medium of refractive index n_1. The second exposure refers to a ray travelling over the same path with a new refractive index n_2. Interference occurs when the two path lengths travelled by the rays are a factor $\frac{N\lambda}{2}$ apart. Where λ is the wavelength of the light and N is an integer.

$$\frac{N\lambda}{2} = P \left(n_1 - n_2 \right) \quad \text{where P is the path length} \qquad (A.2)$$

This equation can also be expressed in terms of a density change from equation. (A.1).

$$\frac{N\lambda}{2} = P \quad \frac{|\rho_1 - \rho_2|}{\rho_o} \quad \left| n_o - 1 \right|$$

n_o = 1.00029

ρ_1 = 1.2 kg/m^3 (20°C)

ρ_2 = 1.09 kg/m^3 (50°C)

λ = 0.63.10^{-6} m (red)

P = 7.6~~3~~2 cm)7.62.10^{-2} m)

$$N = \frac{7.62\ 10^{-2} \times 2.92 \times 10^{-4} \times 0.11 \times 2}{0.62\ 10^{-6} \times 1.2}$$

$$N = 6.5$$

It can be seen for a temperature change of 30°C over a path length of 7.62 m, 3.25 fringe shifts (i.e. dark to dark or bright to bright) would occur. The temperature change required to produce one complete fringe shift being 9.2°C. The density of air does not vary in a completely linear manner with temperature - Dia (A.2) but follows a~~s~~ cubic expression - Ref {A.1}. Hence larger temperature changes are required to produce the same density changes as the temperature increases.

APPENDIX 2

THREE DIMENSIONAL RECONSTRUCTION OF REFRACTIVE INDEX FIELDS

APPENDIX 2

THREE DIMENSIONAL RECONSTRUCTION OF REFRACTIVE INDEX FIELDS

During the early stages of this project there was a possibility that this particular problem would be important in the interpretation of holographic data. Practical experience has proved that the fringe patterns observed lay evenly across the whole sample making direct viewing and interpretation possible. Thus this appendix is a review of several techniques outlining the advantages and limitations in implementing them.

The underlying assumption in all the methods considered is that refraction of the light ray is limited, such that the rays can be considered to travel in a straight line through an area of changing refractive index (ref A.2). This implies that a volume of unknown refractive index can be analysed plane by plane. Expressed mathematically the path length is given as

$$\int_{0}^{S_i} f(x,y,z)\,dS_i = \phi_1 \qquad \text{(A.3)}$$

where $f(x,y,z)$ is a function of refractive index

S_i is the path taken by the ray through the volume

ϕ is the overall refractive index along the path S_i

The refraction-less limit implies that the change in refractive index a~~e~~ffects only the velocity of a light ray and does not cause a cuvature in its path.

Hence the previous equation can now be rewritten in two dimensions only

$$\int_{o}^{S_i} f(x,y)dS_i = \phi_1$$

In a double exposure hologram the first exposure represents a reference field which is subtracted from the second exposure producing a hologram of the refractive changes from the reference condition.

Thus

$$\int_{o}^{S_i} f_1(x,y)dS_i - \int_{o}^{S_i} f_2(x,y)dS_i = \phi_d$$

where ϕ_d is the change in refractive index between field $f_1(x,y)$ and $f_2(x,y)$ over a path length S_i.

The holographic information is produced in the form of light or dark fringes due to the refractive index changes and the path length of the ray

$$\frac{n\lambda}{2} = \phi_d \quad S_i$$

where S_i is the path length of the ray

λ is the wavelength of the source illumination

n is an integer value

A dark fringe being produced when n is odd and a light fringe when n is even. The changes in refractive index can also be equated to temperature values of the air for defined path lengths (Appendix 1).

The object in most refractive index field reconstructions being not to relate the fringe pattern to refractive index but to the property which has induced the change in refractive index - ref. (A.2).

Fringe interpretation is an arbitrary method of defining the path length information. The fringes lying closest to the heated surface having the highest order number and those closest to cold surrounding areas the lowest (Fig. 16). In the case of natural convection closed rings lying on or near a heated surface define particular hot spots. Corrections also have to be made for the angle of view (Dia A.3) which is a further function of path length. These points have been drawn out to illustrate the difficulties in extracting useful data from a double exposure hologram. A final limitation is the visibility of fringes, as the average temperature across a path length falls to almost that of the surroundings the fringes broadened (Fig. 1). Broad fringes do not have the sharp appearance of narrow fringes, but appear as smoky traces. It has been found not only difficult to define the width of such a fringe but photographically extremely hard to record. Micro densitometer traces indicate that these fringe patterns fall within the speckle noise level on pulse holograms.

The problems of holographic data collection, suitably accurate to produce good field reconstructions are:-

1. Resolution limit imposed at low frequencies by speckle noise and at high frequency by the size of the holographic plate
2. The ability to attach an order number to the fringes.

3. The angle of view of the field obtainable.
4. The refractive index gradient in that too great a change in refractive index will cause refraction and the refractionless limit assumption will no longer be valid. Too few fringes will limit the possible accuracy of the reconstruction.

Reconstruction Methods

The two parameters which define the appropriate reconstruction method are the quality of the available data and the angle of view by which the hologram can be viewed. The ideal situation would be with an angle of view of 180°. Work has been done in this field by S. Frazer and K. Kinlock - Ref. {2.10} using a complicated beam splitting process in combination with a holographic diffuser - Ref. {2.9}. The apparatus used is still in a development stage using a continuous laser and is as yet not suitable for instantaneous events of vibrationally sensitive objects. There are, however, three main methods developed for the reconstruction of X-ray fields which could be used with holographic data having a viewing angle of 180°.

Frequency Plane Construction

Bracewell - Ref. A.3 gives by far the most succinct and accurate description of this technique. Basically a number of discrete views are taken around the object. Each view is then used to compute the Fourier coefficients for the particular angle at which it lies with respect to the field. Dia (A.4). By repeating this operation for angle of view from $\theta = 0^\circ$ to $\pm 90^\circ$ a two dimensional plot of the field can be constructed in the frequency plane Dia (A.5). Retransformation yields a two dimension plot of the field in the sample plane. Mathematically this process can be expressed as:-

$$f(x,y) = \int_{-\infty}^{+\infty} F(U,V)e^{-i2\pi(Ux,Vy)}\,dU\,dV$$

where the reconstructed field is expressed as f(x,y) and the field F(U,V) represents the frequency plane Fourier transform of f(x,y)

If $h_o(x) = \int_{-\infty}^{+\infty} f(x,y)dy$ is the projection of the field in the x direction. Dia (A.6) and $h_1(x^1) = \int_{-\infty}^{+\infty} f(x^1 y^1)dy^1$ is the projection in an arbitrary direction θ^1

Then the frequency plane can be constructed by taking a series of one dimensional transforms from $\theta = 0^{\circ}$, to $\theta = 90^{\circ}$

$$\text{for } \theta = 0 \qquad F(U,0) = \int_{-\infty}^{+\infty} h(x)e^{-i2\pi(Ux)}dx$$

Theoretically such a system should yield a near perfect reconstruction. However, the quality of ~~a~~ the holographic data will limit the standard of resolution. Further the mathematical operations demand the use of a large and powerful computer to deal with any field of real interest.

Tomographic Reconstruction Method

This method has been recently revived by E.M.I. - Ref. {A.4} for use in their X-ray brain scan machine. It is a surprisingly simple method of reconstruction which appears to produce a high quality of results. An average value for the whole field is first calculated. Then a large number of views around the object taken - Dia (A.6). By choosing a series of views co-incident with a particular area in the field and subtracting the average, a value for that area is found -

Let σ_N be the average value for the whole field.

M is the number of co-incident rays passing through the point F_1 in the field $f(\ell,k)$.

N is the number of points in the field $f(1,k)$

P is the total number of views taken $P = MN$

$\sum_{i=o}^{M} \phi_i$ is the summation of M ray pathlength values coincident through F_1

$$F_1 = \frac{\sum_{i=1}^{M}\phi_i - M(N-1)\sigma_N}{M}$$

A simple case has been taken in Dia (A.7), the error in the unrefined reconstruction for an angle of view of ± 60° was found to be 18%. Dia (A.8). The pathlength data was then refined again reducing the error to 11.4% - Dia. (A.9). The error was calculated from the difference between the real and reconstructed value with respect to the average value σ_n.

$$\text{Error } \% = \frac{\sum_{1}^{N} \frac{\left[V_c - V_a\right]}{\sigma_N} \, 100}{N}$$

V_c calculated value $\qquad$ V_a average value

The process of reconstruction reduces the high frequences information and produces a smoothing effect on the field. E.M.I. have suggested that by convoluting with a sinc function a sharper reconstruction can be obtained. The tomographic technique is particularly useful with fringe limited information and the computational requirements are considerably less than those of the Fourier technique.

Art Methods of Reconstruction

Art is the name given to a series of iterative solutions to be used for the reconstruction of three dimensional fields - Ref. {A.5}. The form of the solutions can be generalised as

$$\rho^{q+1}(i,j) = \rho^{q}(i,j) + \delta(i,j,k,\theta) \left[\frac{R_\theta(k) - R_\theta{}^{q}(k)}{N\theta,k} \right]$$

where ρ is the value of the field at apoint (i,j) in a N x M field where i = 1,N and j = 1,M

q is the number of iterations

δ is a weighting function for particular ray views defined by θ the angle of view and k the origin of the ray

$R_\theta(k) - R_\theta^q(k)$ is the difference between the original path length value and the iterated approximation

N is the number of rays considered to form the point $\rho(i,j)$.

Despite the iterative manner of its operation convergence to a solution is not certain and instability is possible. Basically the problem is that of solving for N unknowns using N-1 equations, which leaves the use of such techniques debateable.

Method of Reconstruction Fields with less than 180° Viewing Angles

This is a far more common occurrence with the reconstruction of holographic data than the previous methods. Sweeney and Vest - Ref. {A.6, A.7} describe several possible methods in detail, some of which are modified versions of those previously outlined. By having a prior knowledge of a particular field certain assumptions are possible. Firstly if the field is known to be symmetrical then the Fourier technique does not require a full 180° of view. Also for a temperature field the value of refractive index will follow a continuous function and the theory of super-resolution is applicable - Ref. {A.8}. Finally a series of real space solutions using complicated weighting functions, are also valid. One such method using a sinc weighting function has been studied in depth. It develops the unknown field in terms of the pathlength information via a weighting function of the form

$$W_{MN}(\rho\theta) = (1 + \mathrm{Tan}^2\theta)^{1/2}\ell \times \mathrm{sinc}\left[(\ell/\cos\theta + \ell x\, m\tan\theta - yN)/\ell Y\right]$$

$$\text{for} \quad -\pi/4 < \theta < \pi/4 \qquad \mathrm{Sinc} = \frac{\sin\theta}{\theta}$$

The solution is found in terms of the unknown field f(x,y) by inverting the weighting function matrix and solving for the coefficients of MXN linear equations.

$$\text{Hence} \quad \left[W_{MN,MN}\right] \times \left[X_{MN}\right] = \left[B_{MN}\right]$$

where $W_{MN,MN}$ is the weighting functions, X_{MN} the unknown values within the field f(x,y) the known path length values

by inverstion

$$\left[X_{MN}\right] = \left[B_{MN}\right] \times \left[W_{MN,MN}\right]^{-1}$$

With the use of a Householder decomposition - Ref. {A.9 } redundancy can be introduced into the equations. A simulated field has been reconstructed - Dia (A.10) (A.11) to demonstrate the power of this technique. The field itself was divided into 13 x 13 segments and the path length information rounded to the nearest whole number to simulate an actual fringe field. The object of the simulation was to find an optimum level of redundancy. The results can be compared with fields of limited angles reconstructed on a tomographic basis. The main drawback to this method is the size of computer core needed to invert the weighting function matrix. For a field size of M^2, M^4 operations are involved in the inversion of a $M^2 \times M^2$ matrix.

APPENDIX 3

A technique for solving an equation of the form

$$\frac{d^2\theta}{dx^2} - K\theta^2 - L\theta + C_1 = 0$$

by the use of the power series $\theta = \sum_{m=0}^{m=\infty} \frac{C_m x^m}{m!} + E$

The power series can be differentiated and substituted into the equation such that

$$\sum_{m=0}^{m=\infty} \frac{(C_{m+2})x^m}{m!} - K \sum_{m=0}^{m=\infty} x^m \sum_{p=0}^{p=m} \frac{C_{(m-p)} C_p}{(m-p)!\ p!} - (2KE - L) \sum_{m=0}^{m=\infty} \frac{C_m x^m}{m!}$$

$$- KE^2 - LE + C_1 = 0$$

if $C_1 = KE^2 + LE$ and $F = 2KE + L$ then

$$\sum_{m=0}^{m=\infty} \frac{(C_{m+2})x^m}{m!} - K \sum_{m=0}^{m=\infty} x^m \sum_{p=0}^{p=m} \frac{C_{(m-p)} C_p}{(m-p)!\ p!} - F \sum_{m=0}^{m=\infty} \frac{C_m x^m}{m!} = 0$$

equating coefficients of C_m

$$C_2 = K C_o^2 + F C_o$$

$$C_4 = 2K C_o C_2 + F C_2$$

$$C_6 = 2K C_o C_4 + \frac{4!\ C_2 C_2 K}{2!\ 2!} + FC_4$$

$$C_8 = 2K C_o C_6 + \frac{2K\ 6!\ C_2 C_4}{4!\ 2!} + FC_6$$

Only even powers of m are considered as the boundary conditions of the expression require the solution of θ be symmetrical for ± x i.e. $\theta = 0$ at $x = \pm L$. Further as K is small with respect to F, only first order terms containing K need be considered. This reduces the expansion of coefficients to

$$\theta = C_o + \frac{(KC_o^2 + FC_o)x^2}{2!} + \frac{(3KFC_o^2 + F^2C_o)x^4}{4!} + \frac{(10KF^2C_o^2 + F^3C_o)x^6}{6!}$$

$$+ \frac{(42KC_o^2F^3 + F^4C_o)x^8}{8!} \neq + E$$

If $B^2 = F$, then the equation takes a more familar form.

$$\theta = C_o \cosh(BX) + E + \frac{KC_o^2}{B^2} \quad \frac{B^2X^2}{2!} + \frac{3B^4X^4}{4!} + \frac{10B^6X^6}{6!} + \frac{42B^8X^8}{8!}$$

From this expression C_o has still to be determined using the boundary conditions. $\theta = 0$, at $X = \pm L$.

APPENDIX 4

Method of calculating a suitable angle of attack for the louvre fin sample.

Diagram (A.12)

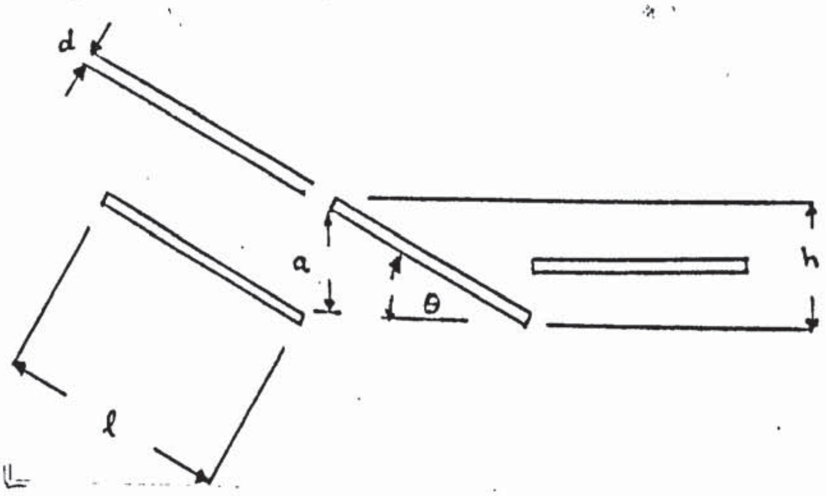

Where d is the width of the louvre

l is the length of the sample

a is the air gap produced between the two angled fins

h is the width of the channel

θ is the angle of the louvre fin

θ can be determined as

$$\sin\theta = h/(l + d/\tan\theta) \qquad (A.4)$$

and a the gap as

$$\sin\theta = a/(l - d/\sin\theta)$$

$$\sin\theta\left(l - d/\sin\theta\right) = a$$

The angle θ can be found by solving equation (A.4) using the Newton Raphson method - Ref. {7.7} which interates using the expression

$$x_{n+1} = x_n - \frac{f(x_n)}{f^1(x_n)} \qquad \text{where } f' = \frac{\partial f(x)}{\partial x}$$

In this case

$$f(\theta) = \sin\theta\,(l + d/\tan\theta) - h.$$

$$f'(\theta) = \cos\theta\,(l + d/\tan\theta) - d/\sin\theta.$$

If θ is expressed in radians the angle which the louvre is to be set for a given, louvre length, thickness and fin spacing can be evaluated from

$$\theta_{n+1} = \theta_N - \frac{\mathrm{Sin}(\theta_n)\left(l + d/\mathrm{Tan}(\theta_n) - h\right)}{\left(\mathrm{Cos}(\theta_n)\left(l + d/\mathrm{Tan}(\theta_n) - d/\mathrm{Sin}(\theta_N)\right)\right.}$$

APPENDIX 5

BOUNDARY LAYER FLOW OVER A FLAT SURFACE

In terms of the boundary layer formation over a surface in a steady incompressible flow situation, the equations which describe its formation are expressed as:

$$\frac{u\partial u}{\partial x} + \frac{v\partial u}{\partial y} = Fx - \frac{1}{\rho}\frac{dp}{dx} + \nu\frac{\partial^2 u}{\partial y^2}$$

and the continuity equation

$$\frac{\partial u}{\partial x} + \frac{\partial v}{\partial y} = 0$$

In the case of flow over a flat surface at low air speeds the equations can be further reduced by neglecting the pressure loss and body force terms, becoming

$$\frac{u\partial u}{\partial x} + \frac{v\partial u}{\partial y} = \nu\frac{\partial^2 u}{\partial y^2} \qquad (A.5)$$

The solution to equation (A.5) was first proposed by Blasius - Ref {7.6} and used a series solution, reducing the partial differentail form of the equation to a complete differential by introducing the co-ordinates η and ψ. Where ψ is the stream function and η has a dimensionless form

$$\eta = \frac{y}{2}\left(\frac{U\infty}{x\nu}\right)^{1/2} \quad \text{and} \quad u = +\frac{\partial\psi}{\partial y}, \quad v = -\frac{\partial\psi}{\partial x}$$

also $\psi = (U\infty \ \nu \ x)^{1/2} \ f(\eta)$

$$\frac{\partial\psi}{\partial y} = u = \frac{u_{\infty} f^1}{2} \qquad \text{where } f^1 = \frac{\partial(f(\eta))}{\partial\eta}$$

and $v = -\frac{\partial\psi}{\partial x} = \frac{1}{2}\left(\frac{U\infty\nu}{x}\right)^{1/2} \left\{ \eta f^1 - f \right\}$

By introducing the stream function into equation (A.5)

$$\frac{\partial\psi}{\partial y} \frac{\partial^2\psi}{\partial x\partial y} - \frac{\partial\psi}{\partial x} \frac{\partial^2\psi}{\partial y^2} = \frac{\partial^3\psi}{\partial y^3} \qquad \text{(A.6)}$$

and by differentiating η with respect to equation (A.6) it is further reduced to the form:

$$f^{111} + f^{11} f = 0 \qquad \text{(A.7)}$$

The expression for the velocity profile, i.e. the variation of velocity in the y direction from the surface of the plate is given as $\frac{u}{U\infty} = \frac{1}{2} f^1$ (A.8)

By finding a solution to equation (A.7) for f in terms of a series expansion, the differential form of the series also being a solution for the velocity profile.

Assuming a solution fo the form

$$f = \sum_{i=o}^{\infty} \frac{C_i \eta^i}{i!} \qquad f^1 \quad \sum_{i=o}^{\infty} \frac{C_{(i+1)}\eta^i}{i!}$$

$$f^{11} = \sum_{i=o}^{\infty} \frac{C_{(i+2)}}{i!}\eta^i \qquad f^{111} = \sum_{i=o}^{\infty} \frac{C_{(i+3)}\eta^i}{i!}$$

If the values obtained for f, f^{11} and f^{111} are substituted into equation (A.8)

$$\sum_{i=o}^{\infty} \frac{C_{(i+3)}}{i!}\eta^i + \sum_{i=o}^{\infty} \eta^i \sum_{p=o}^{p=i} \frac{C_{(i-p)}C_{p+2}}{(i-p)!\ p!} = 0$$

This expression can be expanded and the resulting coefficients of C_i evaluated term by term:

$$C_3 + C_oC_2 = 0, \qquad C_4 + C_1C_2 + C_oC_3 = 0$$

$$C_5 + \frac{C_2^{\,2}}{2!} + C_1C_3 + \frac{C_oC_4}{2!} = 0 \text{ etc.}$$

From the boundary conditions of the problem

$$U = U\infty \quad \text{at} \quad \frac{df}{\partial\eta} = 2$$

at $\eta = 0$, $f = 0$ and $f' = 0$ also at $\eta = \infty$ $f' = 2$

This reduces the number of unknown coefficients in the expansion to be solved by making C_1 and C_o equal to zero. The final expansion for the series being given as

$$f = \frac{C_2\eta^2}{2!} - \frac{C_2^{\,2}\,\eta^5}{5!} + \frac{11C_2^{\,3}\,\eta^8}{8!} - \frac{375C_2^{\,4}\,\eta^{11}}{11!} + \frac{27897\,C_2^{\,5}\,\eta^{14}}{14!} \qquad (A.9)$$

The coefficient C_2 can be found by the method of successive approximation and S. Goldstein - Ref. {5.6} gives this value as $C_2 = 1.32824$.

Finally the velocity profile $\frac{u}{U\infty} = f'$ is found by differentiating equation (A.9)

$$\frac{u}{U\infty} = \frac{\partial f}{\partial\eta} = C_2\eta - \frac{C_2^{\,2}\eta^4}{4!} + \frac{11\,C_2^{\,3}\,\eta^7}{7!} - \frac{375\,C_2^{\,4}\,\eta^{10}}{10!} + \frac{27897\,C_2^{\,5}\,\eta^{13}}{13!}$$

The expansion of this profile is shown in Plot (A.1). The boundary layer depth is calculated at a velocity u, 0.99 of the stream velocity U∞ and expressed as:

$$\delta = 2\eta\left(\frac{U\infty}{\nu x}\right)^{-1/2}$$

and occurs when η has a value of 2.5, thus

$$\delta = 5\left(\frac{U\infty}{\nu x}\right)^{-1/2}$$

APPENDIX 6

Thermal Boundary Depth for a Flat Plate

In the case of the thermal boundary layer over a flat plate, neglecting natural convection and frictional effects; the equation according to Eckert and Drake - Ref {6.3} can be expressed as

$$u \frac{\partial T}{\partial x} + v \frac{\partial T}{\partial y} = \frac{k}{\rho c_p} \frac{\partial^2 T}{\partial y^2} \qquad (A.10)$$

This is very similar to equation (A.7) previously considered (appendix 5). The temperature T lies between the stream value Ts and that of the wall Tw. If a function $y'(\eta) = \frac{T - Tw}{Ts - Tw}$ is introduced into equation (A.10) such that at $\eta = 0$, $y'(\eta) = 0$ and $\eta = \infty$ $y'(\eta) = 1$. Then the equation can be written in the form

$$y'''(\eta) + Pr\, f\, y''(\eta) = 0 \qquad (A.11)$$

where $y'(\eta) = \frac{\partial(y(\eta))}{\partial\eta}$ and Pr is the Prandtl number.

For fluids where $Pr \neq 1$, Pohlhausen - Ref {5.5} proposed a solution for the thermal distribution within the boundary as

$$y'(\eta) = \alpha(Pr) \int_0^{\eta} \left[\frac{f''(\eta)}{f''(o)}\right]^{Pr} d\eta$$

for air $Pr \approx \overset{0.71}{\cancel{0.17}}$, $\alpha = 0.585$.

Further to this a solution similar to that of the hydrodynamic depth can be obtained - Ref {6.1} Handbook of Heat Transfer

where $\eta_{th} = Pr^{1/3} \frac{y}{2} \left(\frac{U\infty}{\nu x}\right)^{1/2}$

If the function of η obtained from the velocity profile is used, $\eta = 2.5$ then

$$\delta_{th} = \frac{1}{Pr^{1/3}} \left(\frac{U\infty}{\nu x}\right)^{-1/2}$$

implying that fluids with a Prandtl number of less than unity have a thicker thermal boundary layer than their hydrodynamic boundary.

$$\therefore \frac{\delta_{th}}{\delta} \cong \frac{1}{(Pr)^{1/3}}$$

For air the Prandtl number is approximately taken as 0.72, thus the ratio $\frac{\delta_{th}}{\delta}$ air $\simeq 1.12$.

APPENDIX 7

Four nickel strips were mounted upon the top surface only of an epoxy resin base - DIA (A.3), as described in chapter (6). Power was applied to the strips each connected in series with a 9 Ω load resistance via a d.c. power pack. The voltage across each strip was noted for a total voltage variation across both strip and load from 1 volt to 10 volts. The strip voltage was displayed as an oscilloscope.

DIA (A.13)

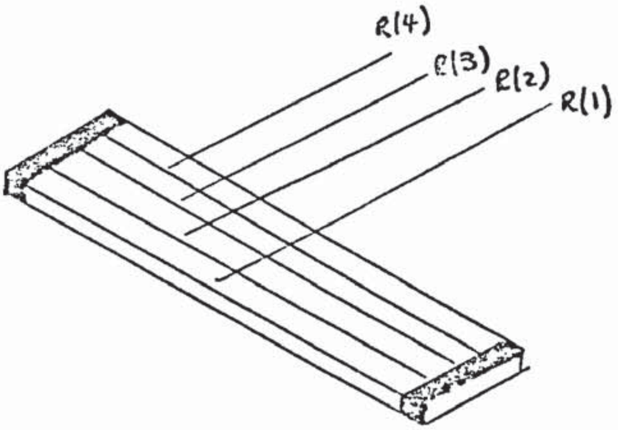

Plot (A.2) shows the variation of applied voltage with strip temperature. The difference in performance between strips seen in these experimental results may be accounted for by the following reasons.

1. In the configuration shown in DIA (A.13) strips 1 and 4 lie on the outside of the sample thus there is likely to exist a different rate of cooling on these strips than the inner strips.

2. The experimental measurements were made on two oscilloscopes 1 and 4 on the first and 3 and 2 on the second. Although care was taken to calibrate both instruments, a difference in display may have existed

between them.

3. The signal change is small (approx. 0.04 volts for each applied voltage change), and the difficulty in reading such a small change has been commented upon in chapter (6).

Despite these drawbacks the results were consistant within the limits of the experiment, such that further development was considered worthwhile.

APPENDIX 8

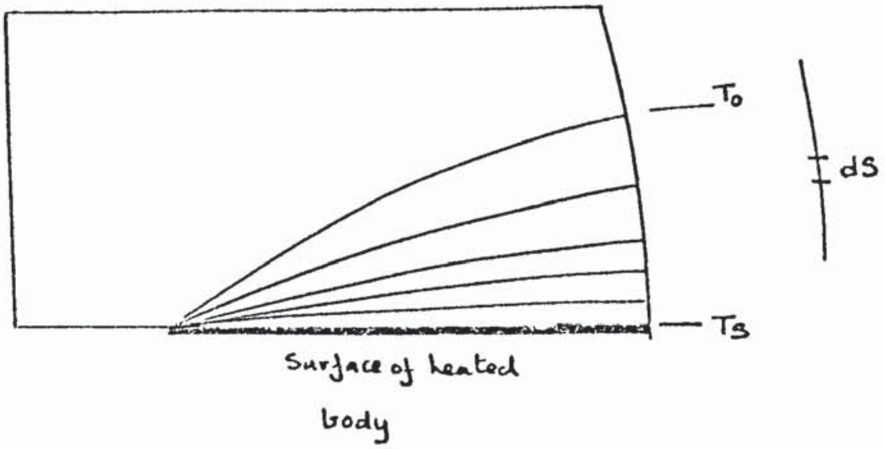

Consider a hot body surrounded by a closed surface S. The rate at which heat is transferred across the surface S can be described by

$$\frac{dQ}{dt} = \int_S (+ k\nabla T - \rho \; cp \; Tq) \; . \; dS$$

If S is chosen so that it is perpendicular to the isothermal fringe distribution surrounding the body, then $\nabla T \; . \; dS = 0$. This is also true for any region outside of the fringe distribution when $T = To$ (free stream temperature) and $\nabla T = 0$.

By chosing S the line integral as shown in DIA (A.14), the previous equation can now be rewritten as:

$$\frac{dQ}{dt} = \int_S - \rho \; cp \; T \; q \; . \; dS$$

and by substituting $\rho = \frac{\rho o \; To}{T}$, the density which is a variable factor, is eliminated

thus $$\frac{dQ}{dt} = \int_S - \rho o \; To \; cp \; q \; . \; dS$$

Finally using Gauss's theorm

$$\frac{dQ}{dt} = - \rho o \; To \; cp \int_V \nabla . q \; dV$$

where V is now the volume enclosed by the surface S.

Using equation (7.11) which explored the possibility of a fluid where $\nabla . q \neq 0$ the rate of heat loss can be expressed directly in terms of the temperature distribution as:

$$\frac{dQ}{dt} = k \int_V \nabla^2 T \; dV$$

Implications of the expression $\frac{dQ}{dt} = k \int_V \nabla^2 T \; dV$

As stated previously in chapter (7) the requirement in evaluating such an integral is dependent upon the accuracy with which the function T (x, y) can be found. At present the standard of the reconstruction does not yield the quality of information necessary. However, by increasing the path length, using a laser with a controllable intensity and a direct fringe reader it should be possible to obtain the standard of information required.

The type of solution for T (x, y) is likely to have the form

$$T\ (x, y) = \sum_{m=o}^{m=\infty}{}^{1} \frac{Am \; x^m}{m!} \sum_{n=o}^{n=\infty}{}^{1} \frac{Bn \; y^n}{n!}$$

It has been found from previous experience that this form of solution is readily differentiable and tends to produce higher derivatives which conform with the boundary conditions required.

Provided the function T (x, y) can be determined, and the higher derivatives found then; it appears that the heat transfer can be computed directly from the temperature distribution without knowledge of the velocity profile within the boundary layer. Further if the samples can be considered as isothermal, the shape of the body does not affect the application of the method.

Disadvantages

The area of largest heat transfer is when the boundary layer is at its thinest. Thus either the power series must approximate this area of the curve extremely accurately or a very high quality of holographic fringe information is required to determine T (x, y). Preferably both these factors could eventually be achieved.

If turbulence occurred then the fringes are likely to become much more difficult to interpret. Firstly, the flow may not be strictly considered as two dimensional and secondarily the fringes tend to broaden making measurement difficult.

DIA. (A.1)

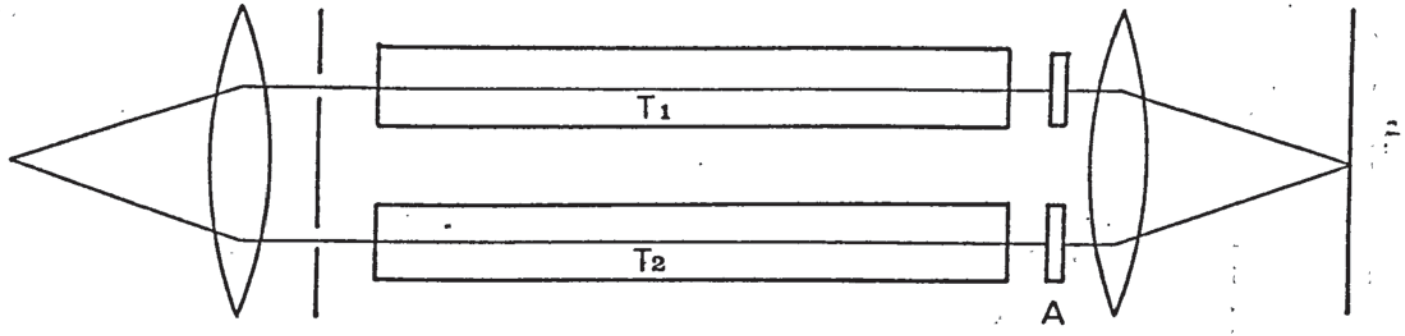

A Compensator

RAYLEIGH GAS REFRACTOMETER.

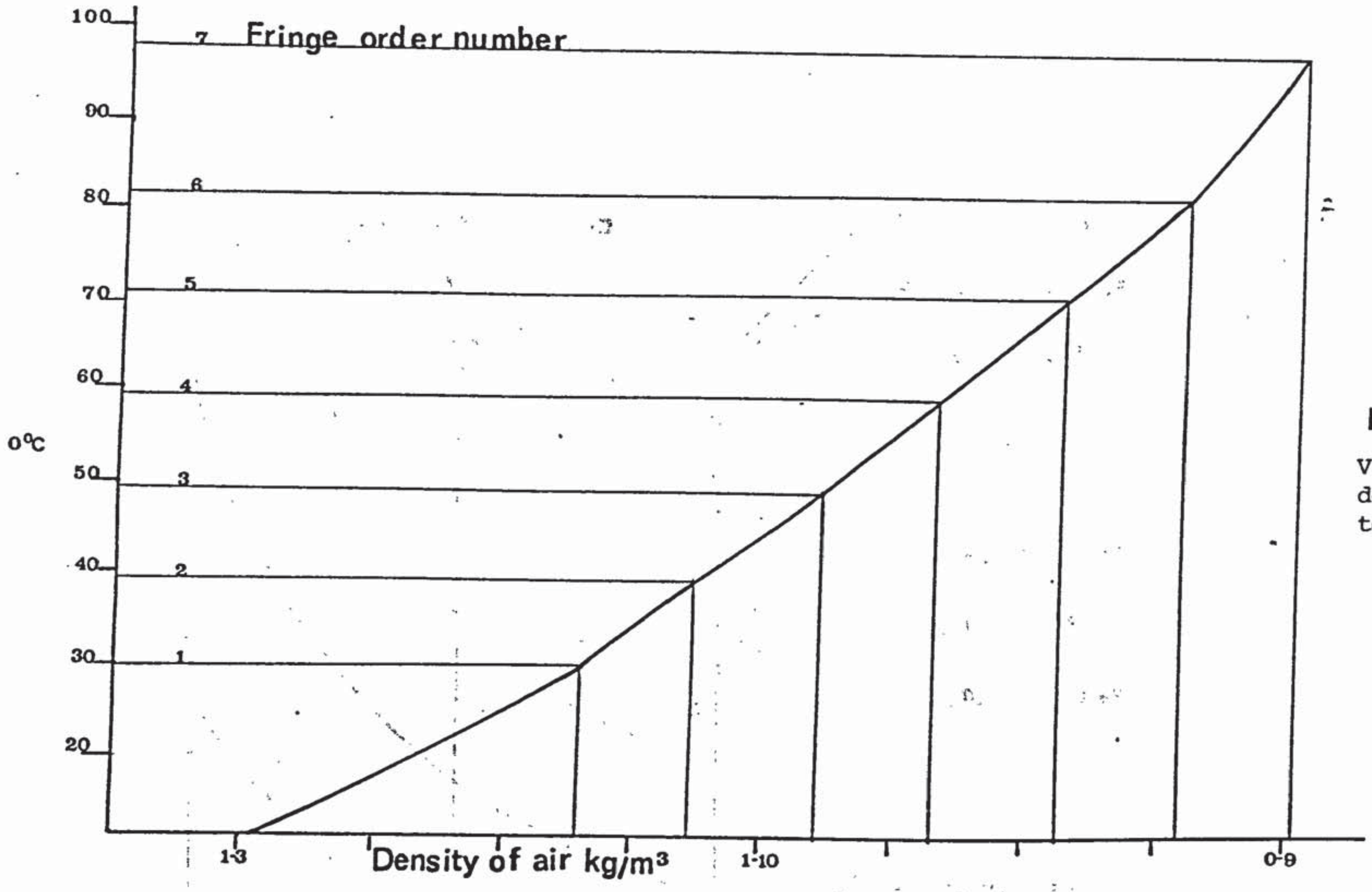

DIA (A.2)

Variation of air
density with
temperature

DIA. (A.3)

TEMPERATURE FIELD

ON PLANE A.

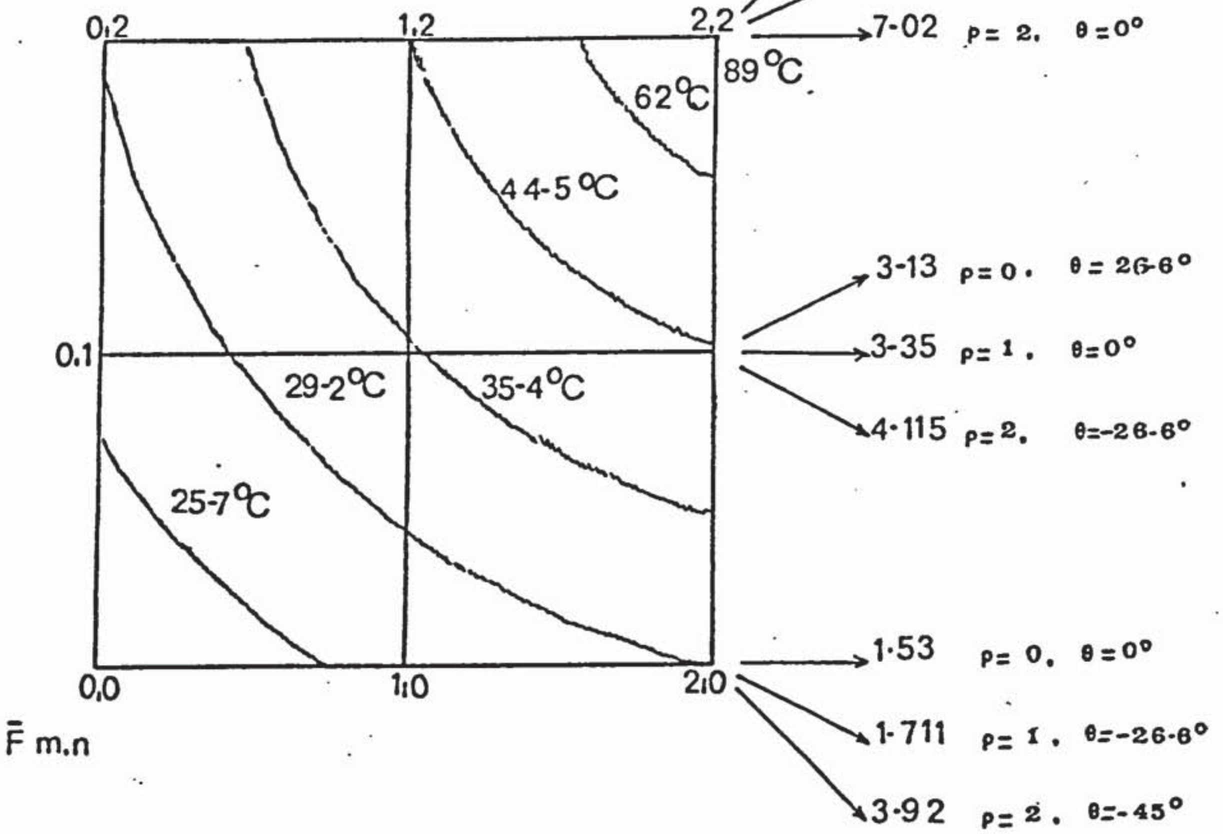

The number refers to the fringe number value of a ray travelling through the field originating at the point F(o,ρ). θ is the angle of view made with respect to the F(m, n) plane.

DIA_ (A.4) Frequency plane reconstruction technique

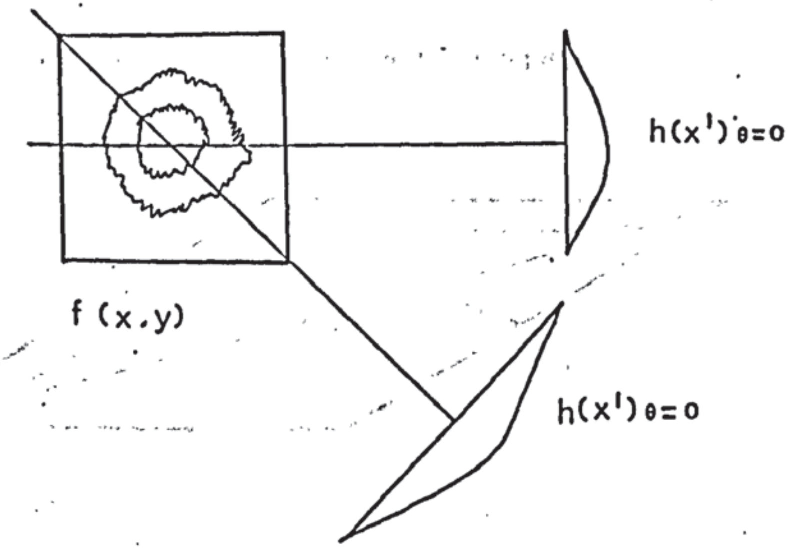

Projection of f(x,y) in the x' direction.

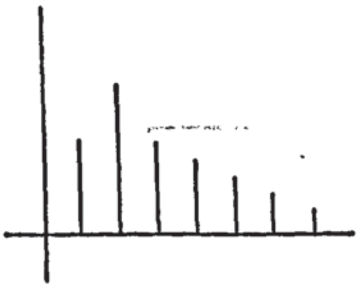

Fourier coefficients of h(x').

DIA (A.5)

Frequency plane reconstruction technique

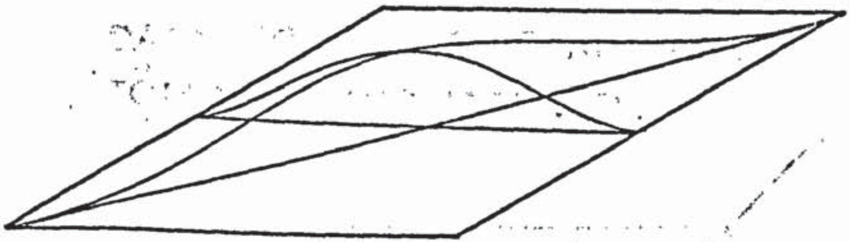

Reconstruction of f(x,y) from fourier plane

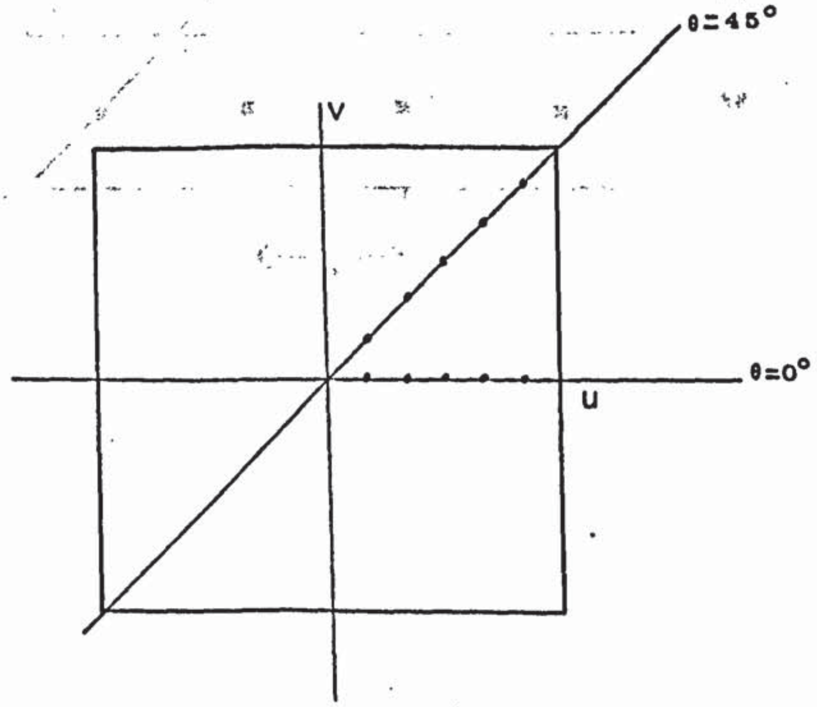

Two dimensional mapping of fourier coefficients

DIA (A.6)

RASTER USED IN THE PREPARTION OF DATA FOR THE SINC, ART AND TOMOGRAPHIC METHOD.

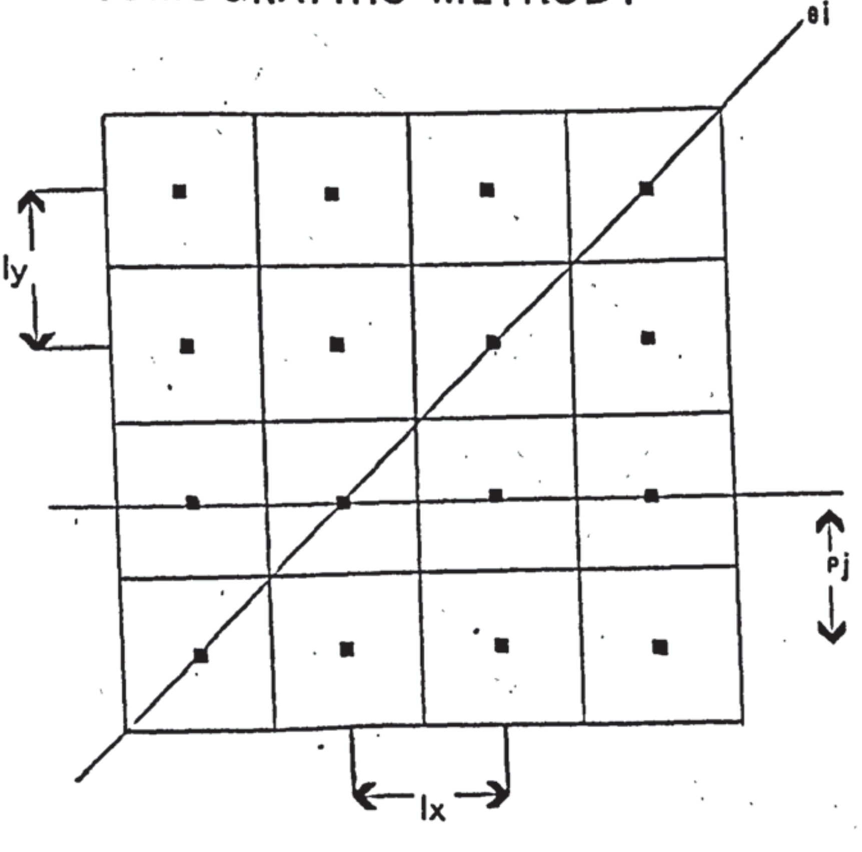

DIA. (A.7)

TEST FIELD FOR TOMOGRAPHIC RECONSTRUCTION

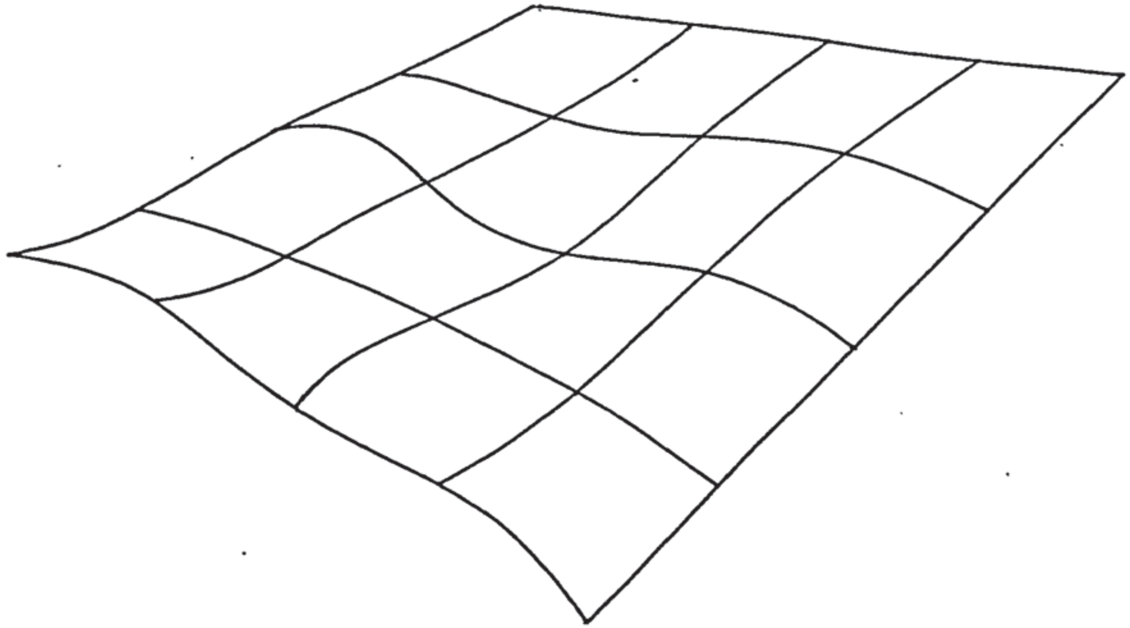

DIA. (A.9)

REFINED RECONSTRUCTION.

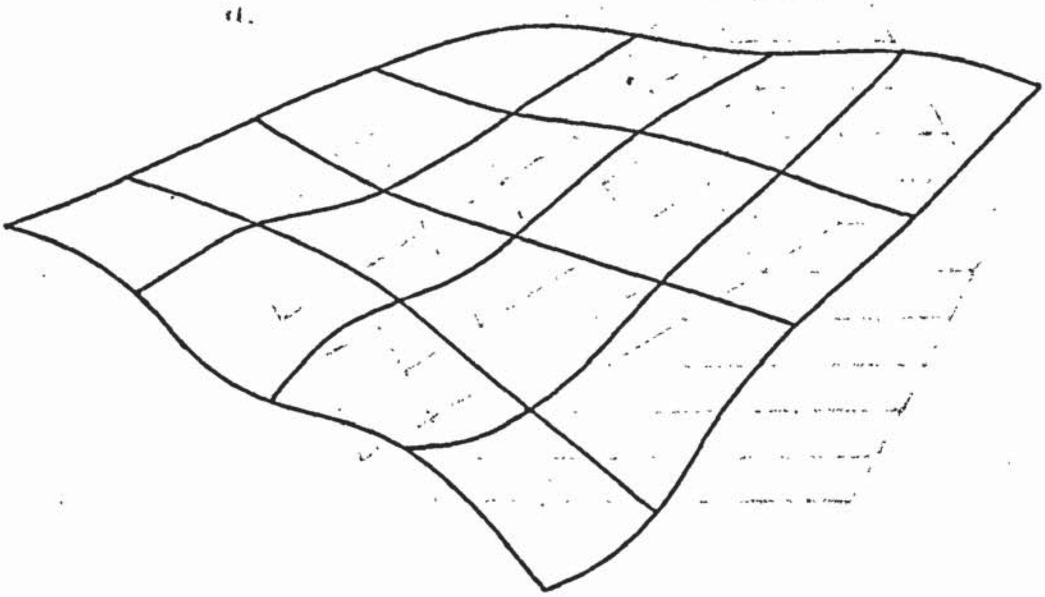

DIA. (A.8)

RECONSTRUCTION OF FIELD

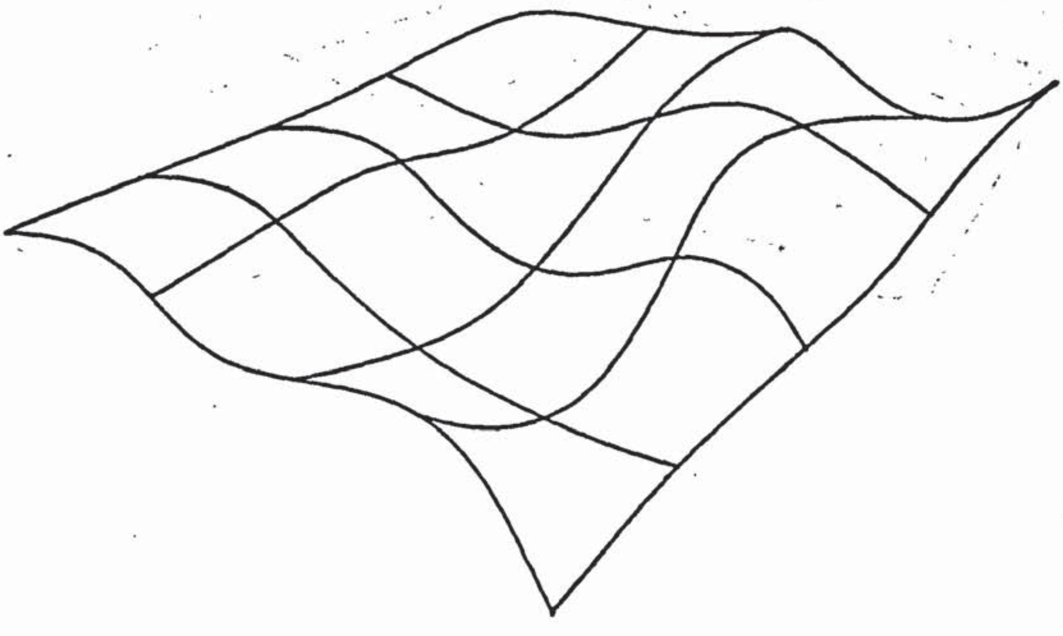

DIA. (A.11)

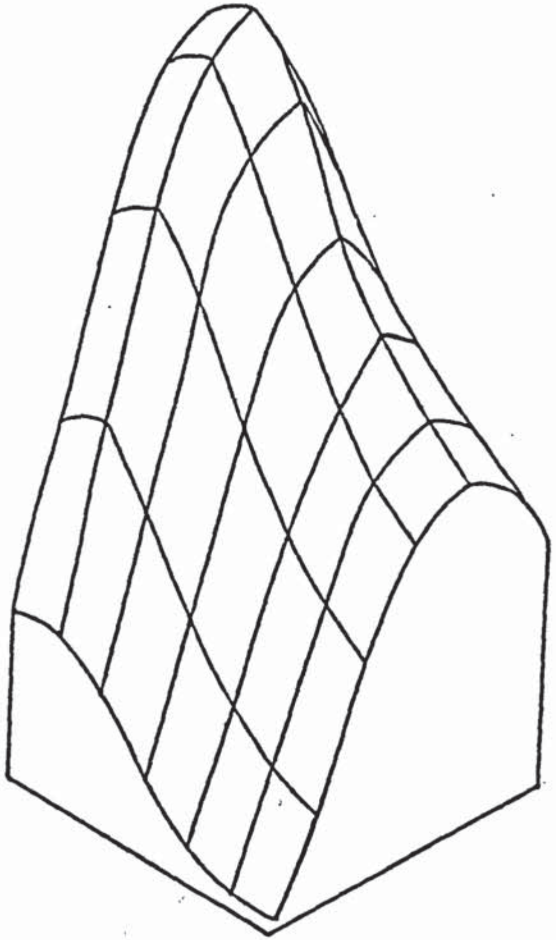

RECONSTRUCTED FIELD BY

SINC METHOD 15% error in field

DIA.. (A.10)

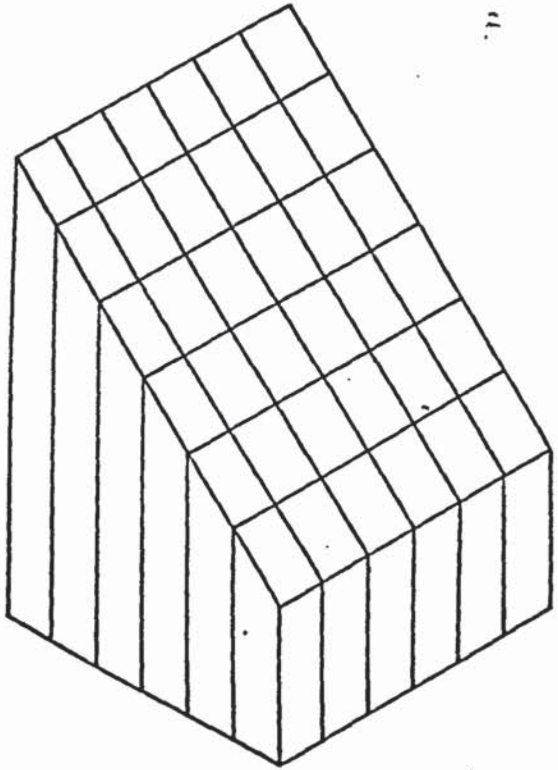

SIMULATED INPUT FIELD FOR

SINC METHOD

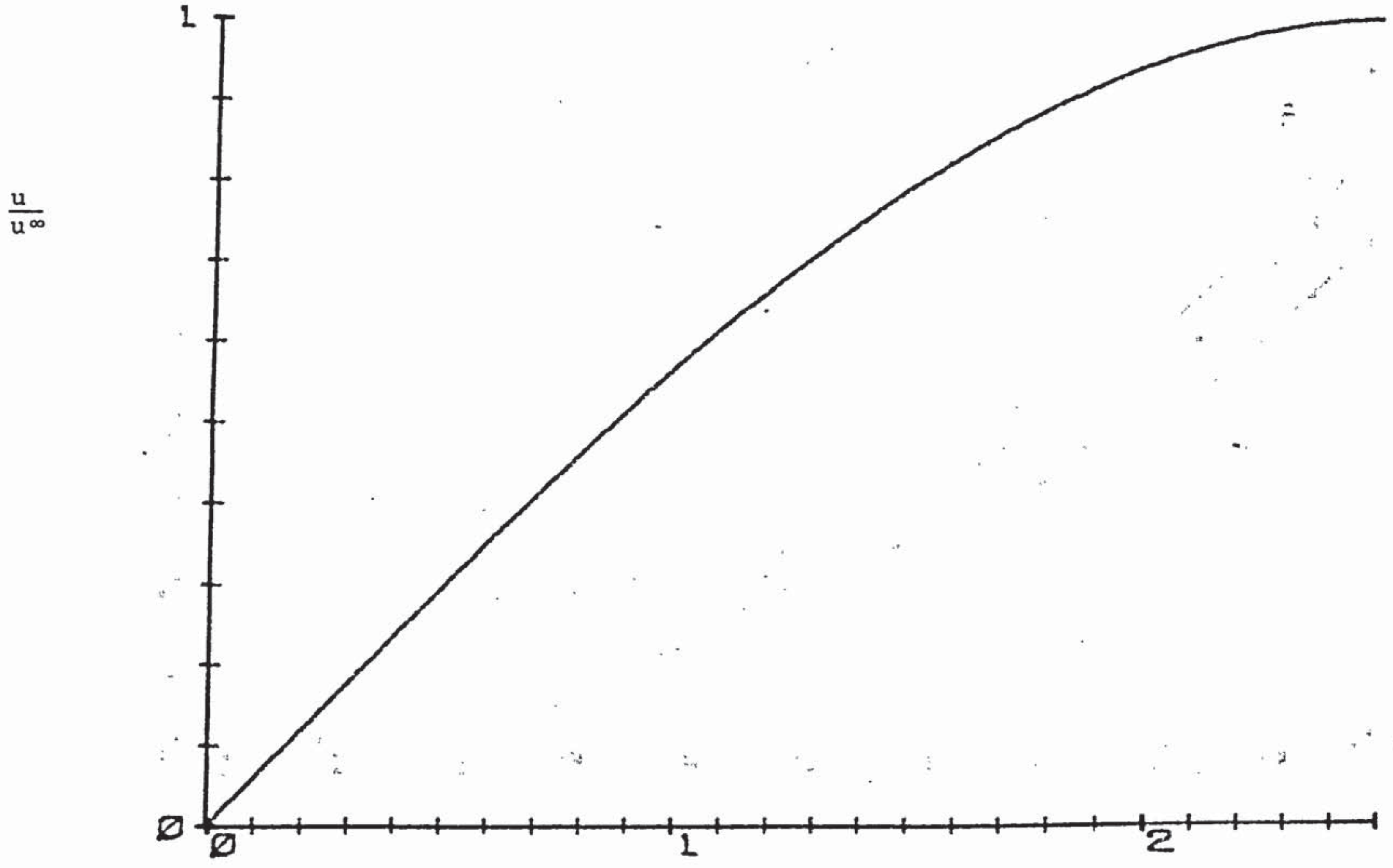

PLOT (A.1) Velocity profile $\frac{u}{u\infty}$ calculated using Blasius similarity variable for the distribution within a boundary layer for a flat plate at a zero angle of attack.

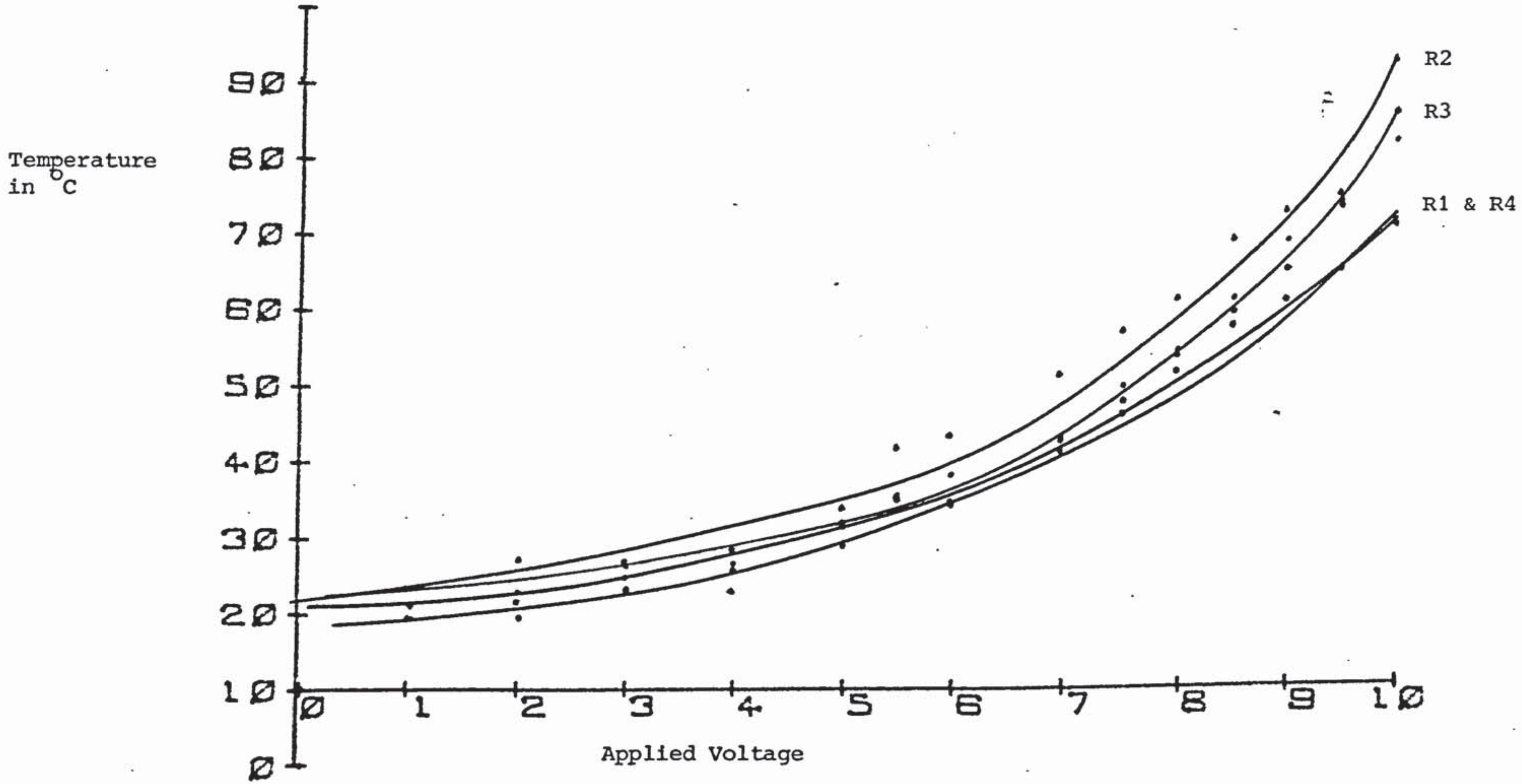

PLOT (A.2) Plot of four trail nickel strips, temperature against applied voltage.

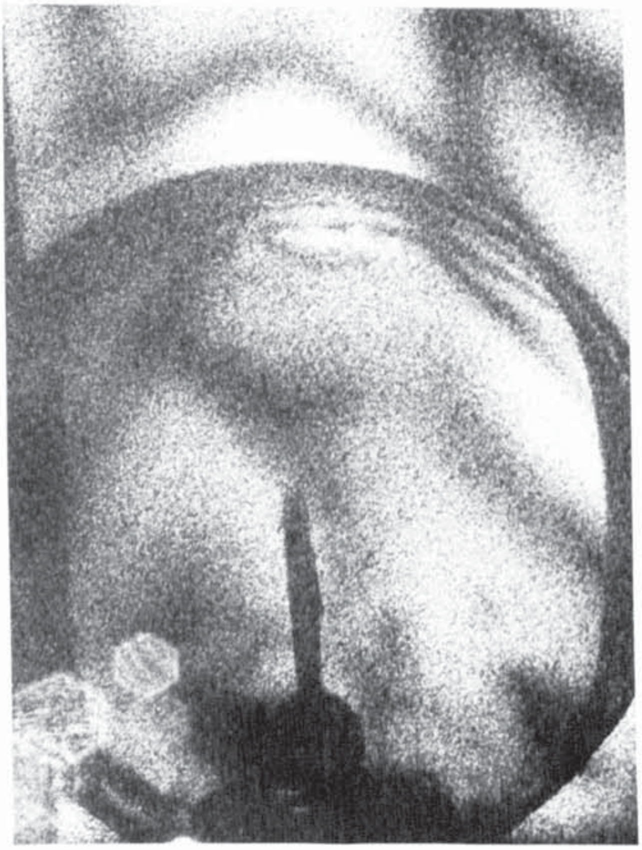

Figure 1 Early double exposure hologram made using a light bulb as an object. The fringes represent heating which has occurred between the double exposures

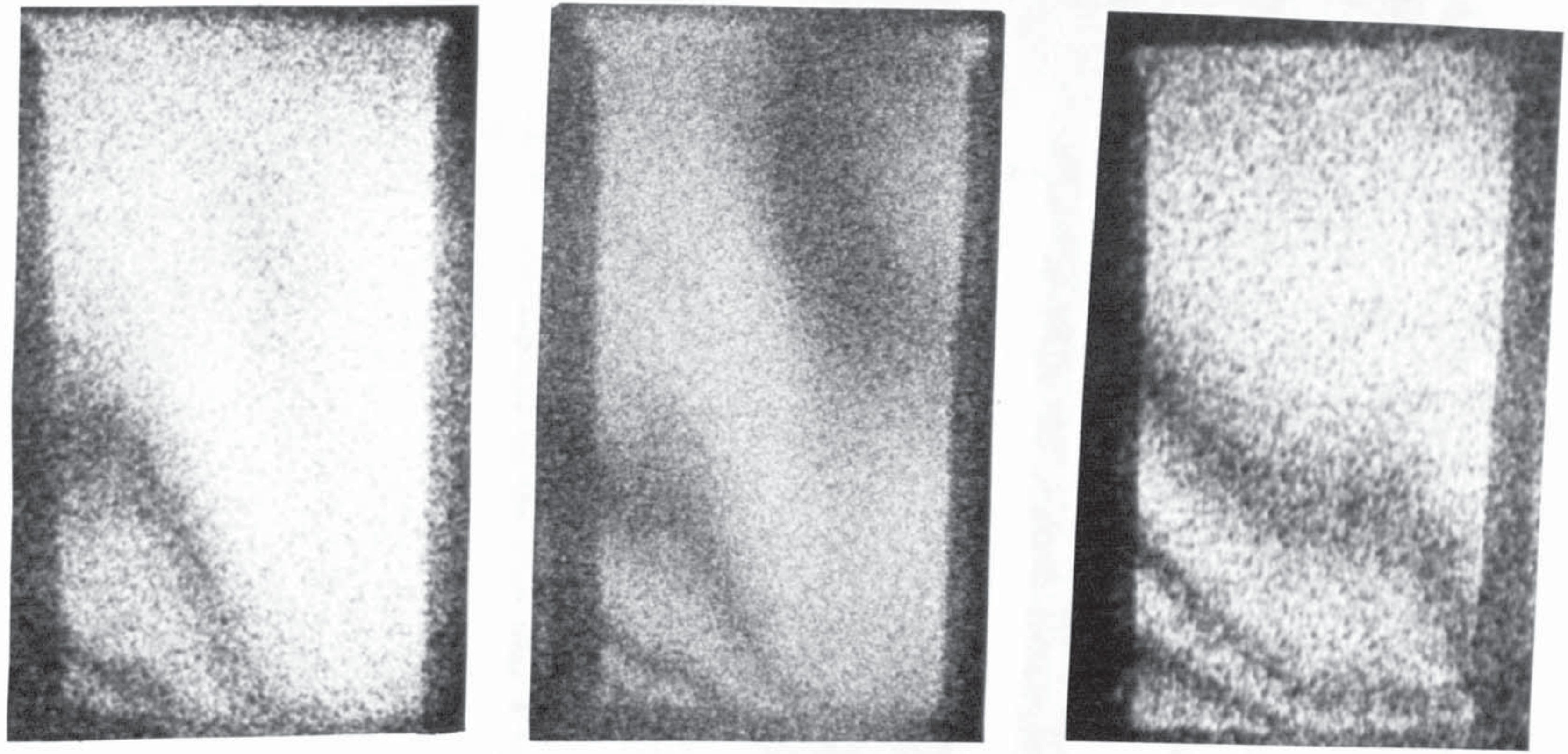

a b c

Figure 2 Examples of Early Double Exposure Holograms.
Three constructions of the same hologram made at different viewing angles. a -12°, b 0°, c $+12^{\circ}$.

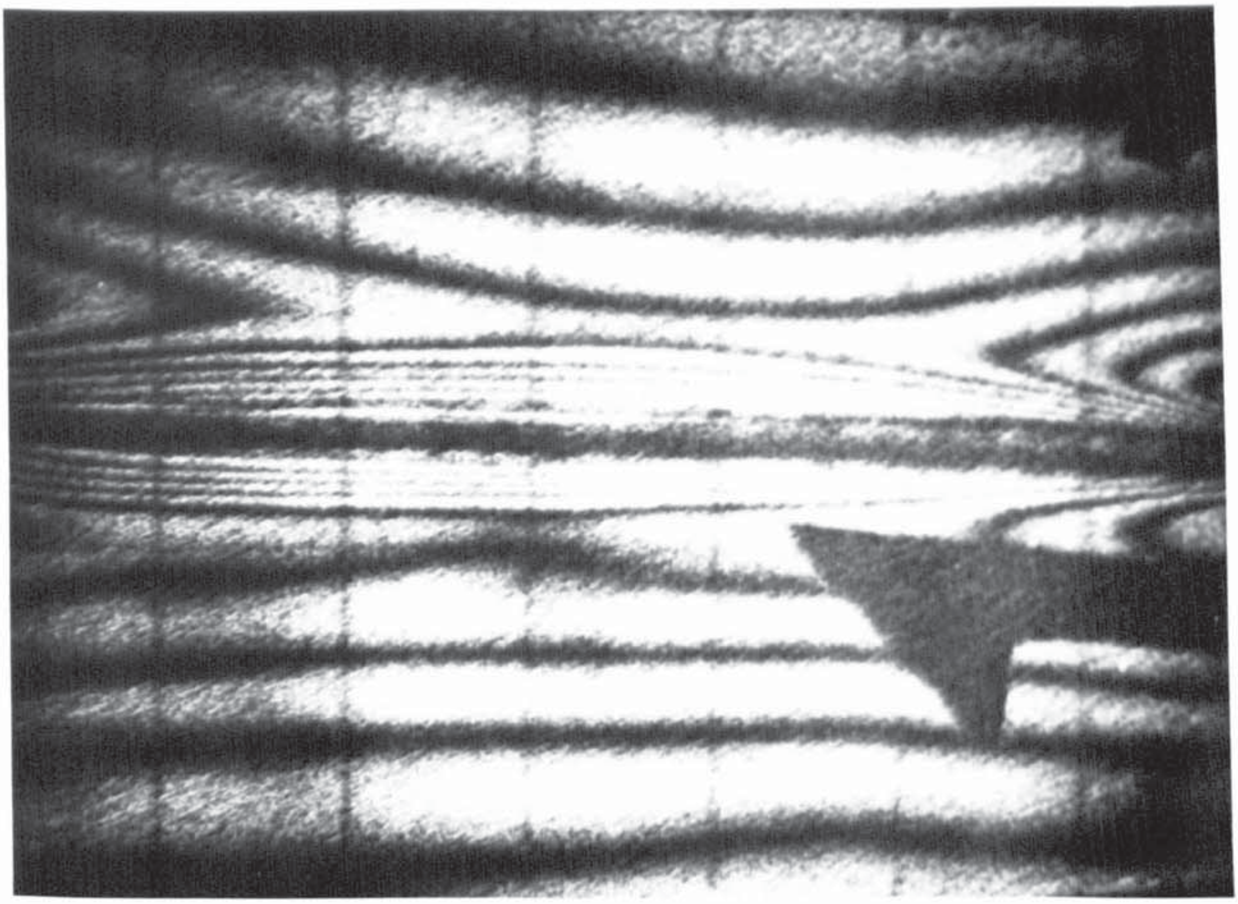

Figure 3 Example of External vibrationally produced fringes superimposed on the flow over a flat plate.

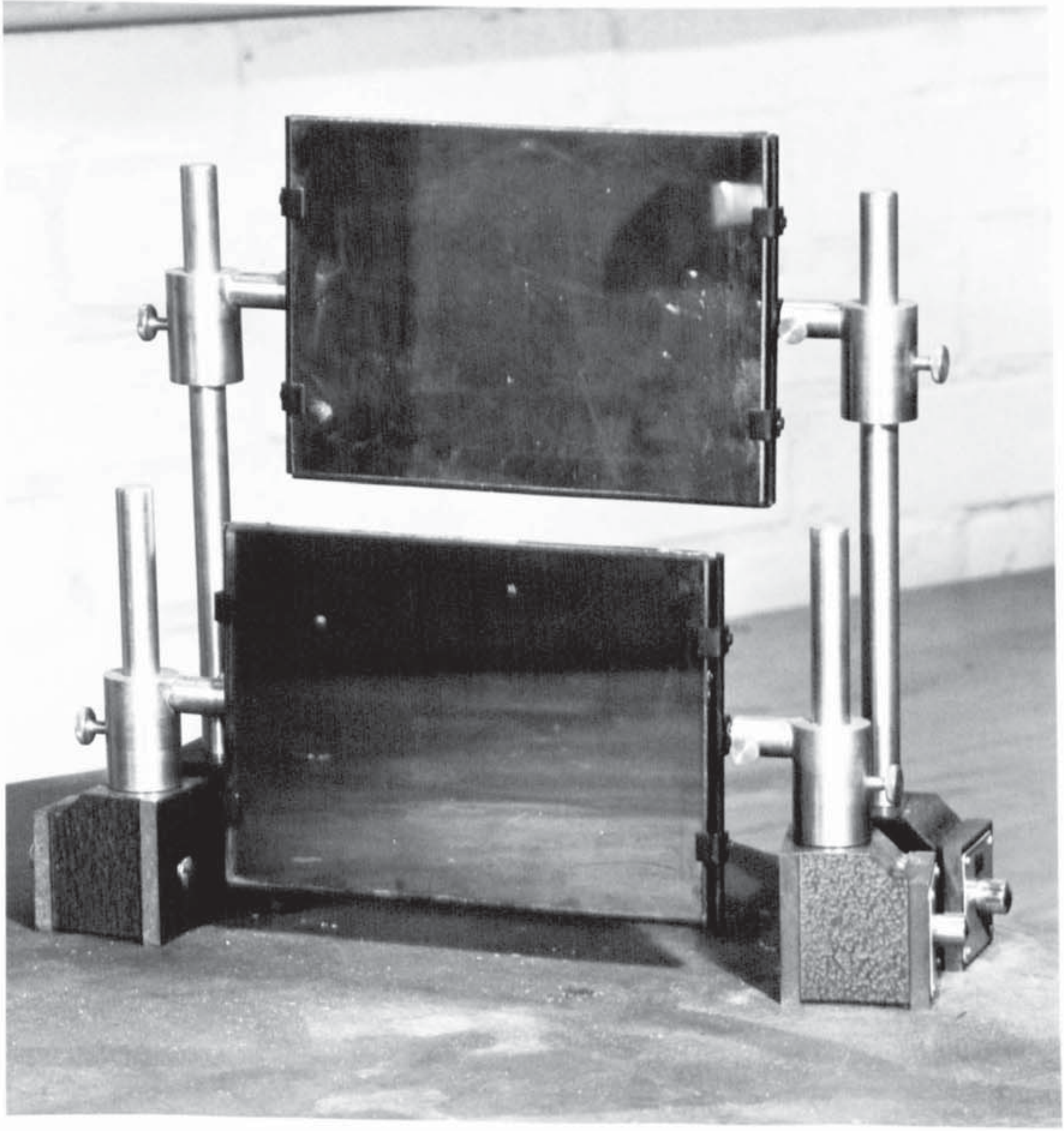

Figure 4 Beam Splitting Mirror Assembly

Fig. 5 Diffuser

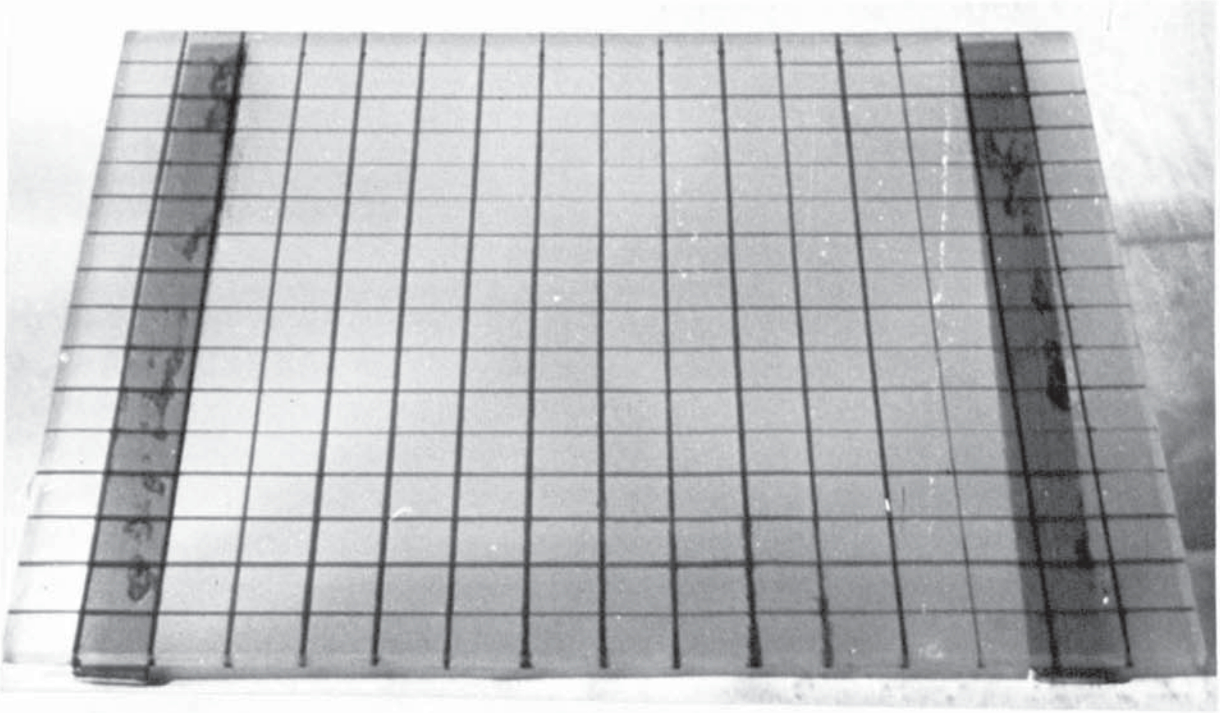

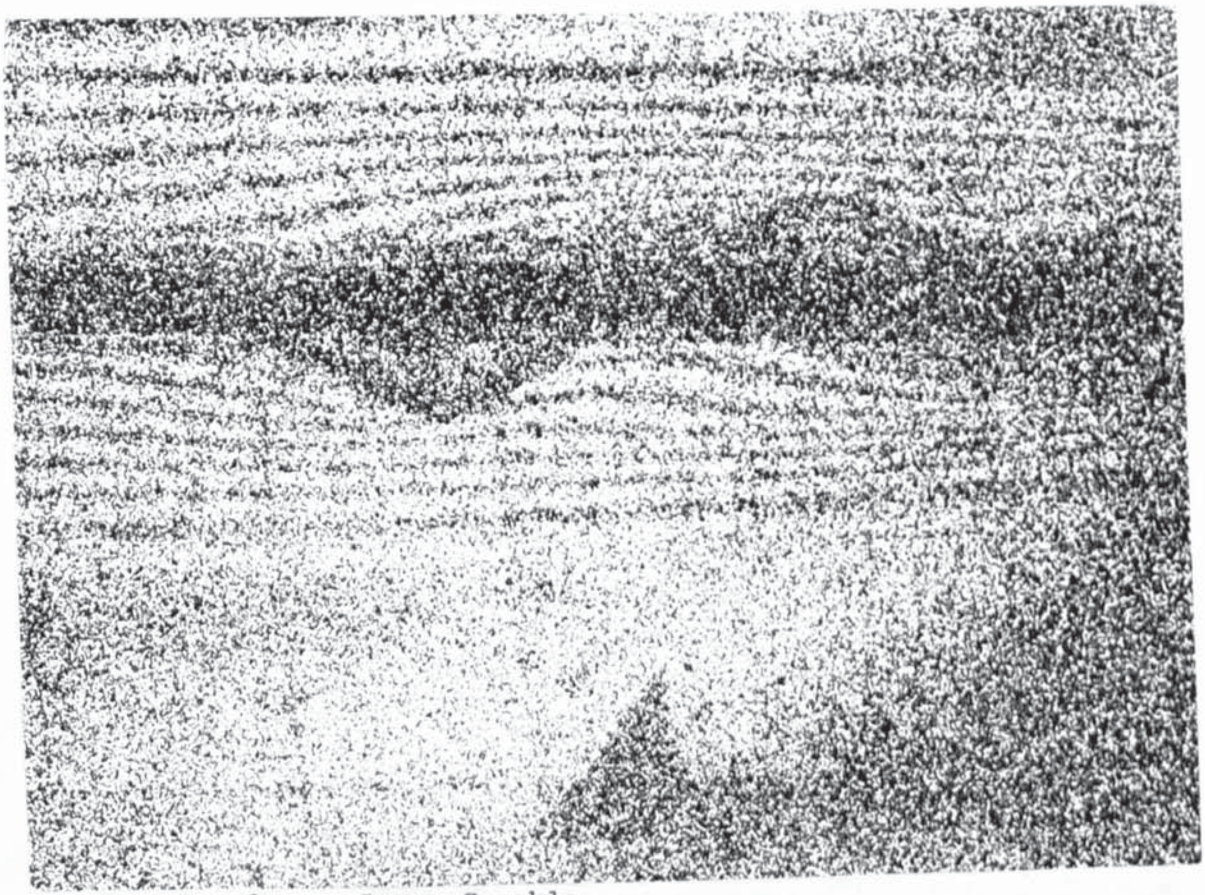

Fig. 6a.   Large Speckle

Fig. 6b.   Out of Focus

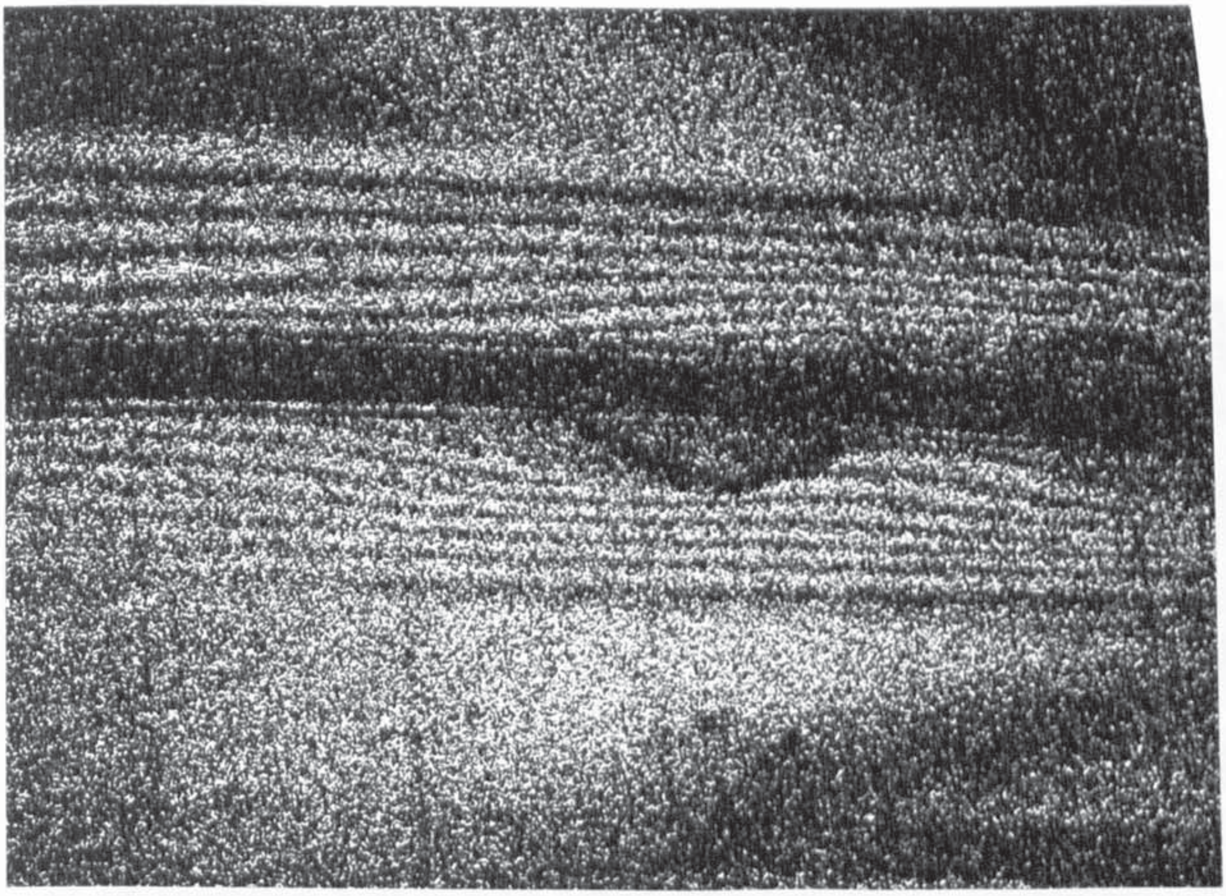

Figure 7 Real Image Reconstruction of Dimple Shape. (Airspeed = 0.609 m/sec.

Fig. 8 Louvre sample mounted in free standing unit

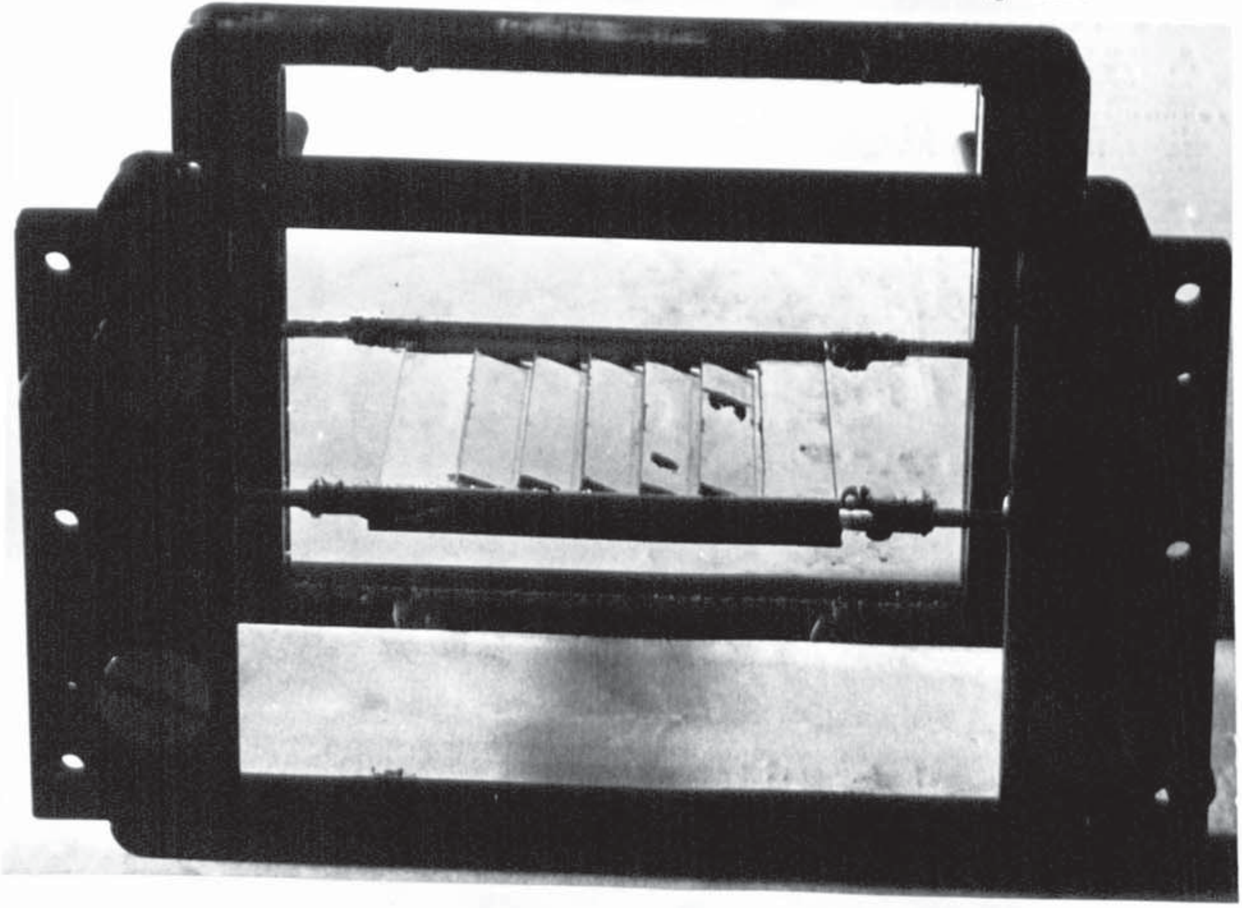

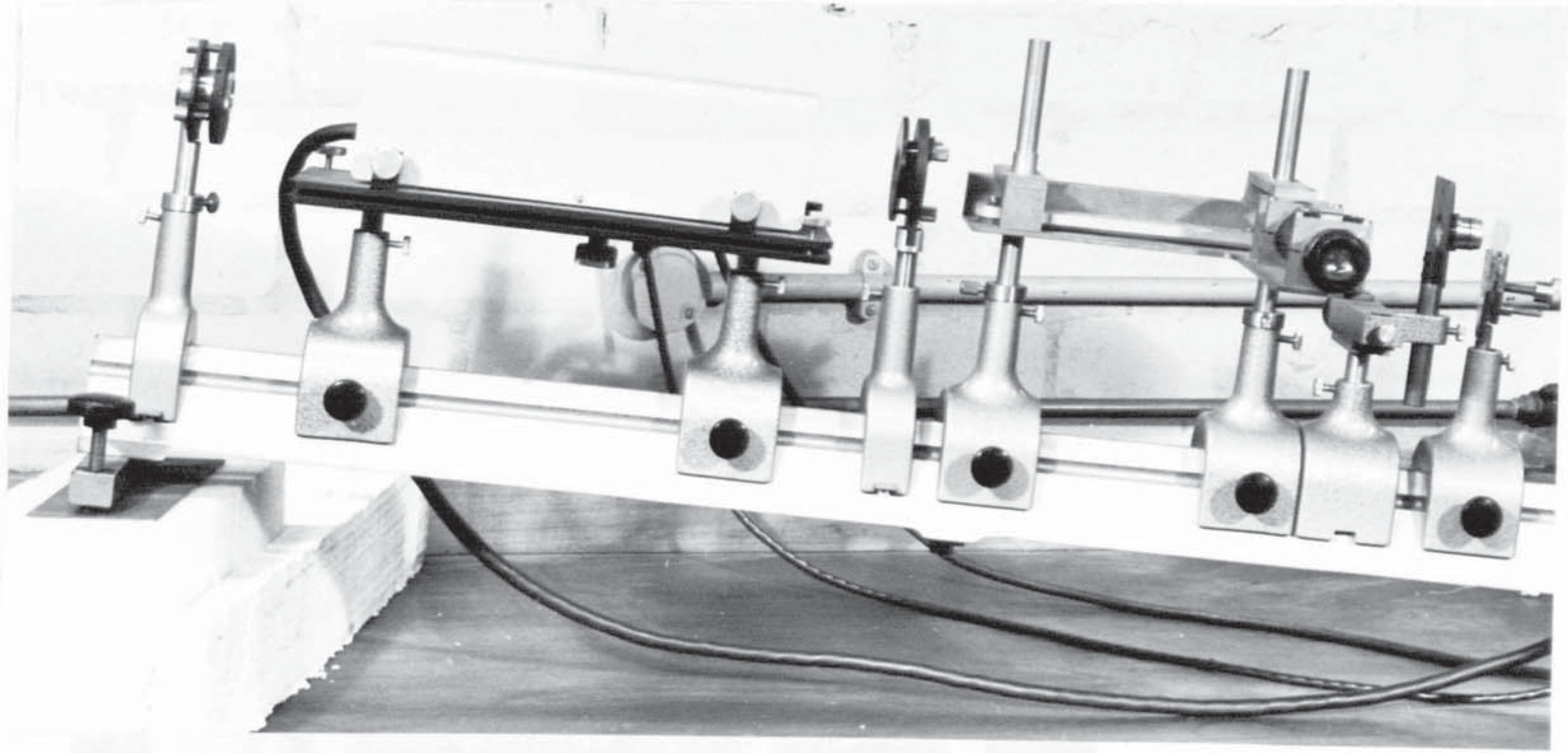

Fig. 9 Telescope alignment system for pulse laser

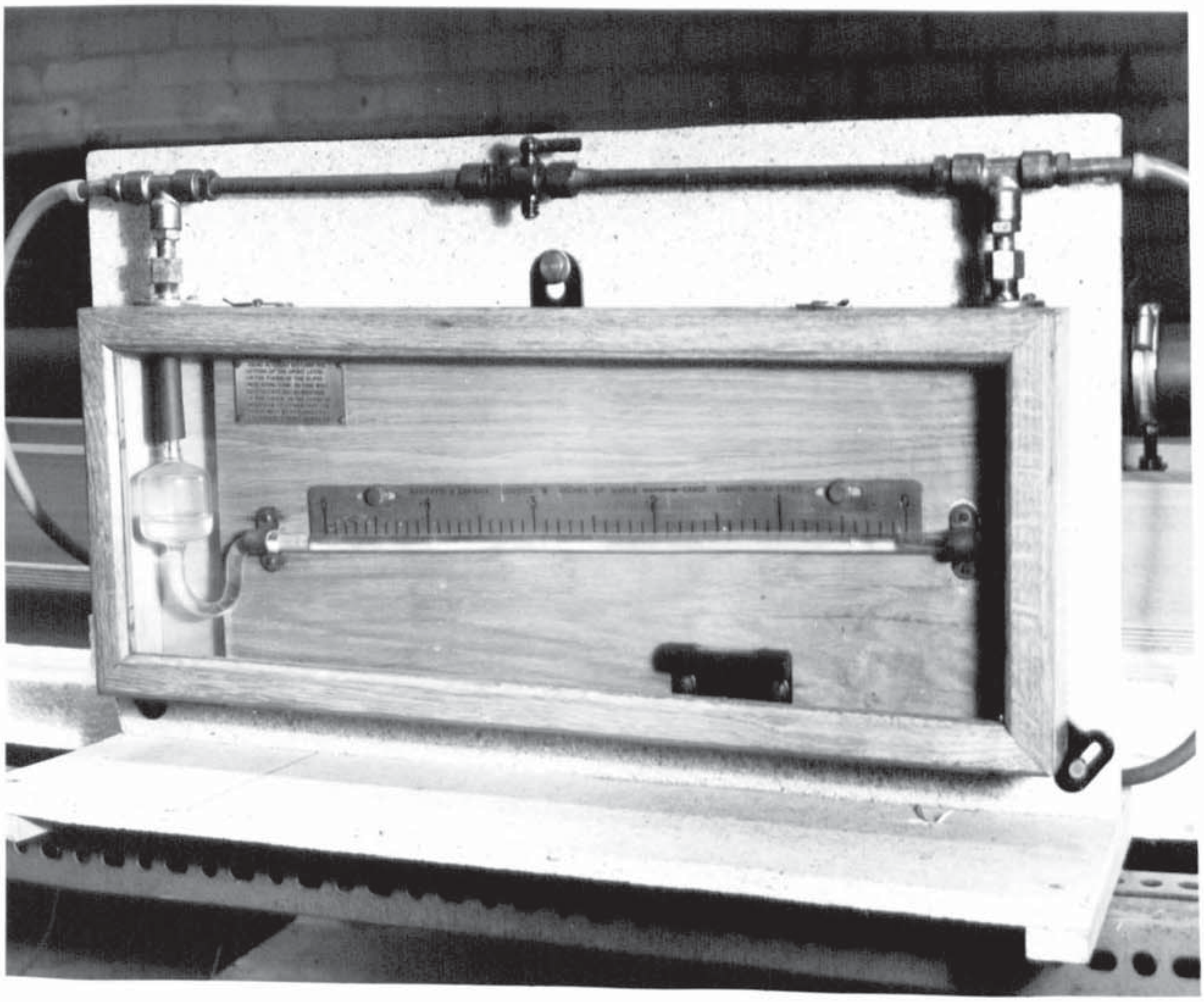

Figure 10 Manometer for Airflow Velocity Determination

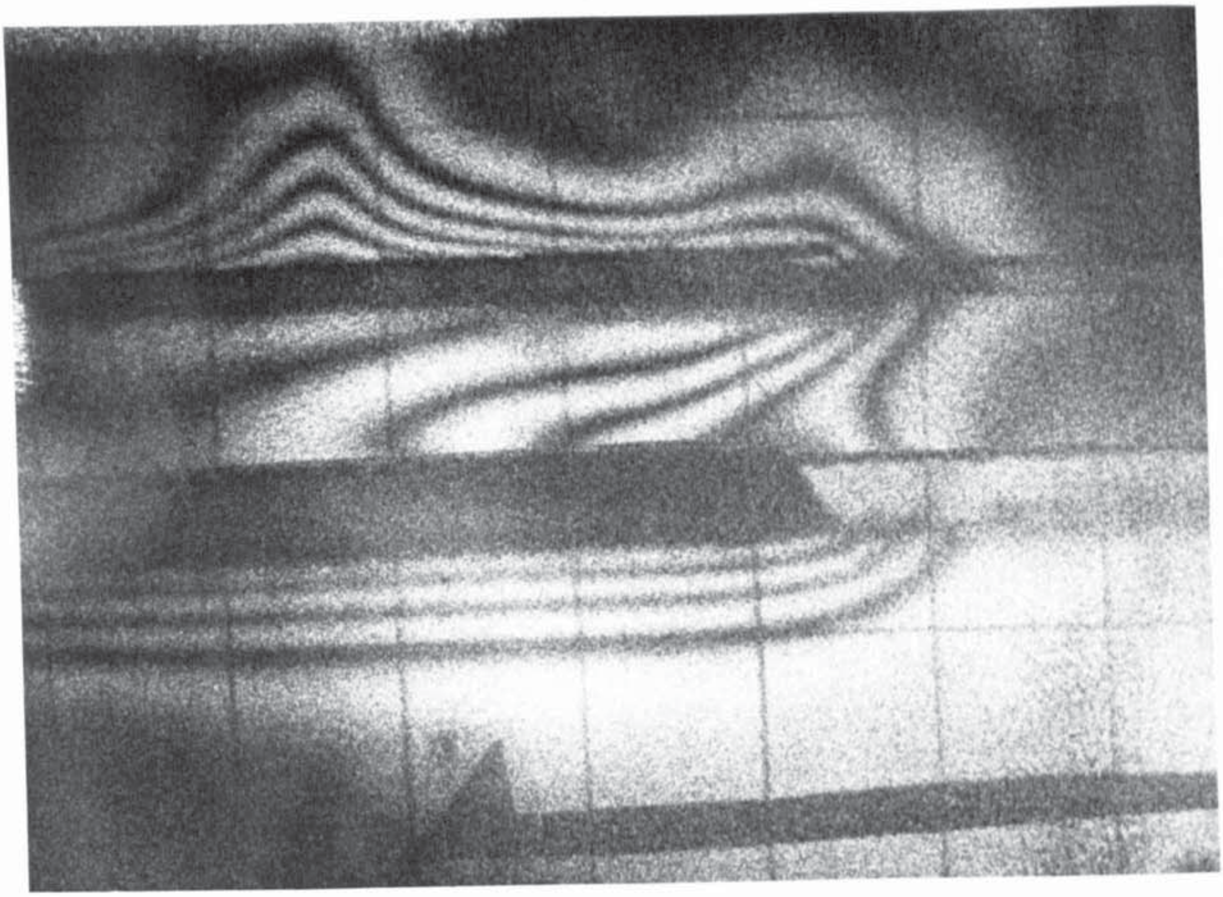

Figure 11a Natural Convection around a flat plate

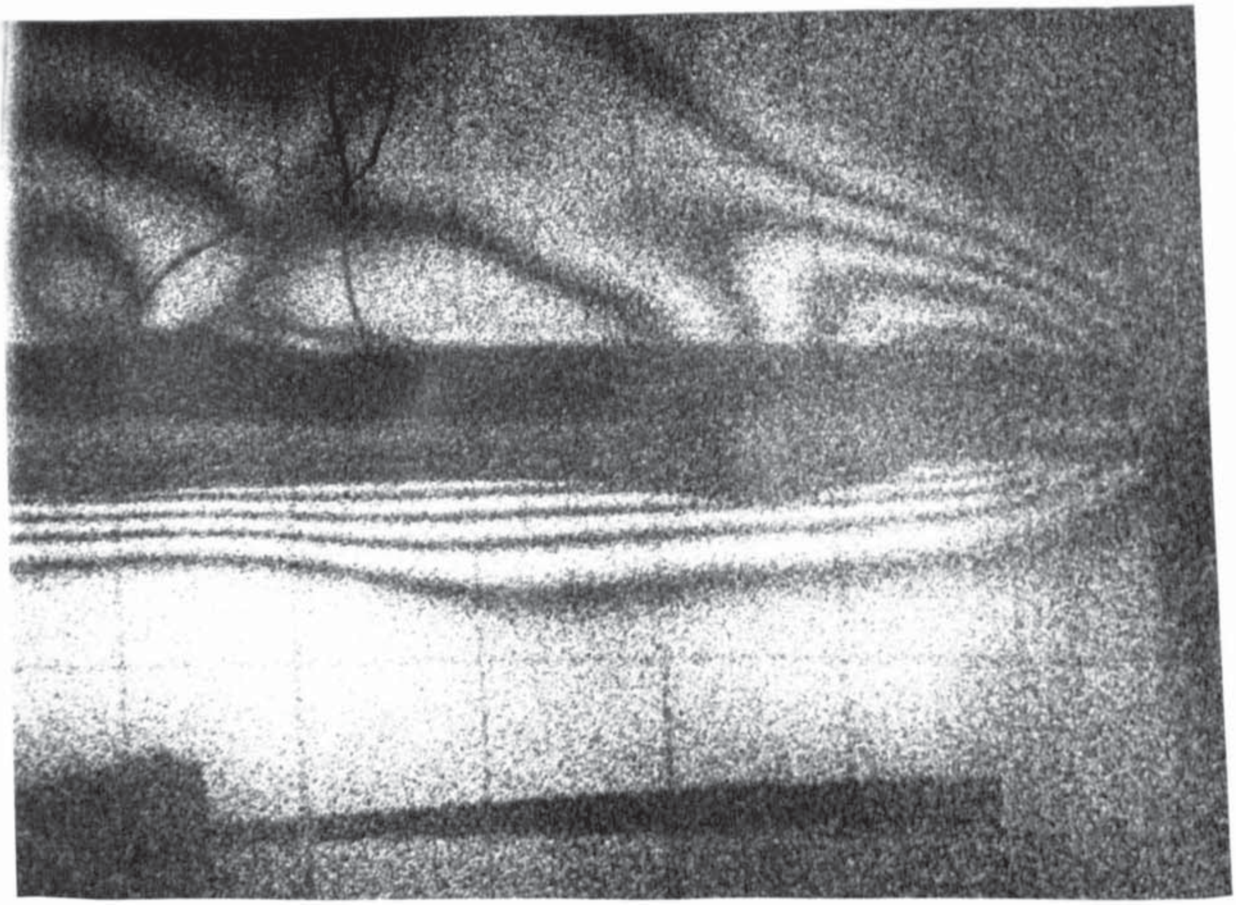

Figure 11b Natural Convection around a pair of parallel flat plates 1.27 cm apart.

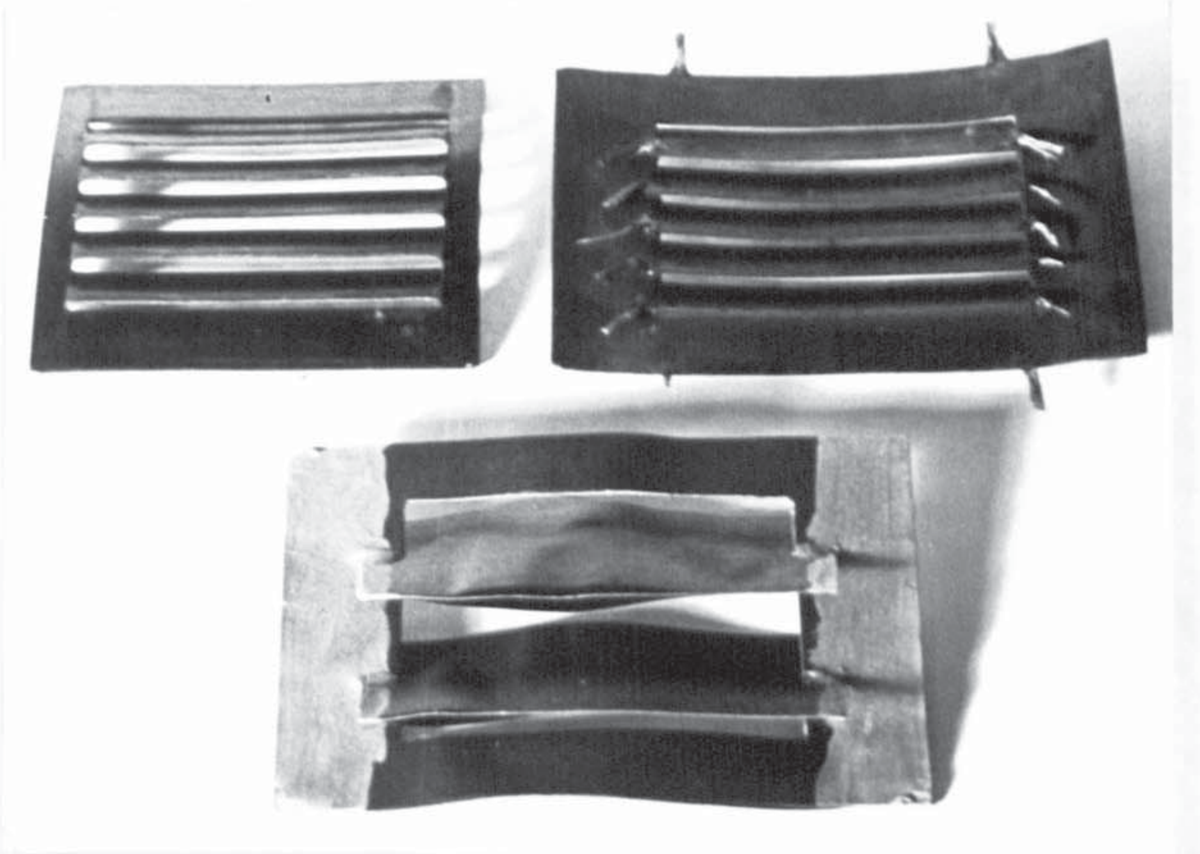

Fig. 13a Resistance paper/epoxy resin sample

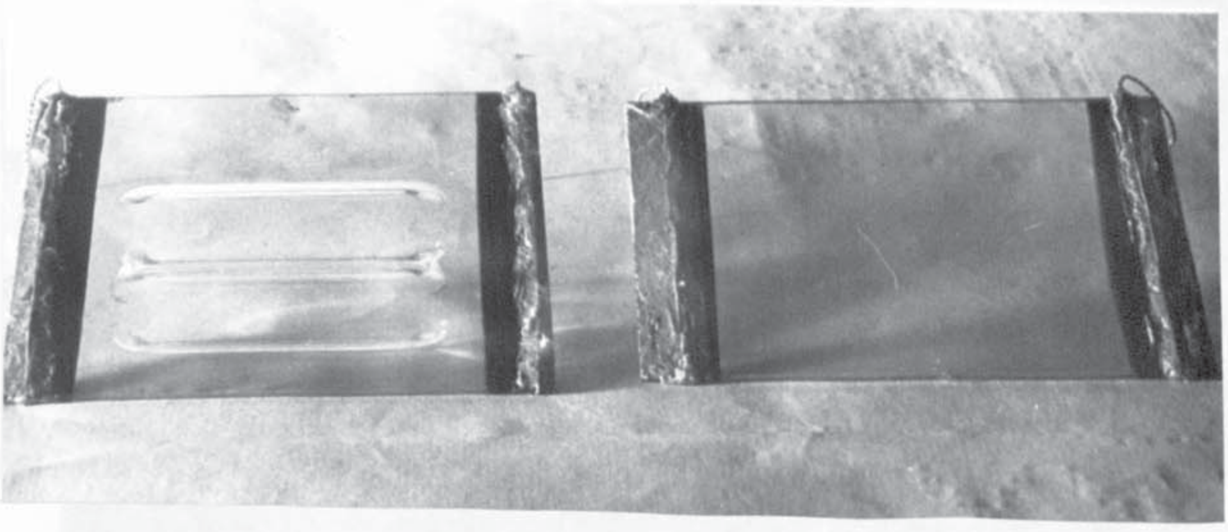

Fig. 13b Dimple sample

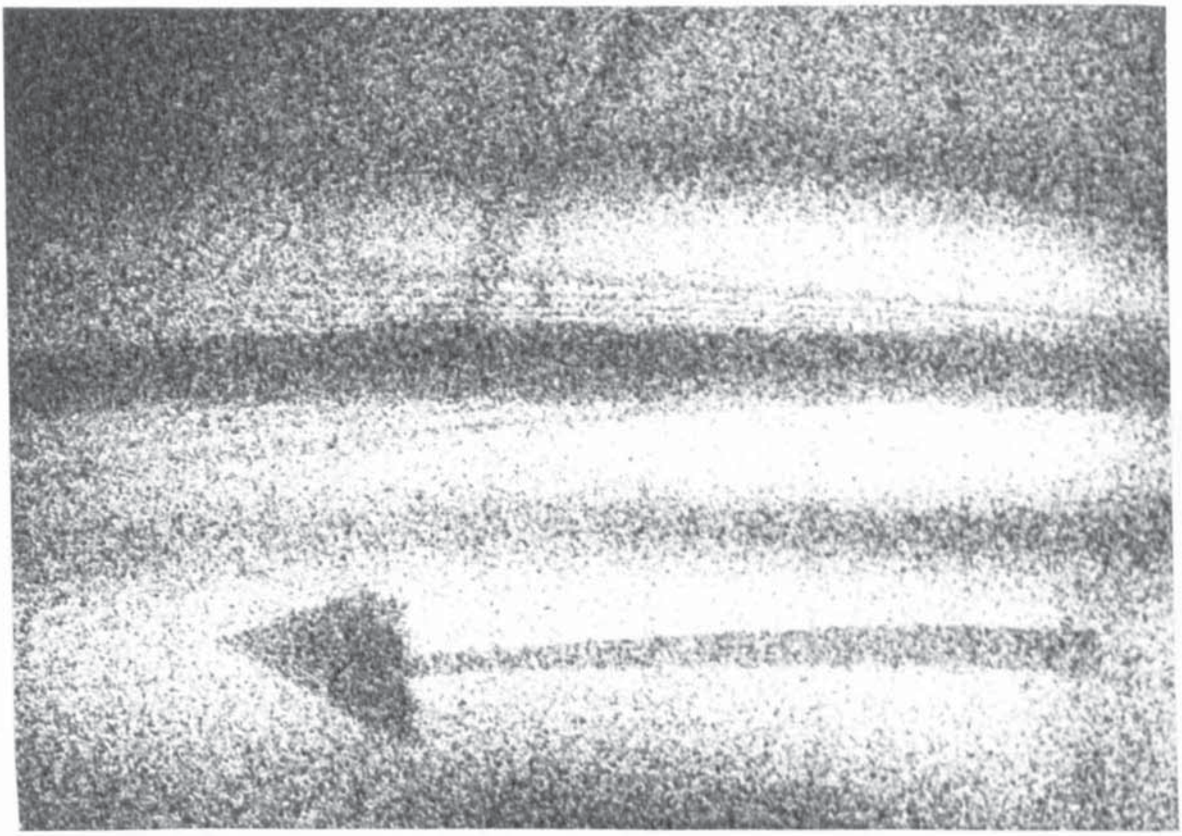

Fig. 14a Flow over flat plate
Airspeed 0.609 mm/sec.

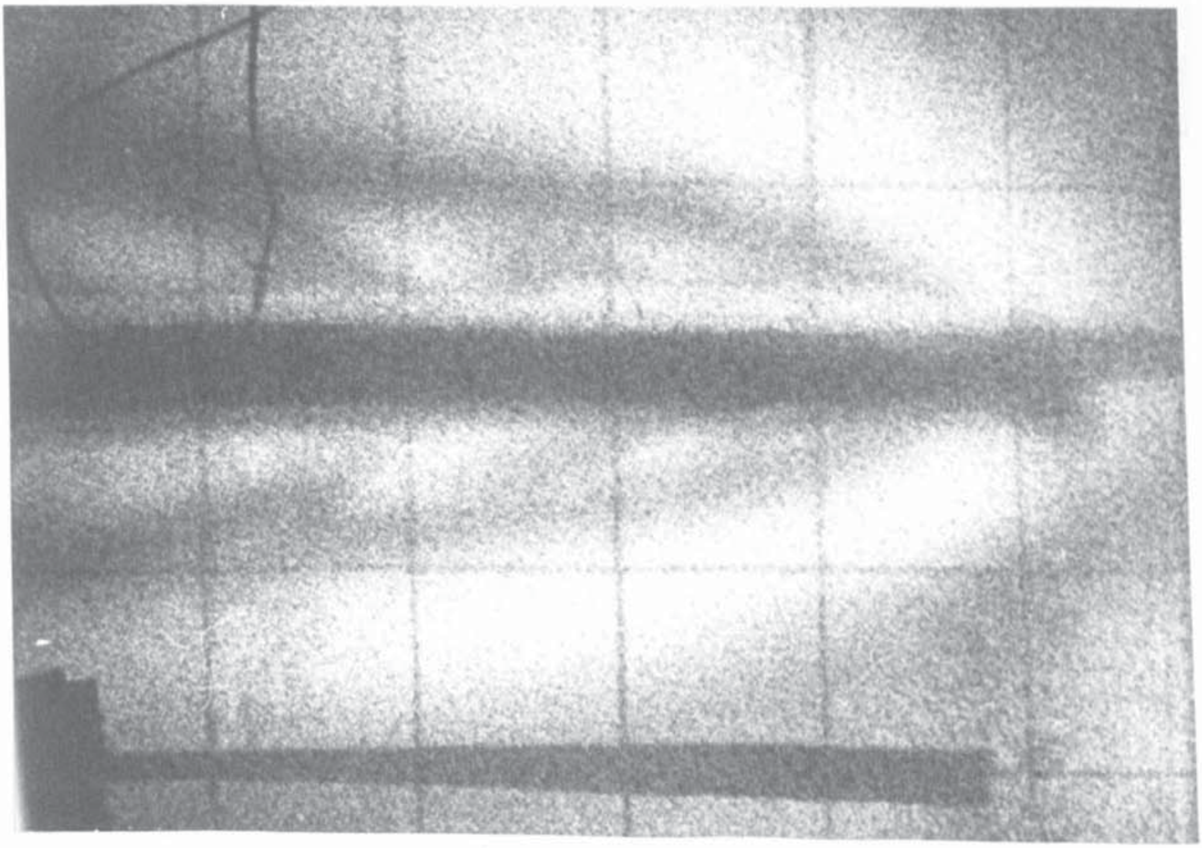

Fig. 14b Flow over flat plate
Airspeed 1.83 m/sec.

Figure 15   Flow between two parallel plates 1.27 cm apart
Airspeed 1.82 m/sec.

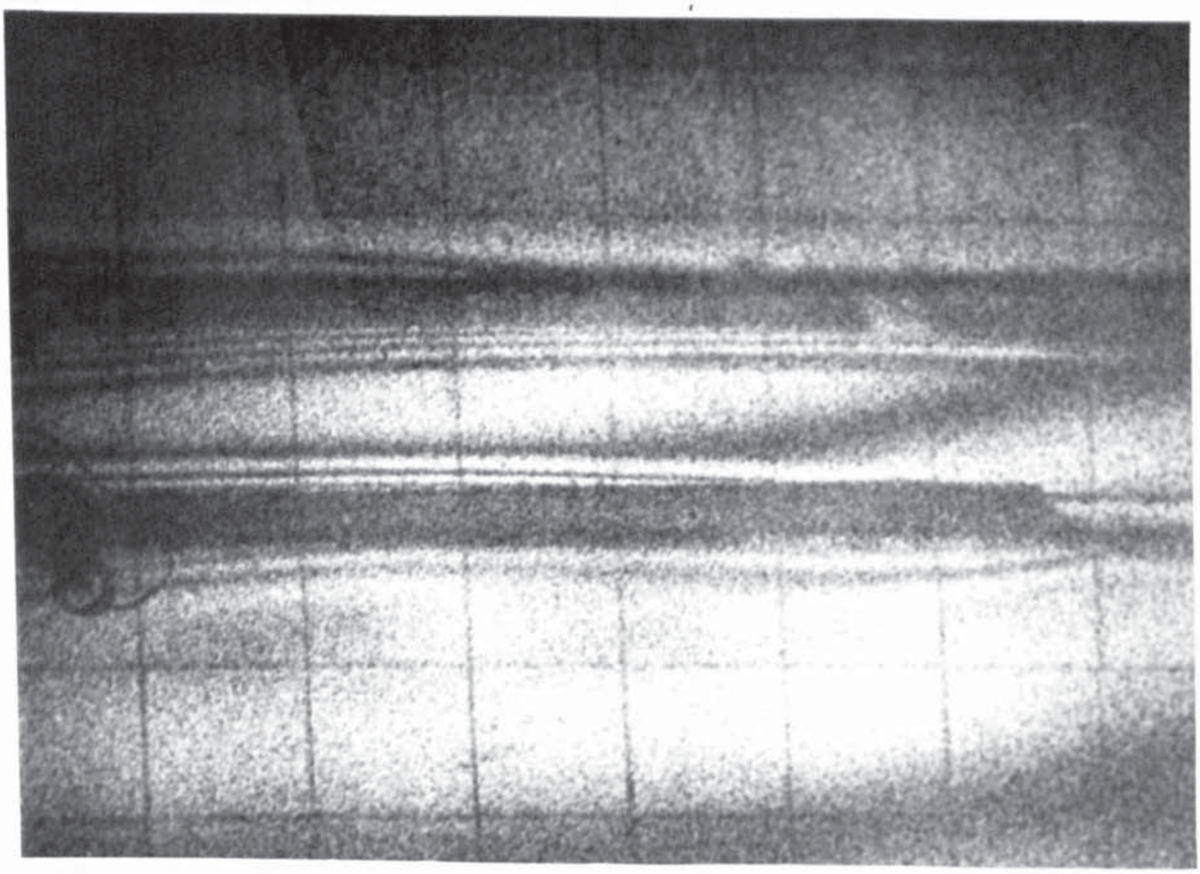

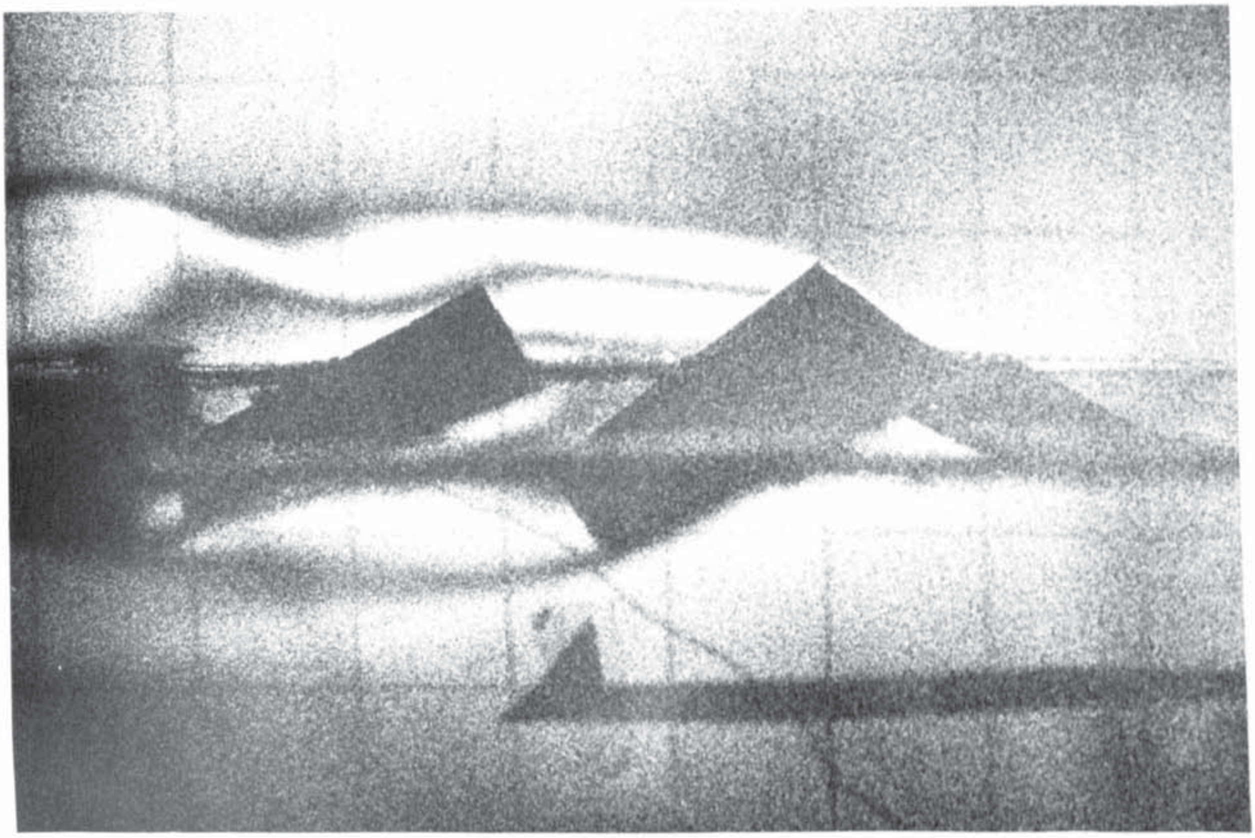

Figure 12 Airflow over fibre louvre sample (Airspeed = 0.608 m/sec.)

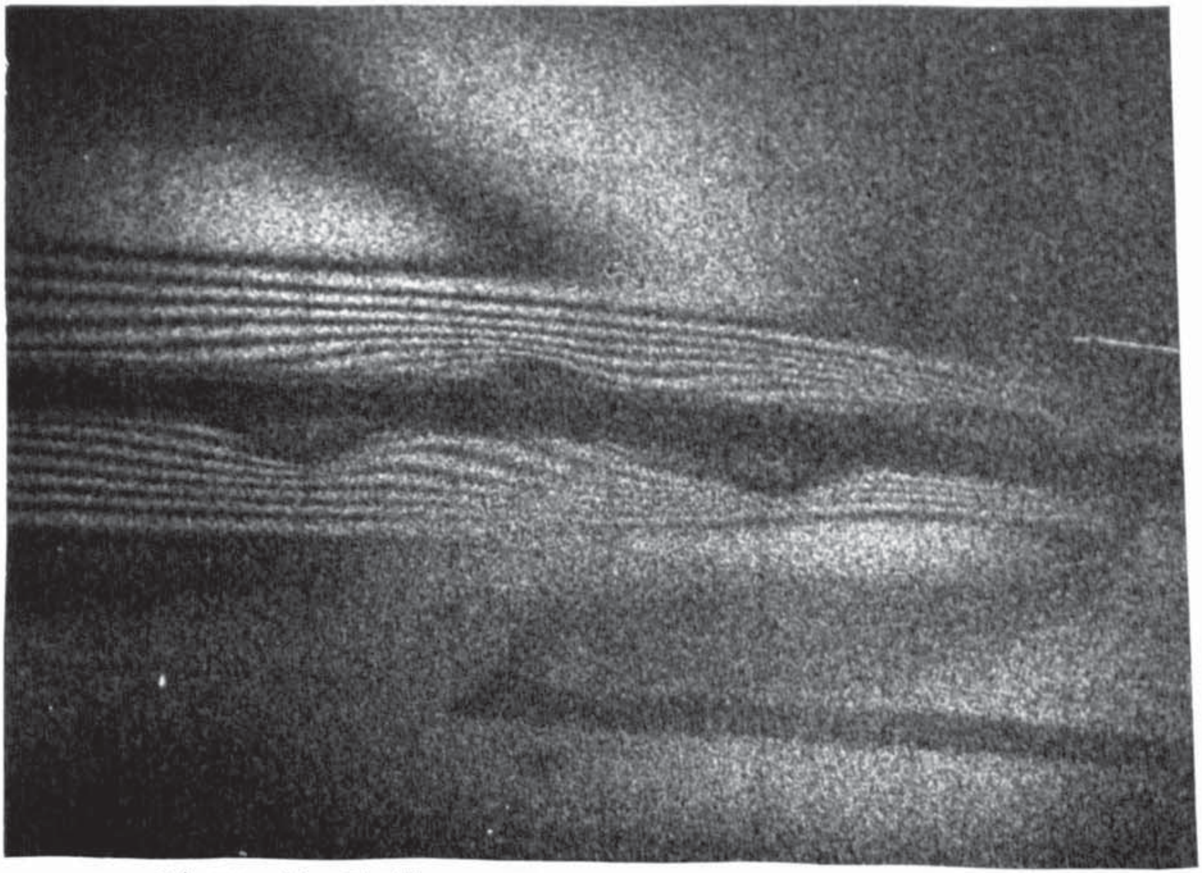

Figure 16 Airflow over rear of dimple sample
(Airspeed = 0.608 m/sec)

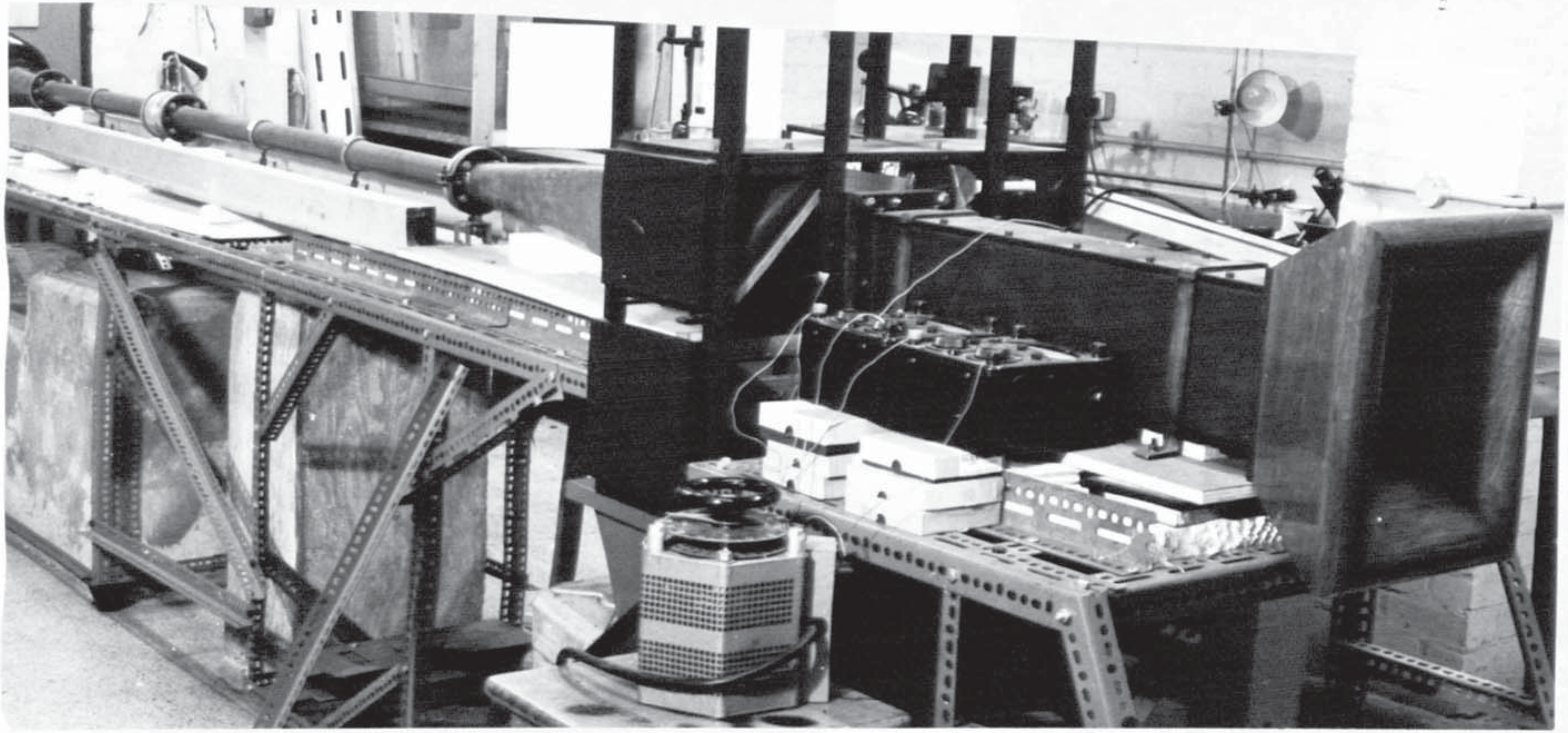

Figure 17 Wind Tunnel and Mach-Zender Interferometric Assembly

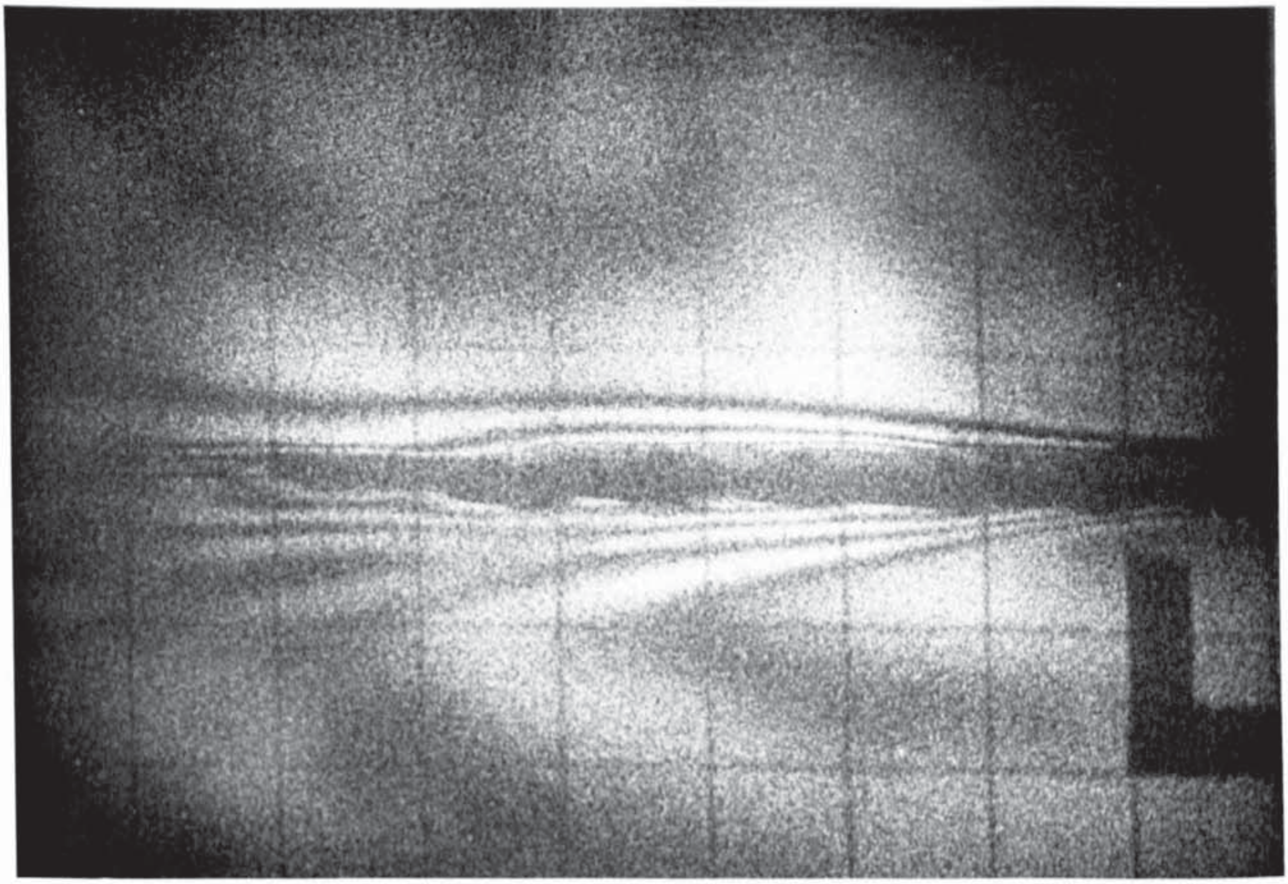

Figure 18 Airflow over louvre sample
(Airflow = 1.83 m/sec'

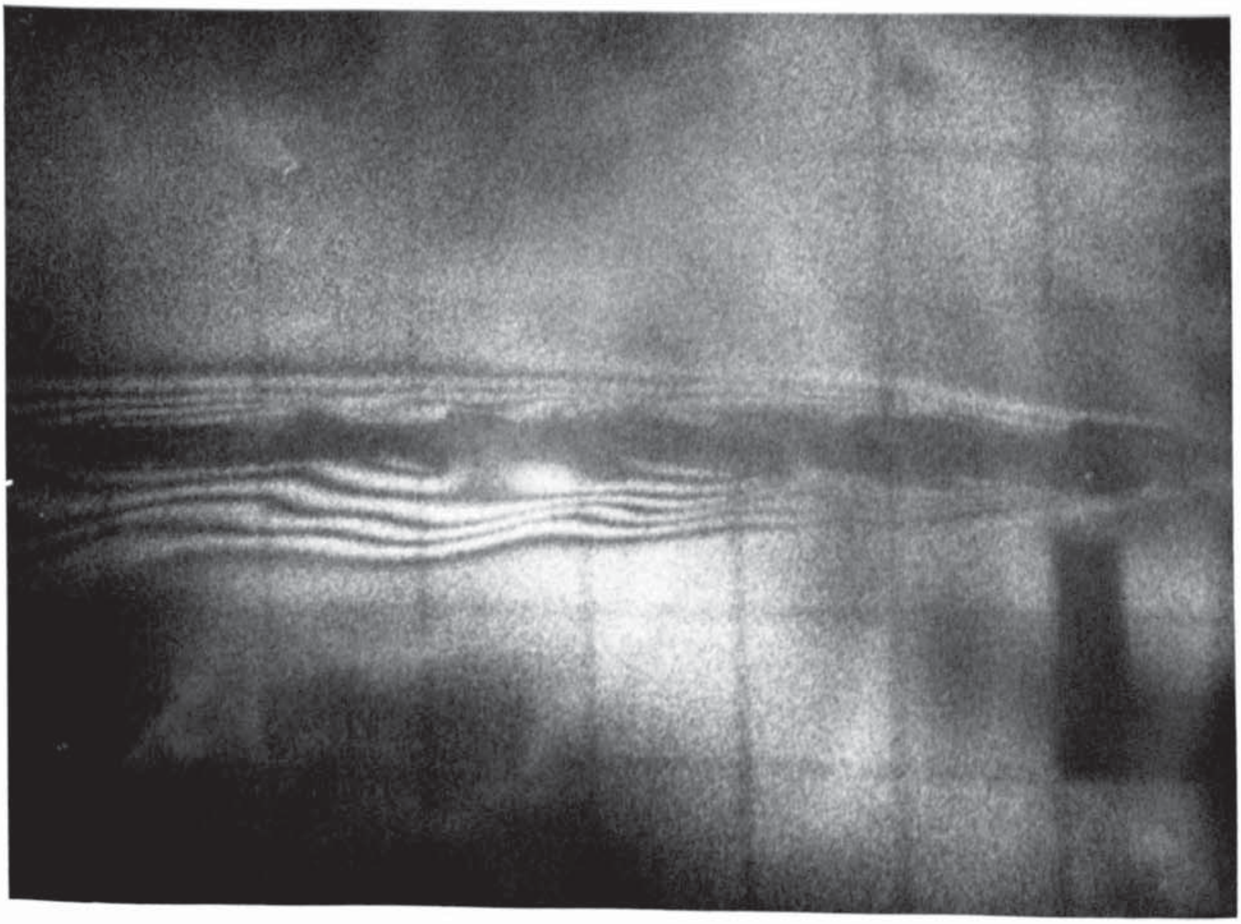

Figure 19 Airflow over louvre sample
(Airflow = 0.609 m/sec)

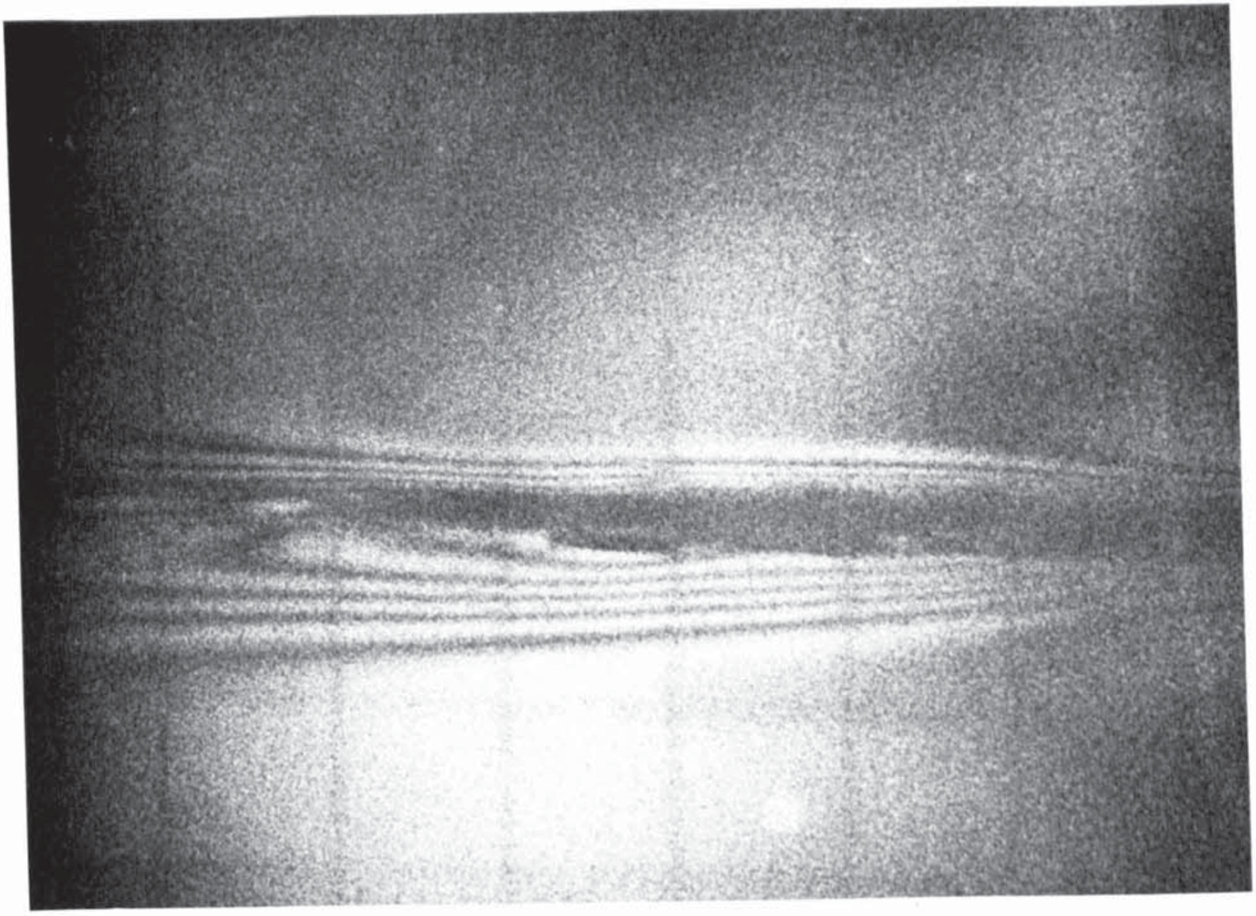

Figure 20 Airflow over louvre sample (Airflow = 0.609 m/sec)

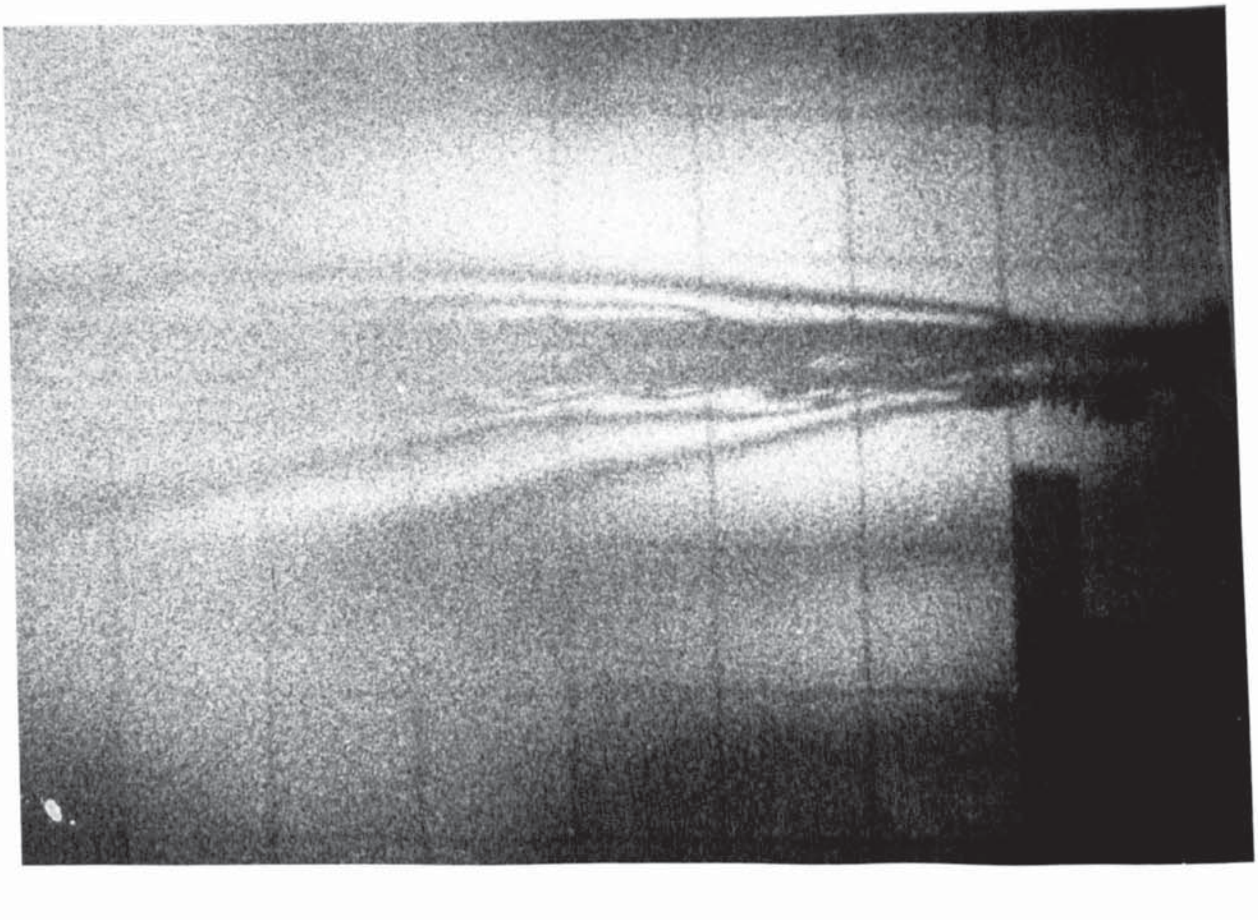

Figure 21 Airflow over louvre sample (Airflow = 1.22 M/sec)

Figure 22.
Block Sample
(Air Speed = 0.608 m/sec)

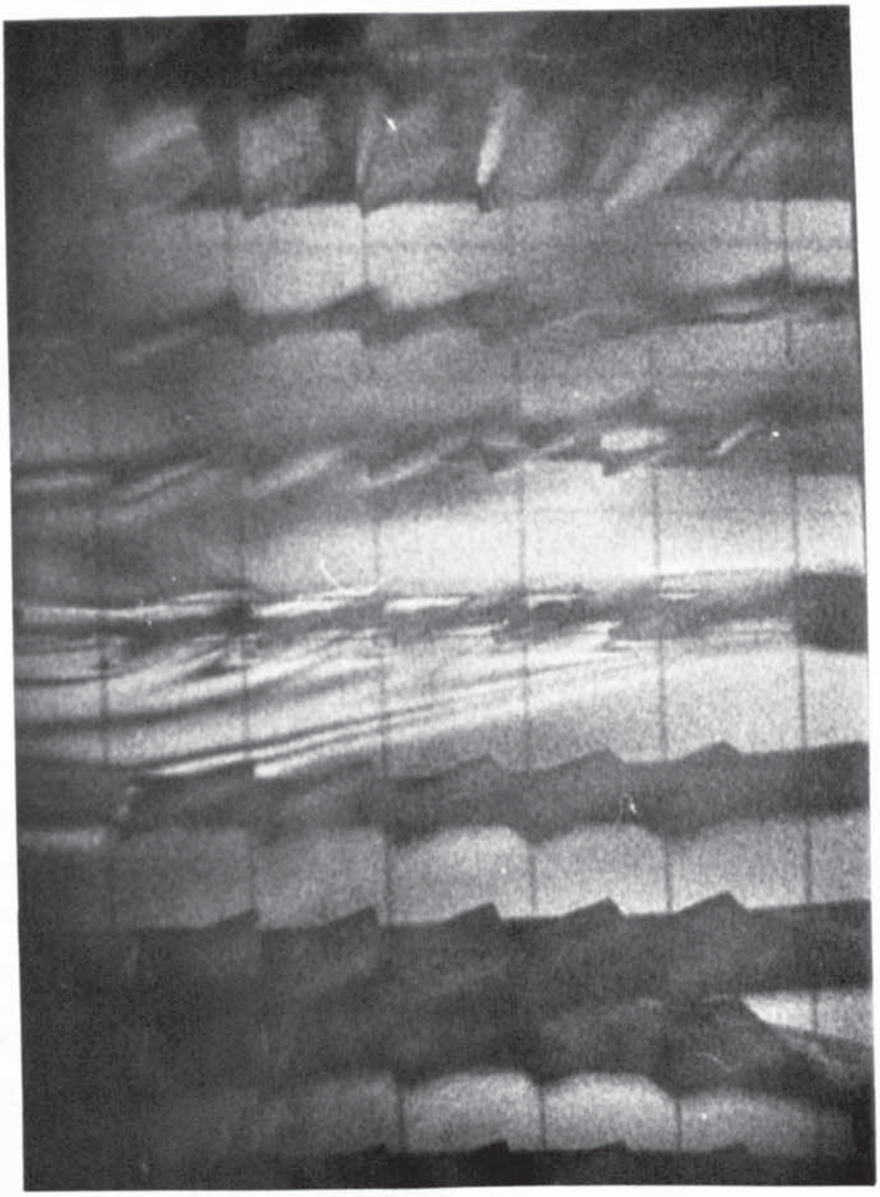

Enlargement of Central
Region to Show Fringe
Distribution

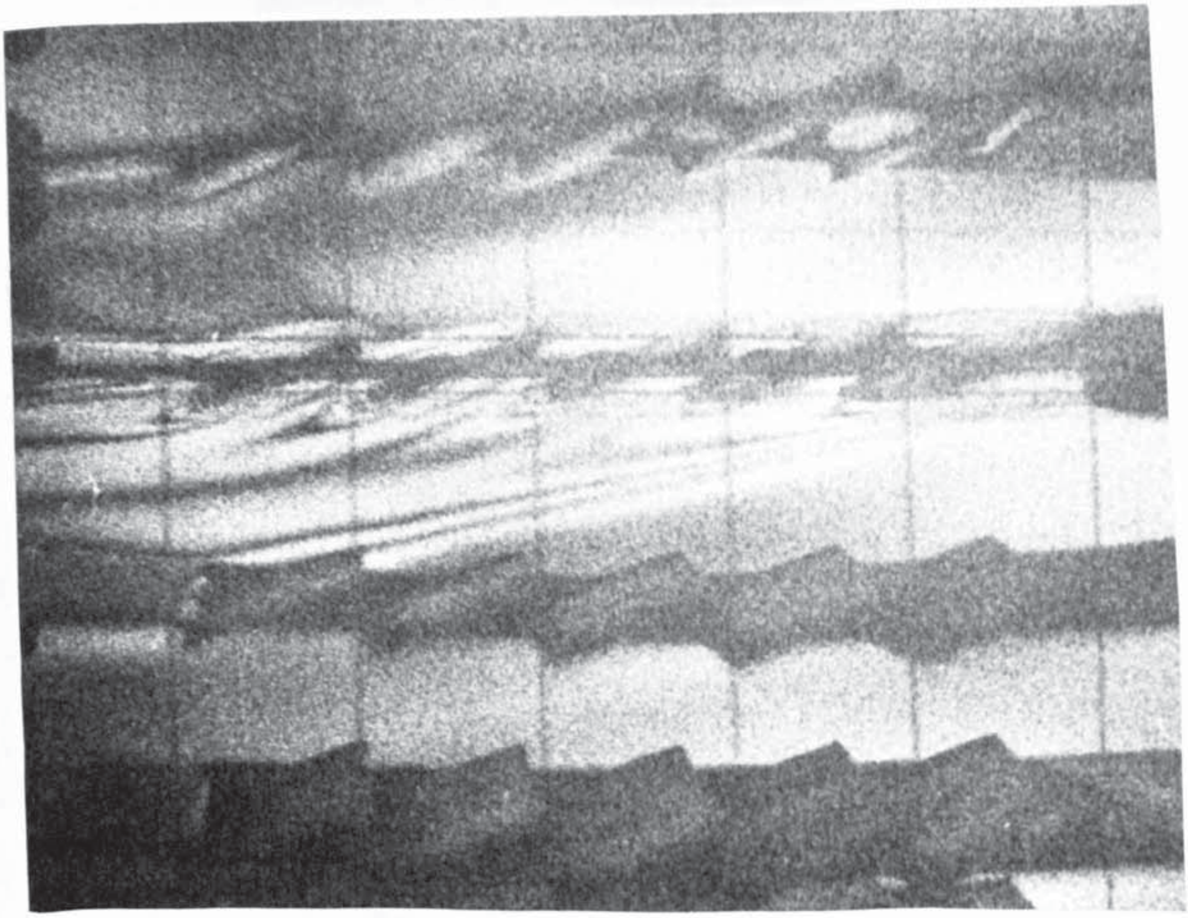

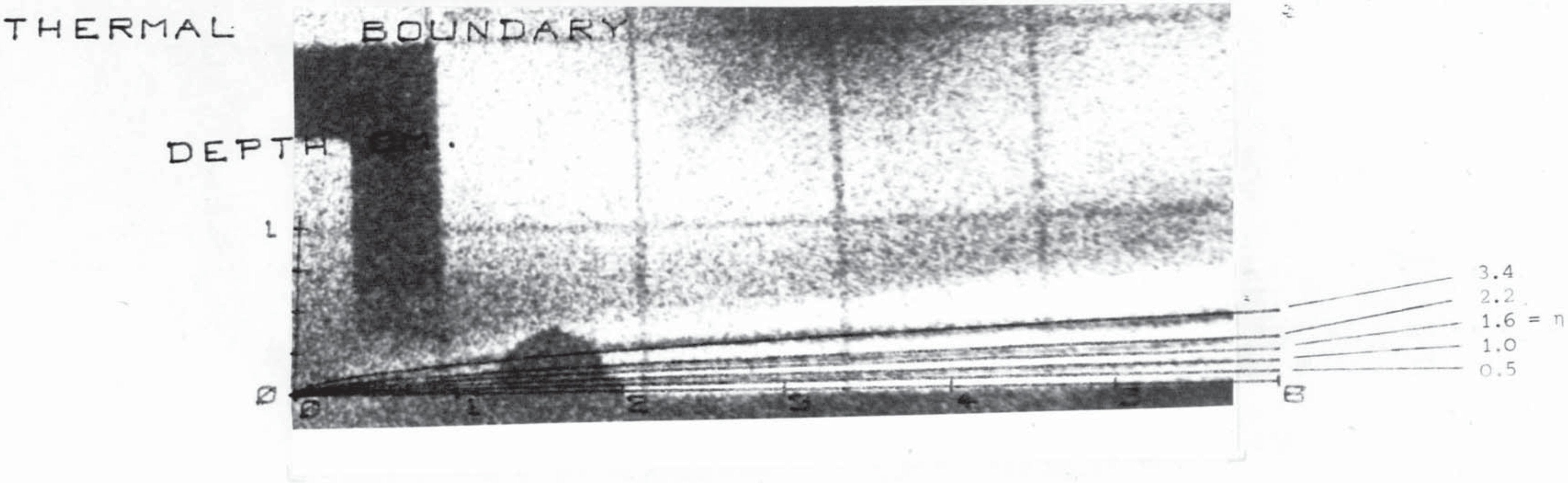

Fig. (23) Comparison between reconstruction of a hologram with a theoretical thermal fringe distribution. Airspeed 0.7 m/sec. Power applied to sample 10 watts, surface temperature 88°C, ambient 22°C.

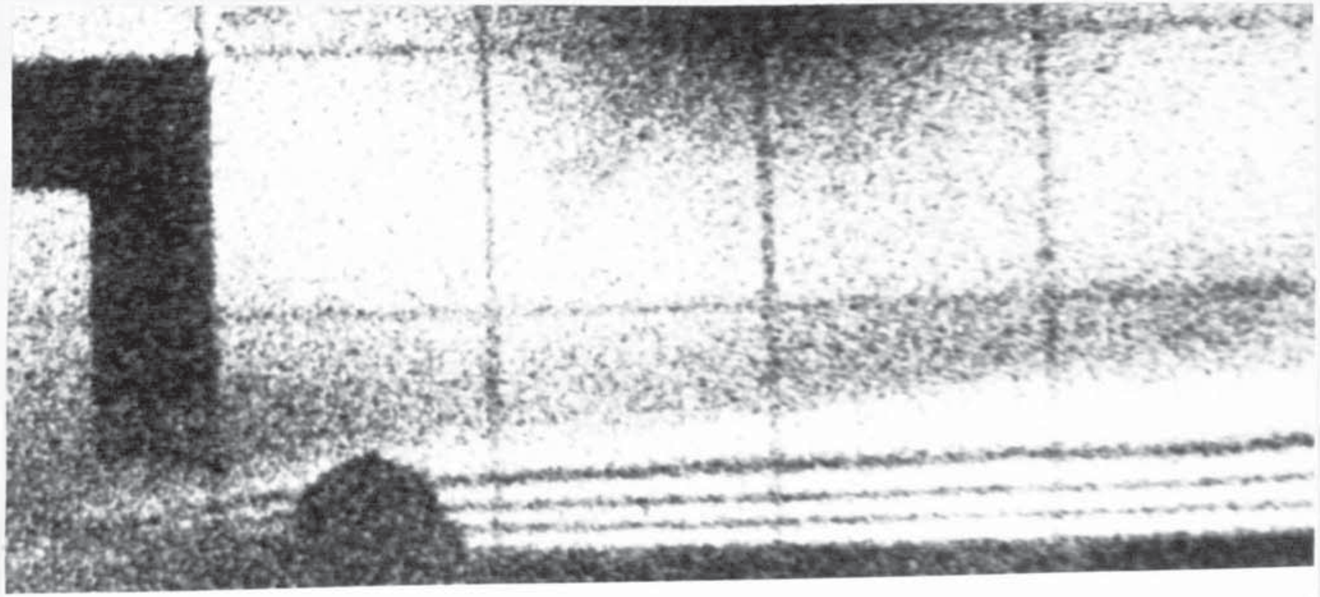

Fig. (23) Comparison between reconstruction of a hologram with a theoretical thermal fringe distribution. Airspeed 0.7 m/sec. Power applied to sample 10 watts, surface temperature 88°C, ambient 22°C.

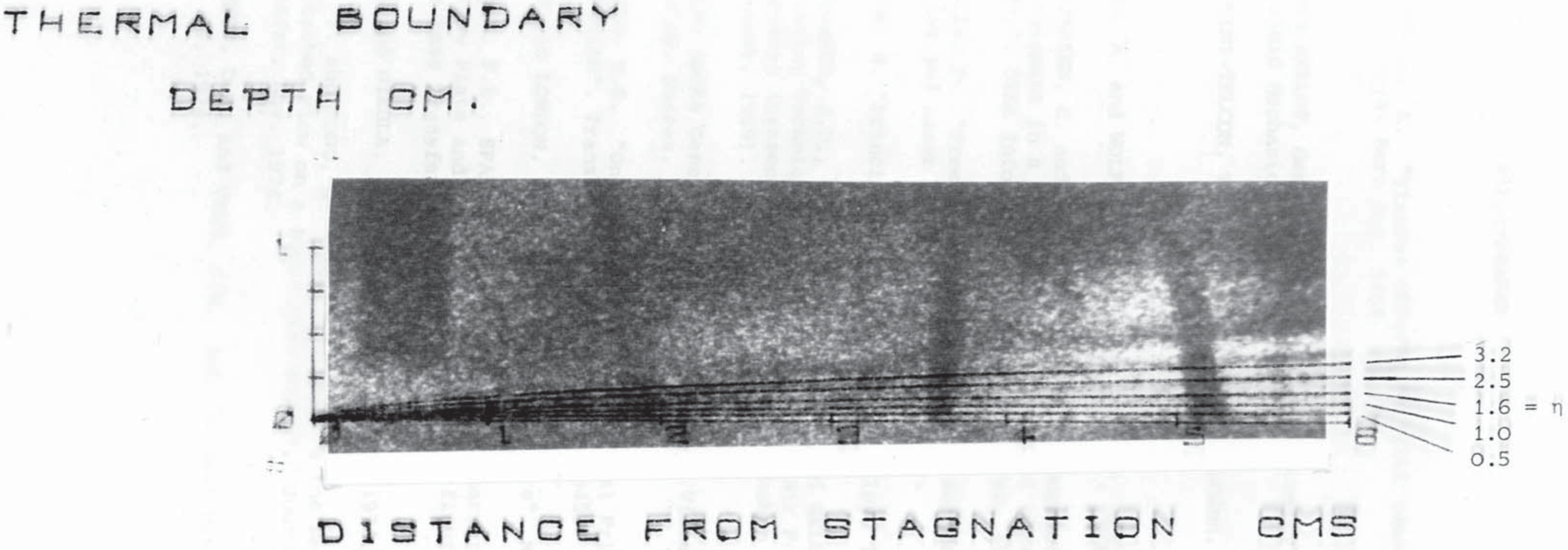

Fig. (24) Comparison between reconstruction of a hologram with a theoretical thermal fringe distribution. Airspeed 1.0 m/sec. Power applied to sample 14 watts, surface temperature 93°C, ambient 22°C.

BIBLIOGRAPHY

{1.1} MacMILLAN, A. "Viscous effects on Pitot tubes at low speed". Journ. Royal Aero Soc. 1954. Vol. 58.

{1.2} COMTE-BELLOT, Genevieve. "Hot Wire Anemometry". Annual Review of Fluid Mechanics, Vol. 8. 1976.

{1.3} TINSLEY-TELCON, T.T., Ltd., Northwood London.

{1.4} BORN, M. and WOLF "Principles of Optics", Pergamon Press, 1970.

{1.5} CASPERSEN, C. and SANSTRUP, H. "Laser Doppler Anemometer Measurement in a Low Velocity Wind Tunnel on a Flat Plate Model". DISA Information Paper No. 17, Feb. 1975.

{1.6} COOLEY, P. "Free Fringe Fields in Mach-Zehnder Interferometry" Optics and Laser Technology, August 1975.

{1.7} SMITH, H. "Principles of Holography", Wiley, 1969.

{1.8} TROLINGER, J.D., O'HARE, FARMER, W.M. and BELZ. "Applied Measuring Techniques". ARO, Inc. Arnold Air Force Station, Tennessee (presented at the A.I.A.A. Workshop Meeting, February, 1969).

{1.9} T.E.M. Smoke Generating Systems for Flow Visualisation. Crawley, Sussex.

{1.10} STOKES, G.G. "On the Theories of Internal Friction of Fluids in Motion". Trans. Cambr. Phil.Soc. 8, 1845.

{1.11} KAYS and LONDON. "Compact Heat Exchangers". McGraw-Hill, 1974.

{1.12} SABOYA, F.E., SPARROW, G.M. "Transfer Characteristics of Two-Row Plate and Tube Heat Exchanger Configurations". Int. I of Heat Mass Transfer, Vol. 19, No. 1, 1976.

{1.13} MONT and SIEGLA. J. Enng. Pwt..Vol. 96, 1974.

{1.14} OTA, T. and KONG, N. "Heat Transfer in the Separated and Reattached Flow on a Blunt Flat Plate". Journal of Heat Transfer, Nov. 1974.

{1.15} SWEENEY, D.W. and VEST, C.M. Int. J. Heat Mass Transfer, Vol. 17, 1974.

{1.16} KAPUR, D.N. and MACLEOD, N. Int. I. Heat Mass Transfer, Vol. 17, 1974.

{1.17} SPARROW, E.M. and GREGG, J.L. Transactions of the ASME (78).

{1.18} BERRY, M.V. and GIBBS, D.F. "The Interpretation of Optical Projections". Proc. Roy. Soc. London, Ser. 314, 1970.

{1.19} MERSEREAU, R.M. "The Digital Reconstructions of Multi-Dimensional Signals from their Projections". Proc. 10th Annual Allerton Conf., on Circuit and System Theory, Oct. 4-7, 1922.

{1.20} PETERS, T.M., SMITH, P.R. and GIBSON, R.D. "computer Aided Transverse Body Section Radiography", Brit. J. Radiol. Vol. 46, 1973.

{2.1} GABOR, D. "A New Microscopic Principle", Nature, 1948, No. 1948, No. 4098.

{2.2} STROKE, G.W. "An Introduction to Coherent Optics and Holography" Academic Press, 1966.

{2.3} LONGHURST, R.S. "Geometrical and Physical Optics". Longman, 1967.

{2.4} BRYANSTON-CROSS, P.J. "Technique for Producing a Clean Aligned Pin Hole for a Pulsed Laser System". Optics and Laser Technology. Oct. 1974.

{2.5} ROGERS, G.L. "The Design of Experiments for Recording and Reconstructing Three-Dimensional Objects in Coherent Light". I. Sci. Instrum., 1966, Vo. 43.

{2.6} I.C. Optical Systems. Franklin Road,London.

{2.7} ROGERS, G.L. "Wavelength Stabilisation with a Resonant Reflector". I.Opt.Am. Vol. 61, 1971.

{2.8} LAMBERTS, R.L. and KURTZ, C.N. "Bleached Holograms with reduced Flare Light". Spring Meeting of the Optical Society of America, 1970.

{2.9} SWEENEY, C.M. and VEST, D.W. "Holographic Interferometry of Transparent Objects derived from Phase Gratings". Appl. Opt., Vol. 9, 1970.

{2.10} FRASER, S.M. and KINLOCK, K. "Large Viewing angle Holograms". Jour of Scientific Instruments (Jou of Phys.E) Vol. 7, 1974.

{3.1} GORLIN, S.M. and SLEZINER, I.I. "Wind Tunnels and their Instrumentation". Israel Programme for Scientific Translations. 1966.

{4.1} GEBHARD, B. "Heat Transfer", McGraw-Hill, 1971.

{4.2} HUNTERLEC Ltd., Tonbridge, Kent.

{4.3} TRIPLEX SAFETY GLASS, Birmingham

{4.4} CHOPRA, K. "Thin Film Phenomena", McGraw-Hill, 1969.

{5.1} SCHLICHTING. "Boundary Layer Theory". 6th Edition, McGraw-Hill.

{5.2} EDE. An Introduction to Heat Transfer Principles and Calculations. Pergamon Press.

{5.3} FISHENDEN, M. and SAUNDERS, O.A. "An Introduction to Heat Transfer". Clarendon Press, Oxfort, 1950.

{5.4} Handbook of Heat Transfer.

{5.5} POHLHAUSEN. Zeitschr. f. angew. Math. und Mech.I., 1921.

{5.6} GOLDSTEIN, S. Modern Developments in Fluid Dynamics. Clarendon Press, 1938.

{6.1} Handbook of Electronics. "The T.T.L. Data Book for Design Engineers". Texas Instruments Ltd.

{6.2} KAYE, G.W. "Table of Physical and Chemical Constants and Mathematical Functions". Longmans 1966

{6.3} ECKERT and DRAKE. Heat and Mass Transfer. McGraw-Hill.

{6.4} McADAMS, W.H. Heat Transmission. McGraw-Hill.

{6.5} KAYE and LABY. "Tables of Physical and Chemical Constants" Longman.

{7.1} KAYS,,W.M. "Convective Heat and Mass Transfer". McGraw-Hill.

{7.2} RUTHEFORD, D.E. "Fluid Dynamics". Oliver Boyd Ltd., 1959.

{7.3} KENNARD, E.H. "International Flow of Frictionless Fluids Mostly of Invariable Density". David Taylor Model Basin Washington, D.C. 20007 Feb. 1967.

{7.4} STAFFORD, L.G. "Areodynamics and Design of Cars". University of London. Quest. 1973.

{7.5} HIRT, C.W. and RAMSHAW, J.D. "Prospects for Numerical Simulation of Bluff Body Aerodynamics". Los Alamos. Scientific Lab. Rep. LA.-UR-76-2112, 1976.

{7.6} BLASIUS. Grenzschichten in Flüssigkeiten mit kleiner Reibung. Z. Math. u. Phys. 56, 1908.

{7.7} KREYSZIG, E. "Advanced Engineering Mathematics", Wiley 1972.

{7.8} CURLE, N. "The Laminar Boundary Layer Equations", Clarendon Press, Oxford, 1962.

{7.9} VAN DYKE "Pertubation Methods in Fluid Mechanics". The Parabolie Press, 1964.

{7.10} TERRILL. "Laminar Boundary Layer near Separation with and without Suction". Dept. of Mathematics, University of Manchester. 1973.

{7.11} CHENG, S.J. "On the Stability of Laminar Boundary Layer Flow". App. Math. 1953.

{8.1} ASSELMAN, G.A.G., MULDER, J., MEIJER, R.J. "A High Performance Radiator", Philips Research Laboratories. No. 729132.

{9.1} BURN, A.H. "Methods of Reducing the Cost of Manufacturing Automotive Radiators from Copper based Materials". INCRA Project No. 219, I.M.I. Ltd., 1974.

{9.2} BEARD, R. and SMITH, G. "A Method of Calculating the Heat Dissipation from Radiators to Cool Vehicle Engines", Automotive Engineering Congress Detroit, Mich., 1971.

{9.3} TENKEL, F.G. "Computer Simulation of Automotive Cooling Systems". S.A.E. Paper 740087.

(A.1) FRANCON, M. "Modern Applications of Physical Optics, a brief review of interferometry". Interscience.

(A.2) HAVENER, G. and RADLEY, R. "Quantitative measurements Using Dual Hologram Interferometry" Aerospace Research Laboratories, U.S.A.F. 1972.

(A.3) BRACEWELL, R.N. and WERNECKE, "Image Reconstruction over a Finite Field". J.Opt.Soc.Am. Vol. 65, 1976.

(A.4) PULLAN, B.R., "Seeing Inside the Body: Medical Imaging". Physics Bulletin, Vol. 26, 1975.

(A.5) BENDER, BELLMAN, S. and GORDON, R. "Art and the Ribosome: A Preliminary Report on the Three-Dimensional Structures of Ribosome Determined by the Algebraic Reconstruction Technique". J.Theor.Biol., Vol. 29, 1970.

(A.6) SWEENEY, D.W. and VEST, C.M. "Reconstruction of Three-Dimensional Refractive Index Fields from Multi-directional Interferometric Information", Appl. Opt. Vol. 12, 1973.

(A.7) SWEENEY, D.W. "Measurement of Three-Dimensional Temperature Fields by Holographic Interferometry". Ph.D.Dissertation. The Univ. of Michigan, 1972.

(A.8) HARRIS, J. Opt. Soc. Am. Vol. 54, 1964.

(A.9) WILKINSON, J.H. und REINSCH. "Handbook for Automatic Computational-Linear Algebra". Springer-Verlag, Berlin, 1971.

ACKNOWLEDGEMENTS

I am pleased to take this opportunity to express my gratitude and thanks to Dr. J. Archer-Hall for many inspiring moments. Prof. S.E. Hunt and Mr P.B. Buckman for their confidence and support. To my always understanding wife Claudette and our baby daughter Zoe (born April 1st this year) to whom words are not enough. Finally to Dr. H. Hess.